

*Advances in Signal Processing
for Non Destructive Evaluation
of Materials*

Proceedings of the VIIth International Workshop

and selected papers from

*16th International Symposium on
Applied Electromagnetics and Mechanics (ISEM 2013)*

X. P. V. Maldague, Editor

É. du CAO

*à la frontière des connaissances
at the cutting edge of knowledge*

*Advances in Signal Processing
for Non Destructive Evaluation
of Materials*

Proceedings of the VIIth International Workshop

and selected papers from

*16th International Symposium on
Applied Electromagnetics and Mechanics (ISEM 2013)*

X. P. V. Maldague, Editor

É. du CAO

*à la frontière des connaissances
at the cutting edge of knowledge*

Publié par:

X. Maldague
É. Du CAO
38, Chemin du Cap-aux-Oies
Les Eboulements (Québec)
CANADA
GOA 2MO

Copyright © 2014 par X. Maldague. Tous droits réservés. *X. Maldague* ne peut être tenu responsable pour l'authenticité, l'exactitude ou les conséquences éventuelles résultant de l'usage des renseignements publiés dans ce volume. Les opinions et affirmations publiées dans ce volume ne reflètent pas nécessairement l'opinion de *X. Maldague*. Les produits ou services publicisés ou mentionnés dans ce volume ne sont pas endossés par *X. Maldague*.

Copyright © 2014 by X. Maldague. All rights reserved. X. Maldague is not responsible for the authenticity, accuracy of information herein or for any outcomes resulting from reliance thereon, and published opinions and statements do not reflect necessarily the opinion of X. Maldague. Products or services that are advertised or mentioned do not carry the endorsement or recommendation of X. Maldague.

ISBN 978-2-9809199-4-7

Dépôt légal - Bibliothèque nationale du Québec, 2014
Dépôt légal - Bibliothèque et Archives Canada, 2014

Imprimé au Canada
Printed in Canada

Table of contents

Preface	vii
----------------------	-----

VIIth IWASPND E

Thermophotonic radar and thermal coherence tomographies	3
A. Mandelis	
Pulsed IR Thermography applied to a two-layer system.....	5
P. Bison, A. Bortolin, G. Cadelano, G. Ferranini	
Thermography and Shearography coupling applied to NDT of CFRP tissue bonding interface on concrete by numerical simulations	11
L-D. Th��roux, J. Dumoulin and X. Maldague	
Post-impact damage characterization of pultruded jute/glass hybrid composites using infrared vision and optical techniques	17
S. Sfarra, D. Paoletti, C. Ibarra-Castanedo, A. Bendada, X. Maldague, C. Santulli and F. Sarasini	
Comparison between optical pulsed thermography and vibrothermography for the assessment of carbon fiber composite materials.....	25
H-M. Montrieux, P. Demy, C. Ibarra-Castanedo, A. Mertens, N. Gerlach, J. Lecomte-Beckers, X. Maldague	
Multivariate Infrared Signal Processing by Partial Least- Squares Thermography.....	29
F. L��pez, V. Nicolau, X. Maldague, C. Ibarra-Castanedo	
Use of infrared thermography to measure fiber orientation on carbon-fiber reinforced composites.....	35
H. Fernandes and X. Maldague	
A comparative study on probability of detection analysis of manual and automated evaluation of thermography images.....	41
Y. Duan, A. Osman, C. Ibarra-Castanedo, U. Hassler, X. Maldague	
Evaluation of laser-based active thermography for the inspection of optoelectronic devices	47
E. Kollorz, M. Boehnel, S. Mohr, W. Holub, U. Hassler	
The Effect of Pre-processing Techniques in Detecting Defects of Thermal Images.....	53
P. Hedayati Vahid, S. Hesabi, X. Maldague	

Selected papers from ISEM 2013

1- Nondestructive evaluation, electromagnetic and mechanical methods

Evaluation of magnetic particle amount and leakage flux density for quantitative evaluation of crack shape in magnetic particle testing	57
---	----

K. Fukuoka and I. Kawagoe	
Eddy Current Testing Using Support Vector Machines	63
M. Chelabi, T. Hacib and Y. Le Bihan	
Eddy-current quality control of the winding connections in the powerful generators	69
M. Roytgarts and A. Smirnov	
Measurement of Tube to Support Plate Gap for Alloy 800 Steam Generator Tubes using Transient Eddy Current	75
R. Underhill, V. K. Babbar, T. W. Krause, B. Lepine	
Quantitative Evaluation of Residual Strain in Austenitic Stainless Steels Using Electromagnetic Nondestructive Evaluation	77
S. Sato, R. Urayama, T. Sato, T. Uchimoto, T. Takagi, Z. Chen, Y. Yoshida	
Evaluation of Wall Thinning in Doubled Layer T-joints by SH-wave Electromagnetic Acoustic Transducers	79
T. Uchimoto, T. Takagi, T. Ichihara, S. Xie, G. Dobmann	
Numerical models of Eddy Current Testing problems for CPU/GPU based clusters.....	81
A. Chiariello, M. Nicolazzo, G. Rubinacci, A. Tamburrino, S. Ventre	

2- Electromagnetic sensors and actuators

Hysteretic Nonlinear Model of Magnetic Shape Memory Alloy Actuator	85
J. Xu, M-Y. Luan and Z-W. Zhu	
Research for a new actuator using electromagnetics and piezoelectrics.....	91
Z. An, M. Xu and B. Feng	
Design of flux-variable SPM synchronous motor.....	97
J-S. Jang, B-T. Kim	
Development and analysis of a novel limited angle torque motor with moving coil	105
Y. Xu, Y. Wei, J. Zou, K. Liu and H. Wang	
Study on Improved Cogging Torque Reduction Method for Single-Phase Brushless DC Motor	111
Y-U. Park, J-Y. So, J-H. Cho, S-H. Rhyu, and D-K. Kim	
Improvement of Torque Characteristics of Switched Reluctance Generator Using Arc Shaped Rotor Pole	117
D. Choi, B. Kim and Y. Cho	
Optimization of Axial Air Gap Single Phase Permanent Magnet Stepper Motor with Claw Poles	123
J. Zou, J. Zou , Y. Xu , W. Li , W. Yanyu	

The Analytical Evaluation of High Speed and High Efficiency Induction Motor for Spindle	129
D-k. Hong, J-H. Choi, D-J. Kim, Y-D. Chun, B-C. Woo, D-H. Koo	
Cogging Torque and Torque Ripple Reduction of IPMSM with Notched Rotor by FEM with Optimization Method	131
H-Y. KIM, Y-B. Kim, W-Y. Lee and P-S. Shin	
Optimization Design of the Rotor Structure of LSPM Using Response Surface Method	133
K-H. Kim, J-H. Jang, W-S. Kang Y-H. Cho	
A Study of Parameter Determination on Interior Permanent- Magnet Synchronous Motor for Agricultural Electric Vehicle	135
Y-K. Kim, J-J. Lee, S-H. Rhyu, and I-S. Jung	
Metal-containing diamond-like carbon composite films for fatigue frequency monitoring	137
H. Miki, M. Takahashi, T. Takeno, J. Fontaine, P. Wang, T. Takagi	

3- Analysis and simulation of electromagnetic devices

Theoretical analysis of energy harvesting from the improved nonlinear magnetic suspension	141
Y. Luo, Y. Bo and X. Zhang	
AC Copper Losses Analysis of the Ironless BLDCM used in a Flywheel Energy Storage System.....	147
K. Liu, J. Hu, J. Zou, Y. Wei and G. Zhu	
Basic Study on a High Efficient Heating of IH Earthenware Pan by the Finite Element Method	153
A. Fujiwara , J. Arai , M. Kobayashi , H. Yonemori	
Design and Characteristic Analysis of Interior Permanent Magnet Synchronous Generator with Increased Magnetic Flux	159
H-G. Jeong , J-Y. So , D-H. Chung , C-H. Cho , and D-K. Kim	
Transient Performance of Novel Permanent Magnet Synchronous Motors Made of Soft Magnetic Composite Core.....	165
T. Ishikawa, Q. Viet Ho, K. Takahashi, and N. Kurita	
Full 3D Eddy Current and Temperature Field Analysis of Large Hydro-generators in Leading Phase Operations	171
N. Wang, L. Liu, H. Zhou, S. Yang	
Three-Dimensional Simulation of a Corona Discharge in a Needle-Plane Configuration	177
J. C. Momente , L. A. Neves , G. F. D. Zafalon , A. S. R. Pinto , C. R. Valêncio, S. Yang and J. M. Machado	

High frequency transmission line model of induction motor employing 3D electromagnetic field simulation..... 181

H. V. Jorks, E. Gjonaj, T. Weiland

4-Electromagnetic smart fluids, electromagnetic processing of materials

Vibration Control System with Digitally Adjustable Electromagnetic Damping and Stiffness 185

C. Zhai, M. Xu and B. Feng

Accurate Computations of the Magnetic Field for Magnetic Fluid Seal..... 191

Z. Jibin, J. Zou , Y. Xu, M. Zhao, K. Liu, Y. Wei , H. Wang

A Novel MR Fluid Shock Absorber with MS Materials..... 197

J-H. Lee, D-Y. Kim, K-H. Hwang, Y-H. Lee and M-K. Park

5-Innovative materials and applications

Broadband Thermo-Acoustic Ultrasound Transducers For Non Contact Materials Testing..... 205

M. Daschewski, A. Harrer, J. Prager, M. Kreutzbruck, T. Lange, M. Weise and U. Beck

Charge Measurement With Farady Cups And Labview 207

K. Dastoori , D. Thompson, B. Makin

Design and Development of MR Actuator with Safety for Leg Power Assist Devices 209

M. Nakano, H. Nakano, K. Tsuchiya

6- Electromagnetic functional materials and adaptive systems

Two-position Magnetic Lock..... 213

M. Woloszyn , P. Jankowski

Effect of the magnetic field in the air zone for receiving guided waves based on magnetomechanical effect..... 219

J. Xu, D. Kong, X. Wu, M. Cong

7- Applied superconductivity

Development of noncontact Flywheel system with High Temperature Superconducting magnetic bearing..... 227

I. Murakami, K. Nakashima, M. Gyoda, T. Shimada, and Y. Ando

8- Laser and particle beams, plasmas

Free vibration states of a slender beam with a linear time varying mass235

C. Ma, X. Zhang, Y. Luo and C. Zhang

9- Micro electro-mechanical systems (MEMS)

System for detecting the presence of shielding wires in transmission lines by RF scattering..... 243

E. A. B. Santos , A. J. B. de Oliveira , M. T. de Melo , J. F. A. G Wavrik

10- Nanotechnology applications

The Interpolating Element-Free Galerkin Method Applied to Quantum Wells and Quantum Dots Infrared Photo-Detectors..... 251

L. K. Sperotto, A. Passaro, G. N. Marques

11-Biomedical engineering

Sensitivity of Magnetic Probes for Identifying Sentinel Lymph Nodes: A Numerical Study.. 255

M. Sekino, T. Ookubo, H. Ohsaki, M. Kusakabe

12- Inverse problems

Analysis of an inverse problem in QWIP device 259

D. Pedroso, C. Delfino, A. Passaro, G. Vieira

Preface

The *7th International Workshop on Advances in Signal Processing for Non Destructive Evaluation of Materials (7th IWASPND E)* was held at the Pavilion Alphonse-Desjardins of Université Laval, Quebec City (Quebec, Canada) from July 31th to August 2nd, 2013. The *7th IWASPND E* was a combined event along with the *16th International Symposium on Applied Electromagnetics and Mechanics (ISEM 2013)*.

The idea to organize such a joint event was indeed fruitful for attendees since this was an opportunity for more interaction and discipline cross fertilization. Interestingly, additional papers from *ISEM 2013* were published as a special issue of the *International Journal of Applied Electromagnetics and Mechanics* by IOS Press¹.

Scientific content

These proceedings contain a selection of full-length papers, which were submitted just after the combined event with the scientific sponsorship of the Japan Society of Applied Electromagnetics and Mechanics, the Japan Society of Maintenology and the support of the *MIVIM Canada Research Chair*².

The present volume contains 51 papers. In addition to the *7th IWASPND E* papers especially dedicated to infrared thermography for Nondestructive Evaluation, the proceedings propose papers on the following topics: Nondestructive Evaluation, electromagnetic and mechanical methods; Electromagnetic sensors and actuators; Analysis and simulation of electromagnetic devices; Electromagnetic smart fluids, electromagnetic processing of materials; Innovative materials and applications; Electromagnetic functional materials and adaptive systems; Applied superconductivity; Laser and particle beams, plasmas; Micro electro-mechanical systems (MEMS); Nanotechnology applications; Biomedical engineering; Inverse problems.

To be noted, a 581 page abstract book including accepted short papers (2 page summaries) was published and presented at the meeting, including five plenary talks by prominent experts on topics of emerging interest³.

On the agenda this year again, was the *Workshop Best presentation Award*: the paper from Dr. Fernando López was selected to receive the 2013 Award (see p. *ix*).

1. refer to the website for the details: www.iospress.nl.

2. *Multipolar Infrared Vision Infrarouge Multi-polaire*.

3. *Abstract Book of the 16th International Symposium on Applied Electromagnetics and Mechanics - International Conference and of the 7th IWASPND E Workshop*, X. Maldague (Ed.). Pub. Éd. du CAO, 581 p., 2013, ISBN 978-2-9809199-3-0.

International Workshop Context

The *VIIth Workshop* edition has deep ground since we have to go back in August 1993 when the *IInd Workshop* took place. At the wrap-up session, attendees were quite enthusiastic about a Workshop Series with editions to be held every four years, hence: the *VIth Workshop* took place in 2009, the *Vth* (2005), the *IVth* (2001) and the *IIIrd Workshop* in 1997 commemorating the tenth anniversary of the *Ist Workshop* which was organized in August 1987 by Professor Chen of the Southeastern Massachusetts University. Besides the *Ist* edition held in Lac Beauport, a nice resort area located in the hills, at some 20 minutes North of Québec City and the *VIth* edition held in London (Ontario), all the Workshops took place on Université Laval's campus.

Interestingly, as for the *VIIth* edition, the *VIth* edition was also a joint event co-organized with the *Canadian Institute for NonDestructive Evaluation (CINDE)* as the first "NDT in Canada" conference.

Close to two hundred (171 to be exact) people attended the combined event *VIIth IWASPND + ISEM 2013*, from 15 different countries, making the conference a truly international event!

Interestingly, the experience gained from the past two Workshop editions organized as «combined event» indicates this is indeed a winning approach and thus we are planning also the same approach for the *VIIIth Workshop* edition already planned for late Summer 2017, please check the website¹ for the latest news!

Finally, we would like to thank our principal sponsors: the Japan Society of Maintenology, the Japan Society of Applied Electromagnetics and Mechanics, the Université Laval and the companies FLIR, Infolytica Corporation, JENOPTIK | Defense, Techno-Test, Visioimage. Their generous support made the event successful. Many thanks are due to the *MIVIM Canada Research Chair* and in particular to Ms. Clémence Gaborieau for her dedicated administrative support. Technical and administrative help and support of the Electrical and Computing Engineering Department of Université Laval is also acknowledged. We would like also to thank the *7th IWASPND + ISEM 2013 Local Organization Committee*². A special thank is also due to all participants for their kind cooperation and participation which was *essential* to the success of the event.

Prof. Xavier Maldague, Université Laval, Canada
Director *7th IWASPND* and Chairman of *ISEM 2013*

1. intl.gel.ulaval.ca.

2. Abdelhakim Bendada, Marc Genest, Clemente Ibarra-Castanedo, Daniel Lévesque Catalin Mandache, Louis St-Laurent.

VIIth IWASPND E Best Presentation Award

presented to

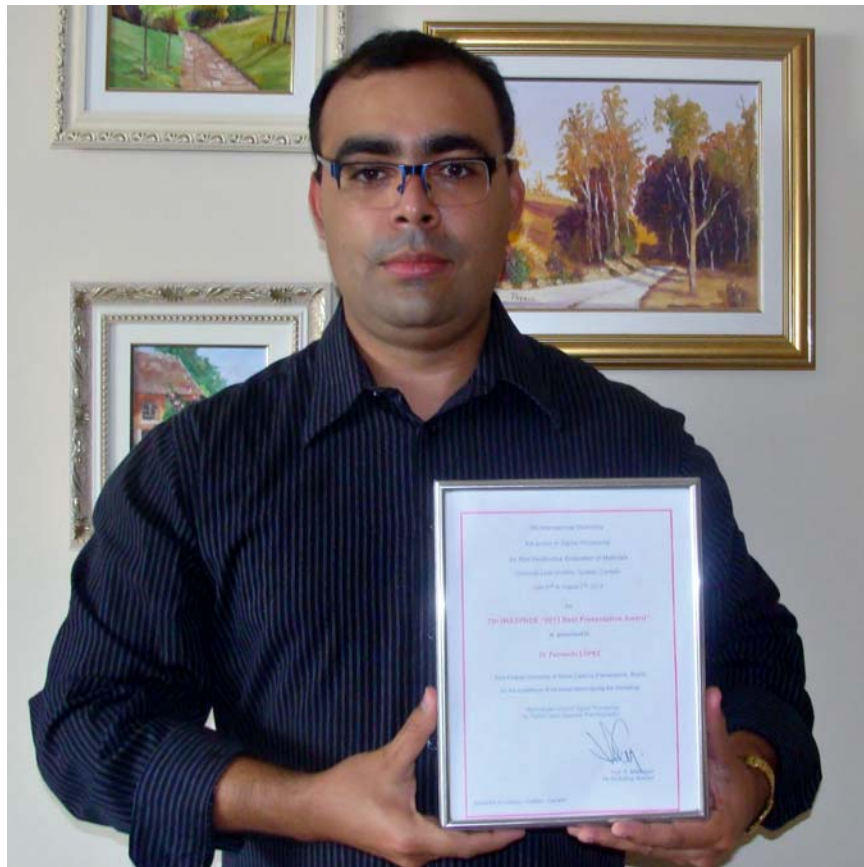
Dr. Fernando LÓPEZ

from

Federal University of Santa Catarina (Florianopolis, Brazil)

for the excellence of his paper :

Multivariate Infrared Signal Processing by Partial Least-Squares Thermography
Co-authors: V. Nicolau, X. Maldague, C. Ibarra-Castanedo



Picture showing Dr. LÓPEZ holding the Award plate.

The *Best Presentation Award*, instituted in 2001, materializes the strong dedication of the Workshop to excellence. It is awarded to the best presentation. Selection proceeds through a secret polling with all attendees being invited to cast their vote at the end of the event.

VIIth IWASPND E

Thermophotonic radar and thermal coherence tomographies

Andreas MANDELIS

Center for Advanced Diffusion-Wave Technologies (CADIFT), Department of Mechanical and Industrial Engineering, University of Toronto, Toronto, Ontario, M5S 3G8, Canada.

Abstract. Energy transport in diffusion-wave fields is gradient driven and therefore diffuse, yielding *depth-integrated* responses with poor axial resolution. Traditional diffusion-wave techniques, limited by the physics of parabolic diffusion, can only produce depth-integrated planar images as they are unable to generate three-dimensional subsurface imaging. This talk will present two new imaging methods developed in the CADIFT for enabling parabolic thermal-wave fields to exhibit energy localization akin to propagating hyperbolic wave-fields. This approach when used with a mid-IR camera results in *depth-selective* (or depth-resolved) photothermal imaging which not only improves axial and depth resolution, but also allows for deconvolution of individual responses of superposed axially discrete sources, opening a new field of subsurface Photothermal Coherence Tomography (PCT) using thermal waves. In this talk I will present two novel thermal-wave imaging methodologies: Matched filter binary phase coded (BPC) PCT and truncated-correlation photothermal coherence tomography (TC-PCT). The physical principles of these methodologies and examples of imaging applications to engineering materials and biomaterials will be discussed.

1 Binary phase coded Photothermal Coherence Tomography

First, I will briefly introduce thermophotonic radar imaging principles and techniques using chirped or BPC modulation, methods which can break through the maximum detection depth/depth resolution limitations of conventional photothermal waves. Using matched-filter principles, BPC-PCT, a methodology enabling parabolic diffusion-wave energy fields to exhibit energy localization akin to propagating hyperbolic wave-fields will be described [1]. It allows for deconvolution of individual responses of superposed axially discrete sources, opening a new field: depth-resolved thermal coherence tomography. Several examples from dental enamel caries diagnostic imaging to metal subsurface defect thermographic imaging will be discussed. Fig. 1 shows BPC-TCT resolving the step of a sub-surface wedge sample.

2 Truncated-correlation Photothermal Coherence Tomography

Next, I will introduce our very recent development of truncated-correlation photothermal coherence tomography (TC-PCT) [2], which exhibits the highest degree of energy localization and image resolution in a parabolic diffusion wave field to-date. TC-PCT enables three-dimensional “crisp” visualization of subsurface features/discontinuities which is not otherwise possible with known optical or conventional photothermal imaging techniques. Examples to be presented include imaging of solids with intricate sub-structures, specifically, holes in steel, trabecular bone structure through cortical and soft tissue overlayers, structural changes in animal bones following demineralization induced bone loss (artificial osteoporosis), and burn depth profiles in tissues. As a consequence of its high axial resolution and nearly lossless character, TC-PCT exhibits sub-surface depth profilometric capabilities over several (~ 4) thermal diffusion lengths, well beyond those of today’s thermal-wave probes. From the perspective of biomedical laser safety, TC-PCT is maximum-permissible-exposure compatible.

Fig. 2 shows TC-PCT “crisp” images of a cortical – cancellous goat interfaces bone breaking through the diffusion resolution and depth barriers.

3 Conclusions

In addition to biomedical diagnostic imaging and engineering materials testing, the two novel non-ionizing modalities constitute photothermal analogs of optical coherence tomography and open the way for applications in diverse areas of research where three-dimensional sub-surface depth-profiling is required.

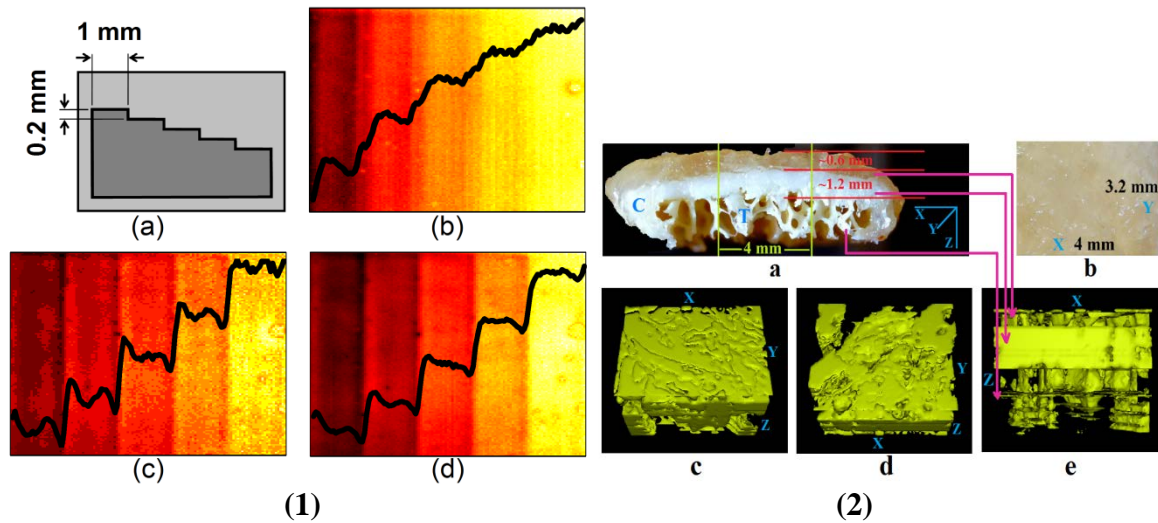


Figure 1: (a) cross section of a step wedge sample. (b) Conventional lock-in thermography phase. (c) BPC peak delay time, and (d) BPC phase images of the step wedge sample using 16-bit code at 3Hz (acquisition time = 5.33s). **Figure 2.** Non-ionizing tomography of bone. (a) Cross-sectional photograph of a goat rib-bone with soft tissue overlayer. Labels C and T refer to the cortical and trabecular regions, respectively. (b) The irradiated tissue surface. (c) The photothermal volume tomogram observed from the tissue surface. (d) The tomogram observed from the trabecular bottom surface. (e) Cross-sectional TC-PCT corresponding to (a).

References

- [1] N. Tabatabaei and A. Mandelis, “Thermal coherence tomography using match filter binary phase coded diffusion waves” *Phys. Rev. Lett.* **107**, 165901 (5 pages) (2011).
- [2] S. Kaipilavil and A. Mandelis, “Truncated-Correlation Photothermal Coherence Tomography: “Crisp” sub-surface imaging breaking through the diffusion resolution and depth barriers” (submitted)

Pulsed IR Thermography applied to a two-layer system

Paolo BISON, Alessandro BORTOLIN, Gianluca CADELANO, Giovanni FERRARINI

ITC-CNR, C.so Stati Uniti 4, 35127, Padova, Italy

Abstract. Pulsed Infrared Thermography is a tool utilized more and more to measure thermal parameters. Sharing the same basic principles of Photothermal Techniques it extends its applicability thank to its imaging capabilities. A data reduction transforms temperature data as a function of time in a log-log space whose 2nd logarithmic derivative presents extrema that allow estimating diffusivity or thickness of a slab and of a two-layer system as well.

1 Introduction

Infrared Thermography (IRT) is a tool utilized more and more to measure thermal parameters and/or the geometry of defects inside materials or in their boundaries [1,2]. Possible fields of applications are: buildings for energetic evaluations [3,4], material science to evaluate ageing under stressing conditions [5], corrosion in pipelines [6].

Sharing the same basic principles of Photothermal Techniques (PT), IRT extends the IR Radiometry applications thank to its imaging capabilities. Contrary to PT community, where thermal waves are widely used to actively stimulates materials under test, in IRT community pulsed techniques are dominant. The classical pulsed PT to measure thermal diffusivity of a homogeneous slab is the Laser Flash technique originated by Parker's work [7]. The ratio of thermal diffusivity by the squared thickness of the plate can be estimated either by measuring times of specific events in the thermal diffusion process after the pulse, or by fitting data by the analytical model of the thermal process. More recently, a data reduction technique of pulsed IRT data has been introduced [8], that transforms temperature data as a function of time in a log-log space. With this representation, data can be fitted by simple polynomial functions describing the deviation from a straight line of -0.5 slope, that is the behaviour of a semi-infinite body. It has been recognized that the 2nd logarithmic derivative of the log-log data presents a maximum in correspondence of a time that allows estimating the ratio between diffusivity and the squared thickness of the slab [9, 10]. The log-log representation has been further applied in the case of a two-layer system [11].

2 Flash technique in reflection mode

The classical experimental configuration for the Laser Flash technique [7] is done in the so called *transmission mode*, i.e., one side of a slab is heated by a short pulse of light while the temperature rise is measured on the other side. In some experimental situations the back side is not accessible, e.g. on in-situ experiments of pipes or in many cases when thermal NDT must be carried out, and therefore the *reflection mode* must be utilized. The solution of the heat conduction problem on one side of a slab of thickness L , heated by a pulse and considering negligible the exchange with the environment is given by the following equation:

$$T(t) - T_0 = T_\infty \left[1 + 2 \sum_{n=1}^{\infty} e^{-n^2 \pi^2 Fo} \right] \quad (1)$$

where $T_\infty = Q/(\rho c L)$ (being Q the energy of the pulse, ρ the density and c the specific heat), T_0 the initial temperature and $Fo = \alpha t/L^2$ the Fourier number (α is the thermal diffusivity and t is time). Figure 1a shows the experimental scheme in reflection mode, while in Fig. 1b the temperature behaviour of the front and back (rear) side of the slab is represented.

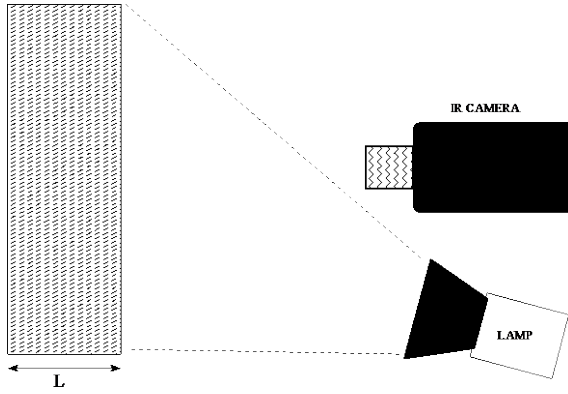


Figure 1a: Experimental lay-out of the Flash technique in reflection mode.

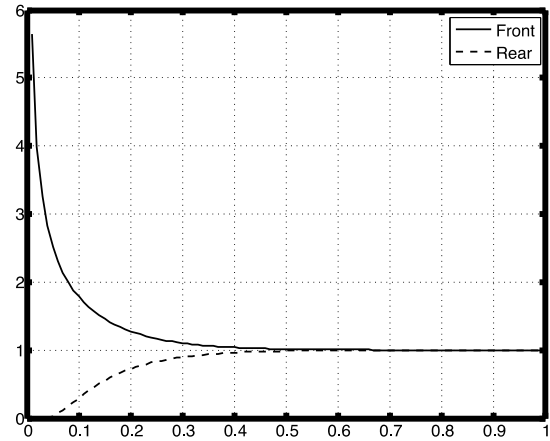


Figure 1b: temperature behaviour of front and back sides of the slab.

2.1 Theta functional relation

It is worth noting how eq. (1) can be transformed in a perfectly equivalent form by means of the functional relation of the *theta* function [12,13]:

$$\vartheta(x) = \frac{1}{\sqrt{x}} \vartheta\left(\frac{1}{x}\right) \quad (2)$$

Equation (2) transforms eq. (1) in the following:

$$T(t) - T_0 = T_\infty \frac{1}{\sqrt{\pi Fo}} \left[1 + 2 \sum_{n=1}^{\infty} e^{-\frac{n^2}{Fo}} \right] \quad (3)$$

where $x = \pi/Fo$. One can recognize that the first term of eq. (3), before the square brackets, represents the solution of the semi-infinite body heated by a pulse. The function inside the square brackets *modulates* the behaviour of the semi-infinite body by forcing the solution to be that of a slab. The function in square brackets approaches asymptotically $\sqrt{\pi Fo}$ as $Fo \rightarrow \infty$, i.e. $t \rightarrow \infty$, leading $T(t) \rightarrow T_\infty$ as in eq. (1). Figure 2a and 2b shows the behaviour of the two functions composing eq. (3), assuming $T_\infty = 1$.

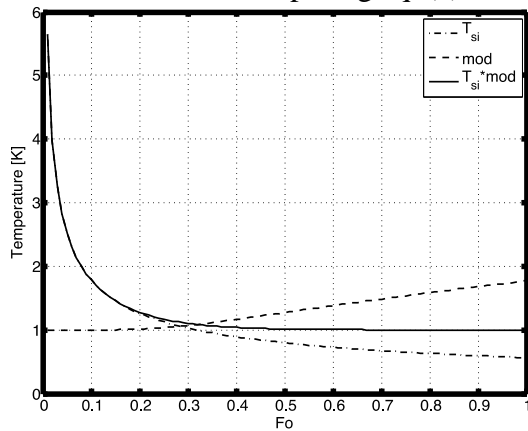


Figure 2a: equation (3) is plotted (continuous line) together with the two factor functions: the one representing the semi-infinite body solution (dash-dot line) and the infinite series representing a modulation of the semi-infinite behaviour (dashed line).

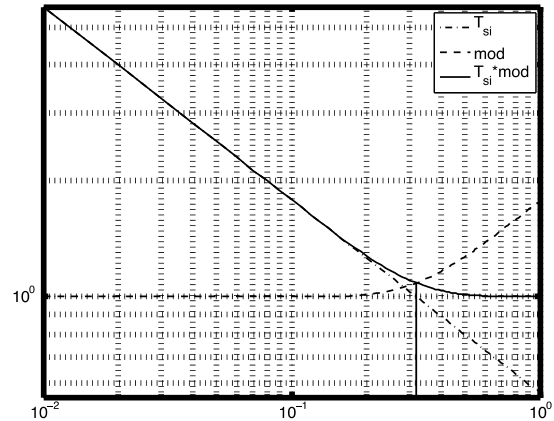


Figure 2b: same as in figure 2a but represented in log-log scale. The point where $T_{si}=1$ (in general $T_{si}=T_\infty$) corresponds to $Fo=1/\pi$. That corresponds also to the maximum of the second derivative of eq. (3) in log-log scale.

In Fig. 2b, where a log-log representation is used, the noticeable point $Fo=1/\pi$ is displayed, that allows to evaluate the thermal diffusivity. This point is more easily identified by looking at the maximum of the 2nd logarithmic derivative of eq. (3) [9]. That can be easily computed once a suitable polynomial fitting of the logarithm of temperature vs. the logarithm of time has been computed [8] on the experimental data.

2.2 Estimation from experimental data

Figure 3a shows the experimental data obtained on a slab of AISI 304 heated on one side by a laser pulse of duration 1 ms. The temperature is obtained by recording a sequence of images with a thermographic camera with a sampling frequency of 500 Hz. Superimposed on the same figure is the fitting function obtained by non-linear least squares fitting of the data [4]. In Fig. 3b the 1st and 2nd logarithmic derivative is represented. It is obtained after fitting the experimental data with a polynomial function of 9th degree. The maximum of the 2nd derivative identify a special value of time that allows determining the ratio between thermal diffusivity and the squared thickness of the slab. The results in the two cases of non-linear least squares fitting and identification of the 2nd derivative of the log-log data is presented in Table 1. The estimation of thermal diffusivity is obtained after the measurement of the thickness of the slab ($L=0.001474$ m) and the values in the two cases are different of less than 7 % (the precision of the classical Laser Flash technique is around 5 %).

Table 1: estimation of thermal diffusivity by non-linear least squares fitting (NLF) and by identification of the maximum of the 2nd logarithmic derivative (LOG-LOG). The thickness of the slab is $L=0.001474$ m.

	$\log(t^*)$	t^*	αL^2	α [m^2s^{-1}]
NLF	n.a.	n.a.	1.78	$3.87 \cdot 10^{-6}$
LOG-LOG	-1.79	0.1670	$(\pi \cdot 0.1670)^{-1}$	$4.14 \cdot 10^{-6}$

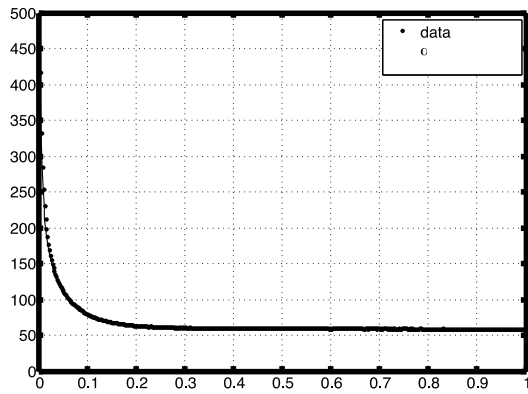


Figure 3a: equation (3) is used to fit the experimental data by means of a non-linear least square fitting procedure. The main parameter of interest is the ratio between diffusivity and the squared thickness of the slab.

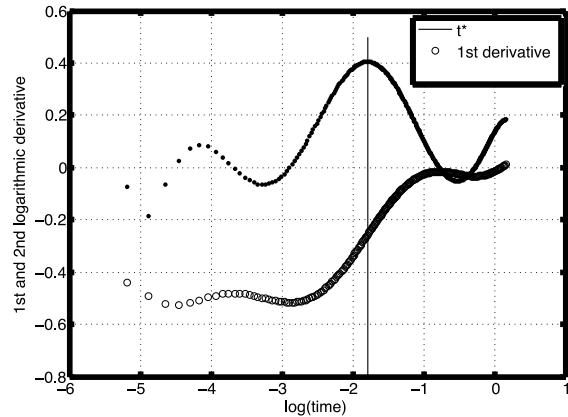


Figure 3b: after fitting the logarithm of temperature vs logarithm of time with a polynomial function of 9th degree the 1st and 2nd derivative is computed and the maximum of the 2nd derivative is used to evaluate the ratio between diffusivity and the squared thickness of the sample as in Tab. 1.

It is worth comparing the residual after the fitting in the two cases. This is shown in Figure 4a and 4b for the NLF and LOG-LOG respectively. In the first case the difference between the eq. (3), evaluated with the optimum fitting parameters, and the data is represented, while in the second the difference between the logarithm of temperature and the 9th degree polynomial fitting function is shown.

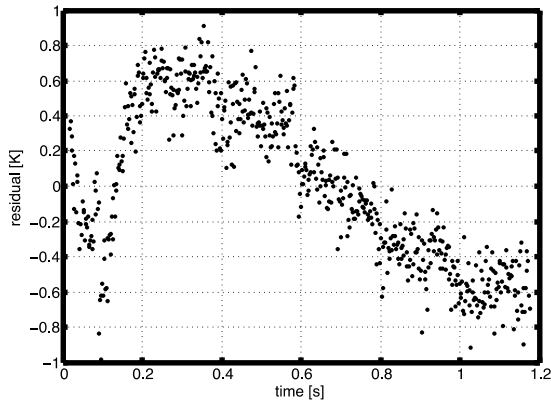


Figure 4a: residual between experimental data and eq. (3) computed with optimum fitting parameters.

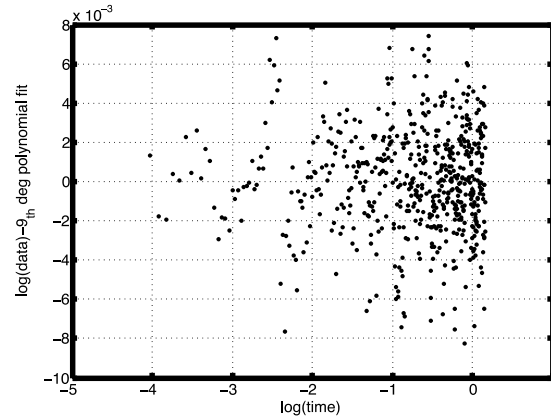


Figure 4b: residual between the logarithm of experimental data and the polynomial fitting function.

The residual in case of the NLF shows a clear trend (they are not uniformly distributed in time around zero). This is evidence of a non perfect adherence of the model to the experiment. On the other hand the LOG-LOG procedure is more flexible in following the data thank to the greater number of degrees of freedom (3 for NLF against 10 for LOG-LOG) and the final residual behaves apparently much better. Nonetheless this greater flexibility can lead to a small modification of the position of the maximum of the 2_{nd} derivative. This can affect the final value of the diffusivity estimation.

3 The Two-Layer system

Equation (3) is a particular specification of a more general solution obtained for a system composed by a finite thickness layer on a semi-infinite body of different thermophysical properties. The solution of the heat conduction problem on the surface heated by a pulse and negligible heat exchange with the environment is given by:

$$T(t) - T_0 = T_\infty \frac{1}{\sqrt{\pi Fo}} \left[1 + 2 \sum_{n=1}^{\infty} \Gamma^n e^{-\frac{n^2}{Fo}} \right] \quad (4)$$

with $\Gamma = (e_c - e_s) / (e_c + e_s)$ the reflection coefficient, ranging from -1 to +1 and accounting for the mismatch between the effusivity of the coating layer e_c and that of the substrate e_s . Figure 5a shows a sketch of the experimental lay-out while Fig. 5b represents the solution of eq. (4) for different values of Γ plotting the logarithm of temperature vs logarithm of Fourier number.

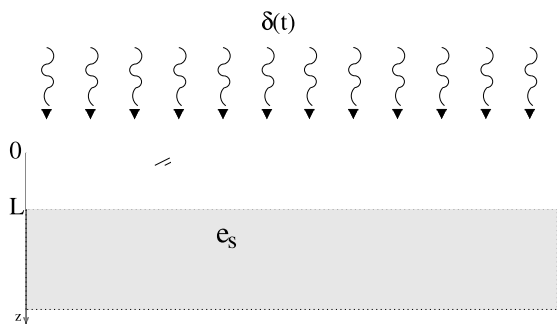


Figure 5a: sketch of the two-layer system. The surface is heated by a delta Dirac pulse $\delta(t)$.

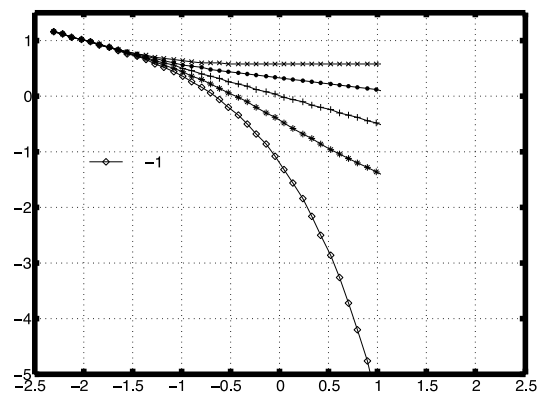


Figure 5b: the solution of eq. (4) for different values of Γ .

Equation (4) becomes eq. (3) when $\Gamma = 1$, i.e. when the effusivity of the substrate is negligible, as it is the case of the slab where the substrate is made of air or vacuum. When $\Gamma = 0$, i.e. the effusivities of the coating and the substrate are the same, the function in square brackets becomes equal to 1 and the eq. (4) is reduced to the solution of the semi-infinite body.

3.1 Computation of I_{1st} and 2_{nd} logarithmic derivative

From eq. (4) it is possible to compute the expected behaviour of the 2_{nd} logarithmic derivative that allows to evaluate the diffusivity of the coating layer by identification of its maximum value, in analogy with the procedure depicted for the slab. Unfortunately the position of the maximum changes with the value of Γ and it becomes a minimum for negative values of Γ . Therefore one must know the value of Γ to identify the value of Fo at which the maximum (minimum) happens. One possible strategy is that of evaluating Γ by analyzing the 1_{st} logarithmic derivative as shown in Fig. 6a and then select the right curve in Fig. 6b to identify the maximum (minimum) position.

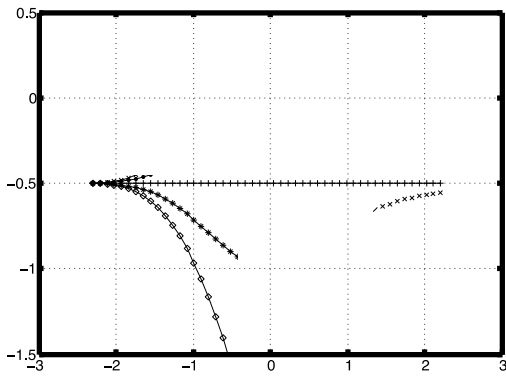


Figure 6a: 1_{st} logarithmic derivative of the solution of eq. (4) for different values of Γ .

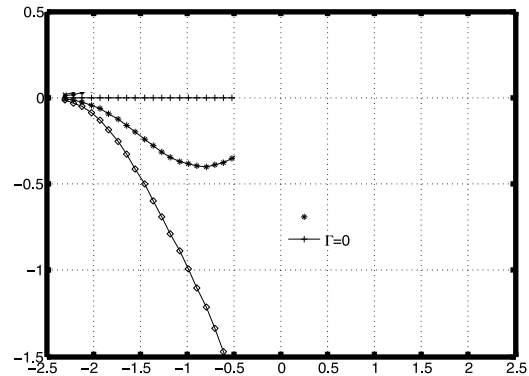


Figure 6b: 2_{nd} logarithmic derivative of the solution of eq. (4) for different values of Γ .

3.2 Estimation from experimental data

Figure 7a shows the experimental data obtained on a slab of marble on which a superficial layer of around $100 \mu\text{m}$ has been transformed in gypsum by sulfation. The surface is heated by a laser pulse of duration 1 ms. The temperature is obtained by recording a sequence of images with a thermographic camera with a sampling frequency of 750 Hz. Superimposed on the same figure is the 9_{th} degree polynomial fitting function obtained by linear fitting the data transformed in log-log space. Figure 7b shows the experimental 1_{st} logarithmic derivative with indicated the estimated value of Γ that allows to find the value of Fo in the maximum of the 2_{nd} derivative. The results of non-linear least squares fitting and identification of the 2_{nd} derivative of the log-log data is presented in Table 2. In this case we are interested to the evaluation of the thickness of the gypsum layer assuming as known its diffusivity value.

Table 2: estimation of the thickness of gypsum layer due to sulfation on a marble slab by non-linear least squares fitting (NLF) and by maximum identification of the 2nd logarithmic derivative (LOG-LOG). The diffusivity of gypsum is assumed equal to $\alpha = 3.2 \cdot 10^{-7}$.

	$\log(t^*)$	t^*	Γ	αL^2	$L [\mu\text{m}]$
NLF	n.a.	n.a.	-0.46	28.4	106
LOG-LOG	-4.2	0.015	-0.45	30.0 ($Fo^*=0.45$)	103

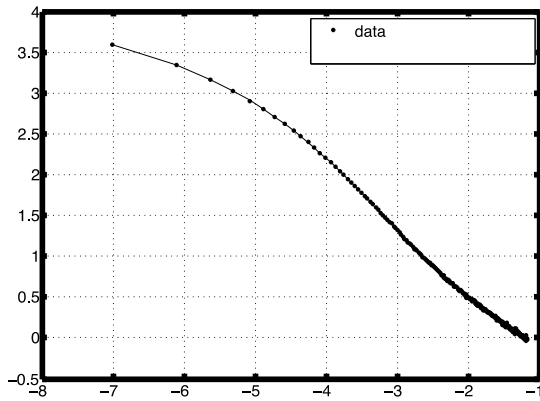


Figure 7a: linear polynomial fitting of the logarithm of the experimental temperature vs logarithm of time.

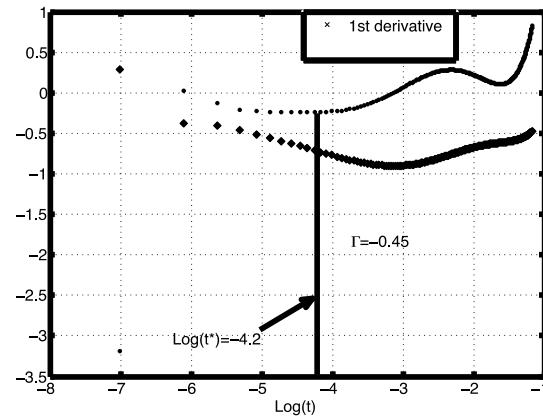


Figure 7b: 1st and 2nd logarithmic derivative of the experimental data for thickness estimation.

4 Conclusions

Pulsed Infrared Thermography has been utilized to measure thermal parameters of a slab and a two-layer system. A data reduction that transforms temperature data as a function of time in a log-log space has been demonstrated to be able estimating diffusivity or thickness by using extrema of the 2nd logarithmic derivative. The results have been compared to those obtained by Non Linear Least Square fitting procedure.

Acknowledgments

Authors are indebted with dr. Fabrizio Clarelli of IAC-CNR for furnishing the marble sulfated samples and for carrying out the experiments.

References

- [1] X.P.V. Maldague, *Theory and Practice of Infrared Technology for Nondestructive Testing*, Wiley-Interscience, 2001.
- [2] X.P.V. Maldague, editor, *Infrared and Thermal Testing*, American Society for Nondestructive Testing, 3rd edition, 2001.
- [3] E. Grinzato, P. Bison, G. Cadelano and F. Peron, R-value estimation by local thermographic analysis, *Proceedings of THERMOSENSE XXXII*, SPIE vol. 7661, 2010.
- [4] A. Bortolin, G. Cadelano, G. Ferrarini, P. Bison, F. Peron, X.P.V. Maldague. High resolution survey of buildings by lock-in IR thermography, *Proceedings of THERMOSENSE XXXV*, SPIE vol. 8705, 2013.
- [5] P. Bison, F. Cernuschi and S. Capelli, A thermographic technique for the simultaneous estimation of in-plane and in-depth thermal diffusivities of TBCs, *Surface & Coatings Technology*, **205** (2011) 3128–3133.
- [6] V. Vavilov, E. Grinzato, P.G. Bison, S. Marinetti and M.J. Bales, Surface Transient Temperature Inversion for hidden Corrosion Characterisation: Theory and Applications, *Int. Journal Heat & Mass Transfer*, **39** (2), (1996) 355-371.
- [7] W. J. Parker, R. J. Jenkins, C. P. Butler, and G. L. Abbott, Flash Method of Determining Thermal Diffusivity, Heat Capacity, and Thermal Conductivity, *J. Appl. Phys.*, **32**, (1961) 1679.
- [8] Shepard S.M., Lhota J.R., Rubadeux B.A., Wang D., Ahmed T., Reconstruction and enhancement of active thermographic image sequences, *Optical Engineering*, **42** (5), (2003), 1337-1342.
- [9] D.L. Balageas, Thickness or diffusivity measurements from front-face flash experiments using the TSR (thermographic signal reconstruction) approach, *Proceedings of QIRT 2010*, Quebec Canada, <http://qirt.gel.ulaval.ca/dynamique/index.php?idM=38>
- [10] D. Balageas. Defense and illustration of time-resolved pulsed thermography for nde. *QIRT Journal*, **9** (1), (2012), 3–32.
- [11] B.K. Jang, J.G. Sun, S.W. Kim, Y.S. Oh, H.T. Kim, Characterization of the thermal conductivity of EB-PVD ZrO₂-Y₂O₃ coatings with a pulsed thermal imaging method, *Surface & Coatings Technology*, **207** (2012) 177–181.
- [12] R. Courant, D. Hilbert, *Methods of Mathematical Physics*. Wiley Classic Library, 1953.
- [13] <http://dlmf.nist.gov/20>

Thermography and Shearography coupling applied to NDT of CFRP tissue bonding interface on concrete by numerical simulations

Louis-Daniel Th eroux^{a,b*}, Jean Dumoulin^b and Xavier Maldague^a

^aDepartment of electrical and computer engineering, Universit  Laval, 1065 avenue de la M decine, Qu bec (Qu bec), G1V 0A6, Canada

^bLUNAM Universit , IFSTTAR, COSYS Department, Route de Bouaye, CS4, 44344 Bouguenais Cedex, France

Abstract. The reinforcement of concrete structures by gluing Carbon Fiber Reinforced Polymer (CFRP) tissues is a commonly used technique in civil engineering. In order to validate the quality of the bonding of those tissues to the structure, only some non-destructive methods are available. The present study sets the emphasis on the simultaneous use of two NDT: active infrared thermography and shearography. The coupling of those two methods is done by the use of square pulsed optical heat as a common excitation source. An early experimentation test has been conducted to verify the feasibility of using a square thermal loading to create a measurable shearographic response. A finite element model has been elaborated under COMSOL® to simulate the thermal and thermo-mechanical behavior of the samples used in the experimental part of the study. Shearographic images were simulated and tools to extract information from these have been implemented such as a phase extraction, unwrapping and unhearing algorithms. Finally, the simulated thermal and mechanical results were cross-analyzed.

Keywords: Infrared Thermography, Shearography, FEM, CFRP, Nondestructive Testing

Introduction

Usage of CFRP tissue is a common reinforcement technique in civil engineering [1, 5]. The installation of the tissue requires technicians to follow a rigorous procedure to avoid the presence of defects in the bonding. The nature of those defects can vary in nature and importance. They can be caused by surface impurity (voids, irregularities, etc.) or by environmental conditions (humidity, moisture, etc.). Taking into account that the presence of those defects which can impair the quality of the bonding, it is of importance to not only detect their presence but also evaluate their effects on the strength of the bonding. To do this, few techniques are available, such as hammer tapping or tearing for example. This study sets the emphasis on two non destructive full field techniques: shearography and active infrared thermography. Shearography is the measure of displacement of a surface subjected to stress. This stress is often induced by using partial vacuum over a surface. However, since we want to use thermography and shearography simultaneously, this stressing technique is not optimal. Instead, thermal loading will be used and investigated in the present paper.

Infrared Thermography and Shearography

1.1. Active infrared Thermography and heat transfer

Active infrared thermography is a non-destructive testing method [8] that is based on the principle of heat diffusion in solids in transient regime. The inspected element is heated (by convection or radiation for example) and an infrared camera measures the evolution of the surface temperature field. For this part, the emphasis will be put on the principle of thermal heat diffusion in solids which can be described by the following equation (1) :

$$\rho C \frac{\partial T}{\partial t} = \nabla \cdot (k \nabla T) + Q \quad (1)$$

1.2. Shearography

To understand how shearography works, one must first be comfortable with the principle of holography. Holography is the measure of the phase of an image. This is done by projecting a coherent light beam on an object. The reflection interferes with a reference beam on a holographic plate which record the phase.

The interference is caused by the difference in Optical Path Length (OPL) between the object beam and the reference beam. If a phase image is recorded for an object initially in a unconstrained state and then a second phase image is recorded for the object in a constrained state, the difference of both phase image is a function of the surface displacement. However, this kind of setup would be very susceptible to unwanted change in the OPL due to vibration of experimental components (mirrors, camera, lenses) and change in the air refractive index. To dodge this problem, instead of interfering with the reference beam, the object beam interferes with a sheared version of itself. This is called shearography. By doing so, the OPL of both beam is very similar and not as sensible to noise the holographic setup. The resulting phase difference is no longer a function of the plane displacement but rather the curl of displacement in the shearing direction. If we assume that the camera and light source are both superposed and have their direction normal to the plane, the relation [11] between the phase difference and the curl of the out-of-plane displacement is reported in equation (2):

$$\Delta\varphi = k \cdot 2 \left(\frac{\partial w}{\partial x} \right) \delta_x \quad (2)$$

With: $k = \frac{2\pi}{\lambda}$ the wavenumber

Laboratory specimens and feasibility experimentation

The use of an optical heat source conditioned by a square pulse is a topic rarely mentioned in literature. Taking this into account, it seems relevant to conduct a feasibility test on this type of thermal loading to make shearographic measurements. Samples used for the experimentation were concrete slab of 10 mm thick with CFRP tissue glued on one of its surface. Defects are made of PTFE discs inserted in the layer of glue. Teflon is used instead of air because it is easier to make such defect of precise depth and dimension. Since PTFE does not chemically bond with epoxy glue, its thermal behavior is similar to air. Heating was made by a 150 W lamp and the heating time was variable. The results presented had a square pulse of roughly 30 seconds. The acquisition is done via a CCD camera with 756 x 481 pixels, each with size of 11 μm . The area inspected is 0.1 m^2 approximately. The laser used is a Nd-YAG with a wavelength of 532 nm.

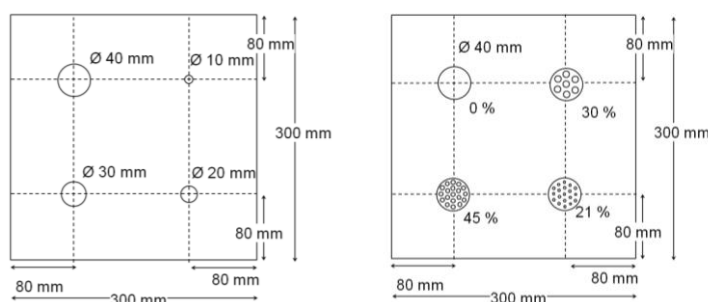


Fig. 1. Schematic of the samples Specimen 1 (left scheme) and Specimen 2 (right scheme).

Experimental results show that it is possible to visually detect defect in the bonding using a thermal load, although results from smaller or partially glued defects are sometime more or less visible. Figure 2 shows an illustration of results obtained.

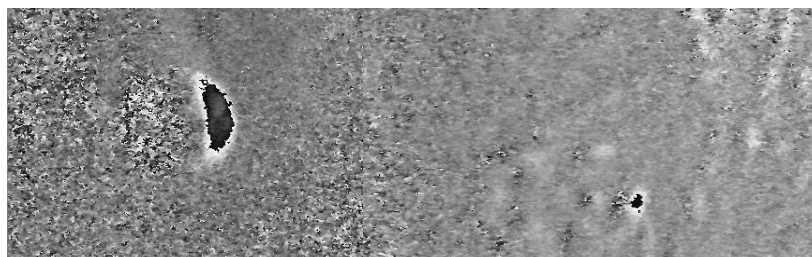


Fig. 2. Shearographic image of the defect in the sample Specimen 1 for a square pulse heating of 30 seconds.

Numerical Model

1.3. Geometry and Meshing

The modeling is done using the software Comsol®. The geometry used is based on the real life sample presented in the previous section. The meshing consist of roughly 130 000 tetrahedral elements. To assure convergence, avoid computation error and to have precise results, the more refined the meshing, the better. On the other hand, to avoid error due to lack of memory and to reduce computation time, it might be reasonable to keep the number of elements to a minimum. Ideally, the minimum elements size should not be bigger than the smallest geometric entity.

1.4. Conditions

This section will present the different condition used in the numerical model to represent as closely as possible the experimental conditions. This part is divided in two sections; first the conditions relative to the thermal response and in second the mechanical response.

1.4.1. Heat transfer in solids

By default, heat conductivity is applied to the entire model. The initial temperature is set at the ambient temperature of 293.15 K. On the exterior boundary of the model, convective cooling of 10 m²K is applied to simulate the flow of air at ambient temperature. Since Teflon does not chemically bond with the epoxy glue, a thermal resistance is applied to the exterior boundaries of Teflon. Finally, the top surface of the model is subject to a square heat flux density of 2000W/m² to simulate the presence of the heating lamps.

1.4.2. Solid Mechanics

All domain entities in the model are considered as being subject to linear elastic behavior since we consider the displacement induced to be infinitesimal. To simulate the fact that Teflon does not adhere with the glue, its exterior surface is considered to be free. All exterior boundaries of the model are considered free as well. The exception is the bottom face of the concrete which is fixed since normally the sample would be laying on a table or on the floor.

1.4.3. Thermomechanical properties

We present in Table 1 and 2 the physical properties considered in our numerical simulations.

Table 1 : Material Properties used in the elaboration of the COMSOL numerical model

Properties	Units	Materials			
		Concrete	EpoxyResin	CFRP Tissue	PTFE
Thermal Conductivity	[W/(m*K)]	1,8	0,2	4,2/0,7/0,7	0,235
Thermal Capacity	[J/(kg*K)]	920	1220	840	1050
Density	[kg/m ³]	1200	1200	1530	2200
Young Modulus	[GPa]	30	10,5	(see Table 2)	0,5
Coefficient of Thermal Expansion	[1/K]	1,20 E-05	2,50 E-05	-0,8/35/35 E-06	1,35 E-04
Poisson Coefficient	-	0,21	0,4	0,33	0,46

Table 2 : Rigidity Tensor of Carbon/Epoxy T300/914 [GPa]

143,8	6,2	6,2	0	0	0
6,2	13,3	6,5	0	0	0
6,2	6,5	13,3	0	0	0
0	0	0	3,6	0	0
0	0	0	0	3,6	0
0	0	0	0	0	5,7

1.4.4. Example of displacement and temperature fields computed

Temperature field and out of plane displacement value are exported from Comsol. Since temperature and displacement are not evenly distributed over an area, the mean value is calculated. The average value is calculated over a centered square area of side equal to the diameter of the defect.

Figure 3 shows an example of numerical results obtained.

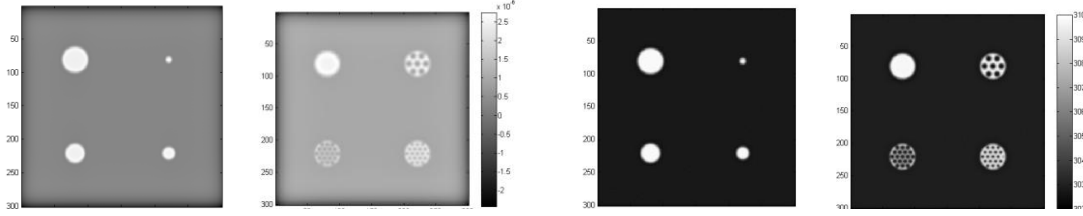


Fig. 3. Out of plane displacement (left) and temperature field (right) for the sample Specimen 1 and 2 respectively for a square pulse heating of 30 seconds.

A quick observation of the data of the sample Specimen 1 reveals a strong correlation between the defects size and the amplitude of the out of plane displacement. Results from the second sample reveal that a high percentage of bonding reduces the overall displacement. Looking at the temperature, observation show that the radius of the Teflon disc and bonding percentage have a smaller impact on the temperature since it only affect transversal heat diffusion.

Results Analysis

1.5. Shearographic image analysis

As explained before, a shearographic image is the phase difference which is proportional to the out of plane displacement difference between two point separated by the shear distance. The first step to simulate a shearographic image from a calculated displacement is to subtract each image by a sheared version of itself. The resulting image can be roughly described as a representation of the curl of displacement in the shearing direction. These value are then converted in the phase difference value, not considering the effect of the phase extraction methods. The resulting shearographic image is a representation of what is measured during an experiment, discarding the effects of noise. To recover the displacement value form a shearographic measure, the phase map must be unwrapped to avoid jump from 0 to 2π . Unwrapping is a subject widely mentioned in literature as in [6, 9]. In our case, the algorithm used is the default Matlab function. The resulting unwrapped image is a representation of the difference of displacement between to point and must be unwrapped. It can be shown that the displacement for a pixel i can be calculated from the following equation:

$$w(i) = \frac{1}{2k} \sum_{j=0}^{\beta} \Delta\varphi(i - j\delta, n) + w(i - (\beta + 1)\delta) \quad (3)$$

Where β is the rounded down expression of i/δ . The expression of displacement on the right hand side of the equation is an unknown parameter. To solve this problem, multiple solutions are available. The first and simpler method is to take into account that one region on the boundary of the image does not have displacement. Since the shearing direction is horizontal, the regions of no displacement must be either on the left or the right. This methods cause the propagation of error along the lines. An algorithm with 2 boundary conditions can be used to prevent this, but, as mentioned before, it still require no displacement on the boundaries of the images. Since this condition is not always met, a more robust approach consists of considering the mean displacement of the image to be zero. Such algorithm, developed by Taillade[10], use a corrected boundary condition presented in equation (4):

$$W_{\text{unsheared}} = \left(\left[\underline{U} - \frac{\delta}{N} \underline{A}_c^t * \underline{A}_c \right] \underline{A}_l^{-1} \varphi \right) \quad (4)$$

With:

$$A_c = \begin{pmatrix} 1 & 0 & \dots & 0 & \dots & 1 & 0 & \dots & 0 \\ 0 & \ddots & \ddots & \vdots & \dots & 0 & \ddots & \ddots & \vdots \\ \vdots & \ddots & \ddots & 0 & \dots & \vdots & \ddots & \ddots & 0 \\ 1 & \dots & 0 & 1 & \dots & 0 & \dots & 0 & 1 \end{pmatrix}_{[\delta, N]} ; \underline{A}_l = 2k \begin{pmatrix} 1 & 0 & \dots & & \dots & 0 \\ 0 & \ddots & \ddots & & & \vdots \\ \vdots & \ddots & \ddots & & & \\ 0 & & & & & \\ -1 & \ddots & & & & \vdots \\ 0 & \ddots & \ddots & & \ddots & 0 \\ 0 & 0 & -1 & 0 & \dots & 0 & 1 \end{pmatrix}_{[N, N]}$$

And N being the number of lines and \underline{U} is a square matrix with each element equal to one and of dimension N by N. Figure 4 shows an illustration of the application of the full procedure to the calculated displacement field for the modeled Specimen 1:

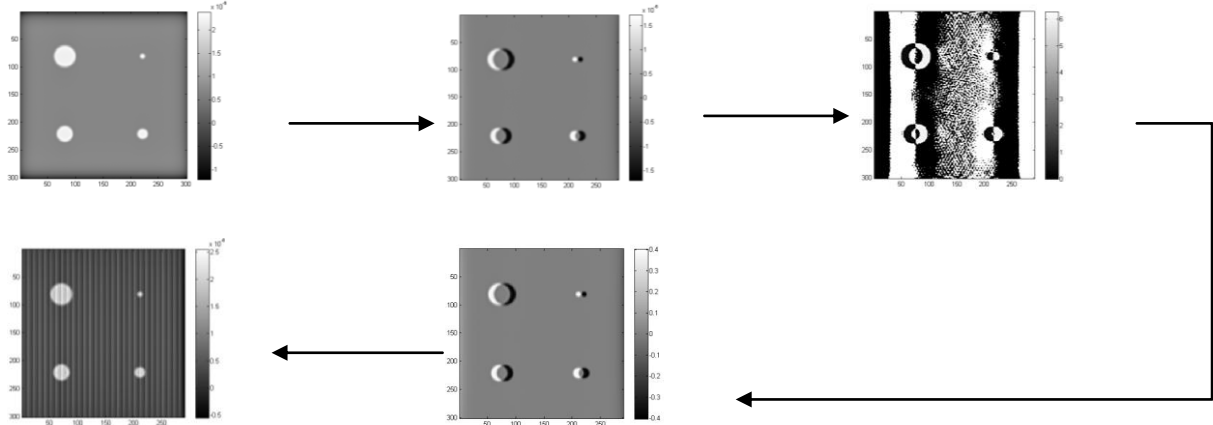


Fig. 4. Simulating a shearographic measurement of the sample Specimen 1.

1.6. Contrast analysis

The running contrast [8] is calculated using the following equation (6):

$$C_{running}(t) = \frac{\theta_d(t) - \theta_s(t)}{\theta_s(t)} \quad (6)$$

Where θ_d and θ_s are the value of any measure (temperature, displacement) of a defective and sound area. Figure 5 shows displacement and temperature contrast computed.

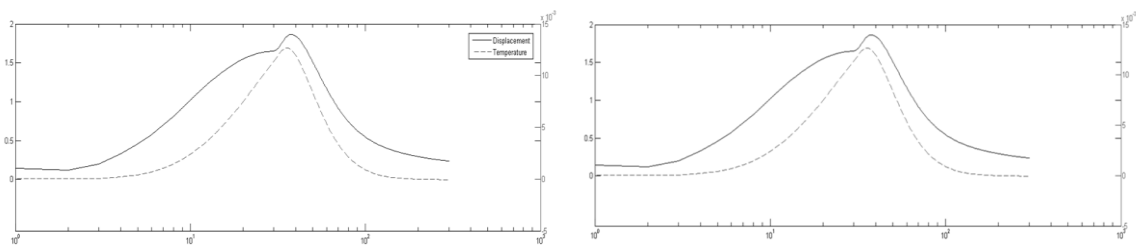


Fig. 5. Comparison of running contrast of temperature and out of plane displacement for a defect of diameter 10 and 40 mm for the left and right graph respectively.

Results show that the evolutions of the contrast of temperature and displacement are different. The time where the contrast is maximum is also different.

Discussion

The analysis of the results shows a correlation between the evolution of contrast trough time and the depth of the defect. This behavior is very well known in non destructive testing by active infrared thermography.

The size of the defects also impact the results, especially the out of plane displacement which increase the greater the radius is. The effect on the temperature is barely noticeable since it only affects the lateral diffusion of the temperature. Multiple improvements could be made on the numerical model to better simulate the experimental conditions. The heating source is defined as homogeneous over the whole surface of the sample as in reality, it is unevenly distributed. The heat flux could be defined by a Gaussian pattern. Another option would be to model the lamp and use a complementary heat radiation modeling approach.

Conclusion

The feasibility experiment have shown that the use of a square thermal loading allow, in some case, the visual detection of defects in the bonding of a reinforced concrete plate. The samples were modeled using COMSOL and thermomechanical behavior were simulated. The analysis of those results showed a relation between time of maximum contrast and depth of the defect. The unhearing algorithm implemented has proven to be quite efficient and robust. Future developments involve conducting experiments using both shearography and thermography at the same time so results can be compared to those simulated. This will allow to make adjustments to the model, so its behavior can be as close as possible to the real samples. This implies modification in the experimental setup. Among notable requirement is the conception of a continuous phase extraction algorithm so shearographic images can be acquire with a higher frequency than the current setup which can acquire an image each 2 to 3 seconds. Also, since the analysis of the results mostly depend on the study of the behavior in function of time, the thermal and shearographic measure need to be synchronized together as well as with the heat source.

References

- [1] ACI Committee 440.2R02-08., *Guide for the Design and Construction of Externally Bonded Systems for Strengthening Concrete Structures*, American Concrete Institute, Michigan, U.S.A., 2008.
- [2] Balageas D.L., Deom A.A., Boscher D.M., *Characterization and nondestructive testing of carbon-epoxy composites by a pulsed photothermal method*, Journal of Materials Evaluation, vol. 45, n° 4, 1987, p. 465-466.
- [3] Dumoulin J., Taillade F., Benzarti K., Quiertant M., Aubagnac C., *Infrared Thermography for the Non-destructive Inspection of CRFP Strengthening*, Concrete International, April 2011, 54-58
- [4] Fabrice M, *Développement et première application d'une installation shearographique*, Thesis for DEA in Science, Liège University, Faculty of Science, 2004-2005.
- [5] Fib Task Group 9.3. *Externally bonded FRP reinforcement for RC structures*, fib bulletin 14, Lausanne, Switzerland, 2001.
- [6] J.A. Quiroga, A. Gonzalez-Cano, E. Bernabeu, Phase-unwrapping algorithm based on an adaptative criterion, *Applied Optics* vol. 34 No. 14, (1995)
- [7] Lamarque T., *Caractérisation de délaminage par interférométrie de speckle à cisaillement avec sollicitation thermique ou mécanique*, PhD Thesis, Paris University, 1998
- [8] Maldague X, *Theory and practice of infrared technology for non-destructive testing*, John Wiley and Sons, 2001.
- [9] M.A. Herraéz, D.R. Burton, M.J. Lalor, D.B. Clegg, Robust, simple and fast algorithm for phase unwrapping, *Applied Optics* vol. 35 No. 29, (1996)
- [10] Taillade F, *Association de la shearographie et des ondes de Lamb pour la détection rapide et quantitative des délaminages*, PhD Thesis, Conservatoire National des Arts et Métiers, 2000 .
- [11] Y.Y. Hung, C.Y. Liand, *Image-shearing camera for direct measurement of surface strains*, Applied Optics, vol.18, n°7, pages 1046-1051, 1979

Post-impact damage characterization of pultruded jute/glass hybrid composites using infrared vision and optical techniques

by S. SFARRA¹, D. PAOLETTI¹, C. IBARRA-CASTANEDO², A. BENDADA²,
X. MALDAGUE², C. SANTULLI³ and F. SARASINI³

¹Las.E.R. Laboratory, Department of Industrial and Information Engineering and Economics (DIIIIE), University of L'Aquila, Piazzale E. Pontieri no. 1, I-67100, Roio Poggio (AQ), Italy

²Computer Vision and Systems Laboratory (CVSL), Department of Electrical and Computer Engineering (DECE), Laval University, av. de la Médecine, G1V 0A6, Quebec city, Canada

³Department of Chemical Engineering Materials Environment (DCEME), University of Roma Sapienza, Via Eudossiana no. 18, I-00184, Rome, Italy

Abstract

The use of an intelligent and integrated NDT approach applied to a hybrid jute composite (JC) made with natural fibers has been explored in this work in order to reveal emerging defects after an indentation test. In particular, the fiber content (wt.%) of the sample investigated was 40 jute + 25 glass with a stacking sequence of Surface veil/Chopped strand/Jute/J/C/S. The sample was analyzed by: a) near-infrared reflectography (NIRR) and transmittography (NIRT), b) short-wave infrared reflectography (SWIR), c) infrared thermography (IT), d) holographic interferometry (HI) and e) digital image correlation (DIC) techniques. The first two inspections, combined with the Canny edge detector and the distance transform (DT), were useful to highlight the fibers distribution and the areas with a low concentration of fibers, respectively. In the third inspection, two different methods of heating were applied: pulsed thermography (PT) and square pulse thermography (SPT). The first one linked to a mid-wave IR camera, while the second one combined to a long-wave IR camera. IRT data were processed using different algorithms, such as: principal component thermography (PCT) and thermographic signal reconstruction (TSR). Comparing the TSR and the optical results, two zones invisible to the naked eye and surrounding the indented area can be identified (Figure 2). These zones were quantitatively confirmed using the MOIRE Software package (DIC script) described in the final paper, illuminating the sample by means of a speckle pattern induced by a laser Nd : Yag 250 mW.

Keywords: infrared vision, digital image correlation, holographic interferometry, hybrid composites, indentation

1. Introduction

The rapidly expanding use of composite components in automotive, construction, sports and leisure and other mass production industries has focused attention on continuous production techniques with the optimal properties. Pultrusion is one of the most successful techniques for the continuous manufacturing of structural profiles from composites. Pultruded composites are traditionally

manufactured using thermosetting resin systems. These profiles are produced by pulling a carefully specified mass of wetted-out reinforcement material through a heated metal die containing a cavity of the desired cross-section [1]. Pultrusion method is chosen among many other methods of producing fiber reinforced polymer composites due to its main advantage i.e., its ability to produce continuous long constant cross section profile with various shapes by only changing the die design, which is not possible with other production method. Besides that capacity, it also offers an automatization process with limited labour for operating at tremendous production rate and is often referred to as the most cost-effective method of producing fibre reinforced polymer composites. Pultruded fiber reinforced polymer composites have also proven to be the most suitable choice under corrosive environments due to its durability and capability as compared to composites manufactured by hand layup and spray layout. With long and continuous profile and possible percentage of fiber loading greater than 60% in composites, it is the most suitable composite to be used in the applications such as in building and construction industries.

Currently, the pultrusion technology is still in the infancy state; taking into account this state, the NDT methods are essential for quality control of the new products to be marketed [2, 3].

In particular, the integration of optical and infrared NDT methods seems a good choice to detect various type of defects like resin bubbles, resin-rich areas, resin-lean areas, foreign inclusions, delaminations, voids and, above all, the effect of the impact damage on the surrounding areas [4, 5, 6], while the use of thermographic signal reconstruction (TSR) technique [7], the Canny edge detector [8] and the MOIRE Software package [9] are the novelties introduced by the authors in this work respect to the [4, 5, 6] studies with the intent to optimize the *a posteriori* NDT inspection procedure. Readers can see how the combination of the experimental results into a unique approach exalts the discussion of the topic.

2. Materials, composite manufacturing and mechanical testing

The dimensions of the sample analyzed in the present research were 140 mm x 22 mm x 2.8 (± 0.1) mm and the span-to-depth ratio was 20:1. Unsaturated polyester resin Crystic P9901 by Scott Bader (Wollaston, Norths, UK) was used for the production of the laminate. Chopped strand mat (**C**) was supplied by Hengshui Yixing Fiberglass Co. Limited (Hengshui, China), while jute fibers (**J**) were supplied by Alam Fiber Impex Ltd. in twisted roving form: the thread diameter being approximately 1 mm. A protection surface veil (**S**) was used, which is made of polyester fibers through non-woven process and finished with resin, to obtain layers of 0.2 mm thickness. For composite manufacturing, a thermoset pultrusion machine was used at MMFG Composites Sdn. Bhd, Subang Jaya, Selagor, Malaysia. The continuous fiber roving was first impregnated with unsaturated polyester resin in a resin impregnation tank. There was a pulling device to pull the jute fibers impregnated with resin through a steel die to obtain the desired shape. The heating time to reach the exothermic peak of the resin (around 50 °C), was 5 min. The tough, low viscosity resin

needed no post-curing. The pulling device, which drew the stock through the die, determined also the production speed: this was approximately 100 mm/min. Indentation test was carried out according to the method followed in [10], by simply supporting the sample on a steel plate with a 30 mm diameter circular opening, using a 10 mm diameter hemispherical indenter and a 5584 universal testing machine by Instron in displacement control with 1 mm/min cross-head speed.

3. Experimental results

Indentation test was used as a low strain rate simulation for low velocity falling weight impact test, in the assumption that damage produced and the mode of failure is comparable [11]. In this respect, linear stiffness can be measured from this test, as the slope of the elastic section of force-displacement curve (255 ± 35 N/mm), shown in Fig. 1.

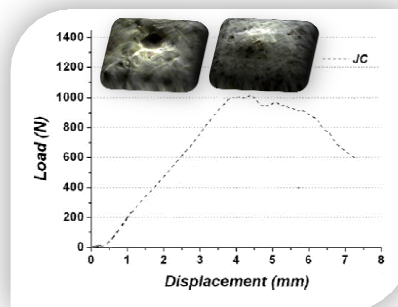


Figure 1: Typical indentation curve and the front and back face of the indented laminate

Indentation damage appears to have a quite considerable orientation along the fibers. Rear damage shows a slight indication of a “butterfly like” shape, which is typical of the combination of a number of damage phenomena in glass fiber laminates [12]. Here, this is likely to be attributed to the presence of chopped strand mat in the laminate, and the effect is extended around the indented area in two characteristic zones. These zones, indicated by the arrows in Figure 2 a-b, were identified by thermographic signal reconstruction (TSR) and digital image correlation (DIC) techniques [7], [9].

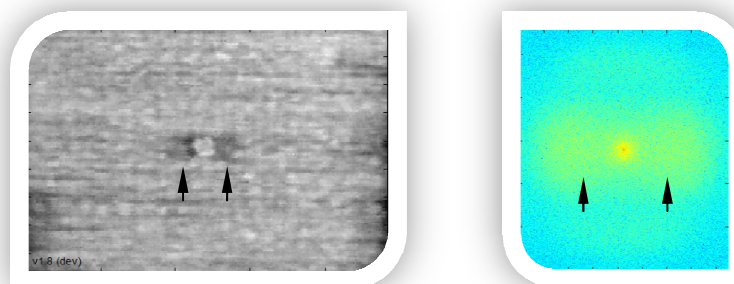


Figure 2: From left (a), to right (b): second time derivative $t=275s$, DIC result using the fast Fourier transform

The result in Fig. 2a is refers to an acquisition made in pulsed thermography (PT) modality [13], i.e. working with an FPA infrared camera (Santa Barbara Focalplane SBF125, 3 to 5 μm), on a 320 by 256 pixel array. The acquisition frequency was set at 45 Hz, while two high-power flashes (Balcar FX 60), giving 6.4 kJ for a ~ 5 ms pulse were used as heating sources. PT data was acquired in reflection mode; the same modality of data acquisition was used in the square pulse thermography (SPT) experiment [14] (Fig. 3a).

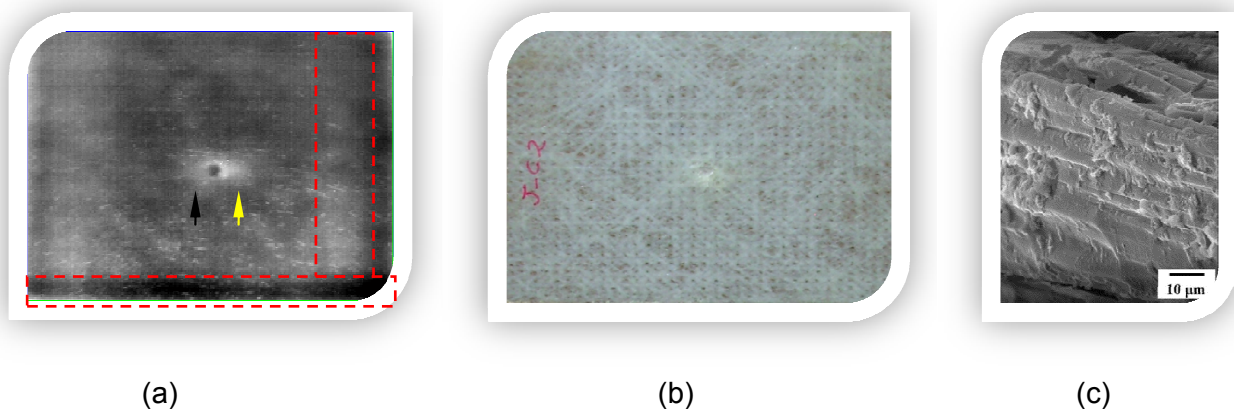


Figure 3: (a) PCT result - EOF6, (b) visible image, (c) scanning electron microscope (SEM) result

It is interesting to note how the principal component thermography (PCT) technique [15] has been very useful to confirm the two zones (Fig. 3a) located to the edge of the impact area (marked by arrows), already shown in Figure 2, as well as to detect two rectangular areas (marked by red dotted rectangles) probably linked to the non uniform application of the polyester resin described in the Chapter 2. This assumption is confirmed seeing the scanning electron microscope (SEM) result in Fig. 3c, where insufficient fiber impregnation is shown [16]. In addition, comparing Fig. 3a with Fig. 3b (visible image) it is possible to affirm that the detected areas are not apparent on the laminate surface.

The damage of the right zone (see the yellow arrow in Figure 3a) appears greater than the other one at least by analyzing the sample with the double-exposure (DE) holographic interferometry (HI) technique (Fig. 4a) [17], while the digital speckle photography (DSP) technique using MatPIV [18] was able to retrieve only the position of the impact (Fig. 4b). During the DE experiment, a soldering iron was used in transmission mode to provide a thermal stress among the two exposures separated by a time interval fixed at five minutes. The displacements induced on the damaged areas by the thermal stress are in agreement among the HI qualitative approach and the DIC-3D quantitative approach [9] (Fig. 4c). Readers can note how the right zone is linked to extended displacements (the red color marked by a yellow arrow) if compared to the left zone. The impact

zone was retrieved with a good contrast in the DIC qualitative result shown in Fig. 2b, although the two zones at the border of the impact area show a similar configuration by using the FFT in a planar visualization.

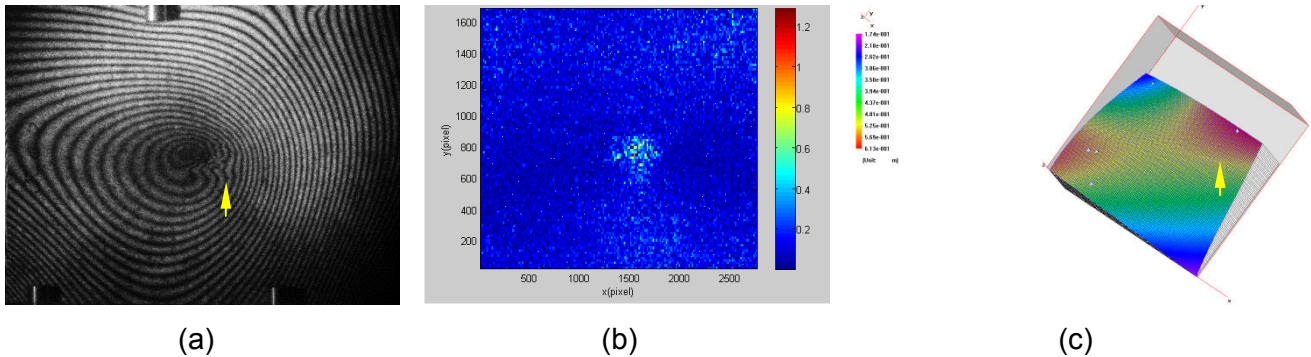


Figure 4: (a) DE-HI result, (b) DSP result, (c) DIC-3D result

In order to verify the fibers distribution and combine the results obtained with the HI and DIC-3D techniques, the sample was also analyzed in the SWIR spectrum (Fig. 5a) working in transmission mode, subtracting the NIRR result to the NIRT result using a wide spectrum as illumination source [4] (Fig. 5b), applying the distance transform algorithm [19] (Fig. 5c) and the Canny edge operator [8] (Fig. 5d) to the SWIR result.

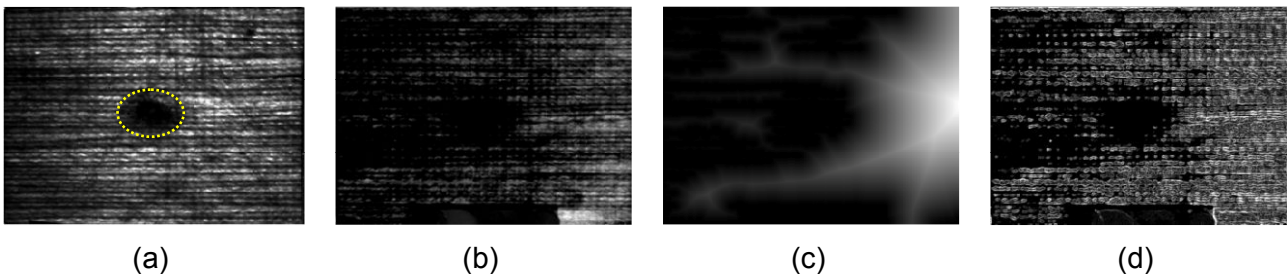


Figure 5: (a) SWIR result at 1300 nm, (b) Subtraction of images among the NIRR and NIRT results, (c) Distance transform result coming from (b) image, (d) Canny edge result coming from (b) image

Fig. 5a shows the presence of two characteristic zones including inside the yellow dashed oval: 1) the internal zone having a dark color caused by the impactor tip, 2) the external zone surrounding the previous one and having a grey color caused by the forces acting during the impact.

Fig. 5b, as well as Figs. 5c,d linked to it, point out a different texture of the fibers among the right (wide interphase) and the left (narrow interphase) sides. This result is in agreement with the HI (Fig. 4a) and DIC-3D (Fig. 4c) results; in fact, the variations (cusps or correlation signal) among the exposures can be observed only to the right of the impact zone, i.e. where the fibers are less densely packed. In Figs. 5c,d the white color is linked to this configuration. It is also possible to

observe that only the SWIR image (Fig. 5a), acquired by a Goodrich camera SU640SDWH-1.7 RT 640x512 pixels, InGaAs, 900–1700 nm, was able to visualize two zones incorporated each other.

4. Conclusions

Reliable damage detection and quantification is a difficult process because of its dynamic and multi-scale nature, which combined with material complexities and countless other sources of uncertainty often inhibits a single non-destructive testing (NDT) technique to successfully evaluate the extension of deterioration in critical structural components. This paper presents an integrated non-destructive testing approach (NDT) for effective damage identification relying on the intelligent integration of the holographic interferometry (HI), digital speckle photography (DSP), digital image correlation (DIC), infrared vision, scanning electron microscope (SEM) and image segmentation NDT techniques. The proposed system has been utilized to identify various type of defects that are connected to pultruded jute/glass hybrid composites taking into account the modality of impact loading.

REFERENCES

- [1] MEYER (R.) *Ed.* - Handbook of pultrusion technology. N.Y., Methuen Inc., 180 p., 1985.
- [2] PILLA (S.) *Ed.* - Handbook of bioplastics and biocomposites engineering applications. Massachusetts, Wiley, 590 p., 2011.
- [3] International Atomic Energy Agency (IAEA). - Non-destructive testing for plant life assessment, http://www-pub.iaea.org/mtcd/publications/pdf/tcs-26_web.pdf, Accessed on 30 June 2013.
- [4] SFARRA (S.), IBARRA-CASTANEDO (C.), SANTULLI (C.), SARASINI (F.), AMBROSINI (D.), PAOLETTI (D.) and MALDAGUE (X). - Eco-friendly laminates: from the indentation to non-destructive evaluation by optical and infrared monitoring techniques. *Strain*, 49(2), 2013, p. 175-189.
- [5] SFARRA (S.), IBARRA-CASTANEDO (C.), SANTULLI (C.), PAOLETTI (A.), PAOLETTI (D.), SARASINI (F.), BENDADA (A.), and MALDAGUE (X.). - Falling weight impacted glass and basalt fibre woven composites inspected using non-destructive techniques. *Compos Part B-Eng*, 45(1), 2013, p. 601-608.
- [6] BENDADA (A.), SFARRA (S.), GENEST (M.), PAOLETTI (D.), ROTT (S.), TALMY (E.), IBARRA-CASTANEDO (C.), and MALDAGUE (X.). - How to reveal subsurface defects in Kevlar® composite materials after an impact loading using infrared vision and optical NDT techniques?. *Eng Fract Mech*, in press, doi: <http://dx.doi.org/10.1016/j.engfracmech.2013.02.030>.
- [7] SHEPARD (S.M.), AHMED (T.), RUBADEUX (B.A.), WANG (D.) and LHOTA (J.R.). - Synthetic processing of pulsed thermographic data for inspection of turbine components. *Insight*, 43(9), 2001, p. 587-589.

- [8] CANNY (J.) - A Computational Approach To Edge Detection. IEEE Trans. Pattern Analysis and Machine Intelligence, 8(6), 1986, p. 679-698.
- [9] PAN (B.), WANG (Z.) and LU (Z.). - Genuine full-field deformation measurement of an object with complex shape using reliability-guided digital image correlation. Opt Express, 18(2), 2010, p. 1011-1023.
- [10] DE ROSA (I.M.), SANTULLI (C.) and SARASINI (F.). - Characterization of indentation damage on carbon/epoxy laminates by means of acoustic emission and IR thermography. E-Journal of Nondestructive Testing 14, 2009.
- [11] CAPRINO (G.) and LOPRESTO (V.). - The significance of indentation in the inspection of carbon fibre reinforced plastic panels damaged by low-velocity impact. Comp Sci Technol, 60(7), 2000, p. 1003-1012.
- [12] SHYR (T.W.) and PAN (Y.H.). - Impact resistance and damage characteristics of composite laminates. Comp Struct, 62(2), 2003, p. 193-203.
- [13] LUGIN (S.) - Pulsed thermography, algorithms for efficient and quantitative non-destructive testing. U.S.A., VDM Verlag Dr. Muller, 105 p., 2008.
- [14] ARNDT (R.W.) – Square pulse thermography in frequency domain as adaptation of pulsed phase thermography for qualitative and quantitative applications in cultural heritage and civil engineering. Infrared Phys Techn, 53(4), 2010, p. 246-253.
- [15] RAJIIC (N.) - Principal component thermography for flaw contrast enhancement and flaw depth characterization in composites structures. Compos Struct, 58, 2002, p. 521-528.
- [16] AKIL (H. Md.), DE ROSA (I.M.), SANTULLI (C.) and SARASINI (F.). - Flexural behaviour of pultruded jute/glass and kenaf/glass hybrid composites monitored using acoustic emission. Mater Sci Eng A-Struct, 527, 2010, p. 2942-2950.
- [17] VEST (C.M.) - Holographic interferometry. U.S.A., John Wiley & Sons, 502 p., 1979.
- [18] SVEEN (J.K.) - MatPIV 1.6.1. <http://folk.uio.no/jks/matpiv/index2.html>, accessed on 01 July 2013.
- [19] SERRA (J.) - Image analysis and mathematical morphology – Vol. 1. N.Y., Academic Press, 610 p., 1982.

Comparison between optical pulsed thermography and vibrothermography for the assessment of carbon fiber composite materials

Henri-Michel Montrieux¹, Philippe Demy¹, Clemente Ibarra-Castanedo², Anne Mertens¹,
Nathalie Gerlach¹, Jacqueline Lecomte-Beckers¹, Xavier Maldague²

1 University of Liege, Department of Aerospace and Mechanical Engineering, Bât. 52/3, LTAS, chemin des Chevreuils 1, 4000 Liège, Belgique.

2 Computer vision and systems laboratory (CVSL), Department of Electrical and Computer Engineering, Université Laval, Québec (Québec), CANADA G1V 0A6

Pulsed thermography and vibrothermography are two active thermography techniques characterized by different heating methods of the specimen. In pulsed phase thermography, a sample is heated by two flash lamps for a short period to inject a Dirac impulse heat in the material. The cooling of the part is monitored with an infrared camera to detect thermal contrast in the image, characteristic of the presence of a defect. In vibrothermography, high frequency vibrations are injected into the sample causing an internal heating observed on surface right above the defect due to diverse phenomena as friction or viscoelastic hysteresis. If pulsed thermography is a well-known technique that has been integrated into the arsenal of industrial NDT methods, vibrothermography is a less common experimental method still subject to theoretical and practical investigations. This article aims to compare the effectiveness of the two methods in the case of different types of composites based on carbon fibers: carbon fiber reinforced plastic (CFRP) plates as well as a completely new material: carbon magnesium composite.

CFRP sample

Sample description:

The sample is a laminated rectangular plate containing 6 square size artificial delaminations of 25 mm made of different materials (Teflon film n°2, Teflon tape n°5, Kapton tape n°6, Flash breaker n°3, Mylar and Teflon film inserted into Kapton tape n°1&4). The tested composite is HexPly_6376C_HTS(12K)_10_35%.

Pulsed thermography:

Pulsed thermography set-up:

The experimental configuration for thermal infrared vision is illustrated in Figure 1. The radiation source is pointed towards the inspected object. The camera records images from the object surface. Data is stored and processed with a computer.

Results Analysis:

Data was processed by pulsed phase thermography (PPT). After the Fourier transform of the time signal, phase and amplitude images are obtained from which we can easily distinguish 5 of the 6 defects present in the sample. The defect made of flash breaker is not so well detectable using flash lamps as heat source.

Vibrothermography

Vibrothermography set-up:

An ultrasound controller sends the vibration signal to a piezo actuator. The actuator is pressed against the specimen (by a pneumatically-driven coupling system) via a coupling material as shown in Figure 2. A time pulse at constant amplitude (Pulse method) or amplitude modulated is used.

Results analysis:

Even if the chosen vibration frequency can affect visibility of each defect, we find that the 6 defects are as or more detectable as in phase thermography (see Figure 4). The Flash breaker defect may this time be easily detected but the Kapton tape insert is, in this case, a bit more difficult to reveal. Note that at 20 kHz, a standing wave has been observed between the two rows of defects and a limited heating zone is noticed in the area of the interface with the transducer.

Conclusion:

Results obtained by both, optical pulsed thermography and vibrothermography, were somewhat similar in this case. It is worth trying to verify if this equivalence is also true in the case of other composite sample types such as carbon magnesium one (CMg in abbreviated).

Carbon magnesium sample

Sample description:

The described metal matrix composites are magnesium matrix based (AZ91 alloy, 9 wt.% Al, 1 wt.% Zn) reinforced with about 45 vol.% high strength long carbon fibers. The used manufacturing technique is the semi-solid thixomoulding injection (Husky HyMet 650) used here with full liquid fraction. Hence, short contact times between fibers and liquid metal during infiltration can lead to bad fiber-matrix adhesion at interface. Further high speed injection requires sufficient geometrical pre-form stability to avoid undesirable defects such as porosity, bad orientation, deflection or fragmentation of the pre-form. The sample used here presents fibers deflection that induces bad impregnation between carbon fibers and magnesium.

Pulsed thermography:

Results Analysis:

There is unfortunately no indication appears on the thermographic images (Figure 5). Indeed, the thermal conductivity of magnesium is very high and the heat that may be trapped by defects is almost instantly dissipated into the magnesium. Therefore pulsed thermography is not useful in this case (at least using a 40 Hz video frame rate).

Vibrothermography:

Results Analysis:

By injecting a 25 kHz vibration signal for 6 s in the sample, it is possible to observe the surface where fibers are emerging out of the magnesium. We see a significant heating due to friction fiber against fiber (see Figure 6). But temperature contrast cannot be detected by observing the healthy face for the same reason that pulsed thermography failed to do so: the thermal conductivity of magnesium. However, if it was possible to reproduce an identical test on a healthy part and one in which the fibers are poorly impregnated, the internal heat source due to friction of the fibers would result on different global temperature gradient of both samples. Thus, detecting a variation of the temperature gradient would be indirect evidence of the presence of debonding and its extent.

Conclusions

Pulsed phase thermography and vibrothermography are useful and may be complementary in the case of conventional CFRP samples with equivalent performance. Note that in the case of vibrothermography, the technique is highly dependent of the conditions of the experiment like the excitation frequency and the coupling characteristics. The pulsed phase thermography is apparently not useful for CMg sample analysis. However, significant heating of bad impregnated carbon fibers in CMg sample has been observed using vibrothermography. Based upon this finding, attempts to evaluate and quantify the total fiber/matrix decohesion surface are currently in progress, even by an indirect method. This is essential because the manufacturing process of these CMg samples remains experimental and its effectiveness must be proven scientifically.

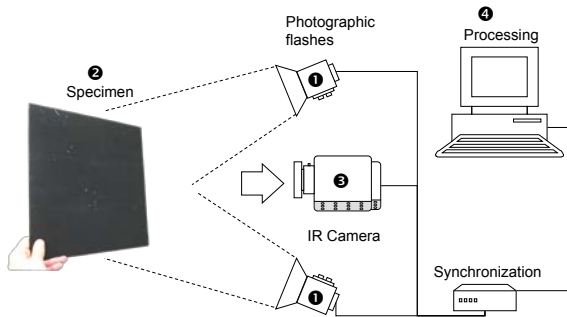


Figure 1: Typical experimental setup for infrared vision

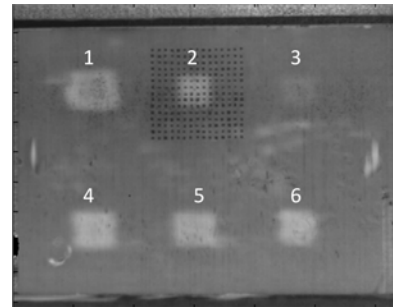


Figure 2: FFT phase thermography image of the sample using 2 flash lamps of 6.2 kJ by reflection for 5 ms

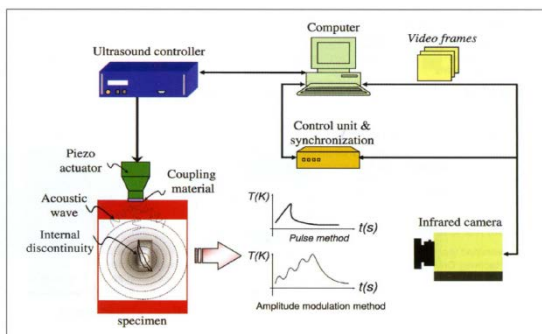


Figure 3: vibrothermography set up

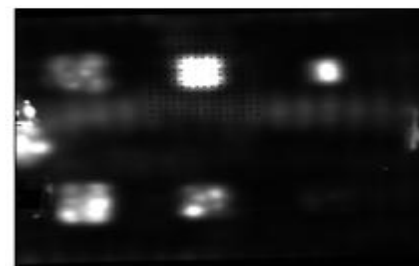


Figure 4: vibrothermographic FFT amplitude image using a 6 seconds 20kHz signal with modulated amplitude

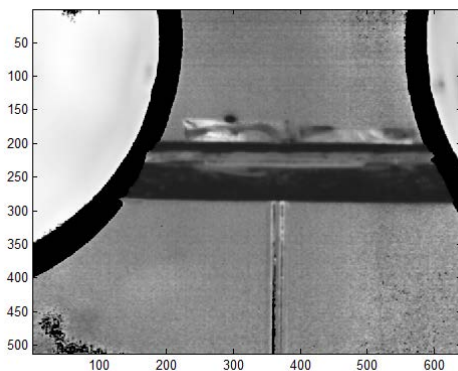


Figure 5: Pulsed thermographic image of CMg sample using 2 flash lamps of 6.2 kJ by reflection for 5 ms

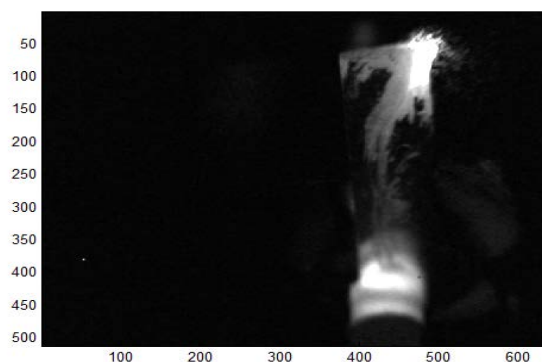


Figure 6: Vibrothermographic image of C-Mg sample (25kHz)

Multivariate Infrared Signal Processing by Partial Least-Squares Thermography

Fernando LÓPEZ, Vicente NICOLAU

*Department of Mechanical Engineering, Federal University of Santa Catarina, 88040-900,
Florianopolis, Brazil*

Xavier MALDAGUE, Clemente IBARRA-CASTANEDO

*Electrical and Computing Engineering Department, Laval University, G1K 7P4, Quebec City,
Canada*

Abstract. This paper introduces and tests a statistical correlation method for the optimization of the pulsed thermography inspection. The method is based on partial least squares regression, which decomposes the thermographic PT data sequence obtained during the cooling regime into a set of latent variables. The regression method is applied to experimental PT data from a carbon fiber-reinforced composite with simulated defects. Results showed that with the new proposed technique is possible to suppress much of the noise affecting the detection of smaller and deepest defects.

1 Introduction

Pulsed Thermography [1] is one of the most popular approaches for the inspection and quantification of defects in materials. Its great prestige lies in its capability to deploy the inspection in transient regime, allowing in this way to display results close to real-time. However, due the physical processes involved during the thermographic measurement, different sources of noise affect the signal acquired by the infrared camera. Furthermore, non-uniform heating during the application of the thermal excitation and thermal losses at the edges of the surface adversely affect the quality of the results. For these reasons, it is often necessary to process the thermographic signals in order to improve – qualitatively and quantitatively – the quality of the results.

Most of the advanced signal processing techniques used nowadays (for instance, differential absolute contrast - DAC, and thermographic signal reconstruction - TSR) are based on the 1D solution of Fourier's law of heat conduction. Despite the great improvement in the quality of the images obtained with Fourier law-based signal processing techniques, its application is subjected to certain criteria, which include: defect depth, thermophysical properties of the material and duration of the transient regime. These concerns motivated the review of an alternative method that could allow the reconstruction of the thermographic signatures while maintaining physical consistency.

This work proposes a statistical correlation method for the treatment of thermographic images called Partial Least-Squares Thermography (PLST). The proposed method – based on partial least squares regression (also known as *projection to latent structures*) – computes loading P and score vectors T that are correlated to the predicted block Y (as in Maximum Redundancy Analysis) while describing a large amount of the variation in the predictor matrix X (as in Principal Component Regression) [2]. The matrix X corresponds to the surface temperature matrix obtained during the PT inspection, meanwhile Y is defined by the observation time during which the thermal images were captured. The result of the decomposition of the X block (along with the correlation with Y) is a new set of thermal images and observation time vectors. The new thermal sequence is composed of latent variables (the new subspace) which consider only the most important variations and unnecessary information present in the original thermal sequence is neglected.

2 Pulsed thermography fundamentals

Figure 1 shows the basic principles of pulsed thermography. The inspection by PT is based on the application – via radiation heat transfer – of a short and high power thermal pulse to the specimen surface (input signal). The amount of thermal energy being absorbed by the surface of the sample will create a thermal front that propagates within the material until it reaches internal defects, which alter the heat diffusion flux. This interaction between the heat flux and internal anomalies - regions with different thermal properties in relation to their surroundings - produces dissimilar behaviors in terms of the temperature decay during the cooling process, which can be observed with an infrared camera (output signal). The deployment of this approach is carried out in transient regime – in contrast with lock-in thermography which is carried out under steady-state conditions – thereby allowing fast and straightforward data acquisition.

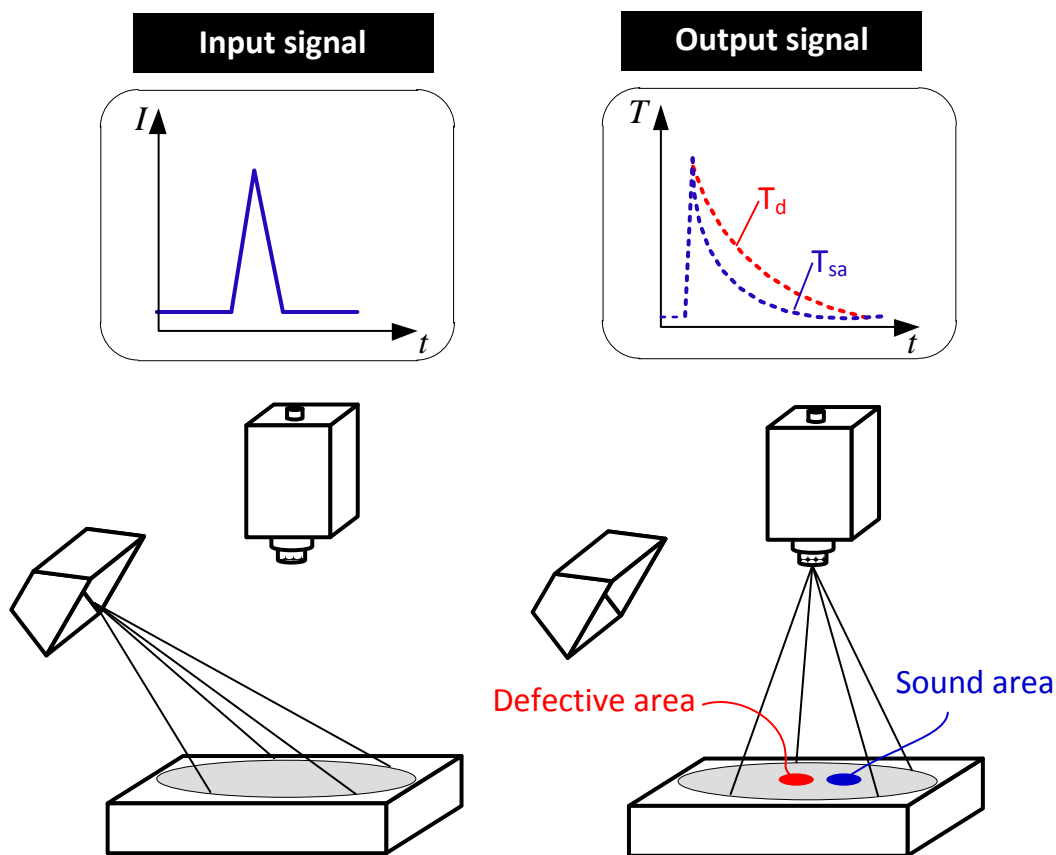


Figure 1. Basic principles of the inspection by pulsed thermography.

3 Basics of partial least squares regression

Partial least squares is a method for constructing predictive models, which was developed by Herman Wold as an econometric technique, although some of the most avid proponents of PLS are chemical engineers (including Wold's son Svante). The basic concept of PLS and how it differs from classical linear regression methods can be seen in Figure 4. While most regression methods rely on the use of all x-values, independently of the content, in order to form a new linear combination of variables, in PLS a few linear combinations

(components or factors) of the original x-values are found and only these linear combinations are considered in the regression equation [3] [4] [5]. In this way, irrelevant and unstable information is discarded and only the most relevant part of the x-variation is used for the regression. The collinearity problem is solved and more stable regression equations are obtained. Furthermore, since all variables are projected down to only a few linear combinations, simple plotting techniques can be used for the analysis.

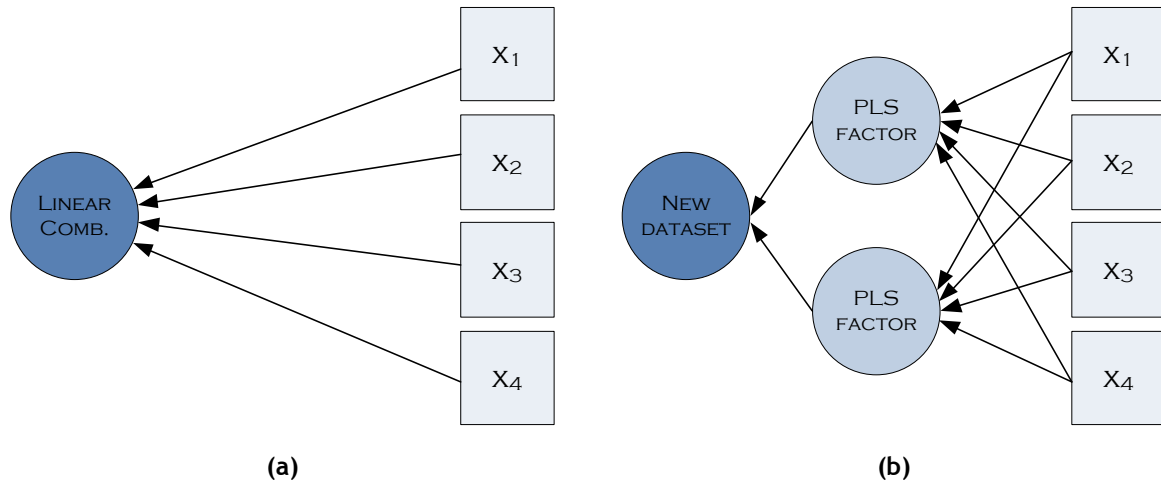


Figure 2: Conceptual illustration of PLS and its comparison with classical linear regression methods..

PLSR decomposes the predictor X ($n \times N$) and predicted Y ($n \times M$) matrices into a combination of loadings, scores and residuals. The PLS model is expressed as [3]:

$$X = TP^T + E \quad (1)$$

$$Y = TQ^T + F \quad (2)$$

In Equations (1) and (2), T ($n \times a$) is known as the scores matrix and its elements are denoted by t_a ($a = 1, 2, \dots, A$). The scores can be considered as a small set of underlying or latent variables responsible for the systematic variations in X . The matrices $P(N \times a)$ and $Q(M \times a)$ are called loadings (or coefficients) matrices and they describe how the variables in T relate to the original data matrices X and Y . Finally, the matrices E ($n \times N$) and $F(n \times M)$ are called residuals matrices and they represent the noise or irrelevant variability in X and Y , respectively.

It can be noted in Equations (1) and (2) that the X -scores (T) are predictors of Y and also model X , i.e., both Y and X are assumed to be, at least partly, modeled by the same latent variables. The scores are orthogonal and are estimated as linear combinations of the original variables x_k with the coefficients, called weights, w_{ka} ($a = 1, 2, \dots, A$). Thus, the scores matrix T is expressed by:

$$T = XW \quad (3)$$

Once the scores matrix T is obtained, the loadings matrices P and Q are estimated through the regression of X and Y onto T . Next, the residual matrices are found by subtracting the

estimated versions of TP^T and TQ^T from X and Y , respectively. Finally, the regression coefficients for the model are obtained using Equation (4):

$$B = WQ^T \quad (4)$$

which yields the regression model:

$$Y = XB + F = XWQ^T + F \quad (5)$$

The decomposition of the predictor X matrix is carried out using the nonlinear iterative partial least square (NIPALS) algorithm.

4 Application of PLSR to pulsed thermography data

The application of PLSR to PT data is achieved by decomposing the raw thermal data into multiple PLS components, each component being orthogonal to each other. Since each of the PLS components is characterized by its variance, it is possible to identify through the PLS components different phenomena affecting the overall thermal regime.

The thermal images obtained during the PT inspection are typically arranged in a 3D matrix, whose x – and y –axis are represented, respectively, by i and j pixels, while the z –axis corresponds to the k frame number. N_x and N_y correspond to the total numbers of pixels in the x – and y – directions while N_T is the total number of frames (see Figure 3 on the left).

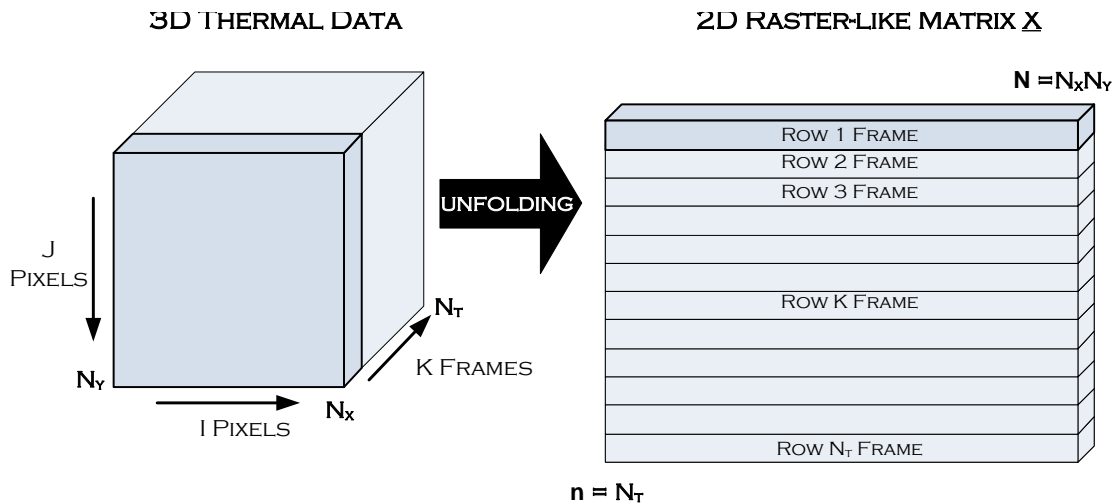


Figure 3: Schematic representation of the transformation of the 3D thermal data into a 2D raster-like matrix.

In order to perform the decomposition of the thermal data sequence into PLS components, it is firstly necessary to transform the 3D thermal data into a 2D raster-like matrix, as shown in Figure 3. This process is known as unfolding. The unfolded X matrix (corresponding to the thermal sequence) has dimensions $N_T \times N_x \cdot N_y$ and physically represents N_T observations (or samples) of $N_x \cdot N_y$ variables (or measurements). On the

other hand, the dimension of the predicted matrix Y – defined by the observation time during which the thermal images were captured – is $N_T \times 1$.

The data used in this study to investigate the applicability of PLSR, consists of a thermal sequence obtained from the PT inspection of a carbon fiber-reinforced polymer. The 3D sequence ($269 \times 252 \times 500$) is mean-centered and converted into a 2D raster-like matrix X (500×67788). The predicted Y matrix is a column-vector (500×1) composed of a time series. The results obtained after the implementation of PLSR to the pulsed thermography data is discussed next.

5 Results

Figure 4 shows a set of six images corresponding to different times after the application of PLSR to the thermal sequence. It can be shown that almost 92 % of the defects can be detected with the new synthetic sequence. Although at longer times (i.e., at 1.16 and 1.75 s) the background noise is reduced; non-uniform heating is still present at the beginning of the IR sequence. The most important finding is that the new sequence preserves the physical coherency of the heat transfer process: shallower defects can be observed at the beginning of the cooling process while deeper defects require a longer observation time to be detected and show less thermal contrast. This latter factor is extremely important and useful for the quantitative analysis of defects.

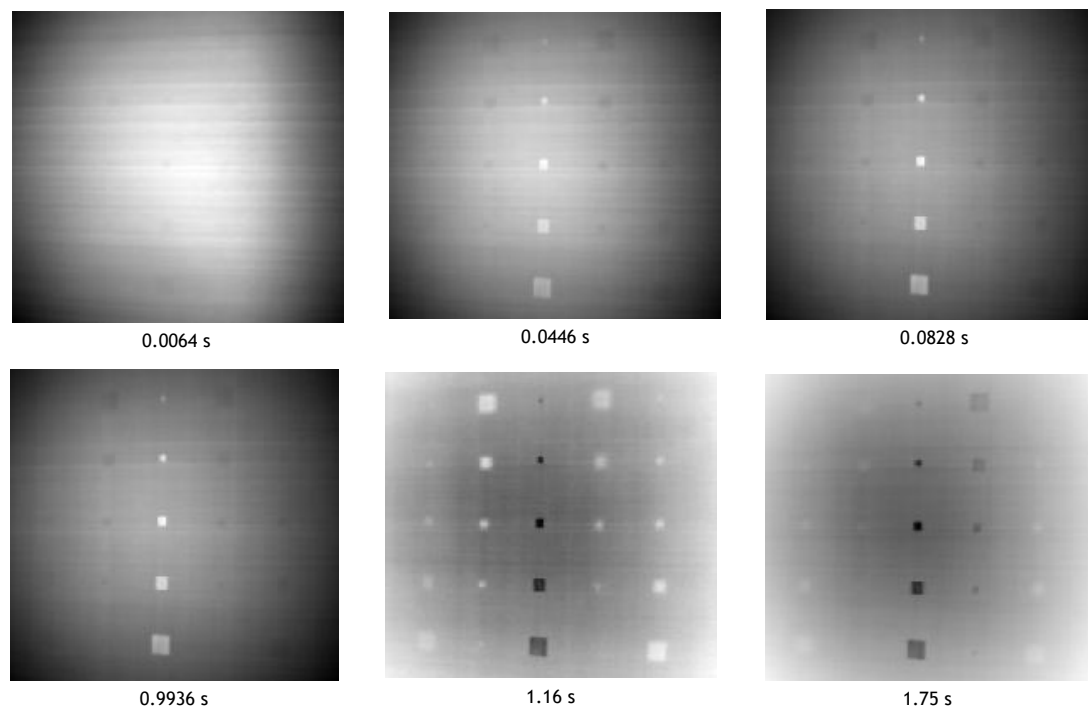


Figure 4: Thermal sequence obtained after the application of the PLS model to raw temperature images.

The reconstructed PLST thermograms conserve the same physical behaviour as in PT data while reducing noise content in the signal. Another interesting feature in PLST, is its extension to situations in which the temperature decay does not follow the 1D solution of the of the Fourier law of heat conduction. Whereas some of the processing techniques are based on the 1D solution of heat conduction equation – and therefore its application is limited to

shallower defects – PLST can be applied to other thermographic inspections (as square pulse thermography - SPT) usually employed for the inspection of materials with low thermal diffusivity and/or deep defects.

6 Conclusions

A methodology and a new method of signal processing of pulsed thermography inspection data has been proposed and tested on experimental carbon fiber-reinforced polymer. The technique, which is based on partial least squares regression, produces a new set of thermal images constructed from the decomposition of the original data into latent variables. The PLSR model allows the components associated with non-uniform heating to be identified and separated. Thus, it is possible to suppress the harmful effects of non-uniform heating and create a new set of images with a considerable reduction in the background noise, while preserving the physical consistency. Further works are toward this direction.

Further studies will include quantitative analysis using the latent variables and the application of PLSR to other signal-types, such as Lock-in and Vibro-Thermography.

References

- [1] X. Maldague, *Theory and Practice of Infrared Technology for Nondestructive Testing*, New York, NY: John Wiley & Sons, 2001.
- [2] L.E. Mujica, J. Vehi, M. Ruiz, M. Verleysen, W. Staszewski and K. Worden, Multivariate statistics process control for dimensionality reduction in structural assessment, *Mechanical Systems and Signal Processing*, 22 (2008) 155-171.
- [3] S. Wold, H. Martens and H. Wold, “The Multivariate Calibration Problem in Chemistry Solved by the PLS Method,” in *Conference Matrix Pencils*, Heidelberg, Germany, 1984.
- [4] H. Martens and T. Naes, *Multivariate Calibration*, Chichester, UK: John Wiley & Sons, 1989.
- [5] T. Naes, T. Isaksson, T. Fearn and T. Davies, *A User-Friendly Guide to Multivariate Calibration and Classification*, Chichester, UK: NIR Publications, 2004.

Use of infrared thermography to measure fiber orientation on carbon-fiber reinforced composites

Henrique Fernandes^{a,*} and Xavier Maldague^a

^a*Department of Electrical and Computer Engineering, Laval University,
1065 de la Medecine Avenue, G1V0A6, Quebec City, Canada*

Abstract. Carbon-fiber reinforced composites are widely used in the industry. One of the key features regarding their quality and usefulness is related to the fiber orientation and content. One technique that is used to test this kind of material is Infrared Thermography (IT). In this paper it is presented a technique based on diode-laser spot heating to measure fiber orientation on the surface of a carbon-fiber reinforced composite manufactured by compression molding of Random-Oriented Strands (ROS) of carbon/PEEK (Polyether ether ketone).

Keywords: fiber orientation, infrared thermography, random-oriented strands, carbon-fiber reinforced composites

1. Introduction

The use of composite materials (CM) is growing more and more every day in several applications, especially in aeronautic structures. The arrangement or orientation of the fibers relative to one another, the fiber concentration, and the distribution all have a significant influence on the strength and other properties of fiber reinforced composites. Thus testing techniques must be developed to assess fiber content. Destructive methods can be employed to evaluate the fiber on a composite, e.g. cutting a section of the material, polishing the area and evaluating it with microscopy. However, the destructive approach is not always an option since the sample will be damaged after inspection and probably unfit for use. Thus, Non-Destructive Testing and Evaluation (NDT&E) techniques must be employed in some cases to assess the material's fiber content.

Infrared Thermography (IT) is a well-known and widely used NDT&E technique for composite material inspection. In active IT an external heat source is used to stimulate the material being inspected in order to generate a thermal contrast between the feature of interest and the background. The active approach is adopted in many cases given that the inspected parts are usually in equilibrium with the surroundings [1]. Qualitative and quantitative assessment of flaws is a very popular application of IT for CM. However there are others such as fiber orientation assessment. In this work we apply IT to assess fiber orientation on a plate's surface. More specifically a "laser spot" technique, that we call Pulsed Thermal Ellipsometry (PTE), is used to assess fiber orientation on the surface of a carbon/PEEK (Polyether ether ketone) plate. The inspected plate was molded with Random-Oriented Strands (ROS) of carbon/PEEK. Figure 1 shows the molded plate. Thus, fiber orientation on the surface is also random since each strand has its own fiber orientation. In this paper the measuring of fiber orientation of individual strands is presented. It shows the feasibility of the proposed NDT&E technique to measure fiber orientation of such material.

*Corresponding author: H. Fernandes; e-mail: henrique-coelho.fernandes.1@ulaval.ca

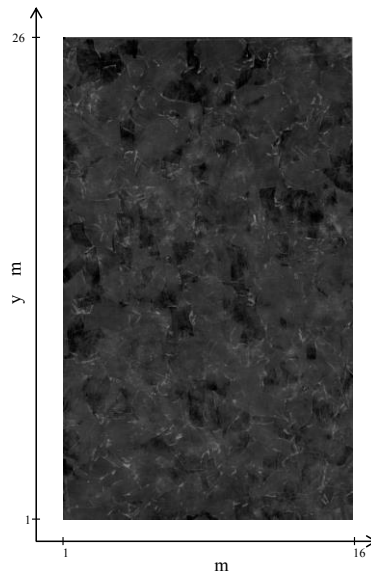


Figure 1 - Random-Oriented Strands (ROS) plate

2. Pulsed Thermal Ellipsometry - PTE

More than one century ago, De Senarmont [2] applied a thermal approach to determine the principal orientations in crystal plates: he covered them with a thin layer of wax, heated them over a small spot and monitored the isotherm shape revealed by the solid/liquid transition contour appearing in the wax layer. The isotherm proved to be elliptical and its aspect ratio is related to the square root of the principal conductivities in the surface plane.

This method, referred to later by Krapez [5-8] as “Thermal Ellipsometry”, was later used for various applications (with, of course, up-to-date experimental equipment) by means of thermography. It was applied on polymer materials to establish a correlation between their draw ratio and the induced thermal anisotropy. It was also used to evaluate the fiber orientation in the case of composite materials using short or long carbon fibers. For the latter problem, authors like Aindow [3] and Cielo [4] showed that heat propagates faster in the longitudinal direction of fiber on the surface of fiber reinforced laminates. In [3], Aindow et al. detected local anisotropy in CFRP (nylon-66) injection moldings by two methods: thermography using infrared scanning, which reveals anisotropy of thermal conductivity, and polarized shear-wave ultrasonic showing elastic anisotropy. For the thermographic method, they recorded isotherms formed around a point source of heat on a plane surface (heat was applied for a period of 15 seconds) using an infrared imaging camera. The isotherms that they observed were ellipses of which the ratio of lengths of the principal axes (b/a) are proportional to the square root of the ratio of thermal conductivities. They assumed that the longest dimension of the counter in each picture indicated the major axis of thermal conductivity in the surface, which in turn is related to the direction of fiber orientation.

Cielo et al. presented in [4] a comparative review of a number of optical techniques for the characterization of non-metallic materials. One possibility reported by them is the evaluation of phase (or fiber) orientation in stretched polymer films or in composites by an analysis of the thermal propagation pattern. A typical configuration is shown in Figure 2. They spot-heated the inspected part by a narrow laser beam and the resulting heat-propagation pattern was analyzed by an IR camera. If the material is oriented, such as the unidirectional graphite-epoxy sheet they inspected, an elliptical thermal pattern is observed, with the ratio between the two principal axes (b/a) being related to the square root of the thermal conductivities in the longitudinal and transverse directions. A test on an isotropic material would

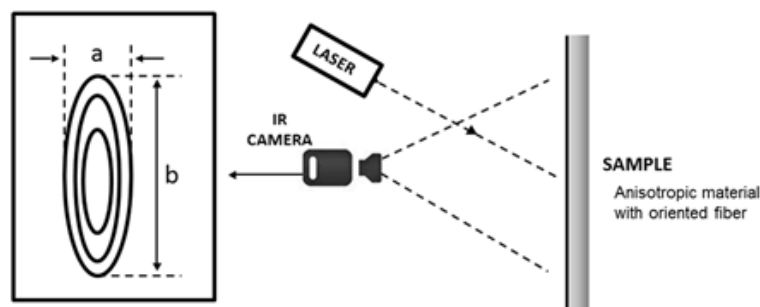


Figure 2 - Thermal analysis laser heat pulse of fiber orientation in composite material

give a circle instead of an ellipse. They illustrated this approach showing results from two 8-ply unidirectional NARMGO 5217 sheets spot heated for a period of 20 seconds with a 0.5 W laser.

A more detailed theoretical analysis was later undertaken through an analytical treatment of thermal diffusion in laminates made of orthotropic layers assuming the surface is submitted to concentrated heating by Krapez in [5]. Three temporal regimes were considered in that study: steady-state regime, transient regime (as obtained during step heating), and modulated regime (in order to analyze how the so-called thermal waves “propagate” in orthotropic laminates). Experiments were performed on carbon-epoxy laminates for all three regimes. In [6], Krapez used the same theory (thermal anisotropy measurements method which consists in analyzing the shape of the isotherms which develop around a heated spot) to develop a thermal inversion method to infer thickness of skin and core layers of a 3-layer carbon/epoxy laminate.

In [9], Karpen et al. used lock-in thermography (harmonic thermal waves) to probe orientation fields of carbon fibers both along the surface and in depth at low modulation frequencies and within a short time. Later, in [10] he developed a theoretical model in order to correctly interpret the measurements.

3. Experiments and Results

The PTE technique using diode-laser spot was applied on ROS plate. The plate was placed in front of the laser beam and a plano-convex lens was placed between the laser beam and the plate. It was used to focus the beam in a small spot. Laser beam formed a 90° angle with plate's surface while camera optical axis formed a 75° angle with plate's surface. A short pulse was shot heating a small circle area on the plate's surface. This small area was previously chosen so the heated area stayed restricted to a single strand. The goal with this configuration was to detect fiber orientation on a single strand since orientation changes according to the strand. Then, heating and cooling down process were recorded using middle

Table 1 - Parameters used in the experiment

Parameter	Value
Diode-laser frequency	805 nm
Beam power used	5W of 30W
Shooting duration	0.1 seconds
Spot size on plate's surface	3 mm
Recording time	20 seconds
Image used to extract fiber orientation	0.2 seconds after beam had stopped

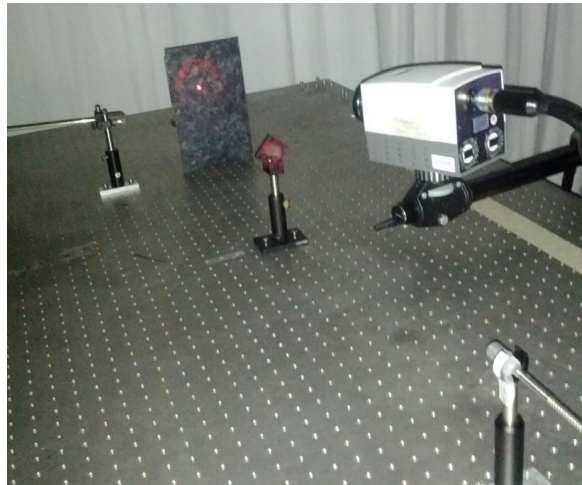


Figure 3 - Diode-laser experimental setup

wave infrared camera (MWIR). As mentioned before, the pattern formed on the plate's surface is elliptical in anisotropic materials, which is the case of carbon-fiber reinforced plates and the ellipse major axis is related with the fiber orientation. The setup configuration prepared in the laboratory is shown in Figure 3 and the parameters used in this experiment are in Table 1.

Two different strands were chosen to show the feasibility of the technique. First strand was spot heated while the plate was in vertical position (same position shown in Figure 1) and then to prove that

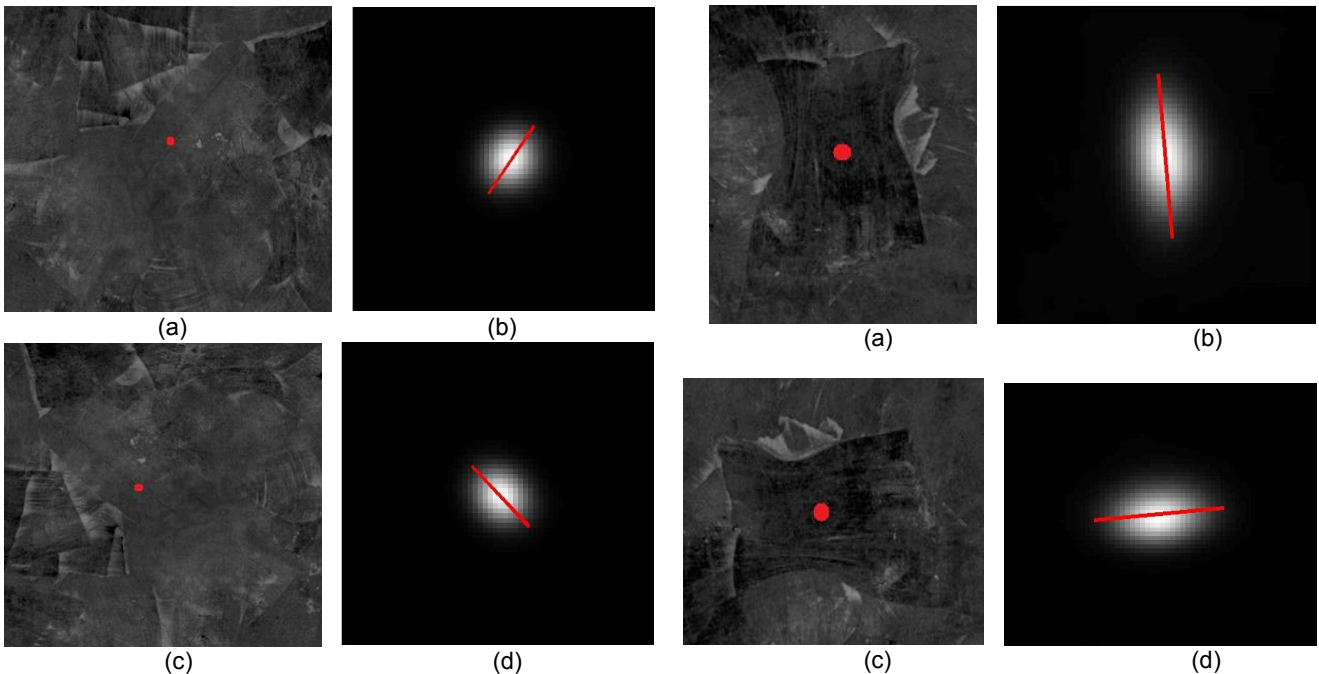


Figure 41 - Fiber orientation measurement of the first strand
 (a) Plate in vertical position, red dot show where beam heated the chip, (b) Ellipse formed after 0.2 seconds after beam has stopped, red line show major axis. Its orientation is 55.99° .
 (c) Plate in horizontal position, red dot show where beam heated the chip, (d) Ellipse formed after 0.2 seconds after beam has stopped, red line show major axis. Its orientation is -47.52° .

Figure 5 – Fiber orientation measurement of the second strand
 (a) Plate in vertical position, red dot show where beam heated the chip, (b) Ellipse formed after 0.2 seconds after beam has stopped, red line show major axis. Its orientation is -85.19° . (c) Plate in horizontal position, red dot show where beam heated the chip, (d) Ellipse formed after 0.2 seconds after beam has stopped, red line show major axis. Its orientation is 6.37° .

the technique works the same strand was heated again however now while the plate was rotated 90° counter clockwise (in horizontal position). Thus the difference between in the two major axes of those two experiments should be around 90° (the difference in rotating the plate from vertical to horizontal position). After this procedure was done for the first strand the same procedure was done for the second chosen strand. Results show that the PTE works well for single strands case. Results can be seen in Figure 4 and Figure 5. Orientation angles are shown with respect to x-axis.

Figure 4 shows the first tested strand. Figure 5b shows the ellipse major axis while the plate was in vertical position. The ellipse major axis orientation is 55.99 degrees measured with Matlab[®]. Figure 5d shows the ellipse major axis while the plate was in horizontal position. The ellipse major axis orientation is -47.52 degrees measured by the same Matlab[®] script. When the plate was rotated (vertical to horizontal position) an error of 13 degrees was introduced between the measurements. Figure 5 shows the other tested strand. Figure 5b shows the ellipse major axis while the plate was in vertical position. The ellipse major axis orientation in this case is -85.19 degrees measured with Matlab[®]. Figure 5b shows the ellipse major axis while the plate was in horizontal position. The ellipse major axis orientation is 6.37 degrees measured by the same Matlab[®] script. When the plate was rotated (vertical to horizontal position) again an error of 1.5 degrees was introduced between the two measurements.

4. Discussion

For both strands, the difference between the two major axis measurements (first when the plate was in vertical and then in horizontal position) should be 90° . However it was not. For the first strand, the difference between the orientation of the two ellipse's major axis was 76.49° (an error of 13.5° approximately). This happened because the exactly position heated in each case was not the same and perhaps in the second case a place nearer the chip border was heated and it got more influence from a neighbor chip which could have different fiber orientations. Additionally, during the plate's molding process heat and pressure are applied on the strands which leads to a high degree of deformation in the shape of consolidate strands in the final plate and it could give to strands a high level of "shape interaction". Thus in some cases neighbors strands can play a bigger role in the heating dissipation of a single strand which could affect the elliptical pattern. For the second inspected strand the difference between the two major axis was 88.44° (an error of 1.5° approximately). Here the error between measurements is smaller. This happened because the second chip is better placed and large enough so the heating spot could hit the same position (no edge or neighbor strands effects).

5. Conclusions and Future Work

In this work infrared thermography was used for non-destructive characterization of composite materials. The Pulsed Thermal Ellipsometry (PTE using a laser spot pulse as excitation source) was tested and showed effective to measure fiber orientation on the surface of a ROS carbon/PEEK specimen. However, the diode-laser laser spot technique (PTE) measures fiber orientation of a small region of plate's surface at a time and this is not good enough for real industrial applications. Thus, this research must continue in order to develop a faster approach which can measure fiber orientation of a bigger area at once.

Acknowledgements

The authors would like to greatly acknowledge financial support provided by Laval University and the industrial partners: Bell Helicopter Textron Canada Limited, Bombardier Inc., Pratt and Whitney Canada Corp., Marquez Transtech Limited, Delastek Inc. and Avior Integrated Products Inc.

The authors would also like to acknowledge the funding provided by the Natural Sciences and Engineering Research Council of Canada (NSERC), the Consortium for Research and Innovation in Aerospace in Quebec (CRIAQ COMP-412), the *Fonds québécois de la recherche sur la nature et les technologies* (FQRNT) and National Council for Scientific and Technological Development (CNPq) a Brazilian governmental agency.

References

- [1] X. Maldague “*Theory and practice of infrared technology for nondestructive testing*”. John Wiley & Sons, New York, 2001.
- [2] M. H. De Senarmont “Mémoire sur la conductibilité des substances cristallisées pour la chaleur”. *Second Mémoire, Annales de Chimie Physique*, Vol. 3, 22, pp 179-211, 1851.
- [3] J.D. Aindow, M.F. Markhan, K.E. Putti k, J.G. Rider and M.R. Rudman “Fibre orientation detection in injection-moulded carbon fibre reinforced components by thermography and ultrasonics”. *NDT international*, Vol. 19, No. 1, pp 24-29, 1986.
- [4] P. Cielo, X. Maldague, J.-C. Krapez and R. Lewak “Optics-Based Techniques for the Characterization of Composites and Ceramics”. *Nondestructive Characterization of Metals*; Montreal; Canada, pp 733-744, 1987.
- [5] J.-C. Krapez “Thermal ellipsometry applied to the evaluation of fibre orientation in composites”. *Journee d'Etude sur la Thermographie*, Paris, France, 1994-171, 1994.
- [6] J.-C. Krapez “Thermal ellipsometry- A tool applied for in-depth resolved characterization of fibre orientation in composites”. *Review of Progress in Quantitative Nondestructive Evaluation*, Seattle, WA, July 30-Aug. 4, 1995, ONERA, TP, n.1995-148, 1995.
- [7] J.-C. Krapez, G. Gardette, and D. Balageas “Thermal ellipsometry in steady-state and by lock-in thermography. Application to anisotropic materials characterization”. In: D. Balageas, G. Busse, G.M. Carlomagno, editors. *Proceedings of the Qirt 96*, Eurotherm Series 50. EETI ed., pp. 257–262, 1996.
- [8] J.-C. Krapez and G. Gardette “Characterisation of anisotropic materials by steady-state and modulated thermal ellipsometry”. *High Temperatures - High Pressures*, v.30(5), pp. 567–574, 1998.
- [9] W. Karpen, D. Wu, R. Steegmuller and G. Busse “Depth profiling of orientation in laminates with local lock-in thermography”, in: D. Balageas, G. Busse, G.M. Carlomagno, editors. *Proceedings of the Qirt 94*, Eurotherm Series 42, EETI editions, pp. 281–286, 1994.
- [10] W. Karpen, D. Wu, and G. Busse “A Theoretical Model for the Measurement of Fiber Orientation with Thermal Waves”. *Res. Nondestr. Eval.*, v. 11, pp. 179-197, 1999.

A comparative study on probability of detection analysis of manual and automated evaluation of thermography images

by Yuxia Duan^{1, 2}, Ahmad Osman³, Clemente Ibarra-Castanedo^{2,*},
Ulf Hassler³, Xavier Maldague²

¹*School of Material Science and Engineering, Beihang University, 37, Xueyuan Road, Beijing 100191, China;*

²*Computer Vision and Systems Laboratory, Department of Electrical and Computer Engineering, Université Laval, 1065, av. de la Médecine, Québec (QC), Canada G1V 0A6;* ³*Fraunhofer Development Center X-ray Technologies (EZRT), Dept. Application Specific Methods and Systems (AMS), Fraunhofer IIS, Dr.-Mack-Straße 81, 90762 Fuerth, Germany*

Abstract

We present a method to extract defects automatically by image segmentation. The images used for segmentation are the raw thermal images and the resulting images obtained by 5 commonly used data processing techniques in optical pulsed thermography. At the end of this article, probability of detection (PoD) analysis results after automated segmentation of raw/processed images are compared with the results obtained from manual evaluation. False alarm which is an important aspect of reliability evaluation of nondestructive technique is also studied.

Keywords: PoD, segmentation, thermal image, binary image, false alarm

1. Introduction

In an earlier paper [1], we inspect a Carbon Fiber Reinforced Polymer (CFRP) specimen with simulated delaminations (Teflon inserts) by optical PT. Then we performed different post-processing routines, including Fourier Transform (FT), Thermal Signal Reconstruction (TSR), Wavelet Transform (WT), Differential Absolute Contrast (DAC), and Principal Component Thermography (PCT). An inspector visually examined the resulting images including the raw Pulsed Thermography (PT) images to give a qualitative evaluation of the appearance of every defect. The inspector recorded the inspection result in terms of whether or not a flaw was found, and then 6 sets of hit/miss data were obtained. It should be noted that the inspector knows the real location of every defect, which may influence the inspector's interpretation. This finally influences the probability of detection (PoD) analysis result. Actually, in the design of a Nondestructive Testing and Evaluation (NDT&E) reliability experiments, human factor including capability and mental acuity of the inspector is an important aspect that needs to be considered [2, 3]. Sometime, several inspectors instead of one inspector are employed to interpret the response or the resulting image [2]. In this paper, we will perform automated segmentation before source data collection which is used for PoD analysis. Compared with thermal image, the segmented image provides visualized information about true defects and false alarms. Analyzing the binary images after automated segmentation would be obviously easier for the inspector.

2. Procedure of automated segmentation

In this section, we present an evaluation method dedicated to automatically segment input thermal images. Assume that N raw images have been recorded by the thermal camera as times: t_1, t_2, \dots ,

* Corresponding author: Xavier Maldague, Xavier.Maldague@gel.ulaval.ca

t_N . The evaluation method is applied on input raw images and it is composed of:

- A data processing step aiming into improving the image contrast and reducing the noise, thus improving the defect detection capability [1].
- A segmentation procedure based on the use of the Contrast Noise Ratio (CNR) image instead of the thermal image, this allows removing the fluctuation in values of pixels corresponding to defect [4-6]. In fact, due to the variation in phase, defects appear bright in some frames and dark in other frames. By using the CNR image, all suspicious regions where a gradient in the grey values occur will appear as bright regions. CNR for every pixel in a thermal image is calculated by:

$$\text{CNR} = \frac{\text{average value over a } 3 \times 3 \text{ pixels area} - \text{average value of reference area}}{\text{standard deviation of the reference area}}$$

It should be noted that the whole thermal image is selected as the reference area to avoid the subjective selection of defect-free-zone.

- After computing the CNR image, a threshold is computed (Otsu's method) and applied on the pixels of the image. The algorithm assumes that the image to be segmented contains two classes of pixels (e.g. foreground and background) then calculates the optimum threshold separating those two classes so that their combined spread (intra-class variance) is minimal [7-9]. This results in a binary image where pixels are set as 0 (background) and 1 (foreground).
- The last step of the segmentation procedure is the fusion of all the binary images corresponding to the input raw images recorded at t_1, t_2, \dots, t_N . The number of true defects and false alarms can be simply computed on the resulting final image. The flow-process diagram of the procedure of automated segmentation is shown in figure 1.

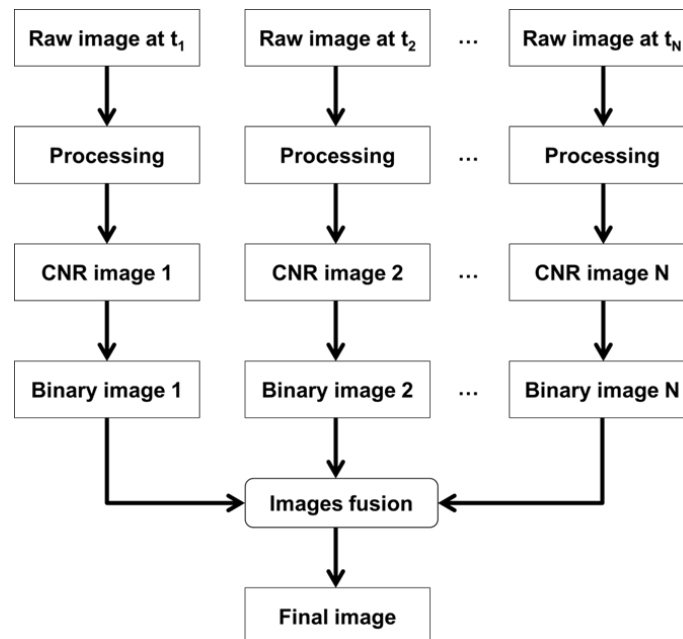


Figure 1. The flow-process diagram of the procedure of automated segmentation.

3. Binary Images after Automated Segmentation

The evaluation method is tested on a CFRP specimen including 25 Teflon inserts simulating delamination. The specimen was tested from both sides giving a total 50 inspection targeted sites (flaws with different aspect ratio (Dimension / depth) values, from 3/1.8 to 15/0.2). The experiment configuration and parameters used in the data processing manipulations are described in our earlier paper [1].

First, the thermal images obtained from TSR manipulation which is slightly more effective than other routines (FFT, WT and DAC) for our specimen, are evaluated to automatically segment the defects. The 1st derivative images (front side inspection) at different times obtained by TSR and corresponding automatically segmented images are presented in figure 2. The binary fusion image is the result of the segmentation of 1st derivative images at time $t_1 = 0.075s$, $t_2 = 0.1s$ and $t_3 = 0.35s$. The fusion image contains 22 true defects and 8 false alarms.

The fusion images for the raw and resulting images processed by TSR, PPT, PCT, WT and DAC are shown in figure 3.

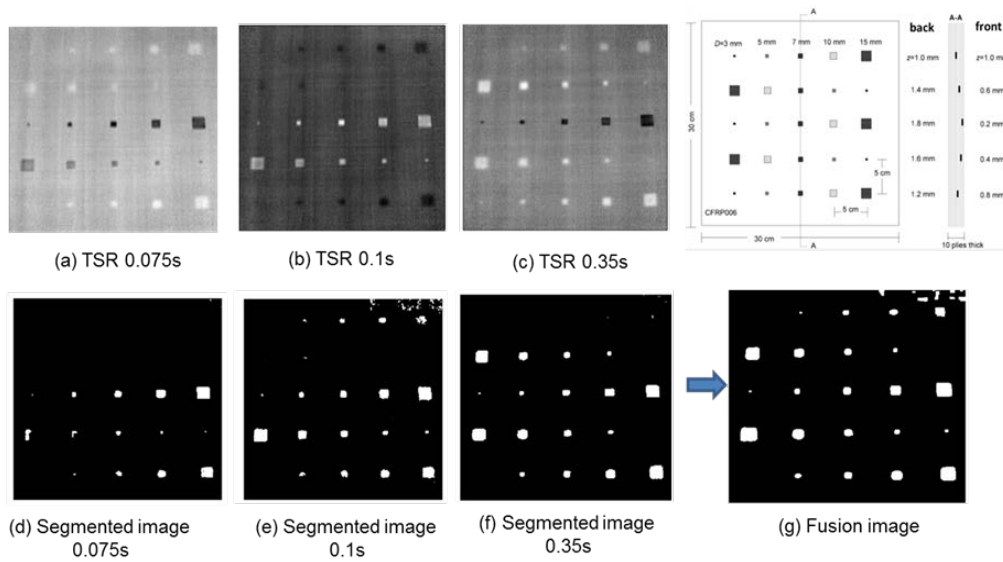


Figure 2. (a) - (c) 1st derivative images (front side inspection) at different times obtained by TSR, (d) - (f) corresponding automated segmentation, (g) fusion image of 3 segmented images.

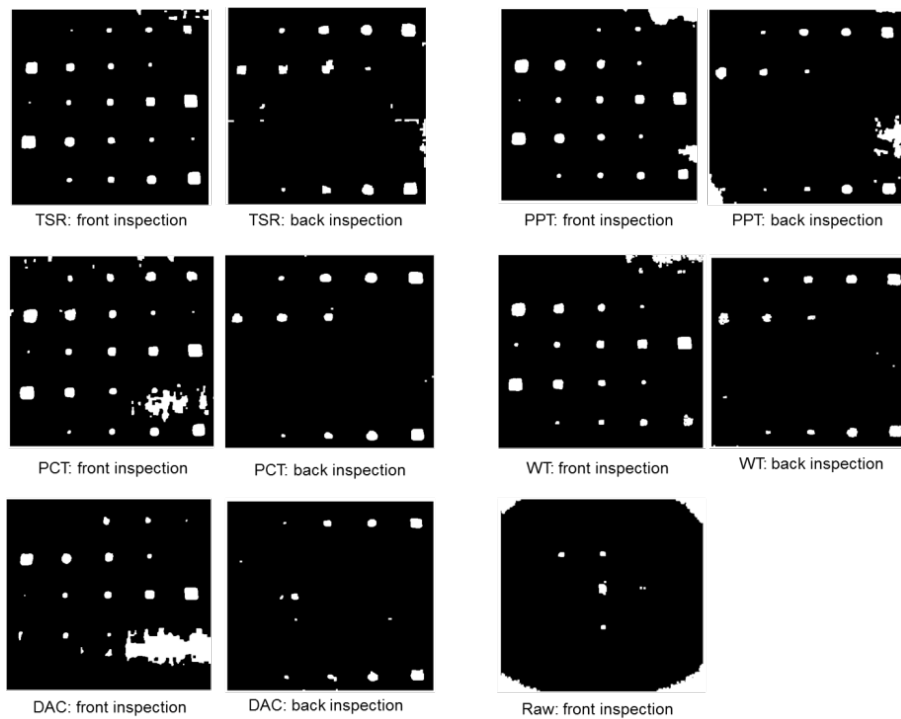


Figure 3. Fusion images for the raw and resulting images processed by TSR, PPT, PCT, WT and DAC.

4. PoD Analysis Results after Automated Segmentation

Table 1 shows the rough comparison of manual evaluation and automated segmentation for the inspection results by non-processed and different data processing techniques.

From table 1, it is obvious that the detection rate of manual evaluation is greater than automated segmentation for the same thermal images (raw or after different data processing manipulation). Inspectors familiar with thermal images can identify more defects relying on their experiences.

Table 1. Rough comparison of manual evaluation and automated segmentation.

Data processing	Manual evaluation		Automated segmentation		
	Number of inserts detected	Detection rate	Number of inserts detected	Detection rate	False calls
TSR 1 st D	40	80%	34	68%	19
PCT	38	76%	33	66%	22
PPT	36	72%	30	58%	14
WT	35	70%	30	58%	10
DAC	30	60%	24	48%	15
RAW	19	38%	5	10%	5

Log-odds model was employed to plot the PoD curves of manual evaluation result as shown in figure 4 [1], and PoD curves of automated segmentation result, as shown in figure 5.

95% lower confidence bounds for each data processing methods were also calculated [10]. Table 2 shows the defect aspect ratio with 90% PoD (r_{90}) and the defect aspect ratio for which a 90% PoD is reached at 95% confidence level ($r_{90/95}$). It should be noted that defect aspect ratio with 90% PoD cannot be determined from the PoD curve because only 5 out of 50 defects were identified from the raw thermal images.

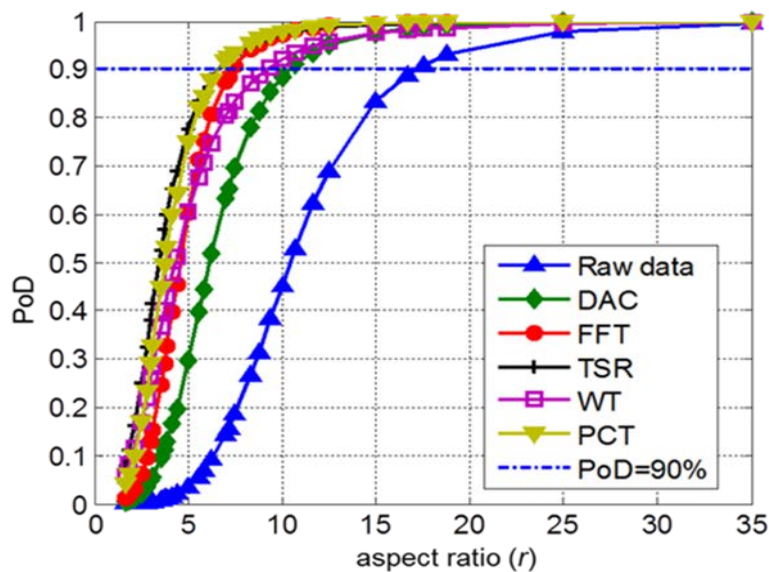


Figure 4. PoD curves of manual segmentation result [1].

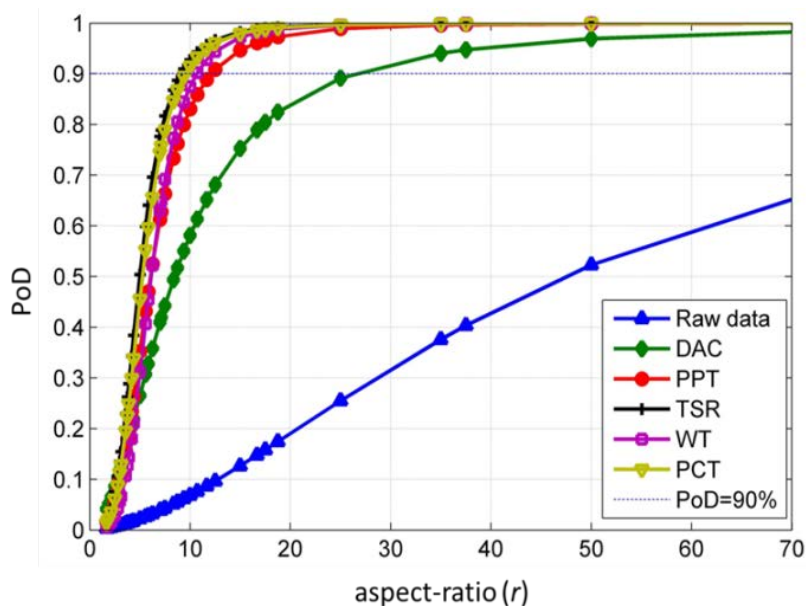


Figure 5. PoD curves of automated segmentation result.

Table 2. r_{90} and $r_{90/95}$ values obtained from manual evaluation and automated segmentation.

Data processing	Manual evaluation		Automated segmentation		
	r_{90}	$r_{90/95}$	r_{90}	$r_{90/95}$	False calls
TSR 1 st D	6.60	11.50	9.07	15.39	19
PCT	6.64	10.91	9.51	16.11	22
PPT	7.37	11.44	12.13	22.77	14
WT	9.20	17.63	10.68	17.82	10
DAC	10.39	16.93	26.06	98.84	15
RAW	17.06	30.04	∞	∞	5

5. Summary

Both Manual evaluation and automated segmentation results prove that TSR and PCT are more effective than other routines in this experiment. The detection rate of manual evaluation is greater than automated segmentation for the same thermal images (raw or after different data processing manipulation). Inspectors familiar with thermal images can identify more defects relying on their experiences.

6. Acknowledgements

Authors wish to thank to the Canada Research Chair in Multipolar Infrared Vision (MIVIM) for providing the CFRP specimen for the PoD studies. The Ministère des Relations Internationales du Québec: Programme de coopération scientifique Québec-Bavière and NSERC are acknowledged as well for their support during the completion of this work.

REFERENCES

- [1] Y. Duan, P. Servais, M. Genest, C. Ibarra-Castanedo and X. Maldague, "ThermoPoD: A reliability study on active infrared thermography for the inspection of composite materials", *Journal of Mechanical Science and Technology*, vol. 26 (7), pp.1985 - 1991, 2012.
- [2] A. P. Berens, "NDE reliability data analysis", in *Metals Handbook*, 9th ed., vol. 17, pp. 1389 – 1470, Ohio: ASM International, 1989.
- [3] US Air Force Aeronautical Systems Center, *Military Handbook 2009: Non-Destructive Evaluation System Reliability Assessment (Department of Defence Handbook)*.
- [4] X. Song, B. W. Pogue, S. Jiang, M. M. Doyley, H. Dehghani, T. D. Tosteson, and K. D. Paulsen, "Automated region detection based on the contrast-to-noise ratio in near-infrared tomography", *Applied Optics*, vol. 43, pp. 1053 - 1062, 2004.
- [5] W. A. Edelstein, P. A. Bottomley, H. R. Hart, and L. S. Smith, Signal, noise and contrast in nuclear magnetic resonance (NMR) imaging *Journal of Computer Assisted Tomography*, vol.7 (3), pp. 391 - 401, 1983.
- [6] T. Varghese and J. Ophir, "An analysis of elastographic contrast-to-noise ratio", *Ultrasound in Medicine & Biology*, vol. 24 (6), pp. 915 - 924, 1998.
- [7] M. Sezgin and B. Sankur, "Survey over image thresholding techniques and quantitative performance evaluation", *Journal of Electronic Imaging*, vol. 13 (1), pp. 146 - 165, 2004.
- [8] N. Otsu, "A threshold selection method from gray-level histograms", *IEEE Transaction on System, Man, and Cybernetics*, vol. 9 (1), pp. 62 - 66, 1979.
- [9] P. Liao, T. Chen and P. Chung, "A Fast Algorithm for Multilevel Thresholding", *Journal of Information Science and Engineering*, vol. 17 (5), pp. 713 - 727, 2001.
- [10] R. C. H. Cheng and T. C. Iles, "One sided confidence bands for cumulative distribution functions", *Technometrics*, vol. 32, pp. 155 - 159, May, 1988.

Evaluation of laser-based active thermography for the inspection of optoelectronic devices

by E. Kollorz, M. Boehnel, S. Mohr, W. Holub, U. Hassler

Fraunhofer Development Center X-ray Technology (EZRT), Dept. Application Specific Methods and Systems (AMS), Fraunhofer IIS, Dr.-Mack-Straße 81, D-90762 Fuerth, Germany

Abstract

An active microscopic thermographic setup is proposed for high-resolution inspection of optoelectronic devices. A laser is used for thermal excitation of the test object. A setup is proposed, which in principle could be used for inline inspection of the chips. A data processing scheme is proposed for interpretation of the images. Experimental results of the imaging as well as of the processing methods are given for some test samples.

Keywords: infrared thermography, inspection, optoelectronic devices, laser excitation, wafer, image processing

1. Introduction

The production of optoelectronic devices for illumination purposes consists of different processing stages. The aim is to detect cracks and voids in the chips as early as possible to sort them out from further processing. Therefore, image acquisition and processing is necessary to analyze each individual chip. Due to small defect sizes, high spatial resolution images are required. The current common inspection modality for such devices is ultrasound.

Alternatively, we propose the use of a thermographic camera in combination with laser excitation to get high resolution images of the devices. The aim is a high throughput of chips during inspection and improved detection of defects in comparison to standard ultrasound technique.

2. Methods

This contribution covers two parts: the image acquisition and processing. Image acquisition comprises the test setup and the used hardware. Image processing deals with an automatic inspection of the chips composed of several steps.

2.1. Image acquisition

The image acquisition is performed with the infrared (IR) camera Ircam Equus 327k SM using a microscopic object lens. The lens is necessary to analyze different chip geometries within the defined field of view (FOV). The acquired thermographic images are quantized with 14 bit, have resolution of 640 · 512 pixels with a pixel size of 7.5 µm. The used Coherent Obis laser has a wavelength of 405 nm for optimal absorption in the given material. It is used in analog modulation mode with a peak power of 100 mW in combination with a function generator Tektronix AFG 3022B. The function generator is necessary for a precise timing of the laser and the camera's image acquisition. There are different combinations possible: reflective or

transmissive excitation and a focused or unfocused laser beam. The optoelectronic devices comprise different layers, mostly of GaN and Si.

2.2. Image processing

Many individual chips are arranged on a wafer before they will be separated in the final production stage. Therefore, we have to define a scanning geometry to analyze the chips in an ordered manner. We implemented a meander scan [1]. An axes manipulation system shifts the wafer piecewise to successively acquire images of the chips. To correct intensity inhomogeneities and bad camera pixels in the acquired images, a non-uniformity correction (NUC) is applied and afterwards a bad pixel correction. Due to the active cooling of the camera chip, so-called coldreflex appears in the images. We correct this effect in a preprocessing step. To detect the apparently defective chips, within a preceding step a 'defect-free' reference has to be generated from various chips within a known healthy region. The chips in the current image have to be separated and compared to this reference chip [2]. Significant deviations from the reference are interpreted as potential defects.

Subsequently the specific steps in the image processing pipeline are described (Fig. 1):

(1) Acquisition of thermographic raw images

The integration or exposure time (i.e. the time during which the detector is sensitive for IR radiation) is set to 1.0 ms. Images can be acquired at a maximum frame rate of 100 fps. The image size is $640 \cdot 512$ pixels with a pixel size of $7.5 \mu\text{m}$. The focus of the camera is adjusted via the optimization of a sharpness criterion.

(2) Non-uniformity correction and bad-pixel replacement

NUC is important because different regions and pixel elements of the sensors deviate from each other in offset and gain. Most common simple non-uniformity correction (NUC) methods are single point correction (SPC) and two point correction (TPC). SPC corrects only for the offset, TPC for offset and multiplicative gain of every pixel. In our case SPC has shown to be sufficient due to low variation in the pixels' gain.

The bad pixel information is integrated in the camera's firmware. There are different options offered by the manufacturer to interpolate the bad pixels, e.g., left or nearest neighbor replacement. We apply a nearest neighbor replacement.

(3) Coldreflex correction

Due to the reflection of the cooled thermographic camera detector (camera detects its own reflection) a circular fixed pattern noise appears, so-called narcissus effect. The dark circular area can be seen in Fig. 1. Lowpass filtering of the image allows to give a brief estimate of this effect and to compensate for it by using the lowpass filtered image as additional gain information.

(4) Intersection points analysis

The aim of this analysis is to get reliable intersection point candidates for further processing. Every pixel in the image is analyzed within a range of radii. For the detection of the intersection points, the minimum and maximum radii, which are

dependent on the object geometry and size, need to be provided. These radii are adjusted such that a circular gray value profile within shows four peaks (for intersections delimiting four chips).

(5) Intersection map via frequency domain

We compute the magnitude spectrum for the above mentioned gray value profile. Depending on the object geometry, the values for specific frequencies can be combined or a single frequency can be used for the intersection map entry of the considered pixel. Procedures (4) and (5) are performed for the whole image. A resulting intersection map is shown in Fig. 1. In this case the map was adjusted to return highest intensities for intersections delimiting four neighboring chips.

(6) Continuation of grid intersection points

A threshold has to be selected for the intersection map to get an initial intersection point list. A connected component labeling is applied to identify each intersection point group uniquely and to remove small clusters. For the remaining labels accurately intersection points are calculated based on mass moments of each cluster to get one coordinate per intersection. The chip size has to be known to continue the grid of intersection points. An adjacency matrix is built via the extracted intersection points and the distances between each point pair. If the distance is located within a certain range the corresponding points are neighbors. For each identified neighborhood relation the missing neighbors are computed and added to the intersection point list. Duplicates are fused. These steps are repeated until convergence. Finally an object (chip) is defined by four corner points and a list with all objects and corresponding corner points is generated.

(7) Chip extraction, reference chip generation and defect detection

Due to possible perspective distortion, the intersection map allows non-quadratic or even skewed objects to be detected. To be comparable, the single objects are resampled to a common cartesian coordinate system. A median projection on all extracted chips leads to a reference image. Afterwards this reference chip can be used to detect defects in the single chip images via difference imaging and correlation analysis.

2.3. Laser excitation

The advantage of the laser-based active thermography to improve the defect localization is demonstrated in Fig. 2. The conventional infrared image of a specimen's backside shows a crack proceeding through several chips indicated by white arrows in Fig. 2 (a). The challenge is to identify the course of the defect. The surrounding surface structures throughout the whole image reveal very similar signals compared to the actual crack. By applying a pulsed and focused laser beam on the central chip (pulse duration 100 ms; laser power 100 mW; beam diameter approx. 200 μm), a lateral heat diffusion is generated within the chip. The crack in the specimen creates a heat barrier that influences the thermal diffusion process and causes the

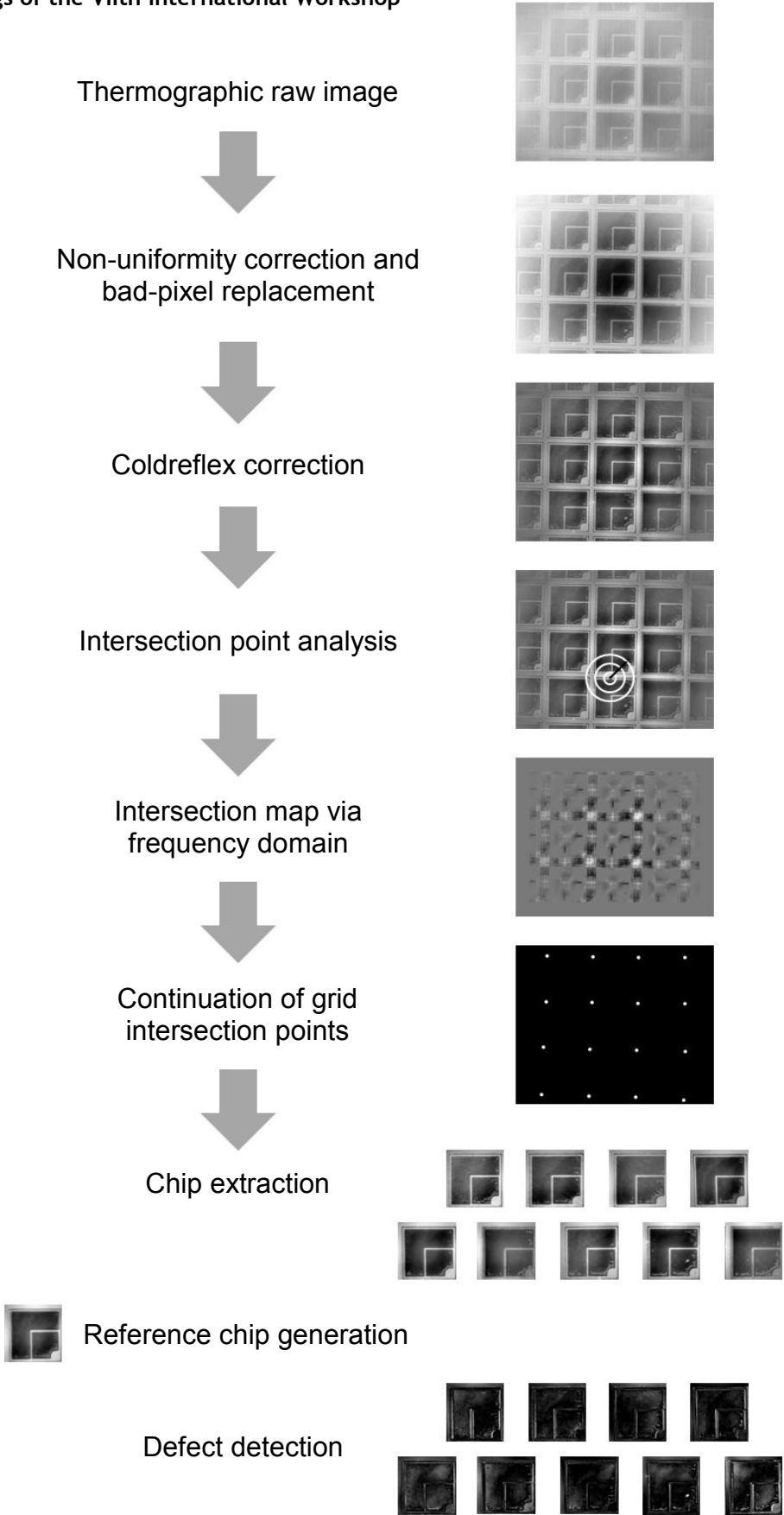


Figure 1: Image processing pipeline for chip extraction, reference chip generation and defect detection.

temperature signal to rise at the defect location. In the difference image in Fig. 2 (b) the crack is clearly visible and distinguishable from the surface structures. The difference image hereby displays the rise in temperature measured in intensity values of the IR camera in relation to ambient temperature.

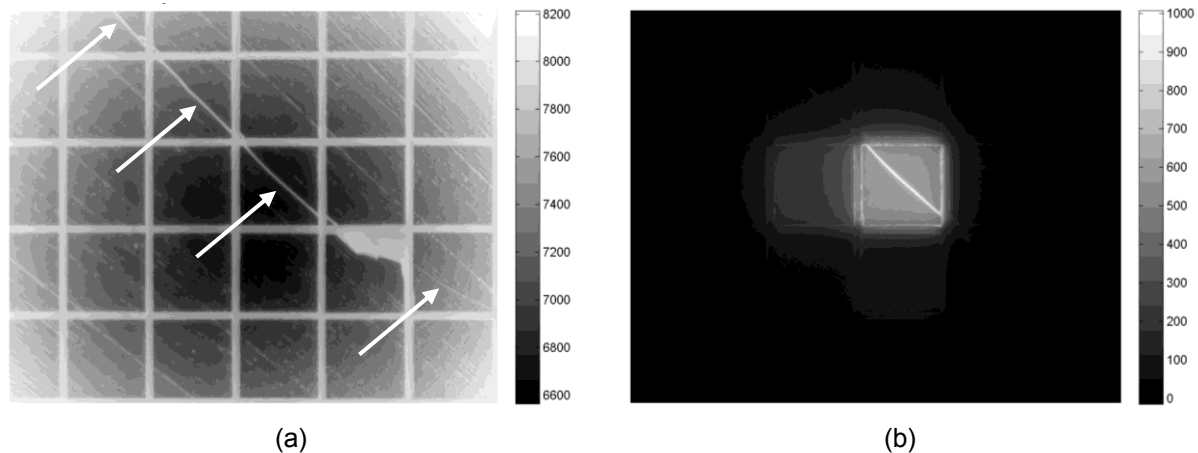


Figure 2: (a) infrared image the backside of optoelectronic chips. The crack through several chips is marked by white arrows. (b) active thermography image. The crack is easily distinguishable from surface structures due to excitation.

4. Discussion

Experiments on test specimens show that the proposed imaging method is very sensitive to cracks. The introduced image processing chain has successfully been tested in emission-only mode. In the remainder of the project, this processing step will be combined with the laser excitation. A diffractive optical element (DOE) will be used to improve the throughput and processing time of the inspection of optoelectronic devices.

5. Acknowledgments

This work has been funded by the German federal ministry of education and research (BMBF).

REFERENCES

- [1] HEY (C.). - *Entwicklung und Implementierung einer Softwareanwendung für die Thermographieprüfung an Leuchtmitteln und Wafern*, Master thesis, Georg-Simon-Ohm Hochschule, Nürnberg, 2012. [in German]
- [2] DAXER (C.). - *Entwicklung und Implementierung eines Vorgehens zur Auswertung thermographischer Aufnahmen von Mikrochips*, Bachelor thesis, Georg-Simon-Ohm Hochschule, Nürnberg, 2012. [in German]

The Effect of Pre-processing Techniques in Detecting Defects of Thermal Images

Peyman HEDAYATI VAHID, Somayeh HESABI, Xavier MALDAGUE

*Computer Vision and System Laboratory, Department of Electrical and Computer Engineering,
Université Laval, G1V0A6, Quebec City (QC), Canada*

Abstract. Pulsed thermography is one of non-destructive testing techniques to detect interested areas (defects) by providing images called thermograms. We suggest an image enhancement method which increases the contrast and leads to an improvement in segmenting defects. Reasonable obtained test images show the effectiveness of suggested approach as compare to PPT, TSR and PCT techniques in preparing high quality results.

1 Introduction

Pulsed infrared thermography is one of the most common thermal techniques in non-destructive testing. It consists of using an external stimulus to heat the specimen and record the temperature decay curve by an IR sensor to observe the presence of subsurface anomalies [1].

Several efforts have been proposed for defect detection in thermal images. Some approaches use thresholding techniques [2] while the others suggest a criterion [3]. Segmentation of thermal images usually has been done by thresholding methods, due to their simplicity.

A most common thresholding technique was proposed by Otsu [2], which the threshold is selected by maximizing the between-class variances or minimizing the within-class variances. Hamadani [3] suggests using the first order statistic properties of image as criteria to obtain the threshold value. He demonstrated a linear combination of mean and standard deviation to extract warm objects of thermal image.

The recorded images by thermal excitation contain some nonuniformity which called heat noise. This is a well-known problem in active thermography and it is due to imperfect heating [4]. Hence, noise filtering is an important pre-processing technique to improve the contrast and better distinguish the defect and non-defect areas.

Morphological filters are the well-known nonlinear filters for image enhancement. Opening and closing are two important operators, which are both derived from the fundamental operations of erosion and dilation [5]. The basic effect of an opening is somewhat like erosion while closing is similar to dilation.

Further enhancement to better distinguish the defect and non-defect areas is also available [6-8]. Thermographic signal reconstruction (TSR) is a method based on signal processing which increases the spatial and temporal resolution of recorded sequence [6]. An approach based on thermal contrast evaluation in time has been proposed in [7]. It is called principal component thermography (PCT) and applied on the sequence of images to extract features and reduce undesirable signals by projecting original data onto a system of orthogonal components. Pulse Phase Thermography (PPT) is a considerably evolved technique which is less sensitive to the optical and infrared properties of the material [8]. The major idea of it is to extract and analyze the response of the specimen on the frequency domain, based on the frequency spectrum.

We used the proposed denoising method in [5] to suppress the generated noise and then apply the detection methods [2, 3].

2 Experimental results

Our proposed approach was compared with TSR, PCT and PPT techniques [6-8] for two different specimens, aluminum and steel.

Fig. 1 shows the results obtained by our method in comparison with the proposed methods in [6-8]. The first column is the thermal images for two steel and aluminum specimens, respectively; the second and third columns illustrate the results obtained from the Otsu [2] and Hamadani [3] methods, respectively. In the rows results of pre-processing techniques have been demonstrated. We find out using the advantage of pre-processing techniques produce more acceptable results. Also opening-closing algorithm is superior over the TSR, PPT and PCT, as being observed in Fig. 1.

	Thermal Image		Otsu method [2]		Hamadani method [3]	
	Steel	Aluminum	Steel	Aluminum	Steel	Aluminum
Without pre-processing						
PCT						
PPT						
TSR						
Opening-closing						

Figure 1: Comparing the results of different pre-processing techniques.

References

- [1] X. Maldague, *NDT Handbook on Infrared and Thermal Testing*, ASNT Handbook Series, technical ed., P. O. Moore ed., ASNT Press, 732 p., ISBN 1-57117-044-8, 2001.
- [2] N. Otsu, *A Threshold Selection Method from Gray Level Histograms*, IEEE Trans. Syst., Man Cybern., vol. SMC-9, no. 1, pp. 62–66, 1979.
- [3] N. Hamadani, *Automatic Target Cueing in IR Imagery*, WPAFB, Ohio: Master's thesis, 1981.
- [4] C. Ibarra-Castanedo, *Quantitative Subsurface Defect Evaluation by Pulsed Phase Thermography: Depth Retrieval with the Phase*, Ph.D. thesis, Laval University, 2005.
- [5] R. Szeliski, *Computer Vision: Algorithms and Applications*, Springer, Heidelberg, 2011.
- [6] S. M. Shepard, *Advances in Pulsed Thermography*, Proc. SPIE 4360, pp. 511-515, 2001.
- [7] N. Rajic, *Principal component thermography for flaw contrast enhancement and flaw depth characterisation in composite structures*, Compos. Struct. 58, pp. 521–528, 2002.
- [8] X. P. Maldague and S. Marinetti, *Pulse Phase Infrared Thermography*, J. Phys., vol. 79, no. 5, pp. 2694-2698, 1996.

**Selected papers
from ISEM 2013**

1-

**Nondestructive
evaluation,
electromagnetic and
mechanical methods**

Evaluation of magnetic particle amount and leakage flux density for quantitative evaluation of crack shape in magnetic particle testing

Katsuhiro Fukuoka^{a,*} and Ippei Kawagoe^a

^a *The University of Shiga Prefecture, 2500 Hassaka-cho, Hikone, Shiga 522-8533, Japan*

Abstract. Because magnetic particle testing (MT) detects microcracks using a simplified method, it is used in nondestructive inspections of ferromagnetic materials in various industrial fields. However, MT can determine only a rough distribution shape of a crack, and a quantitative technique for evaluating the crack shape has not been established in conventional MT. In this study, such a technique that evaluates the crack shape from magnetic particle pattern in MT was considered. In particular, the relationship between the crack shape and number of adhesion magnetic particles was evaluated by image measurements using a high-speed video camera. In addition, the relationship between the crack shape and magnetic flux leakage density was explained using the finite element method.

Keywords: magnetic particle testing, quantitative evaluation, magnetic flux leakage, finite element method, dynamic image

1. Introduction

High-precision nondestructive inspection techniques are required to prevent the occurrence of severe accidents. Because magnetic particle testing (MT) detects microcracks using a simplified method, it is applied in nondestructive inspections of ferromagnetic materials in various industrial fields. Recently, establishing a technology that quantitatively evaluates crack shapes as well as detects cracks with high-precision has become an important research topic [1,2]. We consider developing such a quantitative evaluation technique that employs magnetic particle pattern of a crack in MT.

Upon magnetizing a ferromagnetic material on which a crack exists, a magnetic pole forms in the crack and magnetic flux leaks into the space. When magnetic particles are introduced in this crack, they are magnetized by magnetic flux leakage (MFL) and a magnetic particle pattern forms around the crack. Because MFL is influenced by the crack shape, magnetic particle pattern is unique for each crack shape. Therefore, it is important to extensively evaluate relationships among the number of adhesion magnetic particles, crack shape, and MFL.

In this study, the process of magnetic particle adherence to a crack was observed with a high-speed video camera and the change in the number of magnetic particles was evaluated at each instant. In addition, numerical analysis models were constructed to specify the crack shape, and the relationship between the crack shape and MFL density was explained.

* Corresponding author: Katsuhiro Fukuoka, The University of Shiga Prefecture, 2500 Hassaka-cho, Hikone, Shiga 522-8533, Japan Tel.: +81 749 28 9554; Fax: +81 749 28 9554; E-mail: fukuoka.k@usp.ac.jp

2. Observation of magnetic particle pattern with a high-speed video camera

A cold-reduced carbon steel sheet (SPCC) with its thickness less than its skin depth was selected as the test object to avoid skin effect, and a type A standard test shim [3,4] was placed at the center of the test object. The dimensions of the object were $300\text{ mm} \times 400\text{ mm} \times 1\text{ mm}^t$. The shim had dimensions of $20\text{ mm} \times 20\text{ mm}$ with a 6-mm-long linear artificial crack formed by chemical etching of the shim center. The shim comprised an iron sheet having soft magnetic properties. In this study, three shims with $100\text{ }\mu\text{m}$ thickness and different crack depths (15 , 30 , and $60\text{ }\mu\text{m}$) were used, and they are called 15/100, 30/100, and 60/100, respectively. To use this shim in MT, the surface of a crack was brought into contact with the surface of the object. Black magnetic particles in water-based liquid (suspension) carriers with a concentration of 2 g/L were used. The object was threadably mounted on a tilting table with a 20° inclination angle, and the flow velocity of the suspension was set at 0.2 m/s . The suspension was placed on the object using a tubing pump at a constant flow rate of 100 mL/min .

Figure 1 shows the layout of the object and magnetizer (yoke method). MT was carried out using a continuously magnetizing method. The distance between the magnetic poles of the magnetizer was 165 mm with a pole cross-section of $25\text{ mm} \times 25\text{ mm}$. The magnetizing coil had 820 turns, the exciting current value was $2.25\text{ A}_{\text{rms}}$, and the frequency was 60 Hz . Silicon steel was used as the material for the magnetizing yoke. Because a high-speed video camera was arranged for the object, variable yokes were installed in the poles and the magnetizer was laid down on the object; magnetic particle pattern was observed with the camera. In a previous study, it was confirmed that there was little MFL from the magnetizing yoke to object and that MFL had no influence in MT even if the magnetizer was laid down on the object [5]. The shim was positioned in the middle portion of the yoke leg. A dynamic image was observed from the upper and side surfaces of the adhesion point of magnetic particles, and the magnetic particle width and height were evaluated, respectively. In the side surface observation, a lens adaptor was installed on the camera lens and the image was reflected using a mirror. The lens magnification, shutter speed, and frame rate were set to 300 times, $1/500\text{ s}$, and 250 fps, respectively. After magnetizing the object with the magnetizer, the suspension was applied to it for 12 s . The moment at which magnetic particles began to adhere to the crack was assumed to be 0 s , and magnetic particle pattern was observed for 18 s with the high-speed video camera.

Figure 2 shows an example of the change in magnetic particle adherence to the crack of the shim (60/100: crack depth $60\text{ }\mu\text{m}$) from moment to moment (0 to 18 s). Still images were extracted from the dynamic image, and were used to measure the magnetic particle width through the upper surface observation. This width

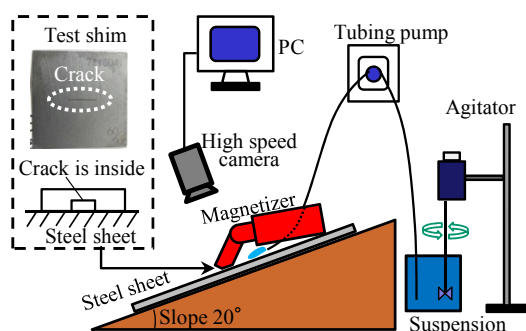


Fig. 1. Layout of the test object and magnetizer.

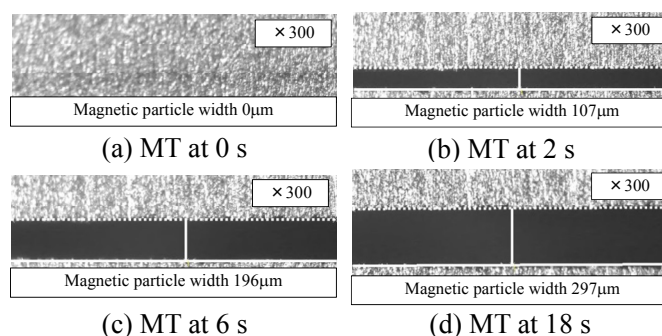


Fig. 2. Adhesion process of magnetic particles.

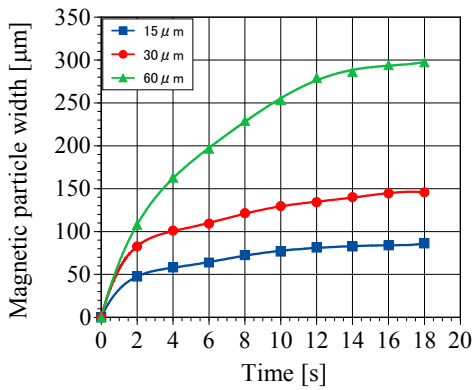


Fig. 3. Time variations of magnetic particle width.

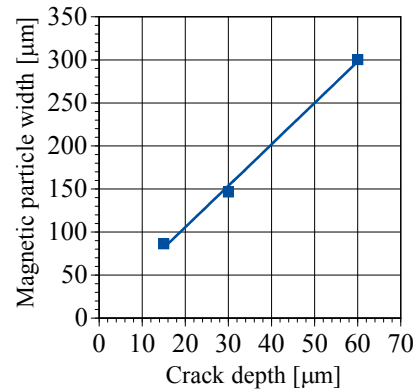


Fig. 4. Magnetic particle width at each crack depth.

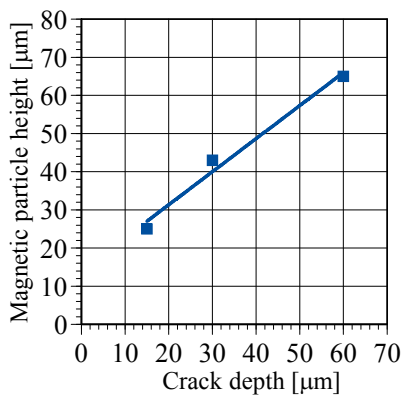


Fig. 5. Magnetic particle height at each crack depth.

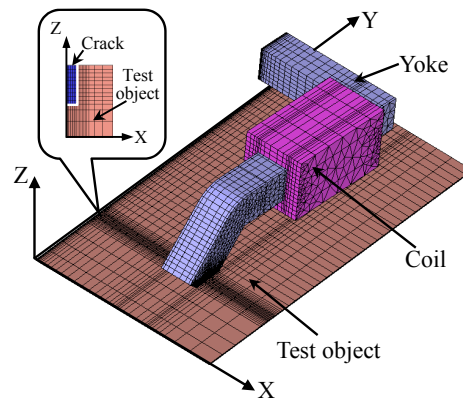


Fig. 6. FEM analytical model.

appeared to thicken with time. Time variations of magnetic particle width at each shim with different crack depths are shown in Fig. 3. In deeper cracks, the increasing rate of magnetic particle width is steep and the magnetic particle width that finally adheres to the crack increases.

Figure 4 shows the relationship between the crack depth and final magnetic particle width at 18 s in Fig. 3. Figure 5 shows the relationship between the crack depth and final magnetic particle height at the same time (18 s). It was confirmed that the final magnetic particle width and height linearly increased with the crack depth. The magnetic particle width is about four times larger than the magnetic particle height at each crack. The relationships between the crack depth D , and the final magnetic particle width W and height H are as follows:

$$D = 0.21W - 1.96, \quad D = 1.13H - 15.0 \quad (D \geq 0, W \geq 0, H \geq 0) \quad (1)$$

Although the above relationships were considered using the crack of type A standard test shims, comparable results were obtained using test objects that directly provided a crack in the steel sheets with electro-discharge machining. In future research, the crack shape parameters will be expanded and the relationship between the crack shape and magnetic particle pattern will be evaluated in detail.

3. Evaluation of the relationship between the crack shape and MFL density with the FEM

Numerical analysis models applying the finite element method (FEM) were constructed to specify crack depth and width, and the relationship between the crack shape and MFL density was explained. Figure 6 shows the proposed analytical model. In this model, actual cracks in the steel sheets were targeted. Thus, the crack of the model did not imitate the shim, and was provided directly in the object. The crack was positioned in the middle portion of the magnetizing yoke leg. For FEM, a 1/2 symmetry model was used for efficient analysis. The half region was analyzed from the crack center located at 0 mm. The air gap between the object and yoke was adjusted to 0.1 mm, considering actual contact conditions. Frequency response analysis was performed with three-dimensional FEM, which considers the nonlinearity of materials using $B-H$ curves for the object (SPCC) and yoke (silicon steel). Compared with nonlinear transient response analysis, frequency response analysis considers the nonlinearity of materials in the model, thus saving analytical time and memory required for computation [4]. The electric conductivity of the object was set to 6×10^6 S/m. The magnetizer size, coil turns, exciting current value, and frequency were the same as those in the above experiments.

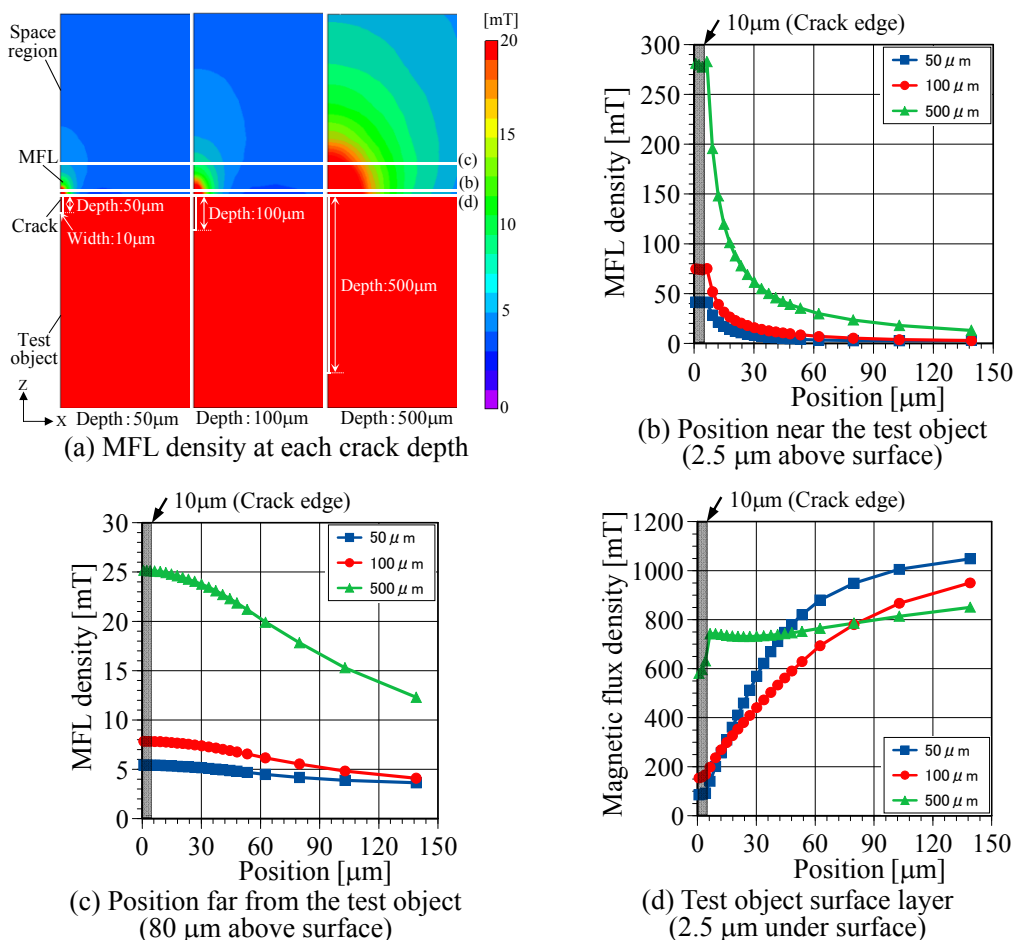


Fig. 7. Magnetic flux density distributions at each crack depth.

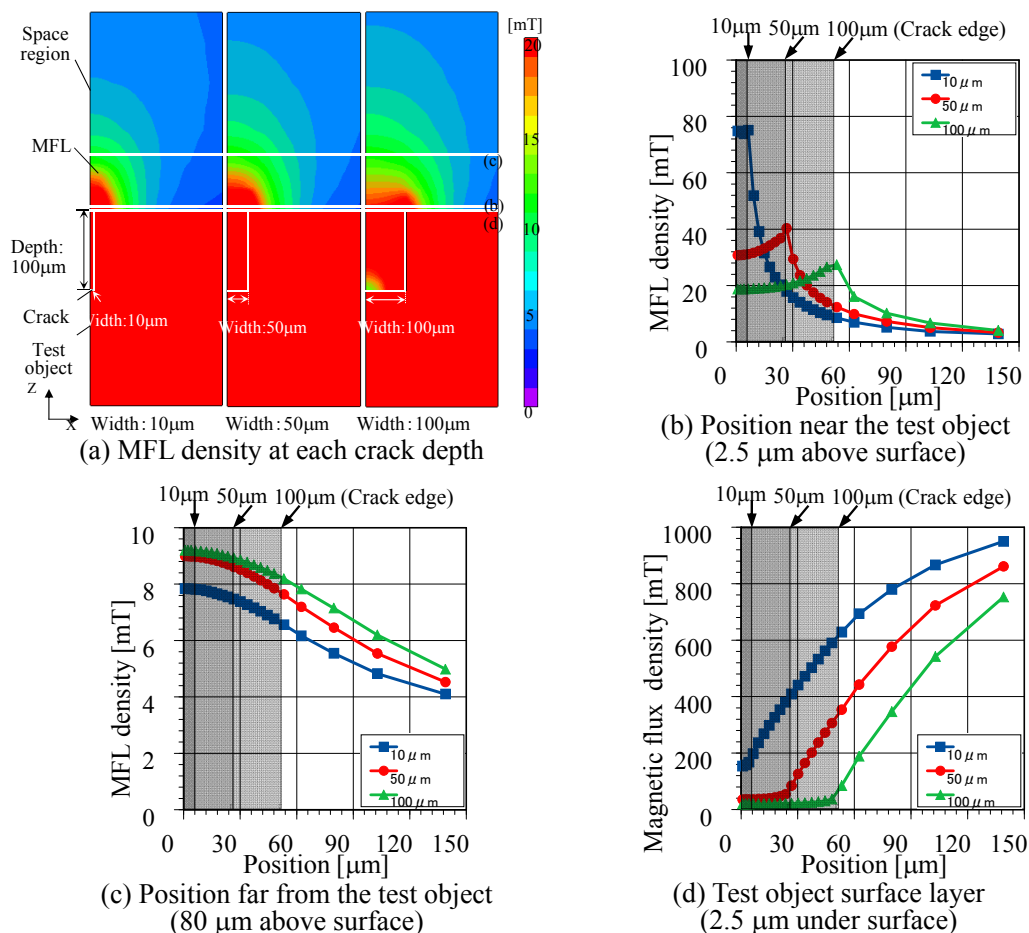


Fig. 8. Magnetic flux density distributions at each crack width.

Figure 7 shows the MFL density distributions in regions around the crack and magnetic flux density distributions in the object surface layer, which were acquired by varying the crack depth (50, 100, and 500 μm). The crack length and width were set to 6 mm and 10 μm , respectively. Magnetic flux density is an absolute value of B_x , B_y , and B_z components. In Fig. 7(b–d), the crack center is located at 0 μm on the horizontal axis. From these results, it is confirmed that MFL density in this region increases and is distributed in the wide area of the deeper crack. At a position near the object (Fig. 7(b)), because MFL density of the vertical component to object surface B_z increases, MFL density is maximum around the crack edge. At a position far from the object (Fig. 7(c)), because MFL density of the horizontal component to object surface B_x becomes predominant, MFL density is maximum at the crack center. Because magnetic flux penetrates into the object far from the crack (position: 90 μm or more), magnetic flux density in the object surface layer at a crack depth of 500 μm decreases compared with that of other cracks (Fig. 7(d)). However, in deeper cracks, the distribution distance for magnetic flux that penetrates under the crack is long, thus increasing magnetoresistance. Therefore, because penetrating magnetic flux is small and magnetic flux density distributed at the object surface layer increases near the crack (position: 40 μm or less), MFL density increases in deeper cracks.

Figure 8 shows the magnetic flux density distributions acquired by varying the crack width (10, 50, and 100 μm). The crack length and depth were set to 6 mm and 100 μm , respectively. From Fig. 8(a), it is confirmed that MFL density is widely distributed in wider cracks. At a position near the object (Fig. 8(b)), because magnetoresistance of the crack partly increases in wider cracks, magnetic flux penetrates under the crack and magnetic flux density distributed at the object surface layer decreases. Thus, MFL density decreases in wider cracks. On the other hand, at a position far from the object (Fig. 8(c)), MFL density increases in wider cracks. Therefore, for wider cracks, it is confirmed that MFL extends to a higher position on the object surface. For magnetic flux density in the object surface layer (Fig. 8(d)), the slope of the graph is constant around the crack. Thus, the rate at which magnetic flux penetrates into the depth of the object is the same at each crack.

4. Conclusions

The process of magnetic particle adherence to a crack was observed with a high-speed video camera, and the change in the number of magnetic particles at each instant was evaluated. The final magnetic particle width and height linearly increased with the crack depth. In addition, numerical analysis models that specified the crack shape were constructed, allowing the relationship between the crack shape and MFL density to be explained. It was confirmed that strong MFL was widely generated in deeper cracks. On the other hand, MFL density decreased and was widely distributed in wider cracks. In future works, the crack shape parameters (depth, width, and length) will be expanded by directly providing the crack in the steel sheets, and the relationship between the crack shape and number of adhered magnetic particles will be evaluated in detail. In addition, a database explaining the relationship between the crack shape and MFL density distribution will be constructed on the basis of the FEM analysis results for a variety of crack shapes. The aim is to establish a system that quantitatively evaluates the crack shape from magnetic particle pattern adhering to the crack.

References

- [1] F.Kojima and T.Fujioka, Quantitative evaluation of material degradation parameters using nonlinear magnetic inverse problems, *Int. J. of Appl. Electromagn. Mech.* **27**(2) (2003), 157-163.
- [2] N.Yusa, Z.Chen, K.Miya, T.Uchimoto and T.Takagi, Large-scale parallel computation for the reconstruction of natural stress corrosion cracks from eddy current testing signals, *NDT&E International* **36** (2003), 449-459.
- [3] R.Nakamura, Characteristics of magnetization indicator piece for magnetic particle testing, *Journal of the Japanese Society for Non-Destructive Inspection* **10**(2) (1961), 68-74. (in Japanese)
- [4] N.Kasai, A.Takada, K.Fukuoka, H.Aiyama and M.Hashimoto, Quantitative investigation of a standard test shim for magnetic particle testing, *NDT&E International* **44** (2011), 421-426.
- [5] K. Fukuoka and I. Kawagoe, Dynamic image measurement of magnetic particles attachment process and analysis of leakage magnetic flux density, *The 15th Symposium on Surface Inspection* (2012), 3-6. (in Japanese)

Eddy Current Testing Using Support Vector Machines

Mohamed Chelabi^a, Tarik Hacib^{a, **} and Yann Le Bihan^b

^aLaboratoire d'Etudes et de Modélisation en Electrotechnique, Univ. Jijel, BP 98 Ouled Aissa, 18000 Jijel, Algérie

^bLaboratoire de Génie Electrique de Paris, Supélec, UMR 8507 CNRS, Univ. Paris 06 et Paris 11, Plateau de Moulon, 91192 Gif-sur-Yvette Cedex, France

Abstract. Eddy current testing (ECT) is a fast and effective method for detecting and characterization of the most extremely small size cracks in conducting materials. The inverse problem solution, based on the measurement signal from the eddy current probe, is a difficult task. In this paper, we report our effort to develop a systematic approach for crack sizing (length and depth) in a conductive plate by the novel combination of Multi Regression Support Vector Machines (MR-SVM) and finite element method (FEM). Large number of rectangular shape cracks were simulated. The forward problem was solved numerically using FEM, that its accuracy was verified experimentally. The mentioned inverse problems were solved using MR-SVM for building polynomial functions to approximate the correlation between searched crack parameters and ECT signals predicted from a ferrite-core probe. The MR-SVM is a statistical learning method that has good generalization capability and learning performance. Data set required to train the MR-SVM was created using FEM and the Cross Validation (CV) technique was used to adjust the MR-SVM hyper-parameters. The results of the inversions are compared with a large number of experimental data. The very good correlation between the measured and predicted cracks parameters proves the applicability of the presented approach.

Keywords: Eddy current testing, Multi regression support vector machines, Crack sizing, Finite element method.

1. Introduction

Eddy current non destructive testing of conductive materials is of importance in many domains of industry and transportation. Crack characterization (sizing and classification of cracks) in steam generator tubes is one of the fundamental issues in the evaluation of the structural integrity of nuclear power plant components. Currently, this task is conducted by certified human inspectors who interpret the Eddy Current Testing (ECT) signals while eddy current probes are scanning inside the tubes. The interpretation of ECT signals, however, is truly a difficult task even for well-trained inspectors and the accuracy of signal interpretation largely depends on their experiences and knowledge. Thus, the automated interpretation of ECT signals is strongly desired [1].

Interpretation of ECT signals for crack characterization is, in fact, to solve the inverse problem of ECT. Approaches that have been proposed for the inversion of ECT signals are usually formulated and solved as optimization problems, so iterative methods are commonly used to solve these kinds of problems. These methods involve solving a well-behaved forward problem in a feedback loop. Numerical methods such as Finite Element Method (FEM) can be used to represent the forward process. However, iterative methods using a numerically based forward model are computationally expensive. In this situation, Artificial Neural Networks (ANN) and other machine learning tools such as Support Vector Machines (SVM) are a good alternative to iterative methods [2] [3].

ANN, a tool used to information processing system that can recognize highly complex patterns within available data [4], has recently been applied to solve the electromagnetic non-destructive testing inverse problem and been proved to have a higher accuracy compared to classical methods [5] [6], though physical processes and parameters are introduced into the model structure.

Despite their advantages, a number of drawbacks still remain like non-convex training problem with multiple local minima, dependence on quantity and quality of training dataset, choice of the number of hidden units, etc [6].

A breakthrough was obtained at this point when a new powerful machine learning method-support vector machines, was developed on the basis of statistical learning theory in the last decade.

**hacib.tarik@gmail.com

Many successful applications in nonlinear classification and function estimation have shown that SVM can handle higher dimensional data better even with relatively fewer training samples and that they exhibit very good generalization ability for complex models [7]. Multi Regression Support Vector Machines (MR-SVM) are parallel distributed information processing models that can provide more than one output in the same time relative to the standard SVM. The goal of this paper is to investigate applicability of MR-SVM for approximation the mapping from the signal to the crack space. A very crucial problem is signal inversion, wherein the crack parameters (length and depth) must be recovered from simulated signals by using FEM. A finite element model are developed and solved using the PDE Toolbox of MATLAB package [8].

The application of the MR-SVM to ECT inversion is used in the case of impedance measurement by eddy currents of the probe. The inversion approach is investigated to estimate length and depth of crack. The eddy current probe impedance is given as input to the MR-SVM and the size of crack is evaluated continuously by output of the MR-SVM.

2. MR-SVM for function estimation

Given a training set $(x_k, y_k)_{k=1}^N$ with input data $x_k \in R^n$ and output data $y_k \in R$, the SVM model for function approximation has the following representation in feature [9].

$$y(x) = w^T \varphi(x) + b \quad (1)$$

The optimization problem is defined as [6]:

$$\max \frac{-1}{2} \sum_{i,j=1}^N (\alpha_i - \alpha_i^*) (\alpha_j - \alpha_j^*) \cdot K(x_i, x_j) - \varepsilon \sum_{i=1}^N (\alpha_i - \alpha_i^*) + \sum_{i=1}^N y_i \cdot (\alpha_i - \alpha_i^*) \quad (2)$$

Subject to the equality constraints:

$$\begin{cases} \sum_{i=1}^N (\alpha_i - \alpha_i^*) = 0 \\ \alpha_i, \alpha_i^* \in [0, C] \end{cases} \quad (3)$$

where the fitting error is denoted by ε . The hyper-parameter C controls the trade-off between the smoothness of the function y and the accuracy of the fitting. α_i, α_i^* are lagrange multipliers, and $K(x, x_i) = \varphi^T(x) \varphi(x_i)$ is the so-called kernel function.

The solution is:

$$y(x) = \sum_{i=1}^N (\alpha_i - \alpha_i^*) \cdot K(x, x_i) + b \quad (4)$$

$$b = \frac{1}{2} \left[\text{Min} \left(y_i - \sum_{i=1}^N (\alpha_i - \alpha_i^*) \cdot K(x_i, x) \right) + \text{Max} \left(y_i - \sum_{i=1}^N (\alpha_i - \alpha_i^*) \cdot K(x_i, x) \right) \right] \quad (5)$$

In this case the observable output is a vector $y \in R^Q$, we need to solve a multidimensional regression estimation problem in which we have to find a regressor w^j and b^j for every output finally we find a linear system (6) [10].

$$\begin{bmatrix} K + D_a^{-1} & 1 \\ a^T K & 1^T a \end{bmatrix} \begin{bmatrix} B^j \\ b^j \end{bmatrix} = \begin{bmatrix} y^j \\ a^T y^j \end{bmatrix} \quad (6)$$

where $j=1 \dots Q$, $y^j = [y_{1j}, y_{2j}, \dots, y_{nj}]^T$, $(D_a)_{i,j} = a_i \delta(i-j)$, $B^j = w^j \cdot (\phi^{-1})^T$ and $a_i = 2 \cdot C$ ($\varepsilon = 0$, least square).

If $\varepsilon \neq 0$

$$a_i = \begin{cases} 0 & u_i^k < \varepsilon \\ \frac{2 \cdot C (u_i^k - \varepsilon)}{u_i^k} & u_i^k \geq \varepsilon \end{cases} \quad (7)$$

u_i^k that is, the square error between every dimension of y_i and all the regressors.

3. Investigated arrangement

The investigated arrangement is shown in Figure 1. The probe is constituted of a pair of identical square coils wound around each end of an U-shaped ferrite core. The two coils are connected in opposition and driven by an harmonic current. The coils are serially connected in such a way that the generated magnetic field is oriented from one pole to the other and it is approximately uniform between the poles [11]. This characteristic can be very useful for the inspection of parts having cracks expanding according to a privileged direction. More specifically, this probe is effective for the detection of cracks oriented along the axis defined by the two poles of the core since the crack is then perpendicular to the eddy current flow occurring between the two poles in absence of crack. The measurement quantity is the coil impedance. The parameters describing the probe are summarized in Table 1. The specimen considered for the experimental validation of the proposed method is a plate made of a nickel-based alloy. Its characteristics are as follows: conductivity: 0.76 MS/m, relative permeability: 1, thickness: 3 mm. Several electro discharge machining notches of different sizes and simulating real cracks were realized in the specimen. Each notch has a 100 μm thickness with a 5 μm margin. Their length and depth are both smaller than 1 mm and have a 20 μm margin.

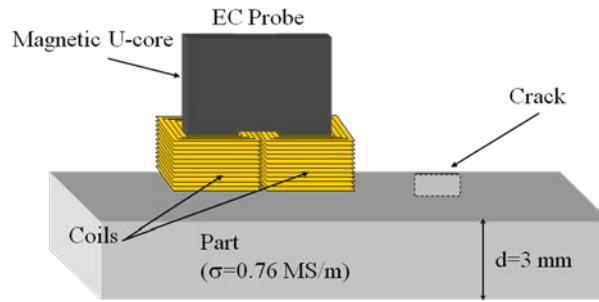


Fig. 1. Structure of the ECT probe and of the specimen

Table 1
 Probe specifications

Pole cross-section	1 mm×1 mm
Pole air-gap	1 mm
Core leg height	1 mm
Core total height	3 mm
Core relative permeability	1100
Coil height	1 mm
Coil cross-section	1 mm×0.45 mm
Coil turn number	202

4. Crack signal computation

4.1. Finite element modeling

The FEM is used as a forward problem solver to collect information for field distribution in the region under investigation. This region contains an ECT probe, disposed over a specimen with crack. The interaction between electromagnetic field, excited from the probe, and the specimen is analyzed numerically in 2D. During the analysis all used materials are accepted to be linear and homogeneous.

Electromagnetic field is excited by the coils, supplied by a constant alternative current of angular frequency ω and attenuates entirely at the boundaries of examined region. The resulting magnetic field distribution is governed by partial differential equation (8):

$$\left(\nabla \times \left(\frac{1}{\mu_0 \mu_r} \nabla \times \vec{A} \right) \right) + j\omega\sigma \vec{A} = \vec{J}_s \quad (9)$$

where, A represents the magnetic vector potential, j is the imaginary unit, ω is the angular frequency of the excitation current (rad/s), $\mu = \mu_0 \mu_r$ is the magnetic permeability of the media involved (H/m), σ is the electrical conductivity (S/m), and J current density (A/m^2).

The numerical solution of equation (9) was performed at zero value boundary conditions using FEM. The PDE Toolbox functions of software package MATLAB are used to develop the simulation program so that the impedance of the scanning probe at different positions can be calculated automatically. To

study the response of the ECT probe to crack's length and depth, a series of simulations were carried out.

4.2. Calculation of the ECT probe impedance

The impedance change of the coils reflects the change in conductivity distribution in a test specimen in the presence of defects. Once the magnetic vector potential values at all the nodes in the mesh region are determined, the probe impedance which is our parameter of interest can be computed from equations (10) [12].

$$Z = \frac{j\omega}{I^2} \oint_{\Omega_s} \vec{A} \cdot \vec{J}_s d\Omega_s \quad (10)$$

where I is the current feeding the probe.

5. Measurement setup and inversion procedure

Experimentations were led on the previously presented specimen with the probe oriented in such a way that a crack is parallel to the axis defined by the two poles of the core (Fig. 1). Figure 2 shows the experimentation system, the probe was moved with a PC-controlled robot, the impedance being measured using a 4192A low frequency impedance analyzer.

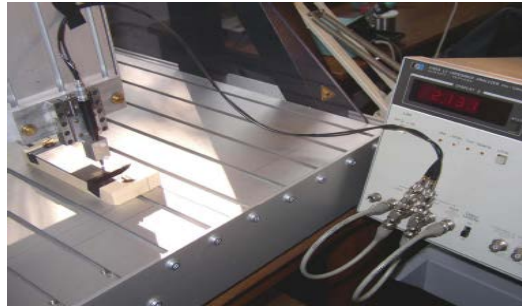


Fig. 2. Experimentation system

Measurements were taken on notches of different length or depth. The probe was moved along the different notches in steps of 0.3 mm in the x direction. Figure 3 shows the comparison between calculated and experimental signals (complex impedance variation ΔZ due to the presence of the crack) for two notch sizes.

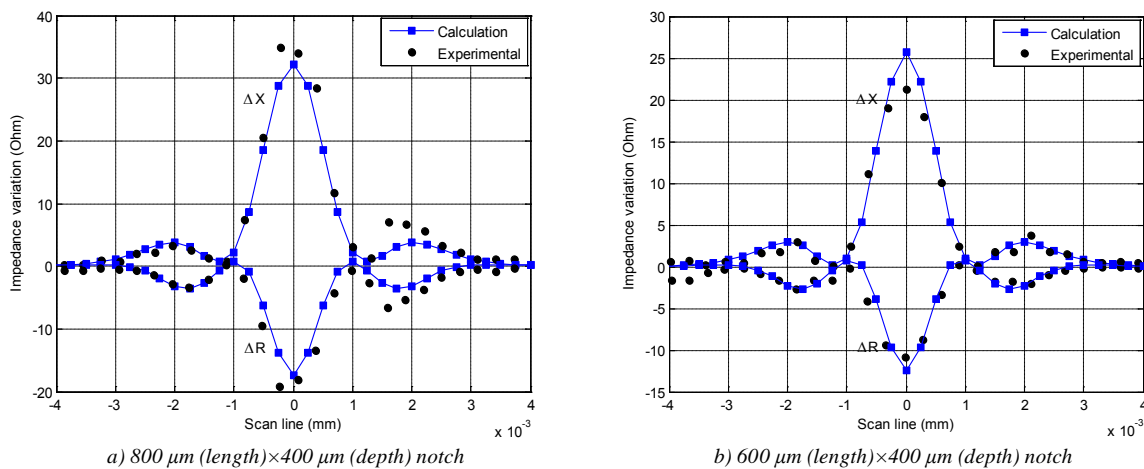


Fig. 3. Real and imaginary parts of impedance variation ΔZ

For notches considered, good agreement is obtained between calculation and experimentation.

5.1. Inversion implementation and evaluation of the MR-SVM

The aim of inversion techniques is to estimate the set of parameters allowing the model operator to explain the available measures in the best way [13]. The application of MR-SVM to the inversion

procedure of the probe coils impedance is trained and tested to extraction of cracks parameters. The MR-SVM input consists in the probe impedance (ΔR and ΔX) while its output provides evaluated cracks parameters (length and depth). All data set have been initially normalized to the range of values between [-1 and 1] with the formula (11):

$$y_{norm} = 2(y - y_{min}) / (y_{max} - y_{min}) \quad (11)$$

where y_{norm} the normalized value, y_{min} the minimal value, y_{max} the maximal value and y the current value of the component variable.

A data set is constituted of above 505 groups (randomly and normalized) of data were divided into two sets. The first 400 groups were used to train the support values and the remaining 105 were used for validation purposes. MR-SVM algorithm is used to modeling, and the RBF kernel function is selected. The cross validation (CV) method is used to optimize the hyper-parameters of MR-SVM.

In this paper, the time elaboration of the MR-SVM model (construction of the data set and tuning the hyper-parameters) is very important. But once the MR-SVM model is built the inversion results are obtained in real time.

Hyper-parameters of MR-SVM obtained for length and depth and corresponding Root Mean Squared Relative Error (RMSRE%) on the validation set are given in Table 2. In this case, the plots of the MR-SVM model predicting cracks sizes compared with the testing data sets are shown in Figure 4.

Table 2
 Parameters in MR-SVM with RBF kernel

Output	γ	σ^2	RMSRE %
Length	10^4	0.0036	0.4911
Depth	10^4	0.0036	0.6715

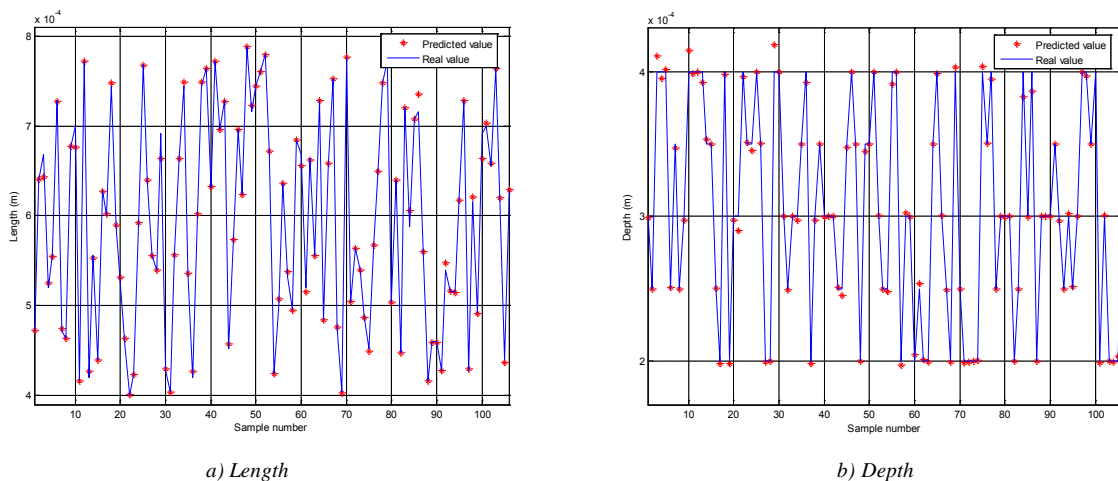


Fig. 4. Comparison between cracks parameters provided by the MR-SVM and ones contained in the testing data sets

The results show that most of the predicted points coincide in most cases with the real ones, which means the MR-SVM models can predict the values of cracks parameters accurately.

6. Results

For the experimental validation of the MR-SVM model developed in this work, two cracks parameters were characterized. The optimized LS-SVM by CV approach was tested on cracks parameters data brought from experiments. These cracks had different lengths (800 μm and 600 μm) and same depth (400 μm). Other information about experimental system that has been used is summarized in the subtitle 5.

MR-SVM results are compared to real value of cracks parameters. The following table (Table 3) shows the good agreement between expected and predicted values of cracks parameters.

Table 3
 Expected and obtained values of crack parameters (Simulation and experimentation)

	Simulation						Experimental			
	Length (μm)	Depth (μm)	Length		Depth		Length		Depth	
			Predicted (μm)	RMSRE (%)	Predicted (μm)	RMSRE (%)	Predicted (μm)	RMSRE (%)	Predicted (μm)	RMSRE (%)
Default 1	800	400	789	1.37	400	0.03	562	29,69	380	4,82
Default 2	600	400	598	0.26	403	0.90	540	9,85	401	0.33

As shown in Table 3, for the inversion of simulation data, the MR-SVM model showed very excellent accuracy (with the error, RMSRE < 1.37 %) in the prediction of not only the crack depth but also the crack length. For experimental data inversion, the MR-SVM model showed worse accuracy in the prediction of only the flaw depth measurement. Note that for such small size cracks there are several possible sources of significant discrepancy between calculation and experimentation, such as for example: uncertainties on the real shape and size of the notches, mechanical and electronic noises, etc.

7. Conclusion

This work presents an investigation of the use of artificial intelligence model for the inverse problem solution in the field of ECT. The solution of the forward problem was obtained using 2D FEM solver. The results from numerical simulation of the experiment show that the correlation between the probe impedance and crack dimensions is non-linear. This allows MR-SVM to be used as a tool for inverse problem solution. The obtained model was adjusted and tested with numerically computed data from the forward problem solution.

The applied data set at the testing stage of the MR-SVM preparation demonstrates their abilities to perform prediction with acceptable accuracy. The conducted physical experiment showed worse accuracy. This is due to the errors and disturbances in the measurements as well as to the insufficient information for MR-SVM training stage. Further works will concern the optimization of the structure of the training data set.

References

- [1] S. Osowski, K. Siwek, and T. Markiewicz, *MLP and SVM networks a comparative study*, in Proc. 6th NSPS, Finland, (2004) 37–40.
- [2] X. Ma, A.J. Peyton and Y.Y. Zhao, Eddy current measurements of electrical conductivity and magnetic permeability of porous metals, *NDT&E International*, **39** (2006) 562–568.
- [3] T. Hacib, Y. Le Bihan, M. R. Mekideche, H. Acikgoz, O. Meyer and L. Pichon., Microwave characterization Using Least-Square Support Vector Machines, *IEEE Transactions on Magnetics*, **46** (2010) 2811–2814.
- [4] A. Ayad, F. Benhamida, A. Bendaoud, Y. Le Bihan and M. Bensetti, Solution of Inverse Problems in Electromagnetic NDT Using Neural Networks, *Przeglad Elektrotechniczny*, (2011) 330–333.
- [5] M. Angeli and E. cardelli, “Numerical Analysis of Eddy Current Non-Destructive Testing (JSAEM Benchmark, Poble#2) Flat Plates with cracks, *Electromagnetic Nondestructive Evaluation (III)*, IOS Press, (1999) 303–314.
- [6] J. A. K. Suykens, *Nonlinear modelling and support vector machines*, in Proc. IEEE IMTC, Hungary, (2001) 287–294.
- [7] V. Vapnik, *Statistical learning theory*, John Wiley and Sons, New York, 1998.
- [8] A. Quarteroni and F. Saleri, *Scientific Computing with Matlab*, Springer, 2003.
- [9] A. Bernieri, L. Ferrigno, M. Laracca, M. Molinara, Crack shape reconstruction in Eddy current testing using machine learning systems for regression, *IEEE Transactions on Instrumentation and Measurement*, **57** (2008) 1958–1968.
- [10] M. S. Fernandez, M. P. Cumplido, J. A. Garcia, and F. P. Cruz., SVM Multiregression for Nonlinear Channel Estimation in Multiple-Input Multiple-Output Systems, *IEEE Transactions on Signal*, **52** (2004) 2298–2307.
- [11] Y. Le Bihan, J. Pavo and C. Marchand, Calculation of the ECT signal of a minute crack by a FEM-BIM hybrid method, *Eur. Phys. J. Appl. Phys*, **28** (2004) 355–360.
- [12] Y. Le Bihan, 3-D Finite-Element Analysis of Eddy-Current Evaluation of Curved Plates, *IEEE Transactions on Magnetics*, **38** (2002) 1161–1164.
- [13] I. Dolapchiev and K. Brandisky, Crack Sizing by Using Pulsed Eddy Current Technique and Neural Network, *Facta Universitatis. Elec. Energ*, **19** (2006) 371–377.

Eddy-current quality control of the winding connections in the powerful generators

Mikhail Roytgarts and Andrew Smirnov
Turbogenerator department, OJSC "Power Machines"
158, Moskovsky pr., 196105, St. Petersburg, Russia
Roytgarts_MB@els.power-m.ru, MRoytgarts@yandex.ru

Abstract. The results of numerical modeling and experimental investigations of electromagnetic eddy-current control processes carried out for the powerful generator winding bars connections are presented. The standard procedure of the electromagnetic quality control was developed and the statistic analysis of results of the brazed connections control in the series of 80 to 300 MVA turbogenerators are carried out.

Keywords: Quality control, powerful generators, winding connections, electromagnetic inspection, numerical modeling

1. Introduction

The currents in the stator winding bars of the powerful generators amount to thousands of amperes, that is why the winding bars being manufactured from tens of transposed strands have the large cross-section dimensions (Figures 1 and 2).

This is particularly characteristic of the up-to-date generators with the indirect ventilation system of winding. In the area of the bars connections the winding non-transposed sections with the pronounced surface effect are created.

The generator reliable operation, first of all, lies in the trouble-free operation of winding, which depends upon the quality of the bars brazed or bolted connections.

The connection quality instrumental control shall take into account the peculiarities of the current distribution in solid connections of the loaded bars, as well as the inspection method and instruments.

This work was aimed at developing and realizing the eddy-current quality control of the stator winding bars connections in the manufacture process of the powerful generators.

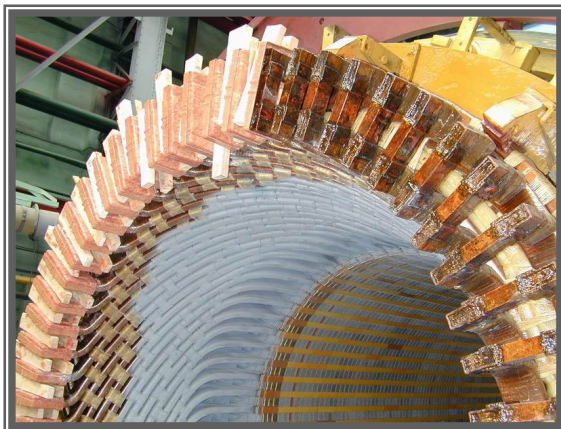


Fig.1. Stator winding bars connections



Fig.2. Stator bars with brazed clamps

With all this in mind, the numerical modeling took into account both the influence of the connections quality deviations upon the current distribution in the generator winding brazed connections, when generator being under load, as well as the peculiarities of the eddy currents distributions in the bars connections in the process of conducting the eddy-current control.

2. Current distribution in winding bar connection

The standard design of the powerful generator stator winding bars connections comprises the copper clamps wherein the stripped from insulation strands of the upper and lower bars are brazed up and a solid copper fork where the abovementioned copper clamps are brazed in (Figures 1 and 2).

For the powerful generators having the indirect cooling of the winding the dimensions of the winding bars cross-sections amount to as much as 40x150 mm, that is why the connection dimensions far exceed the depth of the alternating current field penetration into the copper, which amounts to 9.4 mm at a frequency of 50 Hz:

$$\delta = 66.2/\sqrt{f} \text{ (mm)}, \quad (1)$$

where f is a frequency in Hz.

The currents value in the connection is determined by the generator load conditions.

The problem of numerical modeling of the alternating current distribution in the construction of the winding bars connections was being solved in the standard ANSYS package with the use of the vector magnetic and scalar electric potentials. The use was made of the quasi-stationary formulation of the problem for the linear non-magnetic medium.

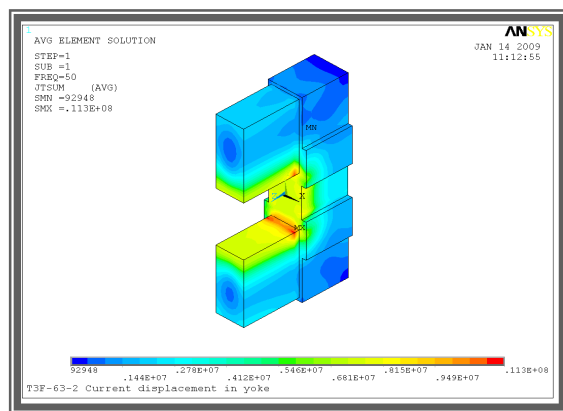


Fig.3. Current distribution in connection of two bars

The results of the three-dimensional numerical modeling of the load alternating current distribution in such construction are presented in Figures 3 and 4.

From these Figures we notice the current density essentially non-uniform distribution, where the distinguishing feature is the increased current density in the zone of the shortest route of the current flow from the upper winding bar to the lower one.

These results are true both for the solid massive connection and for the connection with a layer of high-quality brazing carried out by using the silver brazing alloy.

In actual practice, as the X-ray analysis and dissection of the bar connection show, the brazing defects are being noted. The influence of these deviations upon the generator serviceability become apparent in the increased heat release in the zone of the brazed connection, thus leading to the temperature increase and, finally, to the connection failure, that is cause emergency breakdown in the generator.

The results of the numerical modeling of different variants of the contact surfaces incomplete brazing are shown in Figures 5 and 6. The ohmic resistance increase as compared to those for the perfectly done brazing.

From the data presented we can notice that the contact loss in the zone of the current maximum density gives the same negative effect as the absence of brazing along all other surface. Hence it follows that this zone shall be subject to the brazing rigid quality control.

The permissible increase in the coefficient of ohmic resistance in the winding bars connections depends upon the ventilation efficiency.

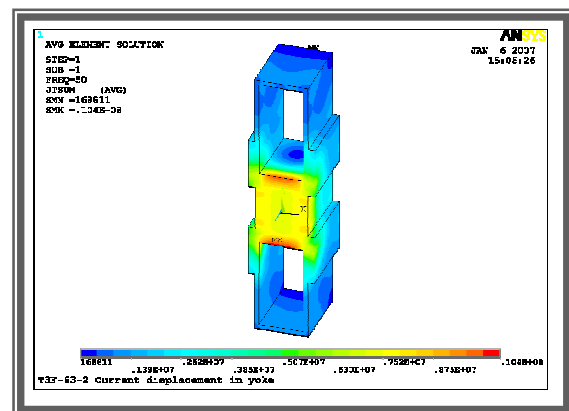


Fig.4. Current distribution in clamp – fork connection

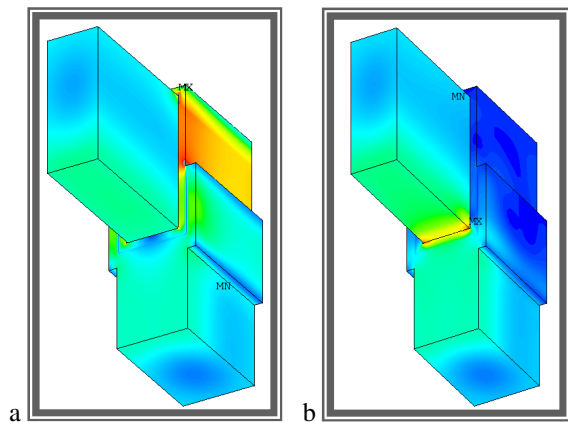


Fig.5. Current distribution with brazing done at the top (a) and at the bottom (b)

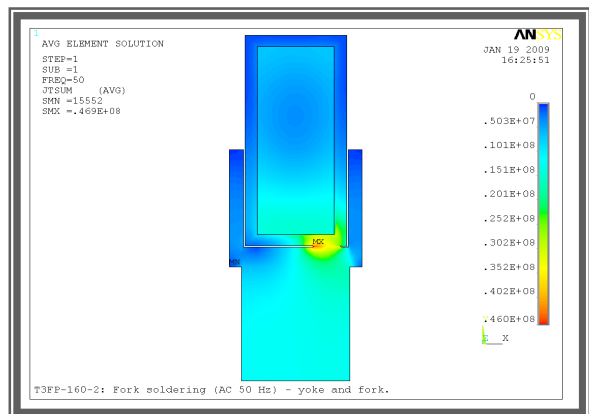


Fig.6. Current distribution at incomplete brazing of fork

3. Eddy-current quality control investigations

For the air-cooled turbogenerators the data of the stator end zone inspection by using the thermal imager showed the deviations in temperature of the brazed connections from the average values do not exceed inaccuracy of measurements.

So to control the quality of the winding bars connection, the contactless non-destructive method of induced eddy currents was used. The use was made of a coil, which induces the a.c. magnetic field, as well as a coil, which measures the magnetic field with due account of the eddy currents reaction in the array under control (Figure 7).

In order to increase the efficiency, the coils with inner magnetic core and external screen were used.

The control device also incorporates the power supply unit, the frequency converter and the indicating unit [1].

To adjust the device, two special specimens were used (Figure 8) – one part of the specimen corresponding to 100% brazing (solid specimen) and the other part of the specimen corresponding to 0% brazing (insulation is used instead of brazing). The dimensions of the specimens used for adjustment correspond to the dimensions of the connections under control.

The eddy-current control is conducted with a frequency of 10 Hz, which in accordance with (1) ensures the depth of the exciting-coil magnetic field penetration equal to 21 mm. The numerical modeling of the eddy-current control process (Figures 9 and 10) demonstrates clearly that the array thickness shall be less than the twice depth of the magnetic field penetration.



Fig.7. Device for eddy-current control BD-1



Fig.8. Specimens for adjusting of device

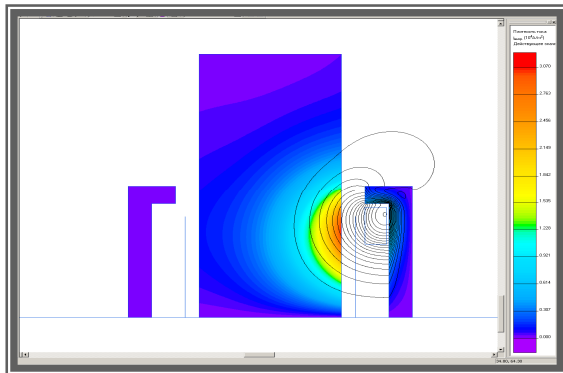


Fig.9. Eddy-current testing with 50 Hz frequency

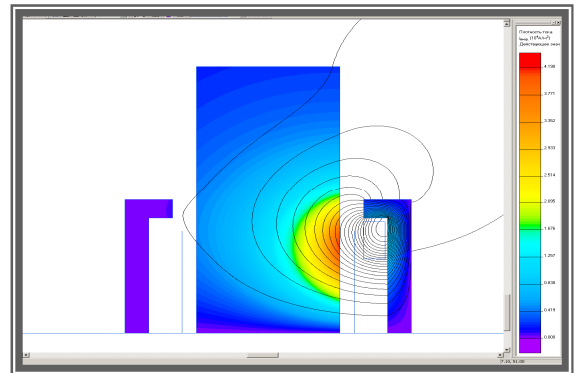


Fig.10. Eddy-current testing with 10 Hz frequency

The norm for the brazing quality is chosen proceeding from the condition that under the load duties the winding bars brazed connection resistance shall not increase by more than 5% as compared with the perfectly done brazing.

4. Results of testing

The results of the investigations conducted were brought to the notice of the production shops and departments and were drawn up as a factory standard (Production Facility Electrosila standard).

The training of the personnel has been conducted and presently the eddy-current quality control of the winding bar connections is used when manufacturing the stator windings of all the 80 to 300 MVA turbogenerators.

As the examples, shown in Figures 11 and 12 is the processing of statistical results of the winding bar connections eddy-current quality control in the beginning of familiarizing with this new technique as well as when this technique has been already mastered.

The abscissa axis shows the measured results of the percentage of brazing, the axis of ordinate shows the number of tested connections.

At the early stages of the eddy-current quality control introduction more than 1% of the brazed connections did not correspond to the norm of 50% brazing, while 9% of the brazed connections did not correspond to the norm of 60% brazing. The center, and to be more precise the median, of the non-symmetrical distribution shown in Figure 11 corresponded to 70% brazing.

The eddy-current quality control having been implemented, along with the possibility of rejecting and correcting the non-conformities, the quality of the brazed connections has improved as a whole. As we can see from Figure 12 after eddy-current test procedure mastering only one brazed connection (that is 2% of the total amount), which drops out of the distribution presented, do not correspond to a norm of 60% brazing and 9% do not correspond to a norm of 70% brazing. The median of the non-symmetrical distribution is located in the zone of 90% brazing.

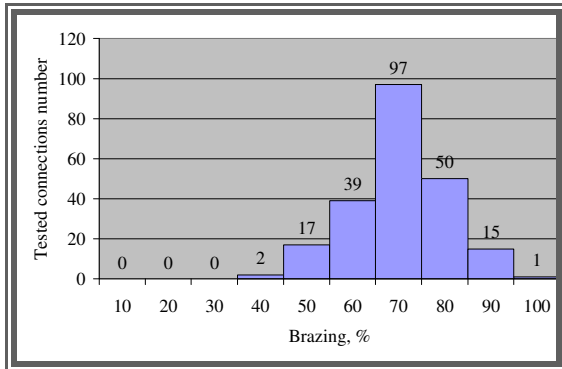


Fig.11. Early stages of the eddy-current quality testing

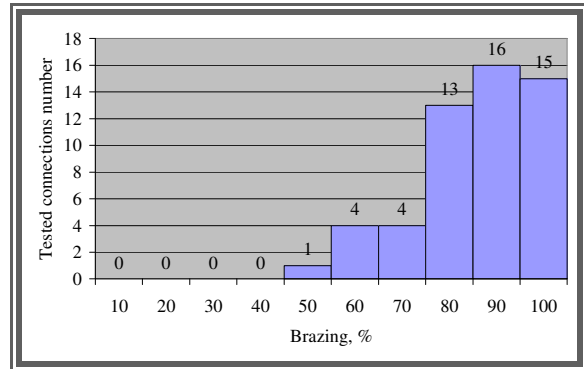


Fig.12. Eddy-current testing after test procedure mastering

5. Conclusion

The experimental and theoretical works on the implementation of the eddy-current quality control of the powerful generator stator winding bar brazed connections have been conducted at the OJSC Power Machines – Production Facility Electrosila.

The numerical modeling has revealed the peculiarities of the current distribution in the bar connection construction and permitted to determine the brazing quality criteria.

Determined by calculations and proved experimentally are the parameters of the eddy-current device, which ensures conducting the winding bar brazed connections control.

Developed and drawn up as a Electrosila factory standard is the procedure of the winding bar brazed connections control by using the eddy-current device.

The introduction of the eddy-current quality control permitted both to reject the low-quality bar connections and to improve the quality and reliability of the winding bar brazed connections as a whole.

After eddy-current test procedure mastering in the series of 80 to 300 MVA turbogenerators 98% stator winding brazed connection correspond to a norm of 60% brazing.

Nowadays the eddy-current quality control is introduced for the rotor winding brazing connections

Reference

[1] V.Siasko, M.Roytgarts, M.Koroteev, P.Solomenchuk. Quality control of brazed connections of turbogenerator stator winding bars at the Electrosila factory. «NDT world», №2, 2010 (In Russian)

Measurement of Tube to Support Plate Gap for Alloy 800 Steam Generator Tubes using Transient Eddy Current

Ross UNDERHILL, Vijay K. BABBAR, Thomas W. KRAUSE

Department of Physics, Royal Military College of Canada, PO Box 17000, STN Forces, K7K 7B4, Kingston, ON, Canada

Brian LEPINE

Inspection, Monitoring and Dynamics Branch, Atomic Energy of Canada Limited, Chalk River Laboratories, K0J 1J0, Chalk River, ON, Canada

Abstract. Inspection of steel support plates from within Alloy 800 Steam generator (SG) tubes in CANDU® nuclear reactors is a critical challenge, since support plate degradation and fouling can lead to tube damage and loss of SG efficiency. Transient eddy current (TEC) technology is being developed to measure the gap between SG tube and support plates, which will facilitate determination of support plate condition. Results from a prototype probe, designed based on finite element modelling, demonstrate the capability to measure small tube to support plate gap variations, providing information, which in turn may be used to assess support plate condition.

1 Introduction

The capability to obtain an accurate assessment of steam generator (SG) tube support structures in CANDU^(R) nuclear reactors, from within the Alloy 800 SG tubes, is an inspection challenge presently addressed by conventional eddy current inspection technologies to only a limited extent. This is an important inspection issue since support plate degradation and fouling can lead to tube damage, through different mechanisms, and loss of SG efficiency. The potential for inspecting and monitoring support plate conditions can be integrated with preventive maintenance programs, thereby advancing station-life management processes. This paper presents finite element (FE) modelling of a prototype probe that was manufactured to be sensitive to variation in gap between SG tubes and support plates under conditions of pulsed excitation and measured transient response [1]. Experimental results from the manufactured probe confirm the sensitivity of the transient eddy current response to variation in gap.

2 Finite Element Modelling and Experimental Results

The proposed probe design was modeled using COMSOL 4.3 and modeled results were used to optimize pick-up coil positions in the as-manufactured probe. Figure 1 shows a solved 3D half-model, with a central coaxial drive coil and four pickup coils labeled PC1 to PC4. The probe and Alloy 800 SG tube are both centered inside a 22 mm inner diameter (ID) steel collar (SS410) simulating the support plate. Models investigated the effect of probe-in-tube shift with respect to the centre of collars with IDs from 16.5 to 22 mm. Near collar centres, modeled signal amplitudes from differentially connected coil pairs were observed to change linearly with tube shift. Experimentally measured TEC coil response also demonstrated a linear response for small shifts from the centre position (0.6 mm gap), in agreement with modelled results, as shown in Figure 2 for a 16.5 mm ID collar.

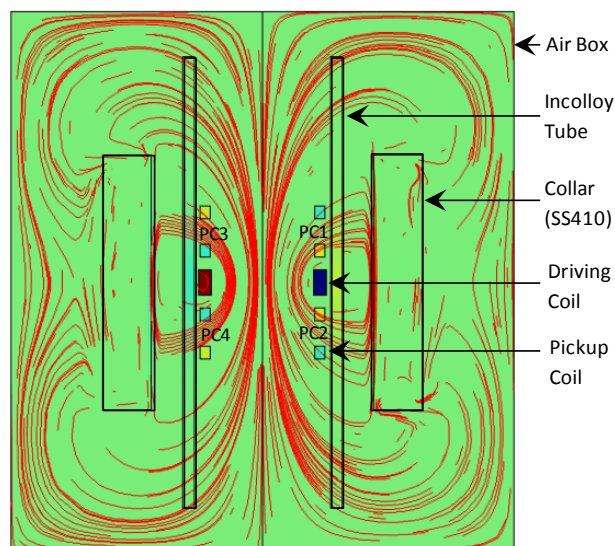


Figure 1: FE model showing current density (J_x) and magnetic flux density (streamlines) at 5×10^{-5} s.

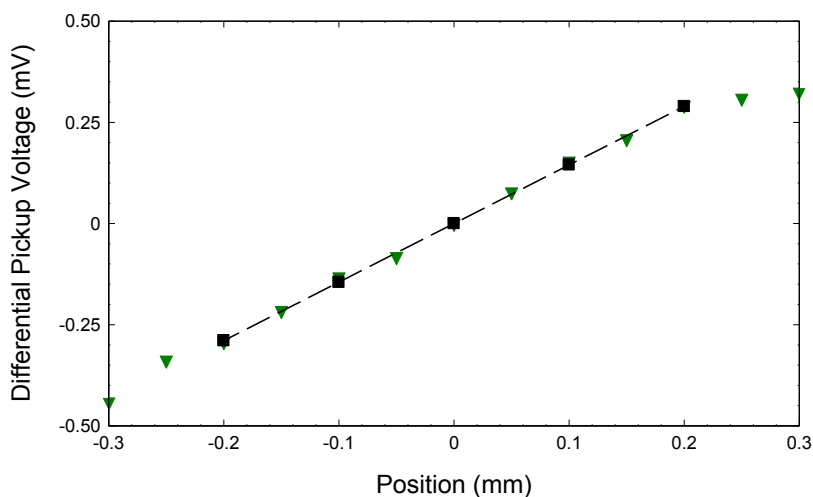


Figure 2: Measured (▼) and modelled (■) response as a function of shift from centre for 16.5 mm ID collar.

3 Summary

Finite element modelling was used to generate the design of a probe that would be sensitive to the variation in gap between an Alloy 800 steam generator tube and SS410 steel support plate. Experimental results obtained from a prototype probe based on this model confirmed the sensitivity and linear response of the transient eddy current response to variation in gap.

Reference

- [1] T.W. Krause, C. Mandache, and J.H.V. Lefebvre, 'Diffusion of Pulsed Eddy Currents in Thin Conducting Plates', *Rev. Prog. Quant. NDE*, **27**, AIP, Melville, NY (2008) 368-375.

Acknowledgements

This work was supported by the Natural Sciences and Engineering Research Council of Canada (NSERC) and the University Network of Excellence in Nuclear Engineering (UNENE).

Quantitative Evaluation of Residual Strain in Austenitic Stainless Steels Using Electromagnetic Nondestructive Evaluation

Seiya SATO

Graduate School of Engineering, Tohoku University, Japan

Ryoichi URAYAMA, Takeshi SATO, Tetsuya UCHIMOTO, Toshiyuki TAKAGI

Institute of Fluid Science, Tohoku University, 2-1-1 Katahira Aoba-ku, Sendai, Miyagi 980-8577, Japan

Zhenmao CHEN

State Key Laboratory for Strength and Vibration of Mechanical Structures, Xi'an Jiaotong University, China

Yasuhiko YOSHIDA

The Kansai Electric Power Company, Inc., Japan

Abstract. In this study, to evaluate residual strain in austenitic stainless steel quantitatively, eddy current testing (ECT) and non-linear eddy current testing (NLECT) are applied. In uniaxial tensile specimens, signal sensitivity to residual strain is large at the region more than 5% of strain, and signal sensitivity is decreased at low strain region in ECT. In contrast, there is a linear correlation between signal and residual strain in NLECT. These changes reflect magnetic phase due to the deformation induced martensitic transformation, which is confirmed by magnetic force microscopy. Biaxial tensile test is also carried out to discuss the anisotropy by biaxial loading.

1 Introduction

When large amount of seismic load is exerted to components in nuclear power plants like the Great East Japan Earthquake, structural integrity evaluation is required[1, 2]. Currently, it is expected to establish nondestructive evaluation techniques that are more reliable and convenient. Electromagnetic method is promising since magnetic properties are sensitive to the microstructure changes due to plastic deformation. In order to put these techniques into practical, it is necessary to figure out the quantitative relationship between residual strain and electromagnetic properties.

In this study, nondestructive methods are investigated to evaluate residual strain due to seismic loading of nuclear structural materials, focusing on the change of electromagnetic properties. Type 304 austenitic stainless steels are discussed as a target material. Uniaxial and biaxial tensile tests are carried out, and electromagnetic nondestructive evaluation method, specifically eddy current testing (ECT) and non-linear eddy current testing (NLECT) are applied.

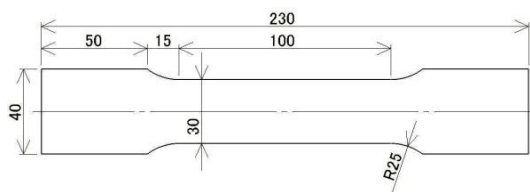


Figure 1: Schematic drawing of uniaxial tensile specimen.

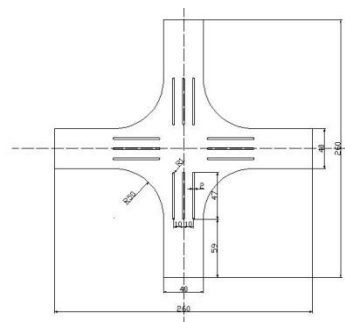


Figure 2: Schematic drawing of biaxial tensile specimen

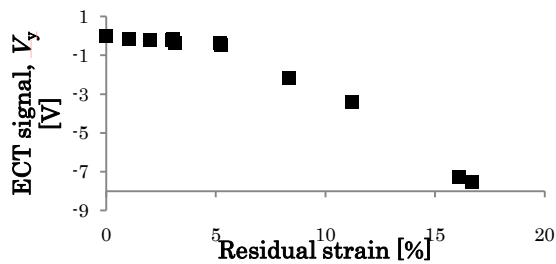


Figure 3: Relationship between eddy current signal, V_y harmonics and residual strain.

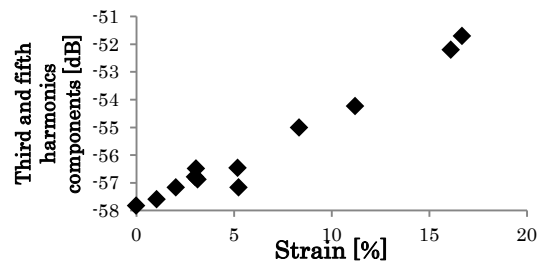


Figure 4: Relationship between third and fifth components and residual strain.

2 Specimen

Figures 1 and 2 show the schematic drawing of uniaxial and biaxial tensile specimens, respectively. The uniaxial tensile tests were carried out and prepare 11 specimens elongated from 1% to 15%. The biaxial test is also carried out to discuss the anisotropy of electromagnetic properties by biaxial loading.

3 Experimental Method

ECT was carried out using eddy current instrument (ASSORT PC II Aswan Ect Co., Ltd.), and eddy current signals V_x and V_y are measured. The probe has two coils. These coils are arranged in tandem. This probe is self-induced differential type one. Test frequencies are 50, 100 and 200 kHz. In order to decrease the lift-off noise, the signals V_y were read after shifting the signal phases so that lift-off signals should coincide with the x direction.

In NLECT, by applying AC current to exiting coil to invoke AC magnetic field into a sample, magnetization process of the sample is detected by the voltage of a pickup coil. The probe has a ferrite core and two coils. Test frequency is 5 kHz, applied voltage is 4.5V and sampling rate is 200 points per cycle. In this study, third and fifth harmonic components S are used as a parameter, where A_1 , A_3 and A_5 are basic, third and fifth harmonic component intensity, respectively.

$$S = 20 \times \log \left(\frac{\sqrt{(A_3)^2 + (A_5)^2}}{A_1} \right) \quad (1)$$

4 Result and Discussion

Figure 3 shows relationship between eddy current signal V_y and residual strain at the frequency of 100kHz. It shows that the eddy current signal increase with residual strain. Though signal sensitivity to residual strain is large at the region more than 5% of strain, signal sensitivity is decreased at low strain region, which leads large SN ratio. It is hard to evaluate small residual strain by ECT in this region. Figure 4 shows third and fifth harmonic components S as function of residual strain in NLECT. There is a linear correlation between third and fifth harmonics components and residual strain. Therefore, NLECT has a capability to evaluate quantitatively residual strain less than 3%, which is hard to evaluate by eddy current testing.

Specimens of biaxial tensile test are measured focusing on the anisotropy of electromagnetic properties. For the purpose, the probe that can measure the polarity is used. The result will be reported in the conference.

Acknowledgement

The authors express our appreciation for making specimens and equipment and their technical assistance to Mr. K. Kuroki and Mr. S. Onuma of Institute of Fluid Science, Tohoku University.

References

- [1] M. Kamaya, INSS Journal, **16** (2009), pp.179-188.
- [2] M. Kawakubo *et al.*, Transactions of the Atomic Energy Society of Japan, **9** (2010), pp.166-173.

Evaluation of Wall Thinning in Doubled Layer T-joints by SH-wave Electromagnetic Acoustic Transducers

Tetsuya UCHIMOTO, Toshiyuki TAKAGI, Toshiaki ICHIHARA, Shejuan XIE

Institute of Fluid Science, Tohoku University, 2-1-1 Katahira, Aoba, Sendai 980-8577, Japan

Gerd DOBMANN

Fraunhofer Institute for Nondestructive Testing, IZFP, Campus E3 1, 66123 Saarbrücken, Germany

Abstract. Electromagnetic acoustic transducer (EMAT) that excites horizontal shear waves is applied to inspection of wall thinning at T-joints with reinforcing plates. Accuracy of sizing and detection are evaluated systematically, taking the consideration of disturbance by weld between reinforcing plates and main pipes.

1 Introduction

Pipe wall thinning is one of the most serious defects in various industries, especially large-scale plants [1]. In nuclear power plants, the access of probes for inspections is limited to outside of pipes, which gives a large constraint for inspections. In Japan there is a special concern on the inspection of local wall thinning at locations under a reinforcing plate that covers outside of the pipe, where a branch pipe is connected to the main one. Because there is a gap between the reinforcing plate and the pipe, it is difficult to inspect inside of the pipe under the reinforcing plate by ultrasonic thickness gauges which are currently applied for the inspection of pipe wall thinning. Pulsed eddy current testing technology was developed in recent years to detect wall thinning [2]. Because of its rich frequency components and applicability of large electric current, the pulsed eddy current method may show promising capability in detection and evaluation the defect in the non-ferromagnetic pipes. The feasibility of magnetic flux leakage method for estimation of wall thinning on pipes under reinforcing plates in nuclear power plants was also discussed [3]. In addition, a recently developed non-destructive method, called magnetic adaptive testing, which is based on systematic measurement and evaluation of minor magnetic hysteresis loops was applied for this matter, and feasibility of detection of wall thinning was shown [4]. However, these methods are sensitive to the geometry of T-joints and more robust methods are now required.

Horizontal shear wave (SH) modes that exist in flat layers have some advantages; they are free of mode conversion, and its fundamental mode SH_0 shows no dispersion. Therefore, observing the attenuation of SH_0 waves that propagate in the main pipe under the reinforcing plate, the detection and depth sizing of wall thinning can be made precisely and easily. In this study, electromagnetic acoustic transducer (EMAT) which can excite SH waves with various wavelength values is applied to evaluation of wall thinning of the T-joint pipes under the reinforcing plates. Accuracy of detection and depth sizing are evaluated systematically, taking the consideration of disturbance by weld between reinforcing plates and main pipes.

2 Experimental

Figure 1 shows a schematic drawing of EMAT for transmission and reception of SH wave. EMAT transducer consists of permanent magnets and a meander coil. The interval of meander coil determines the wavelength of SH wave. In the experiment, test frequencies and wavelength were selected so that only the fundamental mode of SH_0 is excited, taking the consideration of cut-off frequencies of higher modes.

Figure 2 shows one example of specimens that simulate T-joints with reinforcing plates. The main pipe with length of 650 mm was cut from 500A carbon steel pipe JIS-STPY400, and reinforcing plate forged from a carbon steel disk JIS-SS400 were welded to the main pipe. At the centre of the reinforcing plate there is a hole for the branch pipe with the diameter of 216 mm, penetrating the main pipe. There are drilled holes simulating the wall thinning under the reinforcing plate, and its diameter and depth values are systematically varied.

3 Results and Discussions

The transmitter and receiver EMATs are placed on the pipe with the interval of 500 mm as shown in Fig. 2, so that SH_0 wave propagated in the circumferential direction of pipe. Figure 3 (1) shows the waveform of transmitted packets propagating under the reinforcing plate when there is no defect. The first echo after the transmitter pulse is one directly propagating the shorter path of 500 mm between the transmitter and receiver. The second one corresponds the packet travelling in the opposite direction to the first one. Figure 3 (2) shows the packet transmitting a drilled hole with diameter of 20 mm and depth of 5 mm. Due to the presence of hole, the amplitude of the first echo are decreased in comparison with Fig. 3 (1). Discussing the attenuation quantitatively, wall thinning can be evaluated. The details are reported in the conference.

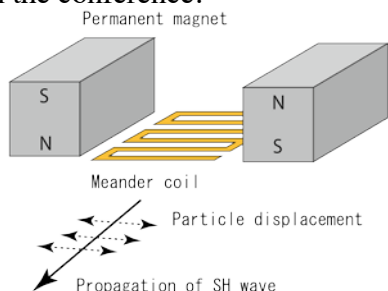
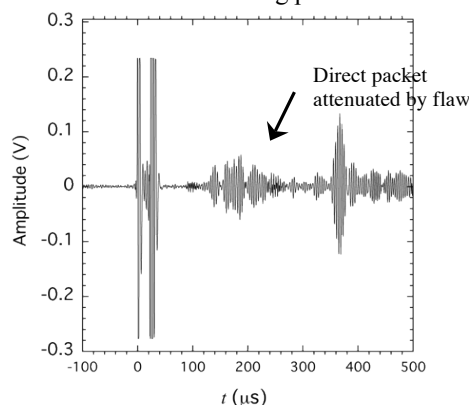
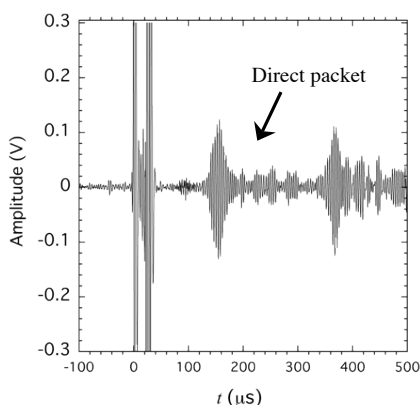


Figure 1: Structure of EMAT and propagation of SH wave.

Figure 2: Specimen simulating a T-joint with reinforcing plate.



(1) Packet transmitting the portion without defect

(2) Packet transmitting a drilled hole

Figure 3: Waveforms of transmitted packets propagating under the reinforcing plate

Acknowledgments

This work was conducted as a part of a Nuclear and Industrial Safety Agency (NISA) project on the Enhancement of Ageing Management and Maintenance of Nuclear Power Plants in Japan.

References

- [1] H.M. Crockett, J.S. Horowitz, J. Pressure Vessel Technology, Vol. 132 (2010) 024501-1.
- [2] S. Xie, Z. Chen, L.Wang, T. Takagi and T. Uchimoto, International Journal of Applied Electromagnetics and Mechanics Vol. 39 (2012), pp.203–211.
- [3] H. Kikuchi, Y. Kurisawa, K. Ara, et al., International Journal of Applied Electromagnetics and Mechanics, Vol. 33 (2010) pp. 1087-1094.
- [4] G. Vértesy, I. Tomás, T. Uchimoto and T. Takagi, E-Journal of Advanced Maintenance Vol. 4 (2012), pp.96-104.

Numerical models of Eddy Current Testing problems for CPU/GPU based clusters

Andrea CHIARIELLO

DIII, Seconda Università di Napoli, Via Roma 29, Aversa, Italy

Massimo NICOLAZZO

CREATE Consortium, v. Claudio, 21, 81125, Napoli, Italy

Guglielmo RUBINACCI

DIETI, Università di Napoli Federico II, v. Claudio, 21, 81125, Napoli, Italy

Antonello TAMBURRINO, Salvatore VENTRE

DIEI, Università di Cassino e del Lazio Meridionale, v. G. Di Biasio, 43, 03043, Cassino, Italy

Abstract. This work provide a contribution on the development and implementation of methods and algorithms for the numerical solution of the eddy current problem for Nondestructive Testing applications via computer clusters based on multi core CPU/GPU. The related hardware configuration is, nowadays, increasingly popular in the framework of High Performance Computing (HPC) for realizing both low cost clusters and high-end clusters. Numerical methods, algorithms and codes previously developed for single core CPU (serial computing) should be almost completely to think over to exploit in full the computational power provided from these new environments. This work represents a contribution in this line with reference to the modeling of the Eddy Current Testing (ECT) problem via an integral formulation.

1 Introduction

Eddy Current Testing (ECT) is a Nondestructive Testing (NDT) method for the imaging of conducting materials with many applications such as, for instance, the inspection of long oil/gas pipelines, heat exchanger tubes in nuclear power plants, aircraft fuselage, aircraft structural components, metal thinning, thickness and corrosion, etc. [1]. In the framework of quantitative methods for ECT [2], complex geometries or complex constitutive relationships (anisotropic materials, ferromagnetic materials, etc.) call for sophisticated numerical methods to treat discretized models with a prohibitively large number of unknowns where High Performance Computing (HPC) is mandatory.

The current trend for HPC relies on sophisticated hardware systems made by clusters of nodes where each node has one or several multi-core CPUs (Central Processing Unit) and one or several GPUs (Graphical Processing Unit). The nodes are typically connected by a fast network interface. Interestingly, the same architecture can be realized with a budget (single/few low-end nodes) or an expensive system (thousands or even more high-end nodes) and even supercomputers. This makes attractive the development of numerical methods, algorithms and codes for such architectures that are becoming very common.

In the recent years a breakthrough in HPC has been the introduction of GPU for scientific computation. The design philosophy of the GPUs is tailored on the inherently parallel nature of graphics rendering, in a picture each pixel is an entry of a large matrices and all the graphic operations are implemented as mathematical operations on matrices. For these reasons GPUs are ideally suited to data-parallel computations with high arithmetic intensity and can be used for scientific application [3-5]. For comparison, the CPU need to be more general possible, hence, a

large part of the chip area is dedicated to a sophisticated control logic and to a large cache memory in order to easily fit the requirement of all the possible applications.

From the scientific point of view, numerical methods, algorithms and codes previously developed for single core CPU (serial computing) should be almost completely to think over to exploit in full the computational power provided from these new environments. The original contribution of this work is in terms of reformulating/revisiting a fast iterative solver for eddy current problems [6].

2 Numerical Model

Here we consider linear materials that can be conductive, magnetic or both, and time-harmonic operations. The numerical model specifically tailored for ECT can be found in [2] and references therein. The formulation is based on an integral equation of the ECT problem where the unknown is the eddy currents \mathbf{J} in the conductive regions:

$$(\underline{\mathbf{R}} + j\omega\underline{\mathbf{L}})\mathbf{I} = \underline{\mathbf{V}}_0. \quad (1)$$

The computational cost for solving (1) is due to $\underline{\mathbf{L}}$ that is a fully populated matrix ($\underline{\mathbf{R}}$ is sparse). $\underline{\mathbf{L}}$ accounts for the inductive coupling between degrees of freedom (DoF). When the number of unknowns n increases, it is only possible to solve (1) by an iterative solver. For doing this, a method to reduce the memory occupation of the stiffness matrix otherwise increasing as $O(n^2)$ and a method for evaluating the matrix-by-vector product with a computational cost smaller than $O(n^2)$ are needed. The fast method we consider, the recursive MGS-QR factorization, has been developed within the nuclear fusion framework [5] and applied to Eddy Current Testing [6]. The idea behind the sparsification through the QR factorization methods is that the field produced by a set of sources grouped in a given region V_S , when evaluated in a different region V_E , it can be described through a low-rank matrix (the rank decreases as the separation between the region increases). Therefore an off-diagonal block $\underline{\mathbf{B}}$ ($q \times p$) of the stiffness matrix can be described as $\underline{\mathbf{B}} = \underline{\mathbf{Q}} \underline{\mathbf{R}}$ where $\underline{\mathbf{Q}}$ is an $q \times r$ matrix, $\underline{\mathbf{R}}$ is an $r \times p$ and r , the rank of $\underline{\mathbf{B}}$, is much smaller than q and p . Consequently, the cost for the matrix-by-vector product decreases from $q \times p$ to $(q+p) \times r$. The computational efficiency can be further improved by using the modified Gram-Schmidt (MGS) combined with a recursive strategy adapted from the adaptive Fast Multipole Method yielding an almost $O(n)$ computational cost. In the full paper we will describe an extension of this method that is suitable for HPC architecture based on mixed CPU/GPU nodes communicating via MPI (Message Passing Interface).

References

- [1] Electromagnetic Nondestructive Evaluation (XI), Book series Studies in Applied Electromagnetics and Mechanics, vol 31, edited by A. Tamburrino et al., IOS Press, October 2008.
- [2] G. Rubinacci, A. Tamburrino, S. Ventre, *Nondestructive Testing and Evaluation*, **24** (2009) 165-94.
- [2] D. Kirk, W. Hwu, *Programming Massively Parallel Processors: A Hands-on Approach*, Elsevier, 2010.
- [3] R. Farber, *CUDA Application Design and Development*, Morgan Kaufmann, 2011.
- [4] F. Villone, A. G. Chiariello, S. Mastrostefano, A. Pironti, S. Ventre, *Plasma Physics And Controlled Fusion*, **54** (2012) 085003.
- [5] G. Rubinacci, S. Ventre, Villone F., Y. Liu, *Journal of Computational Physics*, 228(5), p 1562-1572, 20 March 2009
- [6] F. Calvano et al., in *Studies in Applied Electromagnetics and Mechanics*, Vol. 36, B. P. C. Rao et al (Eds.), pp. 29-36, IOS Press, June 2012.

Acknowledgments

This work was supported in part by the European Commission (SIMPOSIUM Project, grant agreement no. 285549, FP7 Theme FoF-ICT-2011.7.4) and by the Association EURATOM/ENEA/CREATE.

2-

**Electromagnetic sensors
and actuators**

Hysteretic Nonlinear Model of Magnetic Shape Memory Alloy Actuator

Jia Xu ^{a,b}, Ming-Yi Luan ^{a,b} and Zhi-Wen Zhu ^{a,b*}

^a College of Mechanical Engineering, Tianjin University, 92 Weijin Road, Tianjin 300072, P.R.China

^b Tianjin Key Laboratory of Nonlinear Dynamics and Chaos Control, 92 Weijin Road, Tianjin 300072, P.R.China

Abstract. A kind of hysteretic nonlinear model of magnetic shape memory alloy (MSMA) actuator was developed in this paper. Von del Pol nonlinear difference item were introduced to interpret the hysteretic phenomena of strain-magnetic field intensity (MFI) curves of MSMA. Multivariate statistical analysis method was introduced to deal with the nonlinear coupling problem between MFI and stress, and the constitutive relationship among strain, stress and MFI was obtained in partial least-square regression method to describe the variation of strain-MFI curves with stress. The result of significance test shows that all of the items in the constitutive model are remarkable, and the result of forecast test shows that the model can describe the hysteretic nonlinear characteristics of strain-MFI curves of MSMA in different stress well. Based on the MSMA model, the magneto-mechanical coupled model of MSMA actuator was developed, and the relationship between input magnetic signal and output displacement was obtained. The nonlinear characteristics of MSMA actuator were discussed, and phenomena of accuracy aggravation and delay of MSMA actuator in high-frequency magnetic field were explained. Finally the theoretical results were proved by experiment. The new MSMA model has simple form and is easy to be analyzed in theory, which is helpful to application of MSMA in engineering fields.

Keywords: Magnetic Shape Memory Alloy (MSMA), hysteretic nonlinearity, partial least-square regression

1. Introduction

Magnetic Shape Memory Alloy (MSMA) is a kind of smart material. It has many properties such as shape memory, giant strain and rapid response. Based on those properties, the MSMA actuator used in mechanical system can be designed to control vibration. Gauthier et al set up a nonlinear Hamiltonian model of magnetic shape memory alloy actuators [1]. Ahola et al studied the characteristics of magnetic shape memory alloy actuator [2]. Techapiesancharoenkij et al discussed the effect of magnetic stress and stiffness modulus on resonant characteristics of Ni-Mn-Ga ferromagnetic shape memory alloy actuators [3]. Riccardi et al designed a kind of precise positioning actuator based on feedback-controlled magnetic shape memory alloys [4]. Schlueter et al proposed the design principle of actuators driven by magnetic

shape memory alloys [5]. Although many advances were obtained, the modeling problem limits the application of MSMA actuators in industry fields.

In order to design and optimize MSMA actuators effectively, it is necessary to develop its model with high accuracy, which depends on physical model of MSMA. Ohandley set up the first model for strain and magnetization in MSMA [6]. Hayashi et al studied magnetic and mechanical properties of MSMA [7]. Heczko et al discussed the influence of magnetic field and stress on large magnetic shape memory effect in single crystalline Ni-Mn-Ga ferromagnetic alloy [8]. For the hysteretic characteristics of MSMA, most of MSMA models were based on electromagnetics theory and micromechanics theory, and shown as equations with subsection function, which are hard to be analyzed [9, 10]. Usually, research results can only be obtained by numerical method.

* Corresponding author. E-mail: zhuzhiwen@tju.edu.cn

This paper aims to offer a kind of method to develop magneto-mechanical coupled model of MSMA actuator, and analyze its nonlinear dynamical characteristics. Von de Pol item was introduced to interpret the hysteretic phenomena of the strain-magnetic field intensity (MFI) curves of MSMA. The magneto-mechanical coupled model of MSMA actuator was developed where the variation of magneto-elasticity with stress was considered. The relationship between input magnetic signal and output displacement was obtained, and the dynamic characteristics of MSMA actuators were discussed. Finally, the phenomena of accuracy aggravation and delay of MSMA actuators in high-frequency magnetic field were explained.

2. Hysteresis Nonlinear Model of MSMA

The strain-MFI curves of MSMA in different stress were shown in Figure 1. It is obvious hysteretic. In this paper, Von del Pol hysteretic model was introduced to describe hysteretic phenomena of MSMA.

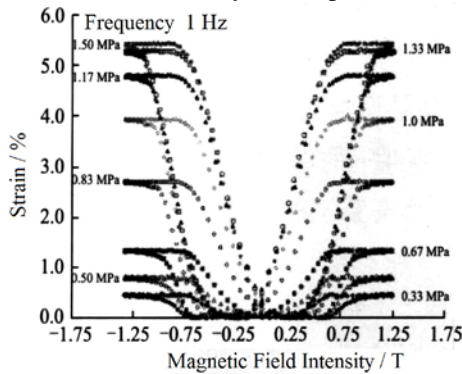


Fig. 1. Strain-MFI curves of MSMA in different stress

The initial Von del Pol model describes hysteretic loop which is symmetrical about the initial point (0, 0). It can be shown as follows:

$$y = f(x) = f_0(x) + a[1 - (\frac{x}{b})^2] \dot{x} \quad (1)$$

where $f_0(x)$ is skeleton curve of hysteretic loop, a and b are coefficients which determine the difference between the skeleton curve and the real curve.

When the strain-MFI curves of MSMA are assumed to be symmetrical about the point G (ε_0, H_0), it can be shown as follows:

$$\varepsilon - \varepsilon_0 = b_1(H - H_0) + b_2(H - H_0)^3 + b_3[1 - (\frac{H - H_0}{b_4})^2] \dot{H} \quad (2)$$

where ε is strain, H is MFI, b_i are coefficients,

skeleton curve is chosen as $f_0(x) = b_1x + b_2x^3$.

$b_4 = H_0$ since the loading curve have the same value as the unloading curve when $H = 0$, and $\varepsilon_0 - b_1H_0 - b_2H_0^3 = 0$ because $\varepsilon = 0$ when $H = 0$. Thus, Eq. (2) can be rewritten as follows:

$$\varepsilon = \phi H + \chi H^2 + \alpha H^3 + \beta(\lambda H - H^2) \dot{H} \quad (3)$$

where $\phi = b_1 + 3b_2H_0^2$, $\chi = -3b_2H_0$, $\alpha = b_2$, $\beta = \frac{b_3}{b_4^2}$, $\lambda = 2H_0$.

In Eq. (3), only the hysteretic characteristics of the strain-MFI curves of MSMA were considered. However, stress can also affect the magneto-elasticity of MSMA. From Figure 1, we can see that the strain-MFI curves vary with stress. Moreover, MFI can also effect the strain-stress curves of MSMA. The strain-stress curves of MSMA in different MFIs were shown in Figure 2.

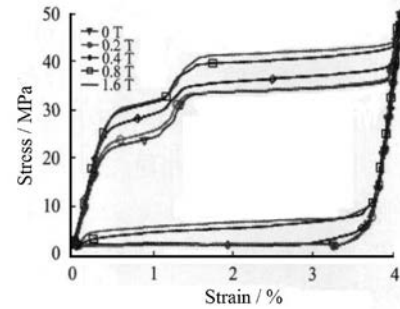


Fig. 2. Strain-MFI curves of MSMA in different MFIs

Obviously, there are coupling relationship among strain, stress and MFI. Supposing that all the coupling items will appear in the model, the basic model of ε can be shown as follows:

$$\begin{aligned} \varepsilon = & a_1H + a_2H^2 + a_3H^3 + a_4H\dot{H} + a_5H^2\dot{H} \\ & + a_6\sigma + a_7H\sigma + a_8H^2\sigma + a_9H^3\sigma \\ & + a_{11}H^2\dot{H}\sigma + a_{12}\sigma^2 + a_{13}H\sigma^2 \\ & + a_{15}H^3\sigma^2 + a_{16}H\dot{H}\sigma^2 + a_{17}H^2\dot{H}\sigma^2 \\ & + a_{18}\sigma^3 + a_{19}H\sigma^3 + a_{20}H^2\sigma^3 \\ & + a_{21}H^3\sigma^3 + a_{22}H\dot{H}\sigma^3 + a_{23}H^2H\sigma^3 \end{aligned} \quad (4)$$

where σ is stress. Obviously, Eq. (4) is very complex, and there must be some items whose effects are not remarkable in the basic model. In the following section, partial least-square regression method was applied to obtain the coupling relationship among strain, stress and MFI.

3. Analysis in partial least-square regression method

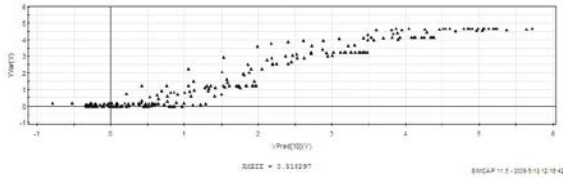


Fig. 3. Distribution result of experimental data

Reading experimental data from Figure 1 and regarding the items in Eq. (4) as independent variables, we obtained the distribution result of experimental data, which was shown in Figure 3. Variable importance (VIP) and values of every coefficients obtained in partial least-square regression method were shown in Table 1.

Table1
 The variable importance of item and value of coefficient

item	Variable Importance	coefficient	value
H	1.55388	a_1	0.877789
H^2	1.24828	a_2	-0.264467
H^3	1.18311	a_3	0.344366
$H\dot{H}$	1.17139	a_4	1.78513
$H^2\dot{H}$	0.907025	a_5	-1.52273
σ	1.50669	a_6	0.312672
$H\sigma$	0.620224	a_7	-0.264381
$H^2\sigma$	0.73831	a_8	-0.154654
$H^3\sigma$	0.870307	a_9	0.0611139
$H\dot{H}\sigma$	0.700915	a_{10}	0.279117
$H^2\dot{H}\sigma$	0.767281	a_{11}	-0.141718
σ^2	1.40988	a_{12}	-0.070063
$H\sigma^2$	0.93707	a_{13}	-0.302388
$H^2\sigma^2$	0.568266	a_{14}	-0.0450251
$H^3\sigma^2$	0.763988	a_{15}	0.0919044
$H\dot{H}\sigma^2$	0.732235	a_{16}	-0.233887
$H^2\dot{H}\sigma^2$	0.685472	a_{16}	-0.151833
σ^3	1.37006	a_{16}	0.251945
$H\sigma^3$	1.09507	a_{16}	0.141662
$H^2\sigma^3$	0.707928	a_{16}	0.0456938
$H^3\sigma^3$	0.711413	a_{16}	0.0612048
$H\dot{H}\sigma^3$	0.876181	a_{16}	-0.183737
$H^2\dot{H}\sigma^3$	0.874935	a_{16}	0.0219349

According to variable importance, the variables which are the most significant (VIP>0.9) in the basic model was chosen as follows: H , H^2 , H^3 , HH , $H^2\dot{H}$, σ , σ^2 , σ^3 , $H\sigma^2$, $H\sigma^3$. Thus, the final relationship among strain, stress and MFI can be shown as follows:

$$\varepsilon = c_1\sigma + c_2\sigma^2 + c_3\sigma^3 + (c_4 + c_5\sigma^2 + c_6\sigma^3)H + c_7H^2 + c_8H^3 + (c_9H - c_{10}H^2)\dot{H} \quad (5)$$

The result of DModX was shown in Figure 4, which shows residual standard deviation (RSD) of samples in X space. We can see that only a little points are strange points, which means that most of forecast data were effective.

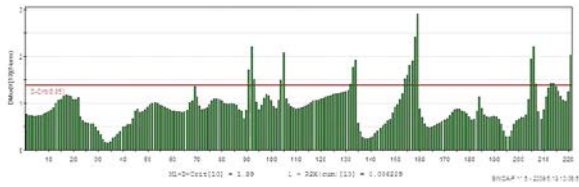


Fig. 4. Result of DmodX

The result of Hotelling T^2 test was shown in Figure 5. We can see that the fitting effect of the model is excellent.

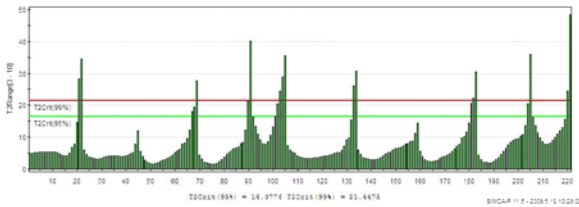


Fig. 5. Result of Hotelling T^2 test

The result of forecast test to Eq. (5) was shown in Figure 6, where red line is real data and black line is forecast value. We can see that Eq. (5) can describe the real curve well.

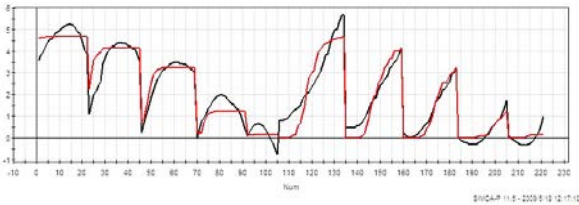


Fig. 6. Result of forecast test

4. Dynamic Model of MSMA Actuator and Experiment

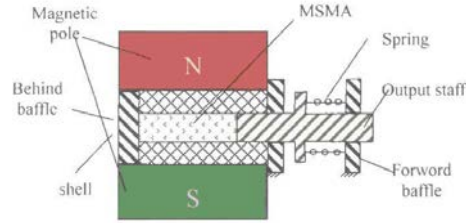


Fig. 7. Structure of MSMA actuator

The typical structure of MSMA actuator was shown in Figure 7, and the equivalent mechanical model of MSMA driving system was shown in Figure 8, where m_r is mass of Terfenol-D rod, m_l is equivalent mass of load, C_r is structural damping of sensor, C_l is equivalent damping of load, k_r is stiffness of Terfenol-D rod, k_l is equivalent stiffness of load, $F(t)$ is excitation force.

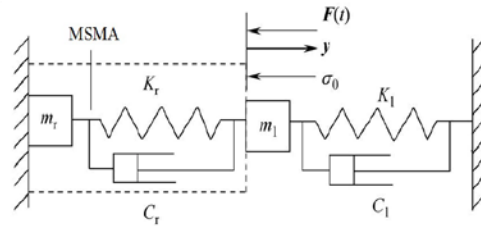


Fig. 8. Dynamic model of MSMA actuator

The mechanical model of MSMA can be shown as follows:

$$\varepsilon = \bar{\varepsilon} - (C_r / E)\dot{\varepsilon} - \rho l_r^2 \ddot{\varepsilon} / (3E) \quad (6)$$

where ε is total strain, $\bar{\varepsilon}$ is strain caused by MFI and stress, $\bar{\varepsilon}$ is determined by Eq. (5), E is Young's elastic modulus, C_r is damping of MSMA, ρ is density of MSMA, l_r is length of MSMA rod.

Since $F = \sigma A_r$ and $y = \varepsilon l_r$, Eq. (6) can be rewritten as follows:

$$m_z \ddot{\varepsilon} + c_z \dot{\varepsilon} + k_z \varepsilon = \frac{A_r E}{l_r} \bar{\varepsilon} \quad (7)$$

where $m_z = \frac{m_r}{3} + m_l$, $c_z = \frac{A_r C_r}{l_r} + c_l$, $k_z = \frac{A_r E}{l_r} + k_l$, m_r is mass of MSMA rod, m_l is equivalent mass of

load, A_r is cross sectional area of MSMA rod, C_1 is damping of load, k_1 is equivalent stiffness of load.

To alternating electromagnetic field in constant frequency, $H = \bar{H} \cos \omega t$, where \bar{H} is the amplitude value of alternating electromagnetic field and ω is the frequency of driving magnetic field. According to Eq. (5) and Eq. (7), we can obtain:

$$m_z \ddot{\varepsilon} + c_z \dot{\varepsilon} + k_z \varepsilon = \frac{A_r E}{l_r} (\bar{F}_1 + \bar{F}_2) \quad (8)$$

where

$$\bar{F}_1 = c_4 \bar{H} \cos \omega t + c_7 \bar{H}^2 \cos^2 \omega t + c_8 \bar{H}^3 \cos^3 \omega t$$

$$\bar{F}_2 = (c_9 \bar{H} \cos \omega t - c_{10} \bar{H}^2 \cos^2 \omega t) \bar{H} \omega \sin \omega t$$

The solution of Eq. (8) is

$$\varepsilon = \varepsilon_0 + \varepsilon_1 \cos \omega t + \varepsilon_2 \cos 2\omega t + \varepsilon_3 \cos 3\omega t + \varepsilon_4 \sin \omega t + \varepsilon_5 \sin 2\omega t + \varepsilon_6 \sin 3\omega t \quad (9)$$

where $\varepsilon_0 = \frac{A_r E c_7}{2k_z l_r} \bar{H}^2$, $\varepsilon_1 = \frac{A_r E}{m_z l_r \bar{\omega}} (c_4 \bar{H} + \frac{3}{4} c_8 \bar{H}^3)$,

$$\varepsilon_2 = \frac{A_r E}{2m_z l_r \bar{\omega}} c_7 \bar{H}^2, \quad \varepsilon_3 = -\frac{A_r E}{4m_z l_r \bar{\omega}} c_8 \bar{H}^3,$$

$$\varepsilon_4 = \frac{A_r E}{4m_z l_r \bar{\omega}} c_9 \bar{H}^3 \omega, \quad \varepsilon_5 = \frac{A_r E}{2m_z l_r \bar{\omega}} c_{10} \bar{H}^2 \omega,$$

$$\varepsilon_6 = \varepsilon_4, \quad \bar{\omega} = \sqrt{(\omega^2 - \omega_0^2)^2 + 2n\omega}, \quad \omega_0 = \frac{k_z}{m_z},$$

$n = \frac{c_z}{m_z}$. The solution can be used in dynamic analysis and design of control law.

Eq. (9) can be rewritten as follows:

$$\varepsilon = \varepsilon_0 + \varepsilon_L + \varepsilon_{NL} \quad (10)$$

where

$$\varepsilon_0 = \frac{c_7 A_r E}{2k_z l_r} \bar{H}^2, \quad \varepsilon_L = \frac{A_r E c_4}{m_z l_r \bar{\omega}} \bar{H} \cos \omega t$$

$$\begin{aligned} \varepsilon_{NL} = & \frac{3A_r E c_7}{4m_z l_r \bar{\omega}} \bar{H}^3 \cos \omega t + \frac{A_r E c_7}{2m_z l_r \bar{\omega}} \bar{H}^2 \cos 2\omega t \\ & + \frac{A_r E c_8}{4m_z l_r \bar{\omega}} \bar{H}^3 \cos 3\omega t - \frac{A_r E c_{10}}{4m_z l_r \bar{\omega}} \bar{H}^3 \omega \sin \omega t \\ & - \frac{A_r E c_9}{2m_z l_r \bar{\omega}} \bar{H}^2 \omega \sin 2\omega t - \frac{A_r E c_{10}}{4m_z l_r \bar{\omega}} \bar{H}^3 \omega \sin 3\omega t \end{aligned}$$

Now we can discuss Eq. (10) as follows:

1) $\varepsilon_0 = \frac{c_7 A_r E}{2k_z l_r} \bar{H}^2$ is constant when \bar{H} is determined. It can be adjusted to zero through calibration;

2) In Eq. (10), only the item $\varepsilon_L = \frac{A_r E c_4}{m_z l_r \bar{\omega}} \bar{H} \cos \omega t$

is linear with \bar{H} . Ideal actuator should be linear, so $\varepsilon = \varepsilon_L$ is ideal;

3) ε_{NL} is nonlinear items in Eq. (10). It is the error between actual output strain and linear scale of MSMA actuator, which is inevitable but can be reduced. From the expression of ε_{NL} , we can see that ε_{NL} is relative with ω . Thus,

(1) To low-frequency magnetic field, ω is small, so ε_{NL} is small but not neglectable.

It means that MSMA actuator can not be regarded as linear approximately even in magnetic field in low frequency, so nonlinear response must be considered when MSMA actuators are applied in engineering fields;

(2) ε_{NL} increases with ω . To high-frequency magnetic field, ε_{NL} is remarkable. It means that accuracy of MSMA actuator will be exasperated in high-frequency magnetic field.

Eq. (9) can also be expressed as follows:

$$\varepsilon = \varepsilon_0 + \bar{\varepsilon}_1 \cos(\omega t + \varphi_1) + \bar{\varepsilon}_2 \cos(2\omega t + \varphi_2) + \bar{\varepsilon}_3 \cos(3\omega t + \varphi_3) \quad (11)$$

where $\bar{\varepsilon}_1 = \frac{A_r E}{4m_z l_r \bar{\omega}} \sqrt{[4c_4 \bar{H} + 3c_7 \bar{H}^3]^2 + (c_{10} \bar{H}^3 \omega)^2}$,

$$\varepsilon_0 = \frac{c_7 A_r E}{2k_z l_r} \bar{H}^2, \quad \varphi_1 = \arccot \frac{4c_4 + 3c_7 \bar{H}^3}{c_{10} \bar{H}^3 \omega},$$

$$\bar{\varepsilon}_2 = \frac{A_r E}{2m_z l_r \bar{\omega}} \sqrt{(c_7 \bar{H}^2)^2 + (c_9 \bar{H}^2 \omega)^2}, \quad \varphi_2 = \arccot \frac{c_7}{c_9 \omega},$$

$$\bar{\varepsilon}_3 = \frac{A_r E}{4m_z l_r \bar{\omega}} \sqrt{c_8^2 \bar{H}^6 + (c_{10} \bar{H}^3 \omega)^2}, \quad \varphi_3 = \arccot \left(\frac{c_8}{c_{10} \omega} \right).$$

Similarly, we can discuss Eq. (11) as follows:

1) There are three kinds of frequency component: ω , 2ω , 3ω in the output strain ε ;

2) The phase of strain is different from that of magnetic field even if the frequency components 2ω and 3ω were both small enough to be neglected;

3) Even to the item $\bar{\varepsilon}_1 \cos(\omega t + \varphi_1)$, its frequency is same as the input excitation force F , while its amplitude $\bar{\varepsilon}_1$ is not linear with \bar{H} . It also means that nonlinear response must be considered when MSMA actuators are applied in engineering fields.

The experimental results of MSMA actuator system were shown in Figure 9 where $\omega = 11\text{Hz}$. We can see that the theoretical solution of Eq. (9) is accord with experiment results, and there are many frequencies in the dynamic response.

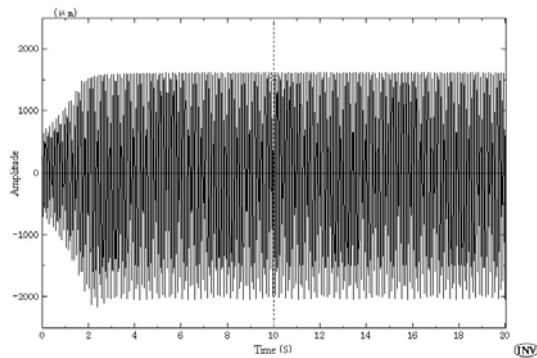


Fig. 9. Experimental result of MSMA actuator when $\omega = 11\text{Hz}$

5. Conclusion

In this paper, a kind of hysteretic nonlinear model of magnetic shape memory alloy (MSMA) actuator was developed. Nonlinear difference item were introduced to interpret the hysteretic phenomena of MSMA. The constitutive relationship among strain, stress and MFI was obtained in partial least-square regression method to describe the variation of strain-MFI curves with stress. The result of significance test shows that all of the items in the constitutive model are remarkable, and the result of forecast test shows that the model can describe the hysteretic nonlinear characteristics of strain-MFI curves of MSMA in different stress well. Based on the MSMA model, the magneto-mechanical coupled model of MSMA actuator was developed, and the relationship between input magnetic signal and output displacement was obtained. The nonlinear characteristics of MSMA actuator were discussed, and phenomena of accuracy aggravation and delay of MSMA actuator in high-frequency magnetic field were explained. Finally the theoretical results were proved by experiment. The new MSMA model has simple form and is easy to be analyzed in

theory, which is helpful to application of MSMA in engineering fields.

6. Acknowledgements

The authors gratefully acknowledge the support of Natural Science Foundation of China (NSFC) through grant no. 11272229, the Ph.D. Programs Foundation of Ministry of Education of China through grant no. 20120032120006, and Tianjin Research Program of Application Foundation and Advanced Technology through grant no. 13JCYBJC17900.

References

- [1] J.Y. Gauthier, A. Hubert and J. Abadie, Nonlinear Hamiltonian modelling of magnetic shape memory alloy based actuators, *Sensors and Actuators A-Physical* 2 (2008), 536–547.
- [2] J. Ahola, T. Lienes and P. Kroneld, On magnetic shape memory alloy actuator characteristics, *Journal of Vibroengineering* 3 (2009), 443–449.
- [3] R. Techapiesancharoenkij, J. Kostamo and S.M. Allen, The effect of magnetic stress and stiffness modulus on resonant characteristics of Ni-Mn-Ga ferromagnetic shape memory alloy actuators, *Journal of Magnetism and Magnetic Materials* 23 (2011), 3109–3116.
- [4] L. Riccardi, D. Naso and H. Janocha, A precise positioning actuator based on feedback-controlled magnetic shape memory alloys, *Mechatronics* 5 (2012), 568–576.
- [5] K. Schlueter, B. Holz and A. Raatz, Principle design of actuators driven by magnetic shape memory alloys, *Advanced Engineering Materials* 8 (2012), 682–686.
- [6] R.C. Ohandley, Model for strain and magnetization in magnetic shape memory alloys, *Journal of Applied Physics* 6 (1998), 3263–3270.
- [7] R. Hayashi, S.J. Murray and M. Marioni, Magnetic and mechanical properties of FeNiCoTi magnetic shape memory alloy, *Sensors and Actuators A-Physical* 1 (2000), 219–223.
- [8] O. Heczko, N. Glavatska and V. Gavriljuk, Influence of magnetic field and stress on large magnetic shape memory effect in single crystalline Ni-Mn-Ga ferromagnetic alloy at room temperature, *European Magnetic Materials and Applications* 3 (2001), 341–344.
- [9] P. Entel; V. D. Bucheikov; V. V. Khovailo: Modelling the phase diagram of magnetic shape memory Heusler alloys. *Journal of Physics D* Vol. 39-5 (2006), pp. 865-889.
- [10] B. Kiefer; H. E. Karaca; D. C. Lagoudas: Characterization and modeling of the magnetic field-induced strain and work output in Ni₂MnGa magnetic shape memory alloys. *Journal of Magnetism and Magnetic Materials* Vol. 312-1 (2007), pp. 164-175.

Research for a new actuator using electromagnetics and piezoelectrics

Zengyong An, Minglong Xu* and Bo Feng

State Key Laboratory for Strength and Vibration of Mechanical Structures, School of Aerospace, Xi'an Jiaotong University, Xi'an 710049, China

Abstract. A new electromagnetic and piezoelectric actuator (EPA) is presented in this paper, which consists of two parts: electromagnetic actuator and piezoelectric actuator, the electromagnetic actuator generates axial displacement and force, and the piezoelectric actuator generates lateral displacement and force. With piezoelectric actuator, the EPA can clamp without power supply. Dynamic model for EPA is built up, static and dynamic performances are simulated by MATLAB. A Closed-loop control experimental system is designed. Results from simulation agree well with that from experiment.

Keywords: Actuator, electromagnetic, piezoelectric, clamp without voltage

1. Introduction

Piezoelectric actuator has got considerable progress in recent years. Different kinds of piezoelectric actuator have been designed to offer any one of the following characteristics: high positioning accuracy, high speed, large forces. So they are needed in applications that require positioning accuracy of the order of nanometers, thrust, and speed. One important class of piezoelectric actuator is inchworm-type class, is a typical actuator, which usually has two clamping and one longitudinal piezoelectric stack [1]. The inchworm actuators have been improved [2-5].

A new electromagnetic and piezoelectric actuator (EPA) is proposed in this paper. The proposed actuator consists of electromagnetic actuator and piezoelectric actuator, the electromagnetic actuator generates axial displacement and force, and the piezoelectric actuator generates lateral displacement and force. With piezoelectric actuator, the EPA can clamp without power supply.

2. The proposed EPA

2.1. Design of EPA

The EPA consists of two parts: electromagnetic actuator and piezoelectric actuator. As shown in Fig. 1, the electromagnetic actuator consists of magnetizer, permanent magnet and coil, which generates displacement and force in axial. The magnetic energy product of permanent magnet is 403KJ/m^3 ; the volume of permanent magnet is $5.495 \times 10^{-7}\text{m}^3$, radius of the coil is 0.01m , turns of the coil is 210, volume of annular gap between two magnetizer is $2.983 \times 10^{-4}\text{m}^3$, the stiffness of spring piece is 1.661N/mm .

*Corresponding author: Minglong Xu, State Key Laboratory for Strength and Vibration of Mechanical Structures, School of Aerospace, Xi'an Jiaotong University, Xi'an 710049, China. Tel/Fax: +86-029-82669093, Email: mlxu@mail.xjtu.edu.cn.

The piezoelectric actuator consists of two diamond clamp structures, two piezoelectric stacks and connecting mechanism, mass of the coil and piezoelectric actuator is 0.1kg. When a driving voltage is applied to piezoelectric stack, the piezoelectric stack extend, the diamond clamp structure contracts in lateral, the cylindrical shell and two diamond clamp structures turn into non-contact, therefore the electromagnetic actuator is unclamping.

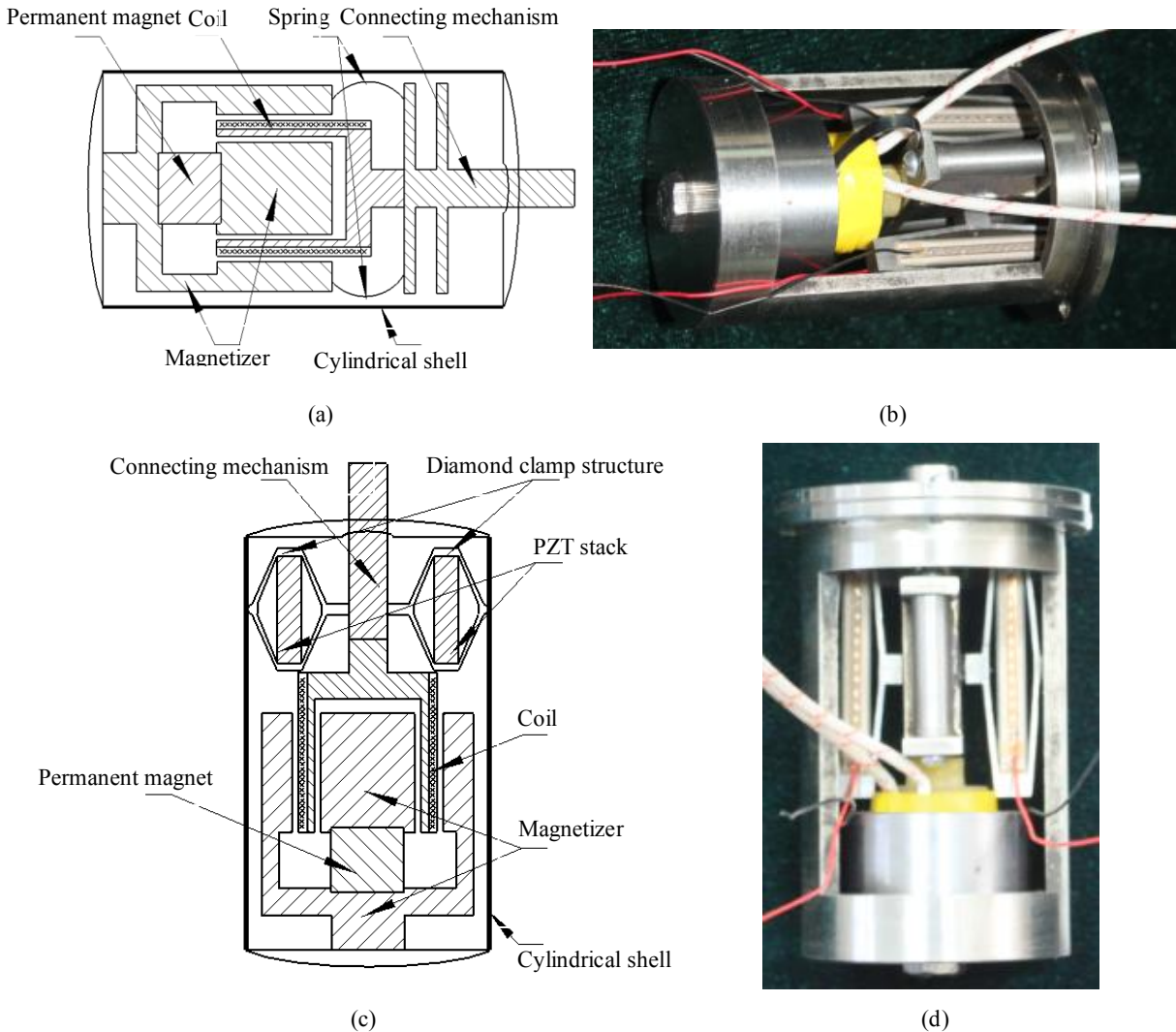


Fig. 1. Schematic of EPA.

The new EPA generates controllable variable displacement and force in different driving current. The working process can be described as follows:

- 1). Without power supply, the piezoelectric actuator is clamping.
 - 2). A driving voltage is applied to piezoelectric actuator, the piezoelectric actuator is unclamping.
 - 3). A driving current is applied to electromagnetic actuator, the displacement is maintainable.
 - 4). Piezoelectric actuator is clamping again by removing driving voltage and keeping displacement.
- It will generate opposite displacement applying opposite current to electromagnetic actuator.

2.2. Dynamic model of EPA

As shown in Fig. 2, the m represents the coil and piezoelectric actuator. The x represents the displacement generated by the EPA. The F_p represents the force generated by the EPA. The F_f represents the friction between the diamond clamp structure and the cylindrical shell.

The model shown in Fig. 4 can be described as

$$m\ddot{x} + c\dot{x} + kx = F_f + F_p \quad (1)$$

x represents the position vector.

m represents the Mass.

c represents the Damping.
 k represents the Stiffness.

F_p represents the pushing force generated by the EPA, which is equal with F generated by electromagnetic actuator.

$$F_p = F \quad (2)$$

$$F = BIL \quad (3)$$

Where B is the uniform magnetization of the annular gap between two magnetizers, I is the current inputted to the coil. L is the wire length of the coil.

$$L = 2\pi rn \quad (4)$$

Where r is the radius of coil, we assume that the thickness of coil is zero, and then r is coefficient. n is the turns of coil.

$$H_e L_e = H_i L_i \quad (5)$$

Where H_e is the magnetic flux of the annular gap between two magnetizers, L_e is the length of the annular gap between two magnetizers, H_i is the magnetic flux of the permanent magnet, L_i is the length of the permanent magnet.

We assume that the magnetic flux is not leaking in magnetizer.

$$B_e S_e = B_i S_i \quad (6)$$

Where B_e is the magnetization of the annular gap between two magnetizers, S_e is the cross-sectional area of magnetization distribution of the annular gap between two magnetizers, B_i is the magnetization of the permanent magnet, S_i is the cross-sectional area of the permanent magnet.

$$H_e L_e B_e S_e = H_i L_i B_i S_i \quad (7)$$

$$H_e B_e V_b = H_i B_i V_M \quad (8)$$

Where V_b is the volume of the annular gap between two magnetizers, V_M is the volume of the permanent magnet.

$$B_e = \mu_0 \mu H_e \quad (9)$$

Where μ_0 is the permeability of air, and the permeability of air is one, μ is the permeability of magnetizer, so B_e can be described as

$$B_e = \sqrt{\frac{B_i H_i V_M}{\mu V_b}} \quad (10)$$

We assume that the magnetization of the annular gap between two magnetizers is uniform, so B can be described as

$$B = B_e \quad (11)$$

So F can be described as

$$F = \sqrt{\frac{B_i H_i V_M}{\mu V_b}} I 2\pi rn \quad (12)$$

When the piezoelectric actuator is unclamping, the diamond clamp structure and the wall of the cylindrical shell is not touching, so the press N is zero, and then the friction F_f is zero.

So with Eqs(2), (3) and (12), we rewrite Eq. (1) as

$$m\ddot{x} + c\dot{x} + kx = 2\pi rn \sqrt{\frac{B_i H_i V_M}{\mu V_b}} I \quad (13)$$

The EPA Eq. (13) can be expressed in the linear state space form as

$$\dot{y} = Ay + Bu, x = Cy \quad (14)$$

y is the system state vector, u is the system input.
 Where

$$y = [y_1 \quad y_2]^T \quad (15)$$

$$A = \begin{bmatrix} 0 & 1 \\ -\frac{k}{m} & -\frac{c}{m} \end{bmatrix} \quad (16)$$

$$B = \begin{bmatrix} 0 \\ \frac{2\pi rn}{m} \sqrt{\frac{B_i H_i V_M}{\mu V_b}} \end{bmatrix} \quad (17)$$

$$C = [1 \quad 0] \quad (18)$$

$$u = I \quad (19)$$

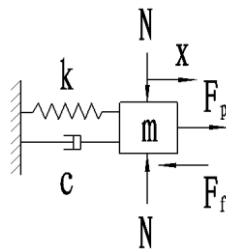


Fig. 2. Dynamical model of EPA.

2.3. Controller for EPA

The EPA controller is based on NI PXI-8196 platform, which consists of a 16 bits A/D card (PXI-6733), a 16 bits D/A card (PXI-6123), the control algorithm is programmed by LabVIEW.

As shown in Fig. 3, the control signal from PXI-8196 is converted into analog voltage by the D/A card, control voltage for the piezoelectric actuator is amplified by a linear voltage driver, and control voltage for the electromagnetic actuator is amplified by a current driver (NF HSA4014). Displacement of the electromagnetic actuator is measured by a laser position sensor (Keyence LK-G80, displacement resolution 0.01 μm), as a feedback signal, analog output from the laser position sensor is sent to A/D card, therefore a closed-loop control system is set up.

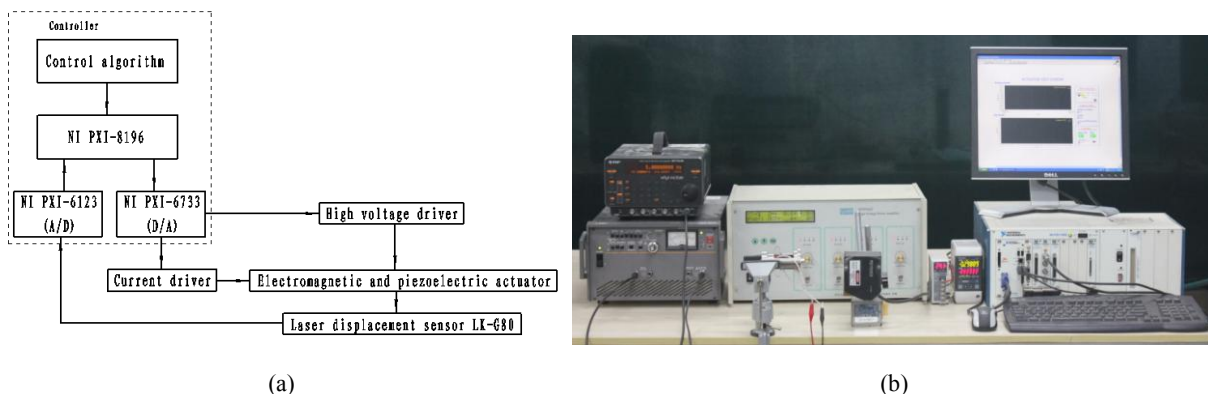


Fig. 3. Control system.

3. Testing for EPA

3.1. Testing of clamping force

Relationship between the clamping force and the driving voltage for piezoelectric stack is tested in MTS(MTS-858). The applied force is measured by a load cell (HBM Z30A), driving voltage is 0V, 24V, 48V, 72V, 96V and 120V. As shown in Fig. 4, with enough applied force, the static friction force is absolutely conquered, the static friction force is converted into sliding friction force, which is defined as the clamping force. With a maximum driving voltage of 120V, the diamond clamp structure and the cylindrical wall is entirely apart, therefore no friction force is measured.

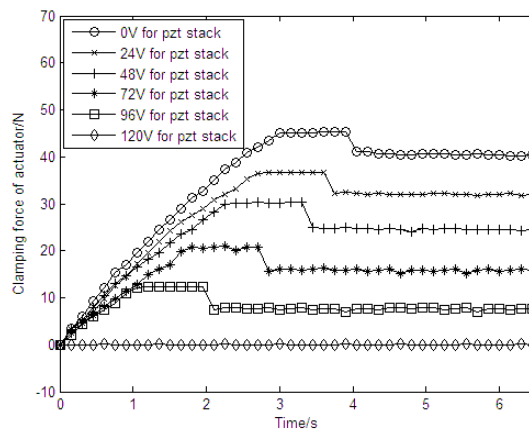


Fig. 4. Clamp force of the EPA.

3.2. Testing of displacement

In static testing, EPA driving current is increasing uniformly, output displacement is measured by the laser position sensor. Relationship between input current and EPA displacement is shown in Fig. 5, the simulation result is linear in whole stage, while the testing result shows slight nonlinear in initial stage (current from 0A to 0.4A) and end stage (current from 1.9A to 2.0A). Comparison shows that testing result is a little higher than that from simulation in the middle stage and lower in other stages. In dynamic testing, a sine driving current is applied to EPA, as shown in Fig. 6, the measured displacement agrees with the driving current, testing result is a little lower than simulation result.

In simulation model, an ideal uniform magnetization between the two magnetizer of the annular gap is adopted, while the actual magnetization is not uniform. Due to magnetic leakage, the magnetization is almost uniform in the middle section, and far from uniform in two end section.

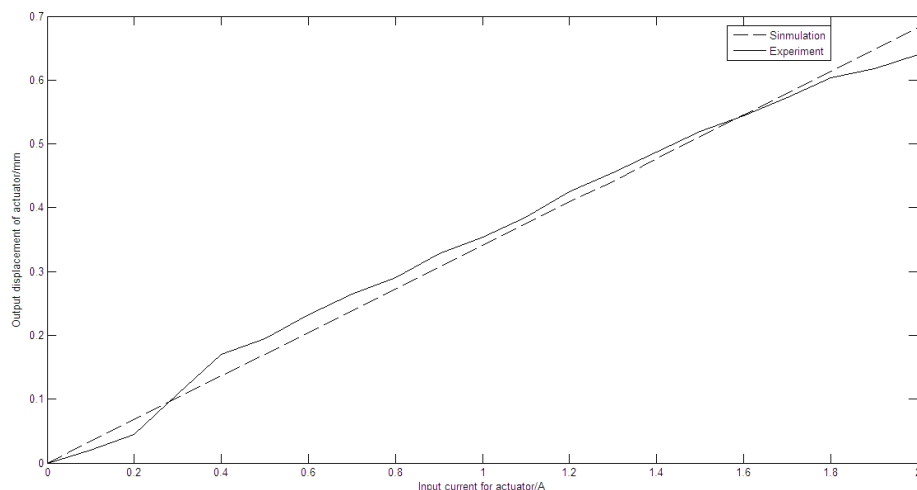


Fig. 5. Static displacement.

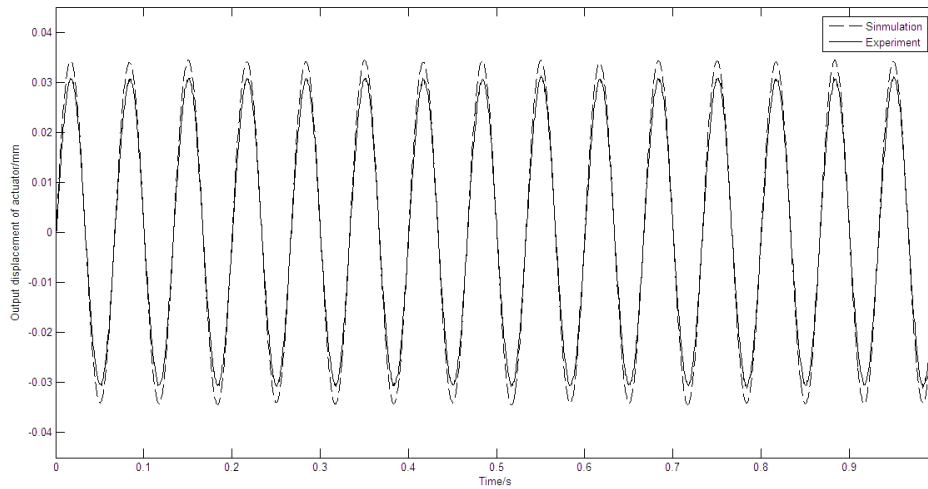


Fig. 6. Dynamic displacement.

Testing characteristics of EPA is shown in Table 1.

Table 1

Experimental results

Accuracy	3 μ m, applied min 10mA current
Output force	1.2N
Displacement	0.64mm, applied max 2.0A current

4. Conclusion

In this paper, a new EPA is proposed. It consists of electromagnetic actuator and piezoelectric actuator, the electromagnetic actuator generates axial displacement and force, and the piezoelectric actuator generates lateral displacement and force. With piezoelectric actuator, the EPA can clamp without power supply. The characteristics of EPA are tested, its accuracy is 3 μ m by applying min 10mA current, its max displacement and force is 0.64mm and 1.2N by applying max 2.0A current. With the position feedback measured by laser displacement sensor, the closed-loop controller designed can control the EPA outputting displacement accurately and clamping without power supply.

Acknowledgements

This work is supported by the National Natural Science Foundation of China (11172229).

References

- [1] R.B. Mrad, A. Abhari and J. Zu, A control methodology for an inchworm piezomotor, *Mechanical Systems and Signal Processing* 17(22) (2003), 457–471.
- [2] B. Zhang and Z. Zhu, Developing a linear piezomotor with nanometer resolution and high stiffness, *IEEE/ASME Transactions on Mechatronics* 2(1) (1997), 22–29.
- [3] J. Frank, G.H. Koopmann and W. Chen, Design and performance of a high force piezoelectric inchworm motor, In SPIE conference on smart structures and integrated systems, 1999, pp. 717–723.
- [4] J. Ni and Z. Zhu, Design of a linear piezomotor with ultrahigh stiffness and nanoprecision, *IEEE/ASME Transactions on Mechatronics* 5(4) (2000), 441–443.
- [5] Z. Zhang, M. Xu, B. Feng and X. Zhang. Research for a new actuator with variable step and large displacement[J]. *International Journal of Applied Electromagnetics and Mechanics*, 2010, 33: 597-604.
- [6] Z. Ni, *Vibration Mechanics*, Xi'an Jiaotong University Press, 1989.
- [7] H. Wang, *Magnetic Material and Application*, National Defense Industry Press, 1989.
- [8] S. Hu, *Automatic Control Theory*, Science Press, 2002.

Design of flux-variable SPM synchronous motor

Jin-seok JANG, Byung-taek KIM**, Member, *IEEE*

Department of Electrical Engineering, San 68 Miryongdong, Kunsan National University, 573-701, Gunsan, S. Korea

Abstract. This paper aims to present a design method of surface permanent magnet synchronous motor (SPMSM) with a variable flux. The equivalent circuit of a motor and an output equation are used to design a motor shape. The operating point of a permanent magnet compared to the thickness of an Alnico magnet are analysed to decide a final shape. Lastly, operating characteristics are analyzed when it is operated at low and high speeds with variable flux through the finite element analysis (FEA).

Keywords: demagnetization, SPMSM, variable-flux, wide operation

1 Introduction

A permanent magnet motor is widely used in many industrial fields because it has less rotor loss and its variable speed control is relatively easy compared with an induction motor. However, the field weakening operation is made at high speed because the flux can't be varied due to the main flux generated by the permanent magnets. This field weakening operation eventually increases the current to become a cause of reduced efficiency[1]. Therefore, many studies on the variable magnetic flux motor are actively underway to improve the problem[2~5]. The motor using two kinds of magnets has no field winding loss and is mechanically concise. But, there is a possibility that a low-coercivity magnet can be demagnetized by the current while operating. It is required to have the design needed to complement this problem.

This study is related to the design of the motor that the demagnetization of SPMSM in the variable flux outer rotor type, using two kinds of magnets is considered. The structure and operating principle of PMSM which has the functions of variable flux are explained. An output equation and an equivalent magnetic circuit are used to design a motor shape that meets the targeted output when the motor is operated at low and high speeds. The operating points of low-coercivity magnets when the designed motor is operated at low speeds are analyzed to decide a final shape. Lastly, the operating characteristics of the low and high-speed motor when it is operated with variable flux are analysed through the finite element analysis (FEA).

2 Structure and Principle of Magnetization

The basic shape of the outer rotor type SPMSM with the 3-phase, 24 pole and 18 slot variable flux structure and a flux diagram at the time of magnetization are respectively shown in Fig 1.(a) and 1.(b).

** Corresponding author: Byung-taek KIM, Department of Electrical Engineering, San 68 Miryongdong, Kunsan National University, 573-701, Gunsan, S. Korea

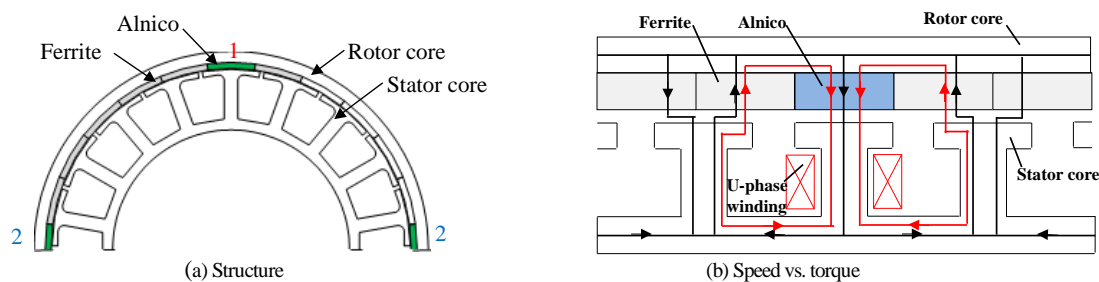


Figure 1: Structure and characteristics of operation

A stator has a salient-pole concentrated winding structure. 20 ferrites (7BE) and 4 Alnico magnets with low-coercivity (Alnico9) are used to vary the flux into the outer rotor type SPM. Alnico magnets are put on the place that it is easy to be magnetized and demagnetized and the 3-phase back EMF is paralleled.

In the process of magnetization and demagnetization, the permanent magnet placed at No.1 in Fig. 1 is arranged at teeth and magnetizing and demagnetizing current are applied to one phase as shown in Fig 1.(b). After the permanent magnet placed at No. 2 is moved to the same place, magnetizing and demagnetizing current are applied. When a magnet is magnetized, a magnetized flux is in the same direction as a flux of ferrite magnet. On the other hand, a ferrite magnet will not be affected when alnico is magnetized and demagnetized because an Alnico magnet has low coercivity when it is demagnetized.

3 Motor Design by using Equivalent Circuit and Output Equations

As resistance of synchronous motor is ignored, the output equation of a 3-phase motor can be formulated as (1).

$$P_{out} = \frac{3E_{ph}V_{ph} \sin \delta}{X_{syn}} = 3E_{ph}I_{ph} \cos \phi \quad (1)$$

where, E_{ph} , I_{ph} and V_{ph} respectively mean phase back EMF, phase current and phase voltage. And, δ is the phase difference between voltage and Back EMF, ϕ is the phase difference between back EMF and current.

As the torque of a SPM type motor is proportional to only the q-axis current and the voltage limit circle is large when it is operated at low speeds, motor control is $i_d = 0$ control to reduce copper losses. Therefore, it is possible to calculate the BACK EMF which meets the output when a motor is operated at low speeds if the maximum output and the current limit are decided because ϕ is 0° in the right section of (1).

Once when the back EMF which meets the output when a motor is operated at low speeds, synchronous reactance is decided to meet high speed operating conditions. If the maximum output power is produced when a motor is operated at high speeds and the voltage limit is decided at the point that the load angle is 90 degrees in (1), synchronous reactance can be estimated from the middle section of (1).

The back EMF and synchronous reactance are induced to (2) and (3) in order to decide the shape which meets decided parameters.

$$E_{ph} = \frac{\omega B_r \delta_m N_{ph}}{\sqrt{2} \mu_m R_{p,Tot}} \quad (2)$$

$$X_{syn} = \frac{4}{3} \omega \frac{N_{ph}^2}{PR_{p,Tot}} \quad (3)$$

where, δ_m , N_{ph} , P and $R_{p,Tot}$ are respectively described as a magnet thickness, the number of turns per phase, the number of poles and the sum of the magnetic reluctance of the air gap and of a permanent magnet in the following formula.

$$R_{p,Tot} = \frac{\delta_m}{\mu_m A_{mag}} + \frac{\delta_g}{\mu_o A_g} \quad (4)$$

The back EMF and synchronous reactance are expressed as a formula related to the shape. (2) and (3) are substituted into an output equation (1) to obtain (5) related to the motor shape.

$$P_{max,h} = \sqrt{2} V_{ph} \cdot \frac{B_r P}{\mu_m} \cdot \frac{\delta_m}{N_{ph}} = k_1 \cdot \frac{\delta_m}{N_{ph}} \quad (5)$$

where, $P_{max,h}$ is maximum output power at high speed.

If (5) is arranged in relation to the number of turns to be substituted in (2), it is possible to get (6) for a cross-section area of permanent magnet.

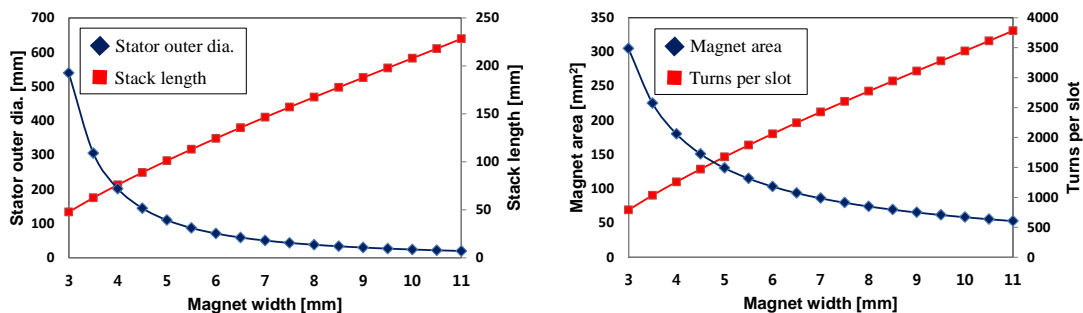
$$A_{mag} = \frac{1}{\delta_m} \left(\frac{1}{\mu_m} + \frac{\delta_g}{\mu_o k_x \delta_m} \right) \left(\frac{\sqrt{2} \mu_m E_{ph} P_{max,h}}{\omega B_r k_1} \right) \quad (6)$$

where, k_x is the ratio between a cross-sectional area of a permanent magnet and of an air gap.

As the number of turns is decided from (5), the pole pitch can be obtained from the following formula if the electrical loading (ac) is decided.

$$\tau = 3 \frac{2 N_{ph} I_{ph}}{p \cdot ac} \quad (7)$$

If the current density, flux density and electrical load are same, an stator outer diameter, stack length, the number of turns and a cross-sectional area of magnet are shown in Fig 2.(a) and (b).



(a) Stator outer diameter and stack length

(b) Area of magnet and number of turns

Figure 2: Design result to magnet thickness

It is possible to decide a motor shape which meets the targeted output to a magnet thickness, using the above design methods.

4 A design of the Alnico Magnet considering Demagnetization

This study predicts the operating points of a permanent magnet in relation to changes in a magnet thickness (δ_m), a design variable which greatly influences the demagnetization of an alnico magnet. A 1/4 equivalent circuit model is expressed to analyze the operating points of an alnico magnet in Fig .3.

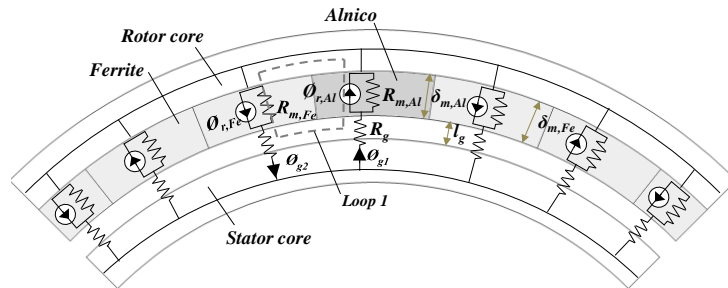


Figure 3: Equivalent magnetic circuit

where, $\Phi_{r,Al}$, $\Phi_{r,Fe}$, $R_{m,Al}$ and $R_{m,Fe}$ are respectively the residual flux and reluctance of an Alnico and a ferrite magnet. R_g and Φ_g respectively mean air gap reluctance and air-gap flux.

Only one alnico magnet is first inserted into a rotor to obtain the load line of an alnico magnet. Other magnets are assumed to be air gaps. Ampere's circuital law is applied to loop 1 which passes through alnico and ferrite magnet and air gaps to get the following formula.

$$H_{Al}l_{Al} + \phi_{g1}R_g + \phi_{g2} \frac{2}{5} R_g + \phi_{g2} \frac{2}{5} R_{Fe} = 0 \quad (8)$$

If (8) is arranged in relation to the shape because Φ_{g1} and Φ_m are equal to Φ_{g2} and $\Phi_m/2$ in an equivalent circuit, one alnico magnet is inserted to get (9) related to load line.

$$B_{Al} = -\frac{6\mu_r\delta_g + \delta_{fe}}{5\mu_r\mu_o} \delta_{Al}H_{Al} \quad (9)$$

At this time, it is assumed that the cross-sectional area of a permanent magnet and area of an air gap are the same because they are almost similar.

If it is assumed that only one ferrite magnet is inserted to calculate the magnetomotive force in an alnico magnet, (10) can be obtained.

$$\phi_m = \phi_{Fe} \frac{R_{fe} + R_g}{5R_{Al} + R_{fe} + 6R_g} \quad (10)$$

The mmf caused by a ferrite magnet can be obtained as shown in the following formula when (11) is arranged.

$$H_{m,Fe} = \frac{u_r B_{r,fe} l_m l_g}{\left\{ 5u_r u_o (l_m + \mu_r l_g) \right\} (5l_{Al} + l_m + 6u_r l_g)} \quad (11)$$

The flux which passes through an alnico magnet, caused by d-axis current can be obtained in the following formula at the time of low-speed and maximum output operation.

$$\phi_{ni} = \frac{5N_{id}}{5R_{Al} + R_{Fe} + 6R_g} \quad (12)$$

When (12) is arranged, the magnetomotive force of an alnico magnet for d-axis current can be obtained in the following formula.

$$H_{m,ni} = \frac{5N_{id}}{5l_{Al} + l_m + (1 + u_r) l_g} \quad (13)$$

The operating points of an alnico magnet, caused by operating current can be obtained in (9), (11), (13) and the b-h cruve of an alnico magnet. When the recoil line is predicted at the obtained operating point and (9) and (11) are used, no-load operating point can be obtained. The amount of flux and the back EMF in a magnet to the thickness of an alnico magnet at no-loading time after low-speed operation are described in Fig. 4.

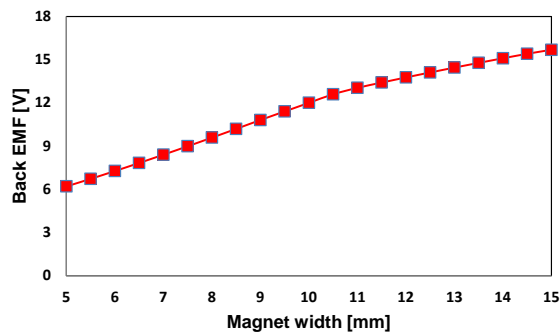


Figure 4: Back EMF for change of magnet width

The minimum width of the magnet which meets the targeted back EMF when an alnico magnet is magnetized is 10mm in Fig. 4. The specifications of the designed motor are described in Table 1.

Table 1
 Specifications of a proposed model

Item	Value	Item	Value
DC link Voltage	310 V	Air gap length	0.8mm
Inverter current limit	5A	Stator outer dia.	348.5mm
Max power(@45 rpm)	141.4w	Rotor outer dia.	390mm
Max power(@1400 rpm)	586.4w	Ferrite magnet width	6mm
Magnet	7BE, Alnico9	Alnico magnet width	10mm
Turns per phase	1080	Stack length	25.3mm

5 Analysis of Motor Characteristics on Flux Control

The waves of air-gap magnetic flux density and of back EMF when an alnico magnet of the designed motor is magnetized and demagnetized are respectively described in fig. 6.(a) and (b). The back EMF is 11.5V (rms) when it is magnetized and 8.5V (rms) when it is demagnetized in fig. 6. It is viewed that the width of variable flux is 35%.

The torque waves when a motor is operated at low speeds and high speeds are shown in Fig 6.(a). On the other hand, the current waves caused by the magnetization and demagnetization of an Alnico magnet at the time of high-speed operation in the same output conditions are described in Fig 6.(b).

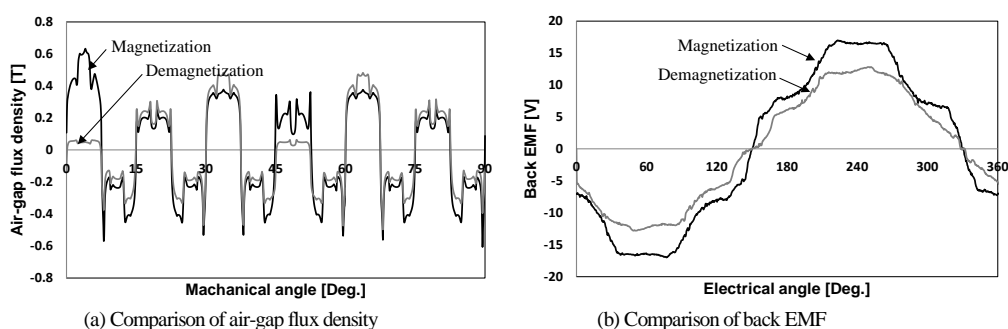


Figure 5: No-load analysis

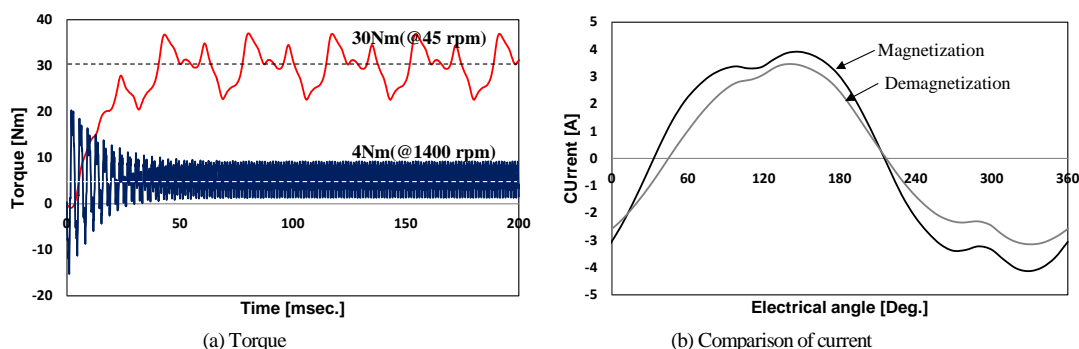


Figure 6: Torque and current characteristics with various flux

The current required for the same output is seen to decrease because the field-weakening effect is obtained as an alnico magnet is demagnetized at the time of high-speed operation in Fig 6.(b).

6 Conclusion

This study presents a design method of a variable magnetic flux motor. It uses an output equation and an equivalent magnetic circuit to design a basic type and decide the magnet thickness that the demagnetization of a low-coercivity magnet is considered while operating. It is thought that the design method of a variable magnetic flux motor, presented in this study will usefully be used in the washer and automotive field characterized by low speed/high-torque and high speed/torque operation.

References

- [1] B. Stumberger, et al., "Design and finite-element analysis of interior permanent magnet synchronous motor with flux barriers," *IEEE Transactions on Magnetics*, Vol. 44, No. 11, pp. 4389-4392, Oct. 2008.

- [2] E. Sulaiman, T. Kosaka, N. Matsui, "Power Density Design of 6-Slot-8-Pole Hybrid Excitation Flux Switching Machine for Hybrid Electric Vehicles, *IEEE Trans. on Magnetics*, vol.47, No.21, pp. 4453-4456, 2010.
- [3] V. Ostovic, "Memory motors," *IEEE Industry Applications Magazine*, vol.9, No.1, pp. 52-61, Jan/Feb 2003.
- [4] J. T. Chen, Z. Q. Zhu, S. Iwasaki, R. Deodhar, "A novel hybrid excited switching-flux brushless AC machine for EV/HEV applications," *IEEE Trans. on Vehicular Technology*, vol.60, no.4, pp.1365-1373, 2011.
- [5] L. Del Ferraro, F. Caricchi, & F. G. Capponi, "Analysis and comparison of a speed-dependant and a torque-dependant mechanical device for wide constant power speed range in AFPM starter/alternators," *IEEE Transactions on Power Electronics*, vol.21, no.3, pp.720-729, May 2006.

Development and analysis of a novel limited angle torque motor with moving coil

Yongxiang Xu, Yanyu Wei, Jibin Zou^{*}, Kai Liu and Hao Wang

Department of Electrical Engineering, Harbin Institute of Technology, Xi Dazhi Street, Harbin, China

Abstract. This paper presents a novel limited angle torque motor (LATM) possessing the feature of small inertia, linear current-torque characteristic and compact structure. The design procedure, optimization and experiments are presented. An analytical technique is proposed for economical design procedure consisting of the calculations of torque coefficient, moment of inertia, resistance and electromechanical time constant. By optimizing the geometric shape of moving coil, small electromechanical time constant and rapid response performance is feasible. Both finite element analysis and prototype test are implemented to verify the proposed theoretical methods. At last the outstanding control characteristic of the proposed LATM is demonstrated with experiment.

Keywords: Limited angle torque motor; Moving coil; Control characteristic; Finite element method.

1. Introduction

Limited angle torque motor (LATM) is primary executive component in aerospace equipment, optical scanning system and micro-position control system^[1, 2]. At present LATM's are primarily employed to position loads in an analogue fashion while simple two-position applications were the majority decades ago. With the features of small physical size, short response time and high magnetic stiffness, Laws relay type LATM's are popularly used in various applications ranging from the simple turn-on and turn-off of servo valves to the accurate tracking of a reference signal^[3].

Typical LATM based on polarized reluctance principle is described as: A salient soft iron rotor is mounted in ball bearings. It rotates about the axis with a fixed maximum displacement (e.g., 15°). The skeleton of stator is formed by four parts, namely two permanent magnets being assembled between two soft iron yokes as the magnetic excitation. To complete the stator, two series connected controlling coils are placed on opposite yokes. Since the reluctances of the magnetic circuit vary considerably with rotor position and saturation as presented in [4], actual motor possesses significantly nonlinear torque-current characteristic.

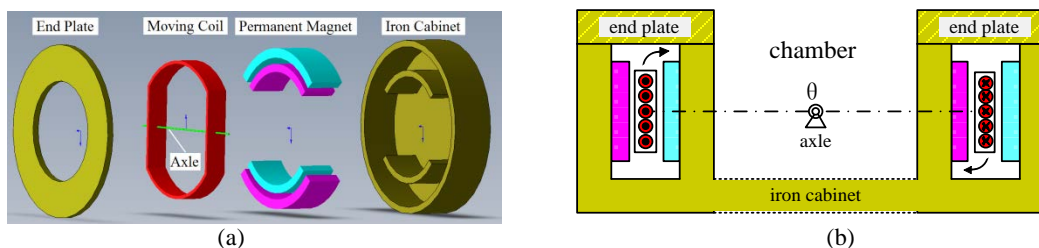


Fig. 1. Explosive view (a) and section view (b) of the proposed LATM

This paper proposes a non-Laws relay type LATM with linear torque-current characteristic for small angular travels applications. The explosive view is shown in Fig. 1 (a). Iron cabinet and end plate together form the out shell. Two sets of arc-shaped permanent magnets are fixed onto the iron cabinet which serves as the yoke. One moving coil is mounted onto a set of axle (reduced to a line in Fig. 1 for

^{*} Corresponding author: Jibin Zou, Department of Electrical Engineering, Harbin Institute of Technology, West Dazhi Street, Harbin, China. Tel.: +86-451-86413613-601; Fax: +86-451-8641361-607; E-mail: zoujibin@hit.edu.cn

simplity) which guarantees the circular segments of the coil lie in the airgaps between magnets. A clear view of the arrangement is depicted in Fig. 1 (b). Two magnetic circuits separately close up with well designed air gaps, within which the magnetic field distribution is uniform and independent of the moving part. When current is applied in the controlling winding, Lorentz force acts on the coil in opposite directions. The produced torque is proportional to the applied current.

In addition, position sensor and other load components, e.g. scanning mirror, are fixed on the moving coil by bracket and enveloped within the chamber. In this way high mechanical strength is obtained due to the compact structure. The elimination of ball bearings undoubtedly is a promising improvement. Also moving coil is prior to iron core for rapid response performance^[5, 6].

This paper concerns the design, optimization and control-related characteristics of the LATM. At first, a primitive design is presented with proposed analytical design procedure including both electrical parameters calculation and optimization of coil shape. Concerning two alternative magnetizing modes, the proposed analytical calculation of torque coefficient is verified by finite element method (FEM). Finally, a LATM prototype is manufactured in lab. The measured parameters are compared with the analytical results and FEM results. A drive system equipped with a regular PI controller is examined and the control-related characteristics are tested.

2. Design and optimization

2.1. Magnetic circuit design

A simplified two-dimension model represented the magnetic circuit is shown in Fig. 2. The model is split into two parts by the dotted line in middle: the left half is represented by physical model, while the right half is represented by its equivalent magnetic circuit.

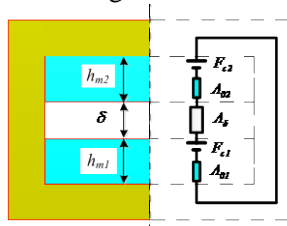


Fig. 2. Magnetic circuit model.

Ignoring the magnetic potential drop in the iron yoke, the air gap flux density is determined by

$$B_{\delta} = \frac{h_m}{h_m + \mu_r \delta} B_r \quad (1)$$

where B_r is the residual flux density of permanent magnet material, μ_r is the relative permeability, δ is the air gap length, and h_m is the total magnet thickness. h_m and δ are determined by the dimensions of iron cabinet which is designed accommodating the requirements of installation.

2.2. Electrical circuit design

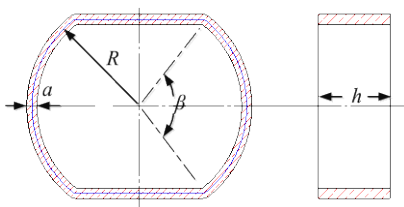


Fig. 3. Coil dimensions.

As shown in Fig. 3, the coil consists of two straight segments and two circular segments. This shape is preferred with less mass and inertia compared to a regular ring shape. Generally the straight segments play a role similar to the end winding in a conventional machine. Since only the circular

segments are responsible for torque producing, the arc angle termed as β is a key parameter. In addition, to make sure the circular segments rotate unimpededly within the airgaps, average radius of circular segments R , coil width a and coil height h are selected according to the air gap dimensions.

The coil space factor k_f is defined in this paper as the proportion between net copper area and overall occupation. Trade off between technical feasibility and operation performance should be considered when k_f is selected.

$$A_{Cu} = k_f ah \quad (2)$$

Defining the average current density over the cross section of coil as J_c , for a coil of N turns, current flowing through it can be written as $I = J_c ah / N$. It is obvious that the proposed LATM possesses only one electrical circuit. The winding resistance R_a is defined by Eq. (3), and the back electromotive force (EMF) E_m is defined by Eq. (4).

$$R_a = \frac{2}{k_f ah} N^2 \rho_{Cu} R (\beta + 2 \cos(\frac{1}{2} \beta)) \quad (3)$$

$$E_m = \frac{1}{3} N B_\delta (12R^2 + a^2) \sin(\frac{1}{2} \beta) \omega \quad (4)$$

where ρ_{Cu} is the electrical resistivity of copper, and ω is the angular speed of moving coil.

Ignoring the winding inductance, voltage equation is given by

$$U_s = E_m + R_a I \quad (5)$$

where U_s is the voltage source. Thus the number of turns can be determined with the following expression

$$N = \frac{U_s}{\frac{1}{3} B_\delta (12R^2 + a^2) \omega \sin(\frac{1}{2} \beta) + \frac{2}{k_f} J_c \rho_{Cu} R [\beta + 2 \cos(\frac{1}{2} \beta)]} \quad (6)$$

2.3. Output characteristic

The output torque is equal to the sum product of lorentz force and the force arm. At null position the value is given by

$$T = \frac{ah}{3} (12R^2 + a^2) B_\delta J_c \sin \frac{\beta}{2} \quad (7)$$

When the coil departs from the null position, the arm varies as a cosine function of the displacement angle while the lorentz force remain the same. Considering that the displacement angle is confined to a small value, the torque drop is effectively negligible.

Correspondingly the torque coefficient is defined as

$$K_T = \frac{1}{3} N B_\delta (12R^2 + a^2) \sin(\frac{1}{2} \beta) \quad (8)$$

2.4. Optimization of coil shape

The moment of inertia of moving coil around axis is given by

$$J = \frac{\rho R ah}{12} [(12R^2 + 3a^2 + 2h^2) \beta + (12R^2 + 3a^2) \sin \beta + (4h^2 + 12R^2) \cos(\frac{1}{2} \beta) + 4R^2 \cos(\frac{3}{2} \beta)] \quad (9)$$

where ρ is the average mass density of coil considering the insulation. Inertia of load is termed as J_0 , giving rise to a total rotor inertia $J + J_0$. The electromechanical time constant is defined as

$$T_{m} = \frac{J_0 + J}{K_T K_E} R_a \quad (10)$$

where K_E is the back EMF coefficient defined by $E_m = K_E \omega$, and K_T is the torque coefficient. It should be noted that the back EMF coefficient is equal to the torque coefficient.

Investigation of Eqs. (3), (4), (9) and (10) reveals that T_m is essentially a function with respect to β . Fig. 4 shows the function curve with an assume J_0 . Apparently the function is monotone decreasing over the whole definition interval ranging from 0° to 180° . And the slope trails off with the increasing of β . These phenomena can be explained by the fact that the straight segments useless for torque output are compressed when the arc angle increases.

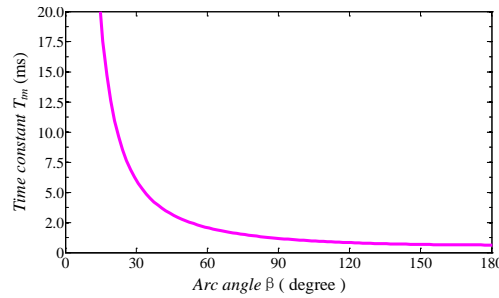


Fig. 4 Time constant as a function of arc angle

Increased β comes at the price of space for the installation of the axle set. Therefore, extra large β is not only unnecessary but also impractical. Then an arc angle slightly larger than $\pi/2$ is selected.

3. Finite element analysis

3.1. Discussion on magnetizing modes

The proposed design procedure is based on the assumption of radial magnetization of permanent magnets. However, parallel magnetization is more common in industry. The calculation of torque regarding magnetization mode is presented in this section.

In the cylindrical coordination system, the output torque can be calculated as

$$T = 2 \int_{\frac{\beta}{2}}^{\frac{h}{2}} \int_{R-\frac{a}{2}}^{R+\frac{a}{2}} \int_{-\frac{\beta}{2}}^{\frac{\beta}{2}} [B_{\delta}(r, \theta, z) J_c(r, \theta, z) r^2 \cos \theta] d\theta dr dz \quad (11)$$

where $B_{\delta}(r, \theta, z)$ and $J_c(r, \theta, z)$ are magnetic flux density and current density at any point $P(r, \theta, z)$. as for the proposed LATM, $J_c(r, \theta, z)$ is constant, while $B_{\delta}(r, \theta, z)$ changes only in circular direction. The torque ratio of parallel magnetization to radial magnetization is calculated as

$$k = \frac{\int_0^{\beta/2} B_{\delta 1}(\theta) \cos \theta d\theta}{\int_0^{\beta/2} B_{\delta 2}(\theta) \cos \theta d\theta} \quad (12)$$

where $B_{\delta 1}(\theta)$ is flux density of parallel magnetization, and $B_{\delta 2}(\theta)$ is flux density of radial magnetization.

The air gap flux density distribution in the circular direction can be calculated by FEM. As shown in Fig. 5, with parallel magnetization the waveform is similar to sinusoidal; whereas the waveform is almost square when radial magnetization is used. Furthermore, the amplitude of flux density with parallel magnetization is higher than that of radial magnetization.

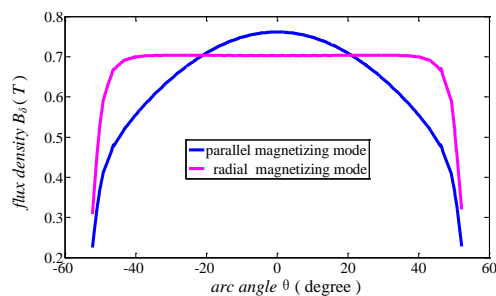


Fig. 5 Flux density distribution in the circular direction

According to the FEM results, the torque ratio k is 0.93. This 7% drop in torque output implies that parallel magnetization is slightly weaker than radial magnetization. Segmental assembling of parallel magnetized permanent magnets should be useful to improve the torque output capability but at the cost of manufacturability. For it is beyond the scope of this study, detailed discussion is not presented.

3.2. FEM calculation of torque coefficient

Output torque is calculated by FEM. Fig. 6 depicts the model with parallel magnetized permanent magnets and shows the cloud figure of flux density plotted on coil occupied space. It is clearly shown that magnetic flux density in air gap is not uniform resulting from end effect, flux leakage and parallel magnetization. When the moving coil rotates around the axis, Lorentz force varies due to the variable flux density. At the same time the force arm also changes slightly. These factors together give rise to calculation error of the proposed analytical method.

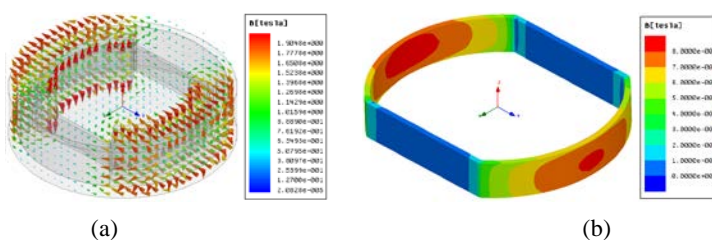


Fig. 6. FEM model: (a) vector figure of flux density (b) cloud figure of flux density

The calculated torque coefficient corresponding to the maximum current (0.3 A) is shown in Fig. 7 as the displacement angle ranges from 0° to 3° . In general, torque coefficient declines as displacement angle increases. It should be noted that the maximum deviation is only 3%, therefore the torque coefficient can be seen as constant. The average torque coefficient is 0.2203 Nm/A according to the FEM.

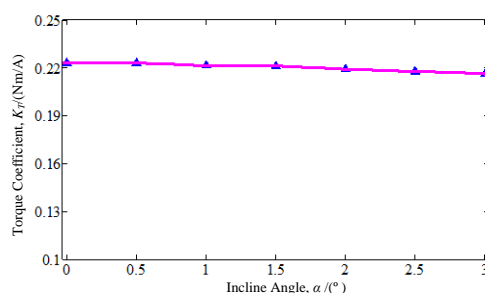


Fig. 7. FEM result of torque coefficient.

Taking the torque ratio k into account, when radial magnetized permanent magnets are used the torque coefficient should be 0.2369 Nm/A, approximately 9% less than the analytical calculated result (0.26 Nm/A). Obviously the design procedure presented in section 2 possesses an acceptable accuracy.

4. Prototyp and experiment

A laboratory prototype using parallel magnetized NdFeB (N38SH) magnets as depicted in Fig. 8 has been built. Measured parameters of the prototype are listed in Table. 1. The measured coil resistance agrees well with the analytical design.

Table 1
Motor Parameters

Parameters	Design value	Measured value
Winding Resistance (Ω)	43.43	42.3
Torque constant (Nm/A)	0.26	0.21
Time constant (ms)	0.978	1.05

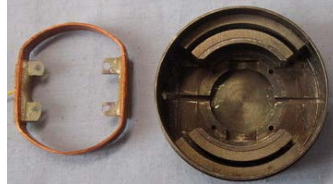


Fig. 8. Laboratory prototype LATM.

To verify the linear output characteristic, a LATM drive system as illustrated in Fig. 9 is established. A conventional PID regulator is implemented with a dsPIC30F2010. Fig. 10 shows the time-response of the LATM tracking a 50-Hz triangular reference. The result indicates that the proposed LATM is well qualified for period signal tracking thanks to its outstanding high frequency response performance.

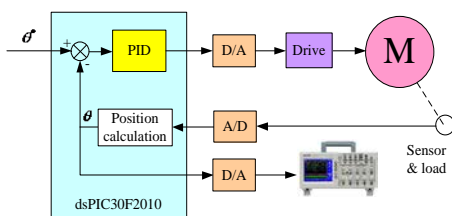


Fig. 9. Diagram of the control system.

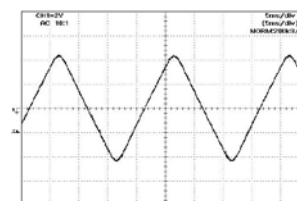


Fig. 10. Time response tracking a 50 Hz triangular reference.

5. Conclusions

A novel LATM with the features of small inertia, linear output torque and compact structure has been proposed in this paper. Rapid design procedure of the LATM has been presented and then verified by FEM and prototype measurement. A simple control system consisting of a PID regulator has been established and the experiment results implied that the prototype LATM has short response time and outstanding control-related characteristic. The LATM proposed in this paper is well qualify for small angular travels applications.

Acknowledgements

This work was supported in part by the 973 Program under Grant 2013CB035605.

References

- [1] Y.Zhang, I.R.Smith, J.G.Kettleborough, Performance evaluation for a limited-angle torque motor, *IEEE/ASME Transactions on Mechatronics*, vol. 4, pp. 335-339, 1999.
- [2] Y.Zhang, I.R.Smith, J.G.Kettleborough, Accurate tracking control of a limited angle torque motor, *Electric Machines and Power Systems*, vol. 27, pp. 1191-1199, 1999.
- [3] C. Tsai, S. Lin, H. Huang, Y. Cheng, Design and control of a brushless DC limited-angle torque motor with its application to fuel control of small-scale gas turbine engines, *Mechatronics*, vol. 19, pp. 29-41, 2009.
- [4] H. R. Bolton and Y. Shakweh, Performance prediction of Laws's relay actuator, *IEE Proceedings B: Electric Power Applications*, vol. 137, pp. 1-13, 1990.
- [5] F. S. Ahmed, S. Laghrouche, M. El Bagdouri, Analysis, modeling, identification and control of pancake DC torque motors: Application to automobile air path actuators, *Mechatronics*, vol. 22, pp. 195-212, 2012.
- [6] H. Yu, T. Lee, S. Wang, *et al.*, Design of a voice coil motor used in the focusing a system of a digital video camera, 2005, pp. 3979-3981.

Study on Improved Cogging Torque Reduction Method for Single-Phase Brushless DC Motor

Young-Un Park ^a, Ji-Young So ^a, Ju-Hee Cho ^b, Se-hyun Rhyu ^b, and Dae-kyong Kim ^{a,*}

^a Dept. of Electrical Control Engineering, Sunchon National University, Korea

^b Korea Electronics Technology Institute (KETI), Korea

Abstract. A single-phase, brushless DC (BLDC) motors have unequal air gaps to eliminate the dead-point where developed torque is zero. These unequal air gaps deteriorate the motor characteristics in the cogging torque. Therefore, this paper proposes a novel design for a single-phase BLDC motor with an asymmetric notch is proposed to solve this problem. In the design method, asymmetric notches were placed on the stator pole face, which affects the variation of the permanent magnet shape or the residual flux density of permanent magnet. Parametric analysis was performed to determine the optimal size and position of an asymmetric notch to reduce the cogging torque. Finite element analysis (FEA) was used to calculate the cogging torque. The FEA results were confirmed by the experimental cogging torque. The improved method decreased about 38.6[%] and 17.5[%] in cogging torque compared to the initial and previous model, respectively.

Keywords: Asymmetric air-gap, asymmetric notch, cogging torque, single-phase brushless DC motor

1. Introduction

Nowadays, the single-phase BLDC motors are used widely in blower applications and home appliances because of their high efficiency and cost effectiveness. Single-phase BLDC motors with a uniform air gap make them inherently non-self starting because they have coincident zero torque positions of excitation. Therefore, single-phase BLDC motors adopt asymmetric air-gaps to make them self starting [1]-[2]. On the other hand, such an asymmetric air-gap can contribute to cogging torque [3].

The conventional methods for reducing the cogging torque of single-phase BLDC motors include the length change of the air-gap, PM asymmetry arrangement, skew of the stator or rotor, and shape change in the stator teeth. Some studies reported decreases in the cogging torque for single-phase BLDC motors by varying the air-gap profile, considering the tapered teeth and trailing edge of the teeth [4]-[5]. Some approaches have proposed an analytical model capable of predicting the cogging torque [6]-[7] and changing the design parameter such as teeth notching [8]-[9] for a symmetric air-gap. To reduce the cogging torque of single-phase BLDC motors with an asymmetric air-gap, the application of an asymmetric notch size and position is required in the case of adopting notches for an asymmetric air-gap.

In our previous work, a novel cogging torque reduction method for single-phase BLDC motors with an asymmetric air-gap was proposed [10]. Although previous work used two notches, the same size and different position of each notch were determined for an asymmetric air-gap.

This paper reports the improved cogging torque reduction method that applied asymmetric size and position variations of each notch for the tapered teeth of a stator in a single-phase BLDC motor. Finite-element analysis (FEA) was used to calculate the cogging torque. Parametric analysis was carried out to determine the size and position of the asymmetric notches to reduce the cogging torque. This proposed stator shape with an asymmetric position notch was compared with the initial model and previous model and the measured performance of the cogging torque was analyzed.

*Corresponding author: Dae-kyong Kim, Dept. of Electrical Control Engineering, Sunchon National University, 540-950, Suncheon, Korea. Tel: +82-61-750-3546; Fax: +82-61-753-3546; E-mail: dkkim@sunchon.ac.kr

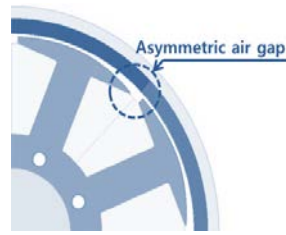


Fig. 1. Initial model with asymmetric air-gap.

2. Cogging torque reduction method of single-phase BLDC motor

2.1. Conventional structure of single-phase BLDC motor

A general single-phase BLDC motor can cause the failure of a trial run because its rotor is arranged where torque is not generated. Therefore, the rotor needs to be arranged where the torque can be generated by the asymmetric shape of the stator, as shown in Fig. 1.

2.2. Analytical expression for cogging torque [10]

The cogging torque is the amount of energy variation according to the amount of rotor rotation and can be expressed as follows:

$$T_{cog} = -\frac{\Delta W(\alpha)}{\Delta \alpha} \quad (1)$$

where W is the magnetic energy of the machine and α is the position angle of the rotor.

For the surface permanent magnet type of BLDC, most energy changes occur in the air-gap part. Hence, only the energy on the air-gap part is considered when calculating the cogging torque. Therefore, $W(\alpha)$ can be calculated through a Fourier series expansion used in equation (2) on an even function as follows:

$$\begin{aligned} W(\alpha) &= \frac{L_s}{4\mu_0} (R_m^2 - R_s^2) \left\{ \int_0^{2\pi} \sum_{n=0}^{\infty} B_{nN_L} G_{nN_s} \cos(nN_L(\theta + \alpha)) \cos(nN_L\theta) d\theta \right\} \\ &= \frac{L_s}{4\mu_0} (R_m^2 - R_s^2) \sum_{n=0}^{\infty} B_{nN_L} G_{nN_s} \cos(nN_L\alpha) \end{aligned} \quad (2)$$

where B , G , R_m and R_s are the flux density, relative air-gap permeance function, inner radius of the rotor and inner radius of the stator, respectively. L_s is the stack height and N_s is the number of stator slots. N_L is the least common multiple of the number of pole and N_s .

The final cogging torque can be expressed as equation (3) by differentiating the air-gap energy obtained from equation (2) according to equation (1) with a rotation angle of the rotor.

$$T(\alpha) = \frac{L_s \pi}{4\mu_0} (R_m^2 - R_s^2) \sum_{n=0}^{\infty} B_{nN_L} G_{nN_s} n N_L \sin(nN_L\alpha) \quad (3)$$

According to equation (3), the cogging torque is determined from the values of B_{nN_L} and G_{nN_L} . When a notch is applied to the stator teeth, the shape of the relative air-gap function begins to change, and N_L changes with the number of valid slots (sum of numbers of actual slots and notches). Thus, the cogging torque can be determined.

$$\begin{aligned} G_{nN_L} &= \frac{N_s}{\pi} \left\{ \int_{\frac{\pi}{N_p}}^{\frac{\pi}{N_p} + \frac{c}{2}} \cos nN_L\theta d\theta + \int_{\frac{\pi}{N_p} + \frac{c}{2}}^{\frac{\pi}{N_p} + \frac{a}{2}} \cos nN_L\theta d\theta + \int_{\frac{\pi}{N_p} + \frac{a}{2}}^{\frac{\pi}{N_p} + \frac{b}{2}} \cos nN_L\theta d\theta \right\} \\ &= \frac{N_s}{\pi n N_L} \left\{ \left[\sin nN_L\theta \right]_{\frac{\pi}{N_p}}^{\frac{\pi}{N_p} + \frac{c}{2}} + \left[\sin nN_L\theta \right]_{\frac{\pi}{N_p} + \frac{c}{2}}^{\frac{\pi}{N_p} + \frac{a}{2}} + \left[\sin nN_L\theta \right]_{\frac{\pi}{N_p} + \frac{a}{2}}^{\frac{\pi}{N_p} + \frac{b}{2}} \right\} \\ &= \frac{2N_s}{\pi n N_L} \left[(-1)^{\frac{nN_L}{N_p}} \left\{ \sin nN_L \left(\frac{a}{2} \right) - \sin nN_L \left(\frac{b+c}{2} \right) + \sin nN_L \left(\frac{-b+c}{2} \right) \right\} \right] \end{aligned} \quad (4)$$

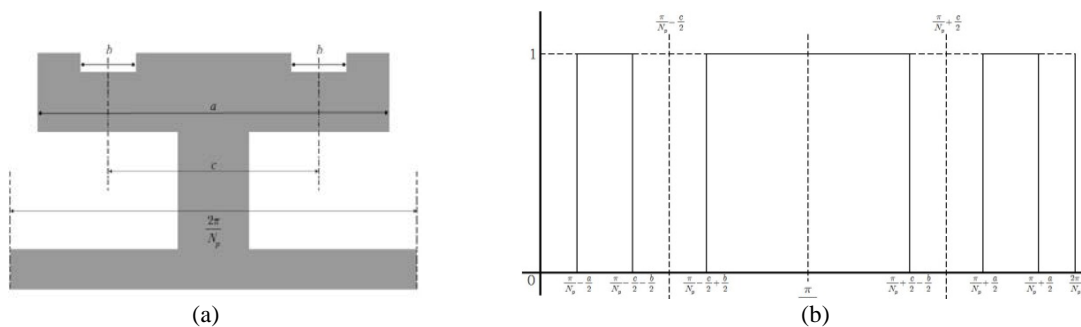


Fig. 2. Stator shape with two notches applied. (a) Stator shape (b) Relative permeance function.

Table 1
 Specifications of the single-phase BLDC motor

Parameter	Unit	Value
Input Voltage	[V _{ac}]	220
Rated Output	[W]	120
Rated Torque	[N·m]	0.38
Rated Speed	[rpm]	3000
Efficiency	[%]	70
Number of slot		8
Number of pole		8
Outer diameter	[mm]	80
Stack length	[mm]	30

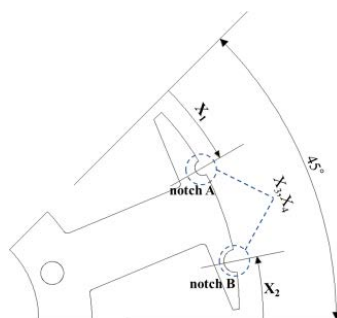


Fig. 3. Variable condition of the size and position angle for notches.

Also, more than two notches can be used if the stator shoe width has a sufficient gap. If the air-gap permeance function assumes that a part of the applied notch is 0, equation (4) can also be calculated through a Fourier series expansion based on the permeance function, as shown in Fig. 2 (a), such that the harmonics term of the air-gap permeance Fourier coefficient changes and the harmonics term increases due to the effect of the notch. In addition, the frequency of the harmonics increases and the size decreases, which eventually reduces the cogging torque.

3. Parametric analysis of the cogging torque using FEA

This paper presents the 120[W] class single-phase BLDC motor with an 8 pole/8 slot structure. Table 1 lists the specifications of the proposed single-phase BLDC motor. Fig. 3 shows the variable condition of the size and position angle for notches.

In the case of adopting notches for tapered-teeth, the application of an asymmetric notch size and position to the teeth is required as the dominant parameters from fig. 2 and equation (4) to reduce the cogging torque for a single-phase BLDC motor. We are adopted two notches because it is easy to predict trends of cogging torque variation according to asymmetric size and position angle of the notch. Parametric analysis was performed to determine the optimal size and position of the asymmetric notch to reduce the cogging torque using FEA. Figs. 4, 5 and 6 show the results of parametric analysis of the cogging torque according to the position angle of the each notch A and B variation at 0.5[mm], 1.0[mm], and 1.5[mm], respectively. The cogging torque was lowest at (39.06[mNm]) when the position angle of notches A and B were 10[°] and 15[°], and size of notches A and B were 1.5[mm] and 1.0[mm], respectively.

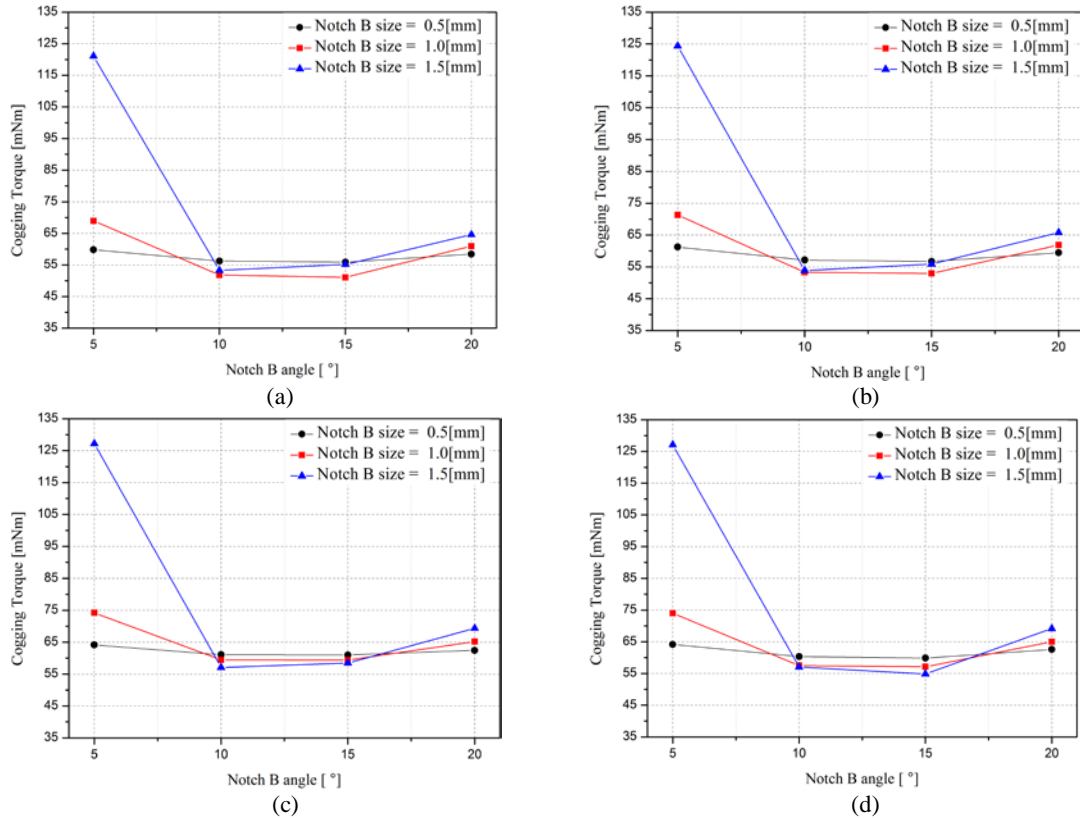


Fig. 4. Parametric analysis results of the cogging torque by variable notch B. (a) Position angle of notch A is 5[°] (b) Position angle of notch A is 10[°] (c) Position angle of notch A is 15[°] (d) Position angle of notch A is 20[°] at 0.5 [mm] notch A size

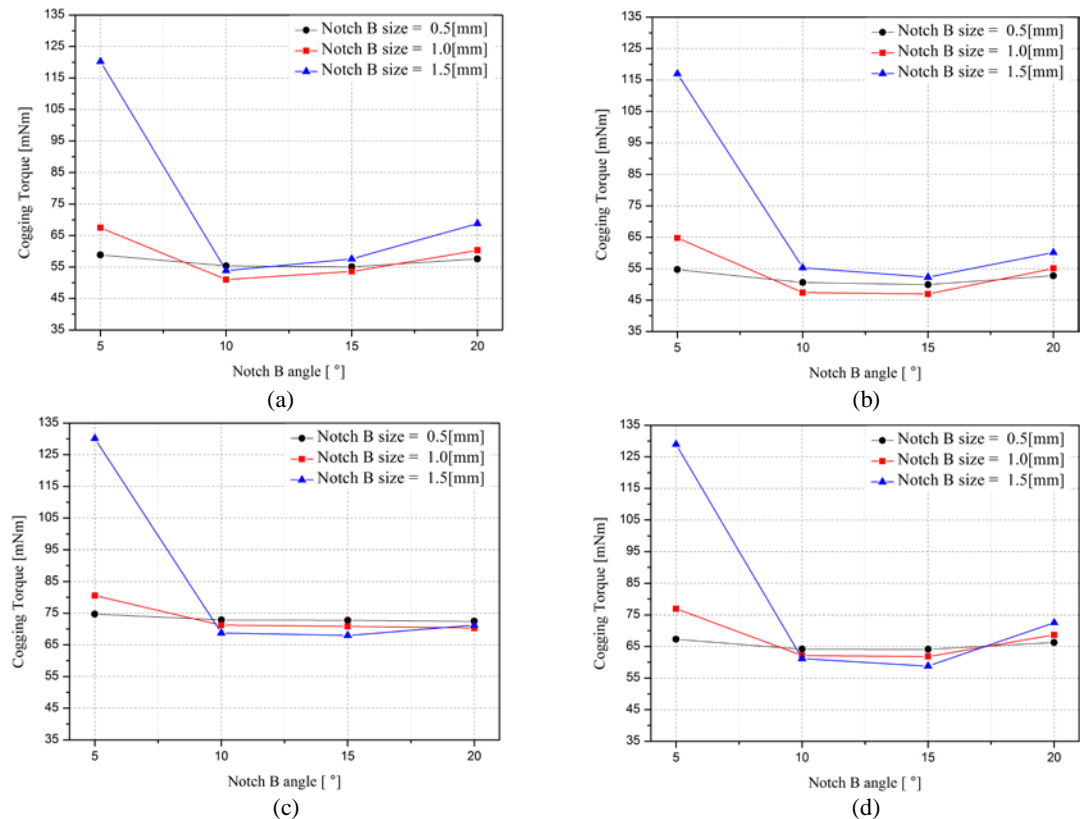


Fig. 5. Parametric analysis results of the cogging torque by variable notch B. (a) Position angle of notch A is 5[°] (b) Position angle of notch A is 10[°] (c) Position angle of notch A is 15[°] (d) Position angle of notch A is 20[°] at 1.0 [mm] notch A size

Fig. 7 shows the cogging torque calculated by FEA from the initial, previous and proposed model. The peak to peak cogging torque of the initial, previous and proposed model were 60.27[mNm], 46.88[mNm] and 39.06[mNm], respectively. The cogging torque reduction ratio of the proposed model was approximately 35.2[%] and 16.7[%], compared to the previous and initial model from FEA, respectively.

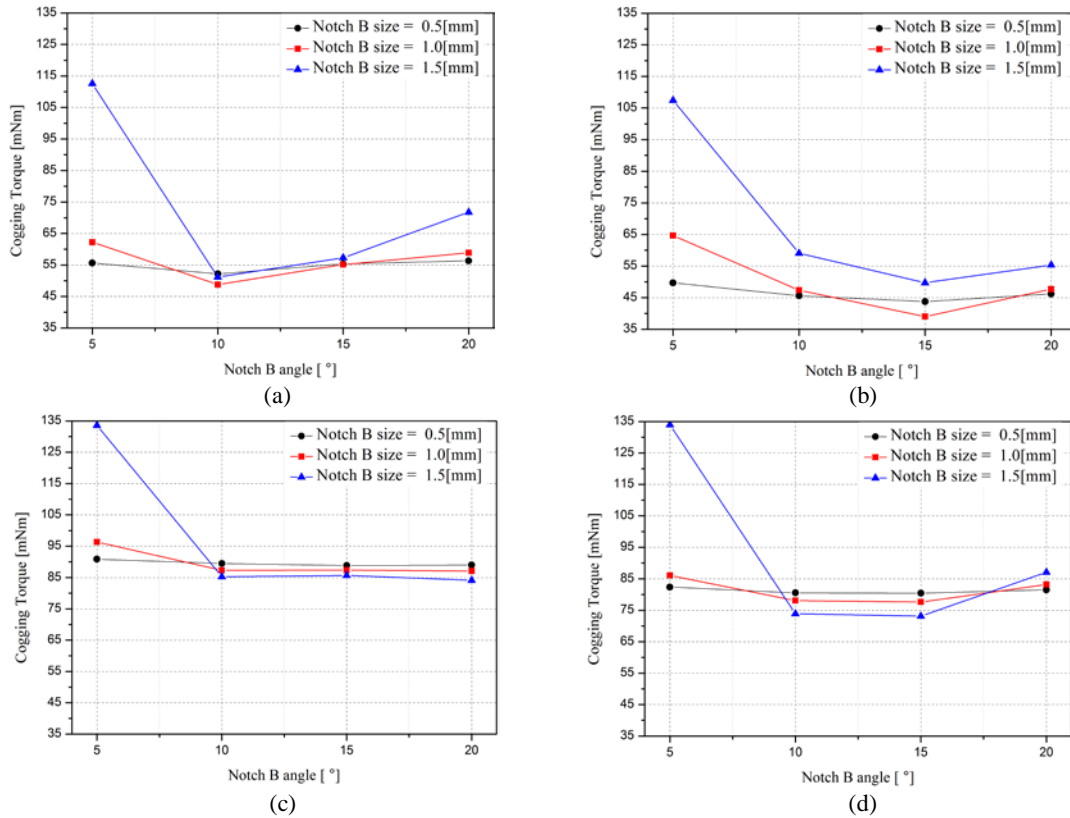


Fig. 6. Parametric analysis results of the cogging torque by variable notch B. (a) Position angle of notch A is 5[°] (b) Position angle of notch A is 10[°] (c) Position angle of notch A is 15[°] (d) Position angle of notch A is 20[°] at 1.5 [mm] notch A size

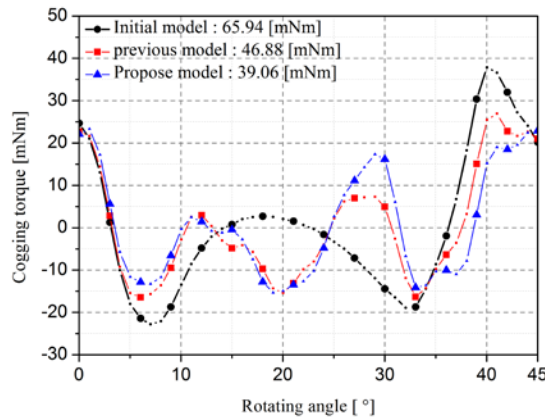


Fig. 7. Simulation results of the cogging torque

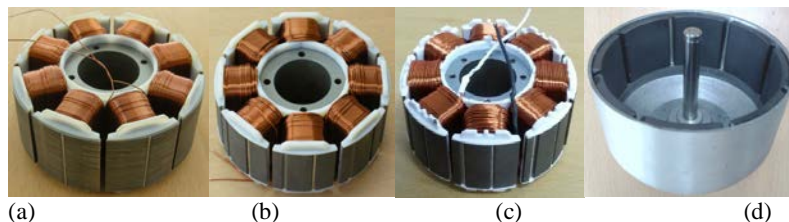


Fig. 8. Manufactured single-phase BLDC motor. (a) Stator of initial model (b) Stator of previous model (c) Stator of proposed model (d) Rotor

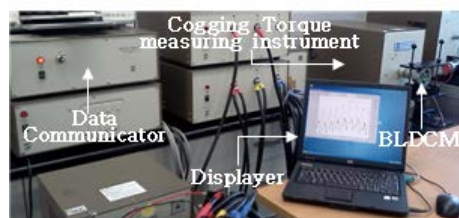


Fig. 9. Experimental composition for single-phase BLDC motor

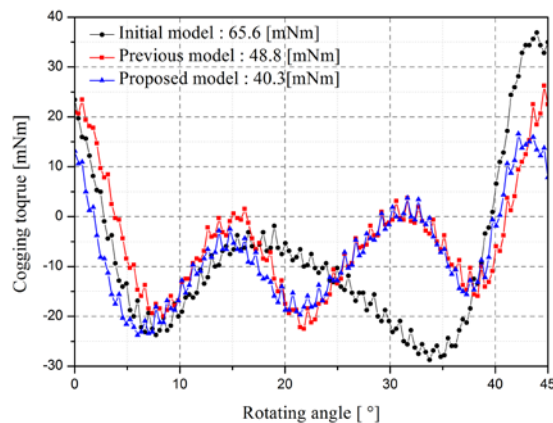


Fig. 10. Experimental results of the cogging torque

4. Experimental results

To verify the analysis and optimal design results, the initial, previous and proposed model were manufactured, as shown in fig. 8, and tested as a single-phase BLDC motor. Fig. 9 shows the experimental set-up for measuring the cogging torque. The cogging torque meter with a 0.001% RPM accuracy was made by SUGAWARA in Japan.

Fig. 10 shows the experimental results of the cogging torque. The peak to peak cogging torque of the initial, previous and proposed model were 65.6[mNm], 48.8[mNm] and 40.3[mNm], respectively. In the experimental results, the cogging torque reduction ratio of the proposed model was approximately 38.6[%] and 17.5[%] compared to the initial and previous model, respectively. Good agreement was observed between the analysis and experimental results.

5. Conclusion

This paper presented a improved cogging torque reduction method for single-phase BLDC motors with asymmetric air-gap. The improved method produced 38.6[%] and 17.5[%] decrease in cogging torque compared to that obtained using the initial and previous model, respectively. The FEA results were confirmed by the experimental cogging torque. This method is considered to be a good alternative for reducing the cogging torque of single-phase brushless motors.

References

- [1] C. Chiu, Y. Chen and W. Jhang, Properties of Cogging Torque, Starting Torque, and Electrical Circuits for the Single-Phase Brushless DC Motor, *IEEE Transactions on Magnetics*, **44** (2008), 2317-2323.
- [2] Mohammed Fazil and K. R. Rajagopal, A Novel Air-Gap Profile of Single-Phase Permanent-Magnet Brushless DC Motor for Starting Torque Improvement and Cogging Torque Reduction, *IEEE Transactions on Magnetics* **42** (2010), 3928-3932.
- [3] K. Bung-Il, Y. Byoung-Yull, P. Seung-Chan, and J. Young-Sun, Novel topology of unequal air gap in a single-phase Brushless DC motor, *IEEE Transactions on Magnetics*, **37** (2001), 3723-3726.
- [4] Weizi Wang, Zhigan Wu, Wanbing Jin and Jianping Ying, A Starting methods for hall-less single phase BLDC motor, *IECON conference of ieee*, **31** (2005), 1605-1609.
- [5] S. Ahmed, P. Lefley, Study of the impact of asymmetrical stator pole arcon the cogging torque for single phase Permanent Magnet BLDC Motor, *EPECS'09*, 1-4.
- [6] J. De La Ree and N. Boules, Torque Production in Permanent-Magnet Synchronous Motors, *IEEE Trans. Industry Application*, **24** (1989), 107-112.
- [7] Li Zhu, S. Z. Jiang, and Z. Q. Zhu, Analytical Methods for Minimizing Cogging Torque in Permanent-Magnet Machines, *IEEE Transactions on Magnetics*, **45** (2009), 2023-2031.
- [8] Yubo Yang, Xiuhe Wang, Changqing Zhu, Chuanzhen Huang, Study of magnet asymmetry for reduction of cogging torque in permanent magnet motors, *ICIEA 2009*, 2325-2328.
- [9] Bin Zhang, Xiuhe Wang, Ran Zhang, and Xiaolei Mou, Cogging Torque Reduction by Combining Teeth Notching and Rotor Magnets Skewing in PM BLDC with Concentrated Windings, *ICEMS 2008*, 3189-3192.
- [10] Young-Un Park, Ju-Hee Cho, Se-Hyun Rhyu and Dae-kyong Kim, A novel cogging torque reduction method for single-phase brushless DC motor, *Journal of Magnetics* (2013), 1-8.

Improvement of Torque Characteristics of Switched Reluctance Generator Using Arc Shaped Rotor Pole

Dawoon Choi¹, Byungkuk Kim² and Yunhyun Cho^{1,**}, *Member, IEEE*

¹ *Dept. of Electrical Engineering, Dong-A University 37, Nakdong-Daero, 550 Beon-Gil, Saha-Gu, Busan, Korea*

² *352-6 Junkdongdong Kangseogu, Busan, Korea, VGM co., Ltd*

Abstract. Recently, the switched reluctance generator (SRG) is emerging to complement the shortcomings of PM machine in renewable energy applications because of its advantages. However, the SRG have fundamental disadvantages such as vibration and noise due to the pulse-driven operation and the reluctance torque variation. This paper is focused on overcoming the disadvantages of the SRG; the rotor geometry is proposed to reduce the torque pulsation and it is designed considering the variation of inductance when the SRG is operated in a generating mode. As a result, it is available to reduce the effect of the torque ripple and vibration. In order to verify the effectiveness, the analysis result of SRG with the proposed rotor structure is compared with a conventional rotor structure under the same specifications and stator dimension. Each model is built as prototypes and the experimental verification is conducted as a result.

Keywords: Switched Reluctance Generator (SRG), Torque ripple, Pole shape

1. Introduction

The switched reluctance machine has major advantages such as low cost, fault tolerance, reliability, wide speed range at constant power, and applicability in many applications [1-3]. However, the SRG have fundamental problems of vibration and noise due to the pulse shaped excitation current waveform. Particularly in wind power generation systems, the generated electromagnetic torque of SRG passes to the shaft of turbine which is one source of mechanical stress of system. And it effects on the life of the turbine [4]. Therefore, the minimization method of torque pulsation, vibration and noise should be studied to apply the SRG in the wind power generation system.

In this paper, the rotor geometry is proposed to improve the torque characteristics of the SRG. The proposed rotor has the arc shape at the end of the pole. The torque ripple is reduced by redesign inductance variation in generating mode of the SRG. To predict the torque characteristics of the SRG, the flux linkage is calculated by FEM analysis, and the excitation current, output current, and inductance variation are considered to obtain the torque curve. According to the rotor geometry, the inductance variation is estimated. As a result, the SRG performance such as the output torque, ripple, and efficiency are compared for each model which has different rotor pole dimension, and the most appropriate rotor geometry is selected. The characteristic of the SRG is analyzed by simulation considering the switching on-off angle and nonlinear magnetic characteristic. In order to verify the effectiveness, the analysis results of SRG with proposed rotor structure is compared with general rotor structure under the same specifications and dimensions of stator. Also, the 1kW class SRG was manufactured with a different rotor. Through the performance testing, the analysis process and results are verified.

** Corresponding author: Y. H. Cho (e-mail:yhcho@dau.ac.kr) Dong-A University, Busan, Korea

2. Nonlinear model of SRG

SRG have fundamental problems of the vibration and noise due to the geometric magnetic pole shape structure and the pulse-driven operation. In particular, the generated torque pulsation of SRG is a main source of mechanical stress of its system. And it effects on the life of its application system. Therefore, to minimize the pulsation torque of SRG, a nonlinear SRG model must be built based on the electromagnetic field finite element (FEM) analysis. This paper is studied to improve the pulsation torque characteristics of SRG considering the rotor pole shape.

2.1 Operating principle of SRG system

SRG system is composed by switched reluctance machine, power converter, and position sensor and so on. Fig.1 shows the assembly construction of the SRG. It consists of 12 stator poles and 16 rotor poles. The rated output power and the output voltage are 1kW, 370V at rated speed of 300rpm. The outer diameter of stator and rotor is 342mm and 275, respectively. And the air-gap length is 0.5mm which is designed by considered manufacturing. The details of SRG specifications are shown in Table I.

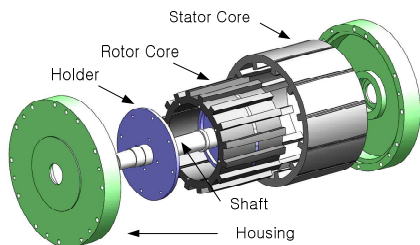


Fig. 1. The assembly construction of SRG structure

Table I
 Design Specifications of SRG

Items	Unit	Values
Rated Power	kW	1
Rated Speed	Rpm	300
Output Voltage	V	370
No. of Phase		3
No. of Stator Poles		12
No. of Rotor Poles		16
Stator Diameter	mm	345
Rotor Diameter	mm	275

The topology of its power converter is three phase asymmetric half bridge. The rotor position information of SRG can be obtained by a position sensor. The controller can create certain control signals according to the angle of the rotor position. The controls signal can drive the switches in power converter to implement excitation and electrical power generation. Fig.2. represents the operation mode of half bridge converter with two switches (SW_1 , SW_2) and two diodes (D_1 , D_2) in one phase. When both SW_1 and SW_2 are turned on, the winding of SRG is excited as shown in Fig.2 (b).

SRG system absorbs energy from the mechanical input power and exciting source during the excitation region ($\theta_{on} - \theta_{off}$) of Fig. 2(a). When both SW_1 and SW_2 are turned off, the winding current releases the excited energy through D_1 and D_2 as shown in Fig. 2(c). Its system offers electric energy to externals loads during the generation region ($\theta_{off} - \theta_q$) of Fig. 2(a).

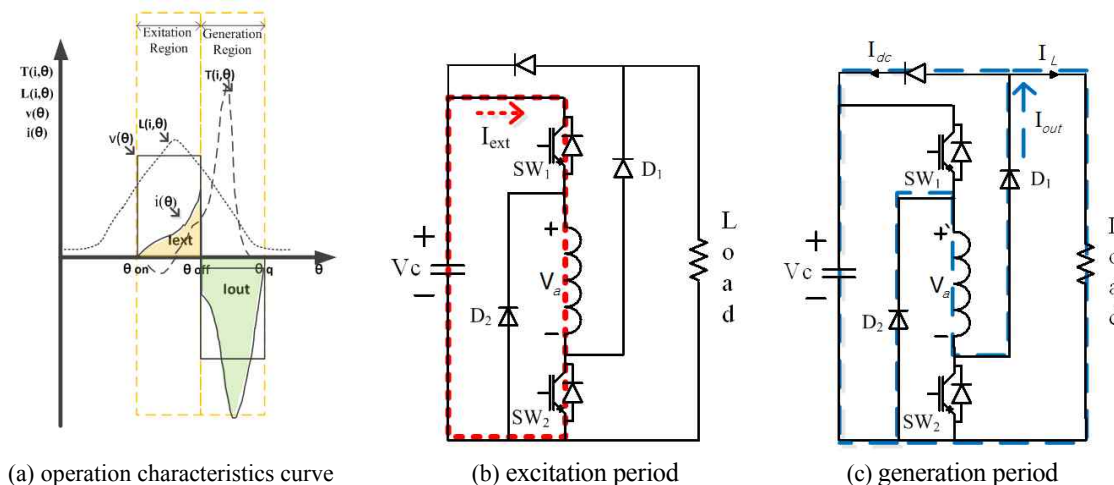


Fig. 2 Operation mode of SRG system

2.2 Nonlinear mathematical model

To analyze the dynamic characteristic of SR machine considering the external control circuit, lots of time and complex modeling is need. This paper introduced the dynamic simulation method of SRM system using nonlinear inductance profile curves of SRG which is computed by FEM analysis.

The basic equation of SRG system can be described as equation (1) and (2) to obtain the dynamic mathematical model of SRG such as electromagnetic equation and flux linkage equation.

$$V_c = Ri_n + \frac{d\lambda(i_n, \theta)}{dt} \quad (1)$$

$$\lambda(i_n, \theta) = L(i_n, \theta) \cdot i_n \quad (2)$$

Where, V_c is the terminal voltage of the winding, R is the phase resistance, i_n is the phase current, $\lambda(i_n, \theta)$ is the phase flux linkage, $L(i_n, \theta)$ is the phase inductance, and θ is the position angle of the rotor.

$$P_e(i_n, \theta) = \left(\frac{1}{2} \sum_{n=1}^m \frac{dL(i_n, \theta)}{d\theta} i_n^2 \right) \omega \quad (3)$$

Where, m is the number of phases, the electromechanical power in SRG is the sum of the individual power developed at each stage. The inductance $L(i_n, \theta)$ is computed by FEM analysis and given to look-up tables in MATLAB/Simulink. Thus, its value of equation (3) can be expressed as the instantaneous torque $T_e(i_n, \theta)$ to investigate the torque pulsation characteristic according to the rotor pole shape structure. The dynamic electromechanical torque of SRG may be calculated using the following current equation:

$$i_n(\theta) = \frac{1}{R} (v(\theta) - \frac{\lambda_n(i, \theta) - \lambda_{n-1}(i, \theta)}{dt}) \quad (4)$$

After calculating the phase current given as equation (4), the instantaneous torque is estimated using the inductance profile by FEM analysis according to the rotor position and the phase current.

As shown in Fig. 2, the SRG is capable of operating continuously as a generator by keeping the dwell angle so that the bulk of the winding conduction period comes after the aligned position, when $dL_n(\theta, i) / d\theta < 0$. And, the equation of the mechanical model is given by

$$T_{ext} + T_e = J \frac{d\omega}{dt} + B\omega \quad (5)$$

Where, T_e is the electromagnetic torque, T_{ext} is the external torque, J is the inertia, B is the viscose coefficient, and ω is the angular speed.

Fig.3 shows the simulation block diagram of the nonlinear mathematic model which is coupled with the electromagnetic and the mechanical equation of SRG. The developed simulation program is used to estimate the torque pulsation characteristics of SRG according to the rotor pole shape structure at the generating operation.

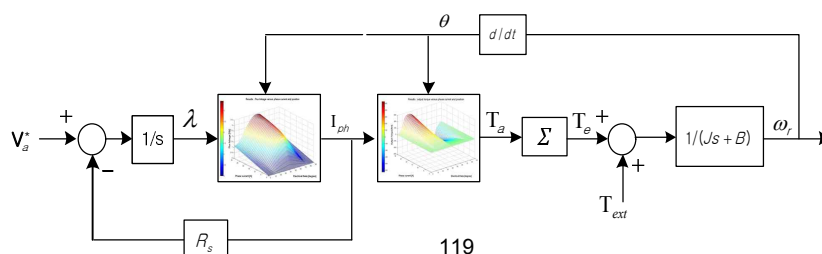


Fig. 3. The simulation block diagram of SRG

3. Simulation results

This paper is studied to improve the pulsation torque of SRG with the convenient rotor pole shape structure. Fig. 4(a) shows the cross section configuration of SRG to design the optimal rotor pole shape structure. The design parameter is the arc shape of rotor pole and the dimension of pole arc is defined as the circle which has two points. The center of circle is defined by the distance, r , which is from the edge of the rotor pole to center of axis. Fig. 4(b) and (c) shows the prototype of the rotor with the conventional pole and the arc shaped pole, respectively. The rotor of Fig.4(c) with the arc pole shape rotor is made after estimating the torque ripple computing by FEM analysis.

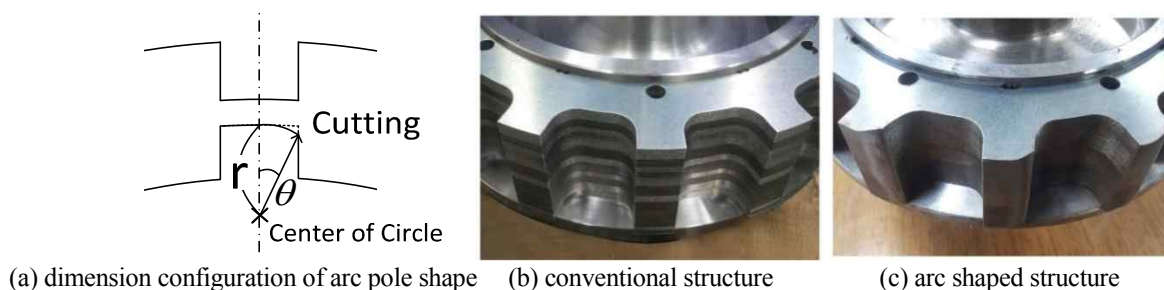


Fig.4. Rotor pole structures of SRG

Fig. 5 shows the inductance profile of SRG about the conventional and the arc pole shaped rotor structure as a function of mechanical angle. In an aligned position, the arc shaped rotor pole structure has lower inductance value than the conventional structure, but, it does not affect the output characteristic because of belonging to the excitation region of SRG. In case of the arc shaped rotor pole structure, because of having larger the variation of inductance than the conventional one as shown in Fig. 5(b), the output characteristic is better. And, the arc shaped rotor pole structure having a lower radius value at unaligned angle position is a factor for increasing the output power.

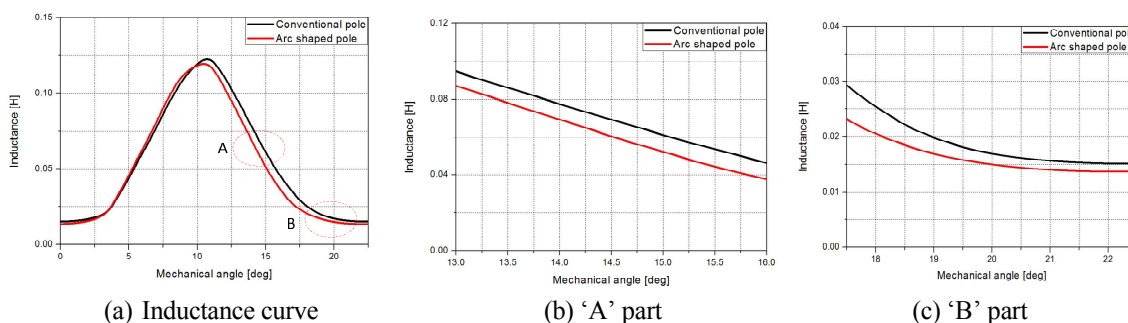


Fig. 5 Compared simulation results according to the rotor pole structure
 (Input voltage, phase current, and torque curve)

To select the proper arc angle of rotor pole tip, the torque ripple characteristics of each SRG model was compared under the same output condition. For comparing in the same output power, the load current, I_L , is set as the same condition value when the excitation current, I_{ex} , is lowest through adjusting the switching on-off angle.

At each model, the excitation current, I_{ex} , and the output current, I_{out} are calculated separately, in order to calculate load current, I_L . Because the output current is divided into the input current and load current, which are shown in Fig. 4(b) and (c). The excitation penalty is also calculated to compare the efficiency of each model, indirectly. The excitation penalty function is defined by the excitation current value and the output current as given in the equation (4) [3]. Table II shows the simulation results of the SRG with different rotor pole shapes. The average torque, torque ripple, and excitation penalty are indicated as a result.

$$\varepsilon = \frac{I_{ex}}{I_{ex} + I_L} \quad (6)$$

Table II
 Comparison results

ArcAngle [deg]	R [mm]	Tavg [Nm]	Tripple [%]	ε
0	0	39.82	135.68	0.394
13	40	39.85	102.14	0.354
18	30	38.89	83.35	0.341
26	20	42.81	121.13	0.452
47	10	48.82	150.53	0.563

In this paper, the torque characteristic is analyzed according to the rotor pole shape of the SRG. We set the arc angle as 18 degree by considering the torque ripple and the efficiency as shown in Table II. Fig. 6 shows the compared simulation results of SRG with the conventional structure (a), and the proposed structure (b). In case of the conventional model, the current is increased dramatically when the excitation switch is off. And the peak value of torque is too large to generate the rated power. In the proposed model, the inductance variation is more larger than the conventional model as shown in Fig 5(b). Thus, the peak value of torque is reduced from 61Nm to 49.5Nm at the same output condition. In addition, the inductance variation is lower at the unaligned position than conventional model as shown in Fig. 5(c), which can improve the output power. For these reasons, the torque ripple is reduced from 135.68% to 83.35%.

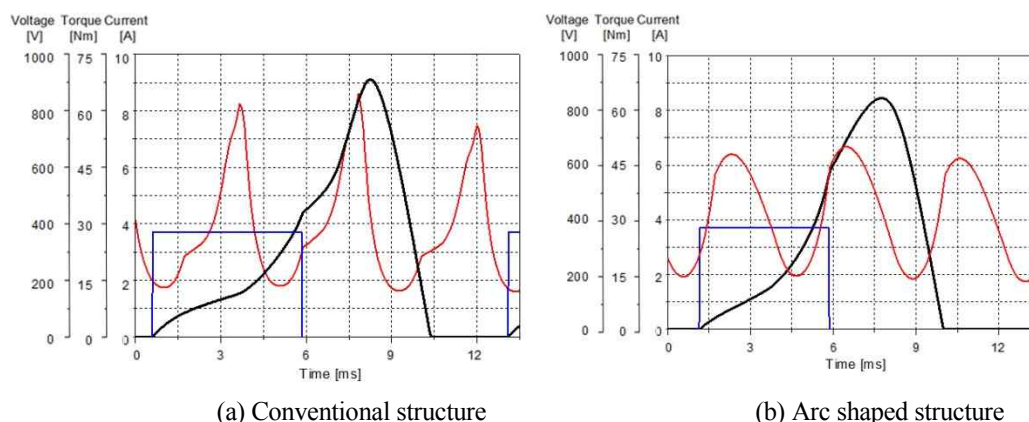


Fig. 6 Compared simulation results according to the rotor pole structure
 (Input voltage, phase current, and torque curve)

Fig. 7 shows a prototype SRG and experiment devices for performance and acceleration measurement to verify the simulation results. The SRG is connected with a geared type induction motor to receive the mechanical input power. The SRG is controlled by its driver which has the output voltage and the output power control algorithm. The acceleration sensor is set on the SRG and the DAQ system is installed to measure the vibration. The environment of experiment is set on the same condition with simulation.

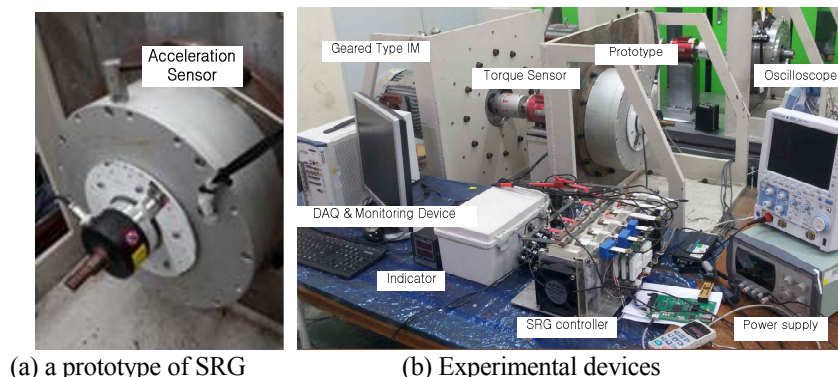


Fig. 7 Performance and acceleration measurement

Fig. 8 shows the experimental results including the output voltage, the phase current, acceleration measurement, and FFT analysis of acceleration measurement according to a rotor pole shape, respectively. For the comparative analysis of each model, the output voltage control is applied at the same shaft speed and the same load conditions. By measuring the acceleration of SRG, the improvement of torque ripple is identified, indirectly. The acceleration measurement is transformed to frequency domain using the FFT. At 240Hz which is fundamental frequency of prototype, vibration reduction effect is obtained more than 40%.

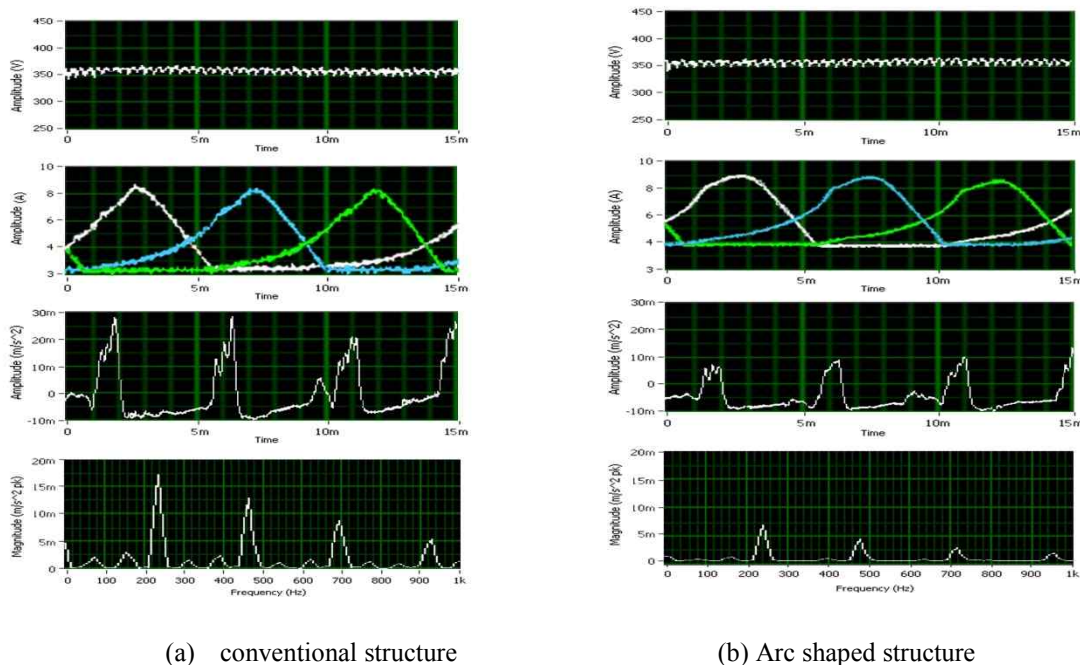


Fig. 8 Performance and acceleration measurement of SRG according to rotor structure

4. Conclusion

This paper proposes the arc shaped rotor pole structure of the SRG to improve torque characteristics and reduce the vibration. The proposed model is compared with the base model, 2% output improvement and 38% torque ripple reduction are obtained as a result. The SRG torque characteristic is predicted through the simulation modeling. And the acceleration measurement is performed to identify the improvement of torque characteristics, indirectly. At the rated speed, the vibration reduction effect is obtained more than 60%.

Acknowledgements

We acknowledge the support of the Ministry of Knowledge Economy(MKE), Korea Institute for Advancement of Technology(KIAT), Human Resources Development of the Korea Institute of Energy Technology Evaluation and Planning (KETEP). We also thank the Ministry of Knowledge Economy, Republic of Korea(No. 20114010203060) for grant fund during the development of this project.

References

- [1] B. Loop. and S. Sudhoff, "Switched reluctance machine model using inverse inductance characterization," *IEEE Trans. Ind. Appl.*, vol. 39, pp 743-752, June. 2003.
- [2] B. Fahimi, A.R.B. Emadi, Jr. Sepe, "A Switched Reluctance Machine Based Starter/Alternator for more Electric Cars", *IEEE Trans. Energy. Conv.*, vol. 19, pp. 116-124, 2004.
- [3] T. J. E. Miller, "Switched Reluctance Motors and their Control." Magna Physics Publishing, Oxford, 1993
- [4] Y.Y. Xia, J. E. Flecher, S. J. Finney, K. H. Ahmed and B. W. Williams, "Torque ripple analysis and reduction for wind energy conversion systems using uncontrolled rectifier and boost converter" *IET Renew. Power Generation.*, vol.5, Iss. 5, pp. 377-386, 2011.

Optimization of Axial Air Gap Single Phase Permanent Magnet Stepper Motor with Claw Poles

Jibin Zou^{a,*}, Jiming Zou^a, Yongxiang Xu^a, wei Li^a, Wei Yanyu^a

^a *Department of Electrical Engineering, Harbin Institute of Technology, Harbin, 150001, P.R.China*

Abstract. A new kind of single-phase stepper motor with axial air gap and claw poles is presented in this paper. The FLUX software for 3-dimensional FEM is used to solve the performance of the motor. The cogging torque and the torque-angle properties are computed numerically. The factors influencing the motor performance are analyzed and the design of the motor is optimized. Experimental results of the prototype motor agree with that of the computation. The computation and experiment analysis indicate that the motor with bevel poles has self-starting ability. To get a good performance, the motor should be designed properly.

Keywords: Stepper motor, single phase, claw pole, permanent magnet, numerical computation.

1. Introduction

The single phase stepper motor has a series of advantages as it is simple in structure, convenient to control and easy to miniaturize. The displacement of the motor is in direct proportion to the number of input signal pulses. Therefore, it can be directly used in open loop control systems which are simple and cheap. For these advantages, single phase stepper motors are often applied in instruments and watch equipments. This paper presents a new kind of single phase stepper motor with claw poles and axial air gap. The structure and working principle are introduced. The Flux software for 3-dimensional FEM is adopted to compute and analyze torque-angle properties. The influence of the pole arc ratio, the bevel angle of poles and the thickness of the magnet are studied based on the motor performance analysis. The results of the experiments agree with those of computations.

2. Structure and principle of the single phase stepper motor with claw poles

Most single phase stepper motors have radial air gap. While the motor presented has an axial air gap. The structure is shown in Fig. 1. The stator is composed of two parts, the inner teeth and outer teeth. They are combined in alternation to form the claw structure. The inner teeth and the outer teeth are connected together by the yoke. The concentric annular winding is fixed in the space formed by the teeth of the stator. The flux passes through the pole of stator, the pole of rotor and the yoke to form a closed loop. The material of the stator pole is soft iron. The rotor poles are NdFeB permanent magnets. The frame and stator are designed together which makes the motor structure simple. Because the magnets are thin flat segments, the film permanent magnet material can be adopted.

For multiple phases stepper motors, the phase windings are excited alternatively to produce a moving magnetic field which makes the rotor rotating. When one phase is excited, the rotor will rotate to a balance position. When

*Corresponding author. Tel.: +0086-451-86413613; fax: +0086-451-86413613; e-mail: zoujibin@hit.edu.cn.

another phase is excited the balance position will change and the rotor will rotate to the new position. While the single phase stepper motor has only one phase, and the number of the stator teeth is equal to the pole number of the rotor. When there is no current flow in the phase winding, the rotor is in the balance position of cogging torque.

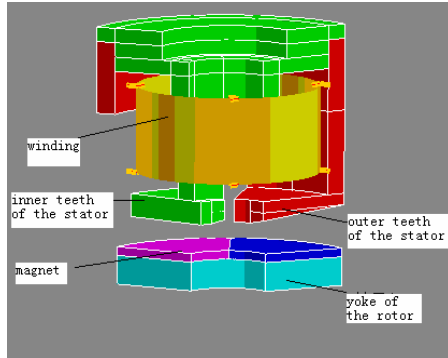


Fig.1. The structure of single phase stepper motor with claw poles

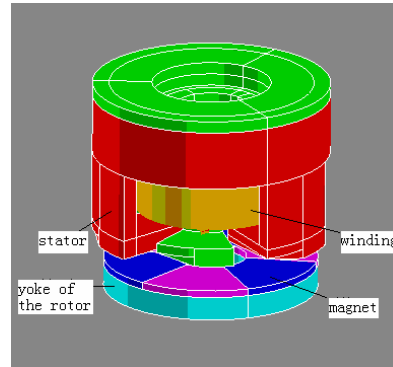


Fig.2. The Flux model of the single stepper motor with claw poles

If the teeth and the magnetic circuit are in symmetry, the balance position of the electromagnetic torque produced by the phase winding current will be the same as that of the cogging torque, and the rotor can not be driven by the current. Therefore balance position of the cogging torque should be changed by a special design. There are generally two methods to shift the balance position of the cogging torque which ensures the self-starting ability of the motor and fixed rotating direction. The first is to make the main magnetic circuit asymmetric, and the second is to use auxiliary poles. The first method is simple. In the presented single phase stepper motor with claw poles, a bevel is formed at each pole by razing out an angle from one side of the stator pole which makes the magnetic circuit asymmetric. This gives the rotor an initial phase shift. When a single pulse signal is applied to the winding, the rotor will rotate a step. When continuous plus-minus pulse signals are applied on the motor, it will run continuously. As the self-starting ability and loading capacity of the motor is related to the initial rotor position, the phase shift of the reluctant torque will have direct influence on the performance of the motor.

3. Dimensional computation of the motor

A FEM tool named FLUX is adopted in the 3-dimension computation of the motor. The FEM model of the motor is shown in Fig.2.

The parameters of the motor are as follow:

The diameter of the stator is 10mm; The axial length of the motor is 9mm; The number of magnetic pole pairs is 3; The step angle is 60 degrees.

The pole arc ratio, the bevel angle of poles, the thickness of magnet as well as the current in the winding are the main parameters that influence the performance of the motor. Therefore, these parameters are adjusted in the computation. Based on the numerical computations the design of the motor is optimized.

4. Computation results and analysis

The performance of the single phase stepper motor can be described by the torque-angle properties. The computation results of torque-angle properties for different currents are shown in Fig.3.

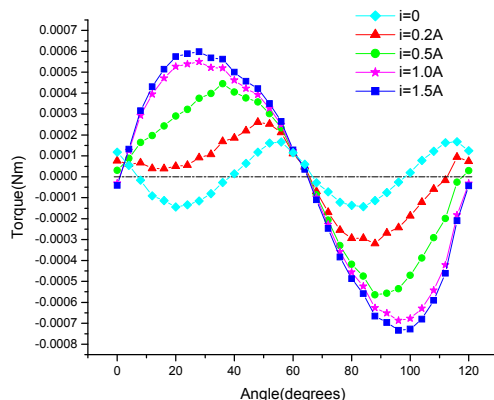


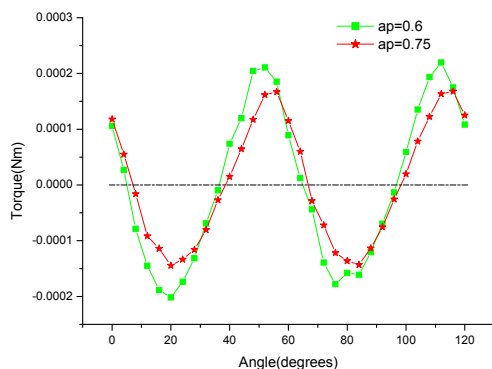
Fig.3. The torque-angle properties for different currents

From Fig.3, it can be seen that the frequency of the cogging torque is two times of torque-angle frequency. Because of the effect of the bevel angle of poles, the balance position of the cogging torque shifts by an angle. The cogging torque and the bevel angle of poles introduce a second harmonic in the torque-angle curve, which leads to distortion. The self-starting ability of the motor is determined by the torque in the initial rotor position. When the winding current is small (take 0.2A for example), the self-starting ability of the motor is weak. It will improve with the increase of the winding current. The existence of the second harmonic decreases the self-starting ability and its influence on the torque-angle properties will become weaker as the winding current increases. Because of saturation of the magnetic circuit, the increase of torque will be lower when the winding current increases above certain value.

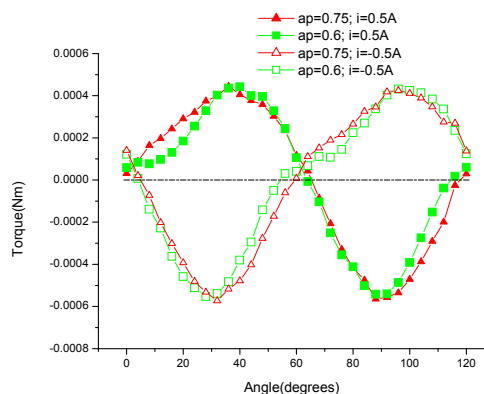
The influence of the pole arc ratio, the bevel angle of poles, the magnet thickness on the cogging torque and torque-angle properties can be analyzed by numerical computation.

4.1. The influence of pole arc ratio

The pole arc ratio will influence the magnetic field distribution and the motor performance. If the pole arc ratio is too big, the flux leakage will increase, while if it is too small, the inner part of the teeth of the motor will become over saturated. Both of these effects will reduce the main flux and influence the motor performance. Fig.4 shows the cogging torque property and the torque-angle properties when the bevel angle of poles is 12° , the thickness of magnet is 0.3mm, while pole arc ratio are 0.6 and 0.75.



(a) The cogging torque



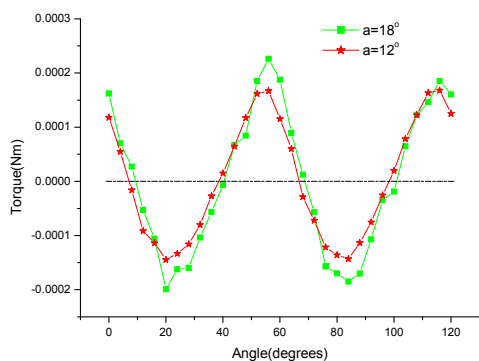
(b) The torque-angle curve

Fig.4. The torque properties when the pole arc ratio are 6 and 0.75

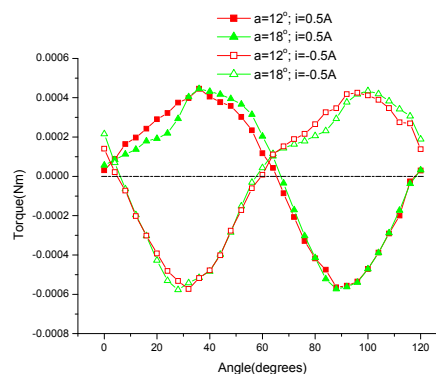
Comparatively, when the pole arc ratio is 0.75, the phase shift of the cogging torque is bigger. The increase of the phase shift favors self-starting ability and loading capacity of the motor. Fig. 4 (b) shows that the second harmonic in the torque-angle curve is smaller when the pole arc ratio is 0.75 than it is at the value of 0.6, which contributes to a strong self-starting ability. Computation results indicate that the reasonable pole arc modulus is 0.75.

4.2. The influence of bevel angle of poles

The phase shift of balance position of cogging torque makes it possible for the single phase stepper motor to achieve a self-starting ability. The single phase stepper motor with claw poles shifts its balance position of cogging torque by the bevel angle of poles. The bevel angle of poles is described as follow: from the centerline of the stator poles the surface of the poles on one side is inclined to increase the air gap and form a bevel. The bevel angle of poles will affect the phase shift of cogging torque. Fig. 5 (a), (b) show the cogging torque and the torque-angle properties when the pole arc angle is 45° , the thickness of magnet is 0.3mm, while the bevel angle of poles are 12° and 18° .



(a) The cogging torque



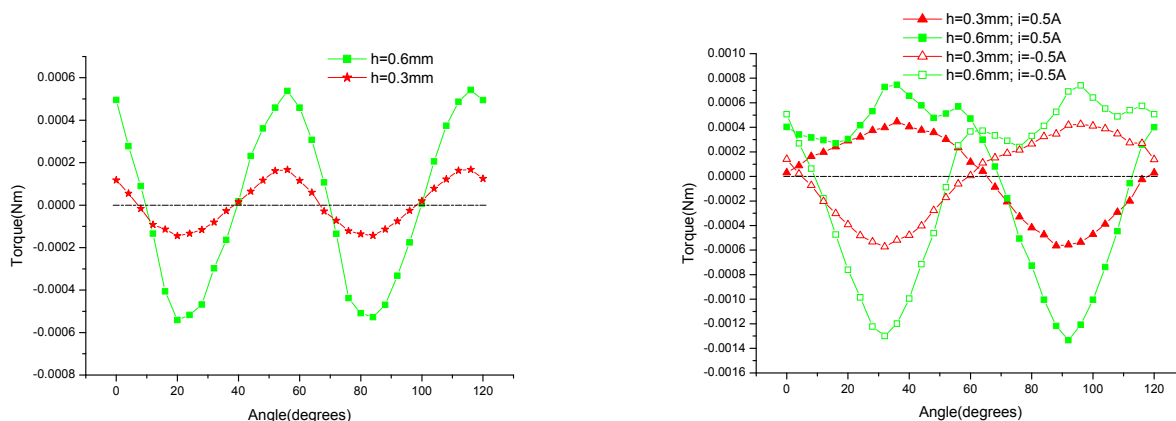
(b) The torque-angle curve

Fig.5. The torque properties when the bevel of magnet are 12° and 18°

From Fig. 5(a), it can be seen that when the bevel angle of poles is 18° , the phase shift of cogging torque is bigger than it is at an angle of 12° . It may seem to be an effective way to promote self-starting ability of the motor by increasing the bevel angle of poles. However the bevel angle of poles also affects the torque-angle properties (Figure 5(b)). Because of the variable air gap, the increase of the bevel angle of poles may influence the torque-angle property. For the designed motor, the reasonable bevel angle of poles is 12° .

4.3. The influence of the thickness of magnet

The thickness of magnet is another important parameter which affects both the cogging torque and the torque-angle properties. The phase shift of the initial position determines the starting ability. The thickness of magnet directly influences the value and phase shift of cogging torque as well as torque-angle properties. Fig.6 shows the cogging torque and torque-angle curves when the thickness of magnet are 0.3mm and 0.6mm.,while the pole arc angle is 45° , the bevel angle of poles is 12° .



(a) The cogging torque

(b) The torque-angle curve

Fig. 6. The torque properties when the thickness of magnet is 6 and 0.75

It can be seen in the figure above that by increasing the thickness of magnet, the amplitude of cogging torque and torque will increase, as well as the phase shift of cogging torque. Because a bigger cogging torque requires a higher current to drive the motor, if the magnet is too thick, it will decrease the starting and loading capacity of the motor. The computation shows that the reasonable thickness of magnet is 0.3 mm for the designed motor.

5. Experiment

A prototype motor is designed and manufactured with the reasonable parameters from computations. The measured torque-angle properties are given in Fig.7. The computation and experiment results are in agreement with each other.

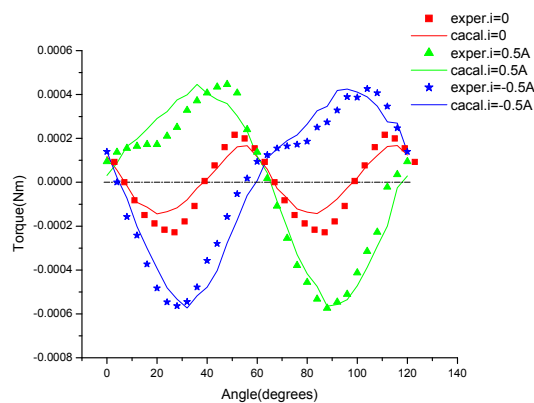


Fig. 7. Comparison between Flux computation result and experiment result

6. Conclusion

The following conclusions can be drawn from the analysis presented in this paper:

- (1) the single phase stepper motor with claw poles can shift the balance position of cogging torque through the bevel angle of poles, which enables the motor to startup and rotate continuously.
- (2) the key point of optimization of the motor is to adjust the phase and amplitude value relationship between the cogging torque and torque-angle curve. Although the cogging torque is necessary for starting the motor, it will cause harmonic in the torque-angle curve, which will decrease the loading ability of the motor. It will be a benefit to get a big torque in the cogging torque balance position.
- (3) The bevel angle of poles and the thickness of the magnet have an obvious influence on the motor performance. The bevel angle of poles affects the balance position of the cogging torque directly. The thickness of magnet has little influence on the balance position of the cogging torque, while it has an obvious influence on the amplitude of the cogging torque. The magnet should not be too thick.

7. Acknowledges

This work was supported by the National Key Basic Research Program of China (973 Program) under Grant 2013CB035605.

References

- [1] Demerdash N A, Nehl T W, Fouad F A, et al. Three dimensional finite element vector potential formulation of manetic fields in electrical apparatus[J]. IEEE Transactions on Power Apparatus and Systems, 1981, 100(10) : 4104-4111.
- [2] Ramesohl I, Henneberger G, Kuppers, et al. Three dimensional calculation of magnetic forces and displacements of a claw-pole generator[J]. IEEE Transactions on Magnetics, 1996, 32(3) : 1685-1688.
- [3] P. Meneroud, M. Azeau, F. Bloch, F. Claeysen. Impact of miniaturization technologies on the structure and performances of micro motor for watches applications[J], Proc. ACTUATOR 2002, pp. 459-465.
- [4] P. Meneroud, et al. Single phase stepper motor using permanent magnet in thick films[J], Presented at PAMM 2005.
- [5] Demerdash N A, Nehl T W, Fouad F A, et al. Finite element formulation and analysis of three dimensional magnetic field problems[J]. IEEE Transactions on Magnetics, 1980, 16(2) : 1092-1094.

The Analytical Evaluation of High Speed and High Efficiency Induction Motor for Spindle

Do-Kwan HONG, Jae-Hak CHOI, Dong-Jun KIM, Yon-Do CHUN,
Byung-Chul WOO, Dae-Hyun KOO

Korea Electrotechnology Research Institute, Changwon, 641-120, South Korea
E-mail: dkhong@keri.re.kr, Tel.: +82-55-280-1395, Fax: +82-55-280-1490

Abstract. This paper deals with the analysis techniques of a high speed and high efficiency induction motor for spindle. The several analysis techniques are introduced to develop a high speed and high efficiency induction motor made by copper die casting. The analysis techniques are composed of magnetic analysis considering losses, structural analysis of rotor and stator, critical speed of rotor, natural frequency analysis of stator. All performances of the prototype are successfully verified.

1 Introduction

The life of high speed induction motor is extended by the reduction of generated heat that has a rotor. The bearing of rotor could be damage from the heat of iron loss which is dominant in the various losses. The life of a copper die casting induction motor is extended by the reduction of generated heat that has a rotor that is smaller than that is found in aluminum die casting induction motors. A copper die casting induction motor can obtain an energy saving effect of about 2-3% compared to previous aluminum die casting induction motors [1]. In addition, copper die casting motors can reduce the size of motors and reduce material costs. In this paper, to develop a three-phase high speed and high efficiency induction motor, the focus is placed on several analysis techniques. At first step, the developed induction motor performance (torque, efficiency) is evaluated by magnetic analysis considering eddy current and core losses. At second step, structural stability of rotor is evaluated by centrifugal force. And structural stability of stator is checked by magnetic force. At third step, the critical speed analysis is performed for dynamic stability. At last step, natural frequency analysis of stator is performed. According to the stator and rotor slot numbers, and stator natural frequencies, forces can be responsible for high magnetic noise levels during starting and braking.



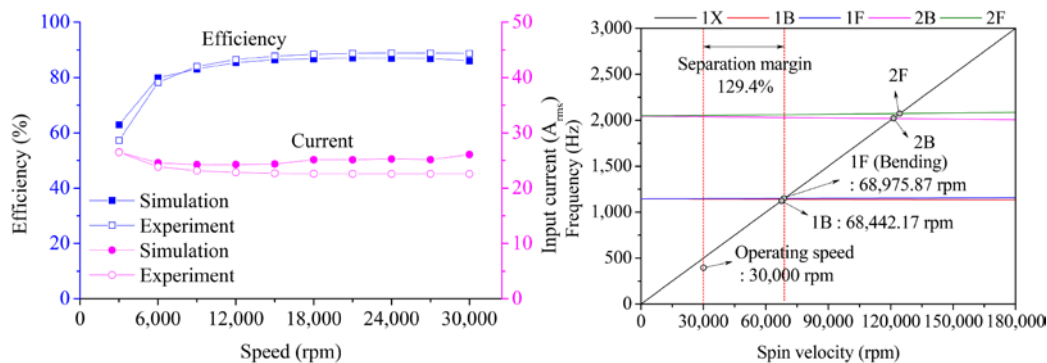
Figure 1: The configuration of prototype, high speed and high efficiency induction motor

Figure 1 shows the configuration of machining center and the copper die casting induction motor and the developed parts which is applied to the several techniques for a high speed spindle system.

2 The results of several analyses

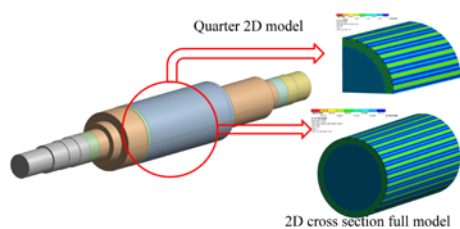
Figure 2(a) shows that the efficiency and current between the simulation and experiment is well matched with a maximum error of 6.5% and 13.4% respectively. The critical speed of the rotor considering rotation and gyroscopic effect should be above the operating speed, 30,000rpm, and have a sufficient separation margin, 129.4% as shown in Figure 2(b). Figure

2(c) shows the maximum equivalent stress distribution of rotor (36,000rpm, 170°C) by centrifugal force. Figure 2(d) shows natural frequency and mode shape of stator. More precisely, the stator elliptical mode is the most dangerous one in motor, so one should avoid this mode with high magnitude saturation vibrations during the whole starting phase. The noise of motor is caused by the relation of pole, slot, bar number [2]. Figure 2(e) shows the maximum equivalent stress distribution of stator (36,000rpm, 78.5°C) by magnetic force. Figure 2(f) shows the comparison experiment with design speed and a error with a 0.8% deviation. Figure 2(f) shows vibration velocity amplitude at motor casing supported by spindle bearing in vertical and horizontal directions (ISO 10816-3). The test results and the detailed results of several analyses will be dealt with in full paper.

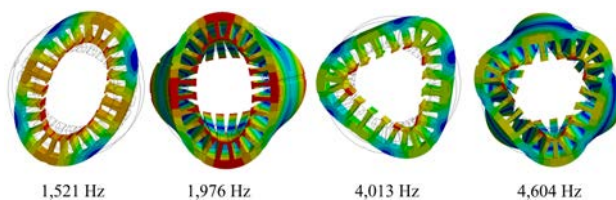


(a) The comparison of experiment with simulation

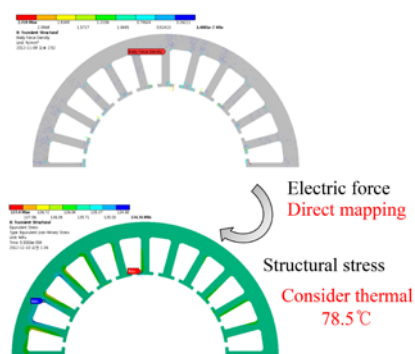
(b) Campbell diagram



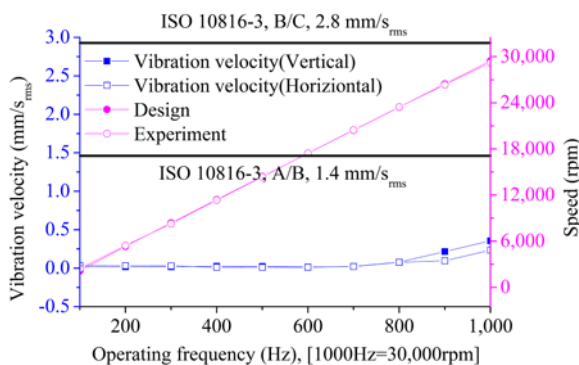
(c) Structural strength of rotor



(d) Natural frequency of stator



(e) Structural strength of stator



(f) The comparison of experiment with design (speed), vibration velocity of casing supported by spindle bearing (vertical and horizontal)

Figure 2: The results of test and several analyses

References

[1] Do-Kwan Hong, Jae-Hak Choi, Pil-Wan Han, Yon-Do Chun, Byung-Chul Woo, and Dae-Hyun Koo, "Analysis of High Speed Induction Motor for Spindle Made by Copper die Casting process," *International Journal of Precision Engineering and Manufacturing*, vol. 13, no.12, 2012, pp. 2251-2257

[2] J. L. Besnerais, V. Lanfranchi, M. Hecquet, G. Lemaire, E. Augis, and P. Brochet, "Characterization and Reduction of Magnetic Noise Due to Saturation in Induction Machines," *IEEE Trans. Magn.*, vol. 45, no. 4, 2009, pp. 2003-2008

Cogging Torque and Torque Ripple Reduction of IPMSM with Notched Rotor by FEM with Optimization Method

Ho youn KIM, Yong Bae KIM, Woo youl LEE and Pan Seok SHIN

Department of Electrical Engineering, Hongik University, Sejong City 339-701, Korea

Abstract. This paper presents a method to minimize torque ripple of V-type IPMSM using PSO (particle swarm optimization) method with FEM. The proposed algorithm includes one objective function and two design variables of the notch on the rotor surface. To verify the algorithm a 50kW IPMSM is simulated and optimized by PSO program.

1 Introduction and PSO Algorithm

An IPMSM (Interior permanent magnet synchronous motor) for electric vehicle is modeled to reduce cogging torque and torque ripple with a Optimization method with FEM. The Optimization PSO is The method has some advantages of the relative simplicity, fast convergence with less computing, and finding all local optimum points.[1] IPMSM is also mechanically stable and has a magnetic torque and reluctance torque by d,q inductance. However, the IPMSM produces significantly large cogging torque due to the same length of mechanical and effective magnetic air gaps. There are many efforts to reduce the torque ripple by various magnetic and mechanical design such as slot shape, magnet, air gap and core configuration. [2,3]

In this study, a Vtype IPMSM and Notch model as shown in Fig.1 is modeled to reduce the torque ripple introducing two notches in the one pole rotor surface. In the proposed algorithm, the position and size of the notch are optimized by PSO[4] and then the torque is calculated by the Transient Magnetics Module of FLUX2D with external circuit is used under the condition of phase current of $I_b = I_c = -I_a/2$ at 1/6 rpm. The simulation model has 8 poles, 48 slots, 1200 rpm and its peak torque is 400 Nm Simulation and Result The objective function (Eq.1) is the minimization of torque ripple of the motor, and 2 design variables are notch width, l_n and notch pitch (angles between notches), θ_N as in Fig.1.

$$\text{Minimize } F_{obj} = \sum_i \left(\frac{\tau_{i+1} - \tau_i}{\tau_i} \right)^2 \quad (1)$$

Where τ_{i+1} is torque ripple at (i+1)-th iteration and τ_i is average torque at i-th iteration for each position of 2 design variables. The constraints are the notch width, $2 \leq l_n \leq 4 [^\circ]$, $d_n = 0.5 \text{mm}$, and $8 \leq \theta_N \leq 23 [^\circ]$. After 4 iterations, the design variables are almost converged to about $l_n = 2.38 [^\circ]$, and $\theta_N = 14.75 [^\circ]$. The minimized cogging torque is about 3.19 Nm, which is reduced to 56% of the initial value (see Fig 2). Fig 2 shows the difference of the locked rotor torque ripples between the round and the notched surface as function of phase current. The minimum cogging torque and torque ripple is a reasonably good values, which means that the proposed PSO optimization algorithm with FEM has a good convergence and availability in BLDC motor design.

2 Summary

In the project, the optimization algorithm is proposed to minimize torque ripple of V-type IPMSM using PSO method with FEM. In the algorithm, the notch shape on the rotor surface of 50 kW IPMSM is optimally designed with 2 design parameters and several constraints for minimizing of the cogging torque and torque ripple. The simulation model of V-type IPMSM has 3-phases, 8-poles, 48 slots with 2 notches on the one pole rotor surface. The arc angle, length and width of the notch are optimized to minimize the torque ripple of the motor. The cogging torque of the model is reduced by 63%, the torque ripple by 4.63 %.

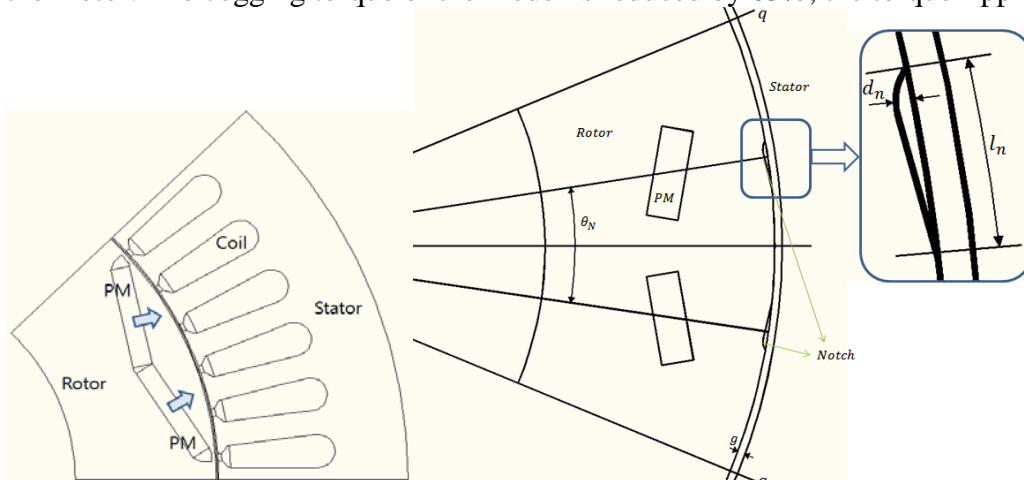


Figure 1: Simulation model of V-type IPMSM and Notch model on the Rotor

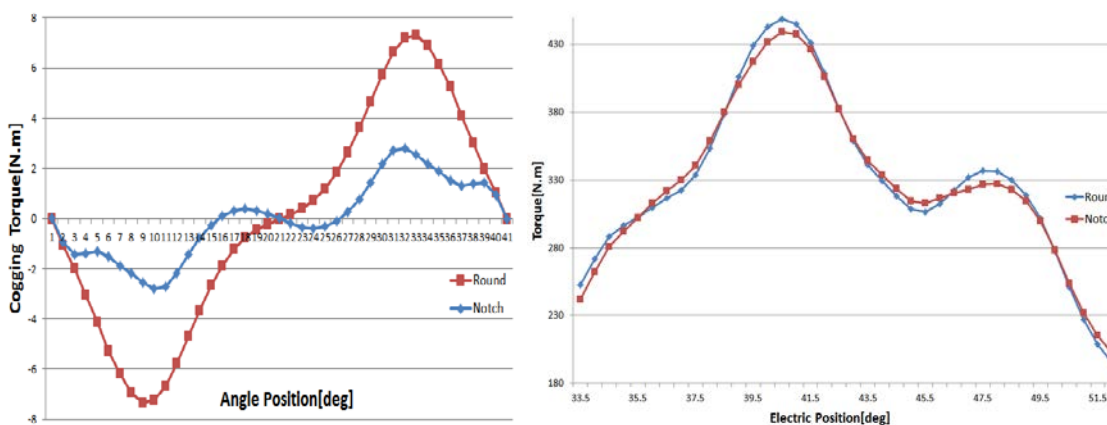


Figure 2: Cogging torque and Torque ripple of IPMSM with and without notches

References

- [1] James Kennedy and Russell Eberhart. "Particle Swarm Optimization." In proceedings of the IEEE International Conference on Neural Networks, volume 4, page 1942-1948, Piscataway, NJ 1995, IEEE
- [2] P.S.Shin, S.H.Woo, C.S.Koh, IEEE Transactions on Magnetics, Vol. 45, no.3, pp. 1214-1217, March 2009
- [3] J.Kwak, S.Min, and J.P.Hong, IEEE Transactions on Magnetics, Vol. 46, no. 6, pp. 2108-2110, 2010
- [4] Y.B. Kim, and et.al., IEEE Transactions on Magnetics, Vol. 45, no.5, pp. 998-1001, May 2011

- This research was supported by Basic Science Research Program through the National Research Foundation of Korea(NRF) funded by the Ministry of Education, Science and Technology(2012010937).

Optimization Design of the Rotor Structure of LSPM Using Response Surface Method

Kwang-hee KIM, Jin-hak JANG, Won-seok KANG Yun-hyun CHO

Electrical Engineering, Dong-A University, Saha-gu, ASI/KR/KS012, Pusan, South Korea

Abstract. In this paper, we will deal with the efficiency and power factor improvement of a 2.2 kW, 2 poles, three Phase Line start permanent magnet synchronous motor (LSPM). The efficiency improvement can be effectively achieved by designing optimization of the rotor structure by using the response surface method and the finite element method. The optimized slot shape of PM was selected for the prototype machine, which improves the efficiency and power factor of LSPM. Finally the performance characteristic of the designed model is compared with that of the initial model.

1 Introduction

The electromagnetic torque of LSPM consists of two components. One is permanent magnet torque generated by the interaction of air-gap magnetic field and stator armature reaction magnetic field. The other is reluctance torque generated by the asymmetry of magnetic circuit of d-axis and q-axis. A reasonable increase of reluctance torque can improve an efficiency and power. [1]

2 Analysis and Optimization of LSPM

In this paper, we discussed an RMS method to the performance improvement by optimizing PM slot. Figure 1 shows basic structure of three phase LSPM motor. The structure of this prototype is that the trapezium shaped PM is inserted in the rotor of three phase induction motor. Figure 2 shows the optimized model. The design variables and experiment ranges are listed in Table 2. The symbols are explained in Figure 2. Two dimensional finite element analysis was utilized to investigate the d-axis, q-axis inductance saliency ratio.[2]

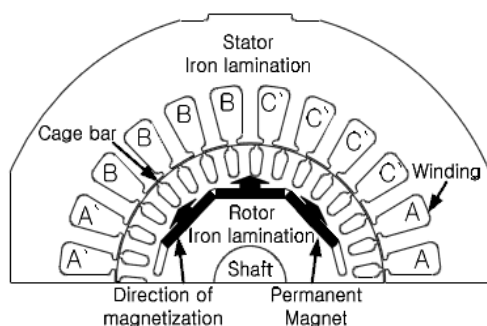


Figure 1: Original Model

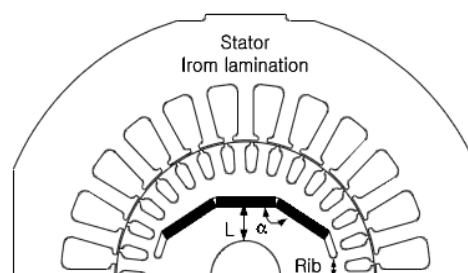


Figure 2: Optimized model

Table 1 Design variables and experiment ranges RSM

Design Variable	Item of design variable	Experiment range	Unit
L	Length from slot to shaft	[6~12]	[mm]
α	Slot angle of side PM segment	[140~ 154]	[deg]
Rib	Air duct gap	[2~12]	[mm]

Figure 3 shows the comparison of the saliency ratio for two models. It obviously indicates that the optimized model has a higher saliency ratio while original model has a lower saliency ratio.

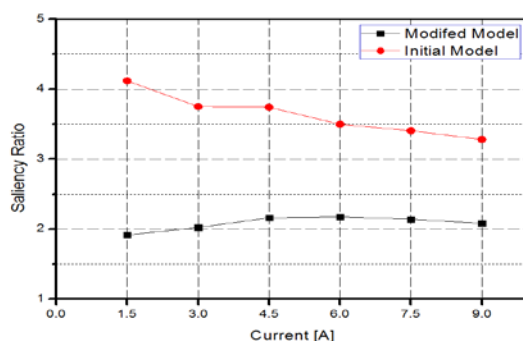


Figure 3: Saliency ratio

Response surface methodology is a collection of statistical and mathematical techniques used for developing, improving and optimizing process. The efficiency and current in steady operating condition are objective functions in RSM, as Figure 4 gives. It is applied to determine an optimization structure of permanent magnet slot in LSPM rotor.

	l	α	R_{ib}
Hi	12.0	154.0	12.0
Cur	[8.863]	[148.0]	[10.92]
Lo	6.0	[140.0]	2.0
Efficiency Maximum			
Current Minimum			

Figure 4: Optimization analysis of Efficiency and Current in RSM

Experiment was set up to test the prototype motors using dynamo test bed as shown in Figure 5(a). and Figure 5(b) shows the Photos of rotor.



Figure 5 (a) Dynamo setup to test the LSPM



Figure 5 (b) Photos of rotor

References

[1] Daqian Jiang, Shumei, Cui Shan Sheng, "Reluctance torque analysis and reactance calculation of IPM for HEVs based on FEM", Vehicle Power and Propulsion Conference (vppc), Sept.2010.
 [2] Liang Fang, Lee, B.H. ; Jung-Pyo Hong, Jung-Pyo Hong ; Hyuk Nam, " Estimation of Magnet Reduction in Single-Phase Line-Start Permanent Magnet Synchronous Motor ", *IEEE Trans. Industry Application*, IAS 2009, Oct 2009, pp 1 - 7.

A Study of Parameter Determination on Interior Permanent-Magnet Synchronous Motor for Agricultural Electric Vehicle

Young-Kyoun Kim, Jeong-Jong Lee, Se-Hyun Rhyu, and In-Soung Jung

Korea Electronics Technology Institute, Yatap Dong, Seongnam, Korea
e-mail: agdokebi@daum.net, Tel.: +82326212869, Fax.: +82326212855

Abstract. The drive-train component of the electric vehicles is frequently using the Interior Permanent-Magnet Synchronous Motor (IPMSM) because that the motor has the advantages of high power density and high efficiency. The IPMSM, owing to their restrictive field weakening range, is designed to be not as easy for a vehicle application. Therefore, this paper presents a procedure of the parameter determination of IPMSM for an electric vehicle.

1 Introduction

Recently, owing to environmental concerns and energy conservation, many people become interested in reducing the carbon-dioxide emissions of an agricultural vehicle. According to any measure, the development of the Agricultural Electric Vehicle (AEV) is essential for the reduction of the carbon-dioxide emissions in agriculture [1]. As the needs of the AEV increase, there is focus on the research of its electric powertrain system. Especially, the electric motor for the traction of the AEV becomes more important part. This traction motor should have a high power density and high efficiency. Interior Permanent-Magnet Synchronous Motor (IPMSM) has not only those advantages but also excellent flux weakening capability [2]. This paper deals with a parameter determination and verification of the IPMSM for the propulsion applications of the agricultural electric vehicle. Because IPMSM has a restrictive field weakening range, the parameter determination of IPMSM is applied in the design procedure to ensure the required specifications, which are instant rated power and continuous rated power of the propulsion of the agricultural electric vehicle. The proposed procedure of the parameter determination is accomplished by coupling between the dynamic equation of the AEV and the voltage equation of the IPMSM motor.

2 Modelling descriptions of analysis model for an Agricultural Electric Vehicle

At the electrical vehicles, the traction motor is the key component that delivers propulsion to driven wheels. Therefore, in order to design the traction motor, the prediction of the vehicle propulsion according to its power characteristic is important and it is accomplished by the mathematical modeling because that the speed-torque characteristic of the traction motor completely determines the vehicle performance. The first step in the performance modelling of the AEV is to produce an equation for the tractive effort. The force propelling the electric vehicle has to overcome the following forces. The total tractive effort required to reach the acceleration a is as follows [2-4].

$$F_t = F_{rr} + F_{ad} + F_{la} + F_{wa} \quad (1)$$

The second step in the performance modelling of the AEV is to produce an equation for the acceleration. The acceleration performance of the AEV is usually evaluated with the time, which is used to accelerate the AEV from zero speed to defined high speed with its full load. The traction power required by acceleration can be estimated.

$$P_{acc} = \mu_r mgv + 0.625AC_d v^3 + 1.05mv \frac{dv}{dt} \quad (2)$$

where μ_r is the rolling resistance coefficient, g is the acceleration of gravity, A is the front area of the AEV, C_d is aerodynamic drag coefficient, v is the AEV speed, m is the AEV mass. The acceleration performance of the AEV is usually evaluated by the speed-torque characteristic of the traction motor. Fig. 1 shows design variables of the IPMSM for the agricultural electric vehicle. In the case of the traction motor, at low speeds, the maximum torque is a constant, until the motor speed reaches a corner speed ω_c after which the torque falls. In order to evaluate conveniently the acceleration performance of the IPMSM, the speed-torque characteristic can be obtained by the voltage equation as follows;

$$V_{abc} = i_{abc}R + L \frac{di_{abc}}{dt} - M \frac{di_{abc}}{dt} + E_{abc} \quad (3)$$

$$T = \frac{i_a E_a + i_b E_b + i_c E_c}{\omega_m} \quad (4)$$

From the above equation, it is realized that the characteristics of IPMSM is totally depended on its parameters, such as BEMF (Back Electromotive Force), inductance, and resistance. Especially, the torque does not fall linearly because of the effect of the phase-inductance.

3 Procedure of the Parameter Determination and Discussion

The speed-torque characteristic of the IPMSM varies as nonlinearity according to the motor parameters. In order to design the IPMSM as the application of the AEV, it is very important to decide the suitable scope of IPMSM parameters, which is corresponding to the given specifications of the AEV propulsion, and it is accomplished by computing the dynamic acceleration (2) coupled with the electrical equation (3) and (4). Therefore, the proposed procedure of the parameter determination is shown in Fig. 2. From the analysis results of the parameter determination process, overall maps of the acceleration performance of the AEV according to the change of the BEMF and the phase-inductance can be estimated. In full paper, more detail results and discussions will be presented.

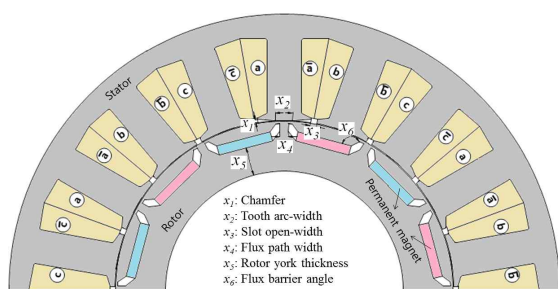


Fig. 1. Design variables of the IPMSM

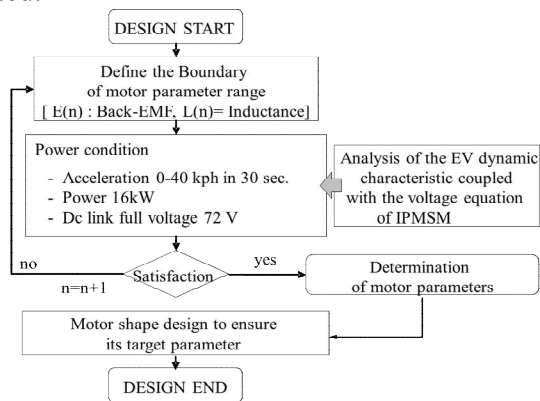


Fig. 2. Proposed procedure of the parameter determination

References

- [1] A. Oida et al., "Study on performance of a model electric off-road vehicle," Agricultural Engineering International: The CUGR journal of Scientific Research and Development, Vol. IV, Oct. 2002.[
- [3] P. Joshi and A. P. Deshmukh, "Vector Control: A New Control Technique for Latest Automotive Applications (EV)", ICETET '08. Conference on, 2008, pp. 911-916.
- [3] Y. Gao and M. Ehsani, "Parametric design of the traction motor and energy storage for series hybrid off-road and military vehicles," Power Electronics, IEEE Trans. On, Vol. 21, Issue 3, 2006, pp. 749 – 755.
- [4] J. Larminie and J. lowry, ELECTRIC VEHICLE TECHNOLOGY EXPLAINED, John Wiley & Sons, Ltd., 2003.

Metal-containing diamond-like carbon composite films for fatigue frequency monitoring

Hiroyuki Miki

Center for Interdisciplinary Research, Tohoku University, Aoba 6-3, Aramaki, Aoba-ku, Sendai 980-8578, Japan

Mami TAKAHASHI, Takanori TAKENO

Graduate School of Engineering, Tohoku University, Aoba 6-6-1, Aramaki, Aoba-ku, Sendai 980-8579, Japan

Julien FONTAINE

Laboratoire de Tribologie et Dynamique des Systèmes, Ecole Centrale de Lyon, UMR CNRS 5513, Ecully, France

Pengfei WANG, Toshiyuki TAKAGI

Institute of Fluid Science, Tohoku University, Katahira 2-1-1, Aoba-ku, Sendai 980-8577, Japan

Abstract. Metal-containing diamond-like carbon (Me-DLC) composite films are attractive as a kind of smart sensors for corrosive environment because of their chemical stability. Those were prepared by hybrid deposition technique combining chemical and physical vapor deposition processes. In this paper, Me-DLC composite films to which molybdenum was selected as an addition were evaluated as a fatigue sensor. Vibration fatigue testings were performed under atmospheric conditions, and the results indicate the possibility of monitoring sensor using of Me-DLCs.

1 Abstract

Vibrations and deformations of the pipes at plants are one of the factors that cause structural fatigue and cracks. In order to avoid serious failure and cut back on the replacement cost of the pipes, precise and real-time monitoring technology is now strongly required. In the real plants, many pipes are placed complexly and exposed to corrosive environment. Therefore, the requirements for monitoring sensors with chemical stability are hopefully thin and able to prepare it on the material directly. According to previous research, we have proposed Metal-containing diamond-like carbon composite films (Mo-DLC) as a fatigue sensor, which shows gauge factor decreasing with number of cycles, especially high cyclic region [1].

In this study, we found the cycle dependence property from bended Mo-DLC composite film under the vibration fatigue test and its mechanism was discussed.

2 Experiments

Mo-DLC coatings were deposited on the flexible ceramic substrates by using hybrid deposition process consisted of chemical vapor deposition (CVD) and physical vapor deposition (PVD). In this study, we selected deposition parameters with a thickness of 400 nm and molybdenum concentration of 17.2 at. %.

The experimental setup used for fatigue process is shown in fig. 1. Specimen was glued on the steel beam indicated in the middle on fig. 1. An electromagnetic coil was synchronized

with natural frequency of the beam and oscillation was induced to the beam. In this study, the resonance frequency of cantilever was set from 60 to 80 Hz.

The electrical resistance of the Mo-DLC coatings was measured by a four-point probe method, and electrical parameters were measured with each step of number of bending cycles in the order of 10^i ($i = 0, 1$ to 7). The data of strain applied to the beam, displacement of the beam and the electrical resistance of Mo-DLC were monitored at a same time. In the vibration experiments, the electrical resistance of the Mo-DLC coatings measured by a four-point probe technique and increased gradually with increasing fatigue cycles from 10^3 to 10^7 .

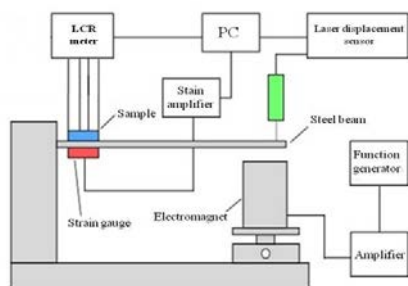


Figure 1: Schematic illustration of the experimental setup for vibration fatigue test.

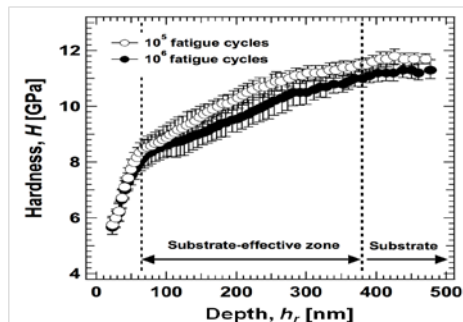


Figure 2: Hardness of Mo-DLC composite films after vibration process with 10^5 and 10^6 cycles.

3 Results

The hardness of Mo-DLC was investigated by nano indentation testing after the vibration test. The hardness of the Mo-DLC coatings after vibration fatigue process was evaluated using a Nanoindenter (Nano Indenter XP, MTS Systems Corporation, USA). Fig. 2 shows the result of hardness tests. There was no clear difference on hardness in the region from the surface to the depth of 70 nm, but slight change could be found below 70 nm. Taking into account the Raman results, the change of the hardness may be due to the structural change of carbon matrix atoms in the matrix [3]. Therefore, possible explanation is that carbon network may change due to the fatigue loading.

4 Summary

In this study Mo-DLC composite films were evaluated as a vibration monitoring sensor. The change of electrical resistance can be attributed to the structural changes of the Mo-DLC films during the cyclic fatigue testings, which were clearly identified from the Raman analysis and nano indentation of the tested Mo-DLC composite films. It is suggested that Mo-DLC composite film has a potential for the fatigue detecting sensor.

Acknowledgment

This work was partly supported by the Grant-in-Aid for Scientific Research (A)(23246038) and (B)(22360043) of Japan Society for the Promotion of Science (JSPS), and Global COE Program, "World Center of Education and Research for Transdisciplinary Flow Dynamics", by Ministry of Education, Culture, Sports, Science and Technology (MEXT) in Japan. The authors express their appreciation to Mr. Takeshi Sato from the Institute of Fluid Science at Tohoku University for his technical assistance.

References

- [1] T. Ohno, T. Takeno, H. Miki, T. Takagi, *Diamond and Related Materials* **20** (2011) 651–654
- [2] T. Takeno, H. Miki, T. Sugawara, Y. Hoshi, T. Takagi, *Diamond and Related Materials* **17** (2008) 713–716.
- [3] J. Robertson, *Material Science and Engineering* **R37** (2002) 129–281.

3-

**Analysis and simulation of
electromagnetic devices**

Theoretical analysis of energy harvesting from the improved nonlinear magnetic suspension

Yajun Luo*, Yan Bo and Xinong Zhang

State Key Laboratory for Strength and Vibration of Mechanical Structures, School of Aerospace, Xi'an Jiaotong University, Xi'an, China

Abstract. In this study, an improved nonlinear magnetic suspension device is investigated for the energy harvesting. The harvester consists of a pair of the suspended magnets, two fixed magnets, and an electromagnet. As the bottom magnet suffers a disturbance, the suspended magnets will move which result in the generation of EMF (electromotive force) of the electromagnet. Then, the vibrating energy can be harvested. The modeling of permanent magnet is carried out. The electromagnetic coupling coefficient of the harvester is obtained according to Maxwell's equation. Moreover, the theoretical analysis of the magnetic repulsive force is finished. The frequency response equation of the nonlinear system is established. The results show the nonlinear characteristics can enhance the energy harvesting.

Keywords: energy harvesting, electromagnetic, nonlinear, magnetic suspension

1. Introduction

Recently, energy harvesting has been attracted more and more attentions [1]. Nonlinear energy harvesting has been shown to be capable of scavenging wider frequency and delivering more power than the linear one, and rendering them more suitable for real application [2-3]. Magnetic suspension system is widely used in the nonlinear energy harvesting for the repulsive force can be considered as a nonlinear force [4]. Stanton et al. [5] proposed a monostable nonlinear oscillation of magnetic levitation. L. Gammaitoni et al. [6] discussed the vibration to electricity energy conversion strategies using nonlinear stochastic dynamics. Tang et al. [7] investigated the use of magnets for improving the functionality of energy harvester under various vibration scenarios. Owens et al. [8] investigates the response of an energy harvester that uses electromagnetic induction to convert ambient vibration into electrical energy.

This paper investigates an improved magnetic suspension device which a pair of permanent magnets is suspended instead of one. The suspended magnets have opposite polarizing direction, which make it possible of improving the electro-mechanical coupling coefficient.

2. Overview of the nonlinear vibration harvester

Figure 1 shows the configuration of the nonlinear electromagnetic energy harvester, where a pair of the annular permanent magnets is suspended by the repulsive force generated by the fixed upper and bottom permanent magnets. The polarization of the two suspended magnets are opposite with each other. Moreover, an electromagnet coils is wounded on a case that is made of nylon materials. As the bottom magnet suffers a disturbance, the suspended magnets will move along the vertical direction under the repulsive force reaction from the two fixed permanent magnet. Under this circumstance, the

*Corresponding author. Yajun Luo, State Key Laboratory for Strength and Vibration of Mechanical Structures, School of Aerospace, Xi'an Jiaotong University, Xi'an, China, Tel. +86 0 29 8266 5721; E-mail: luoyajun@mail.xjtu.edu.cn.

magnetic repulsive force is served as a kind of elastic forces that could store and release the excitation energy.

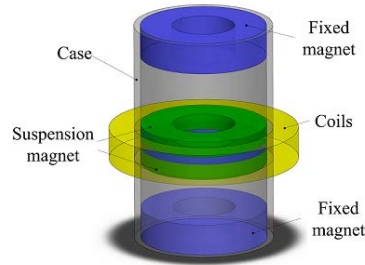


Fig. 1. Configuration of the nonlinear electromagnetic energy harvester.

3. Modeling of the energy harvester

3.1. Permanent magnet modeling

Figure 2 shows the current model of annular permanent magnet. The magnet can be simplified to a volume current density $\mathbf{J}_m = \nabla \times \mathbf{M} = \mathbf{0}$ and a surface current density \mathbf{J}_s . \mathbf{M} and \mathbf{r} are the magnetization vector and the unit surface normal, respectively. Assuming that the permanent magnet is uniformly polarized by a magnetization vector, i.e. $\mathbf{M} = M\mathbf{z}$, along the longitudinal direction with the unit vector \mathbf{z} , the volume one becomes zero, and the surface current density is

$$\mathbf{J}_s = \mathbf{M} \times \mathbf{r} = M\boldsymbol{\phi} \quad (1)$$

As for the surface current density, we find that $\mathbf{J}_s = \mathbf{0}$ on the top and bottom surfaces of the shell because the magnetization and surface normal are either parallel. There are two remaining surfaces to consider: the inner and the outer.

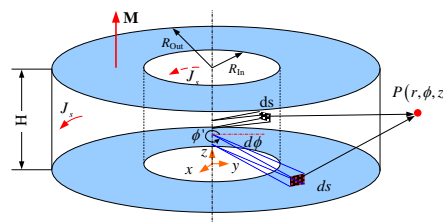


Fig. 2. Current model of annular permanent magnet.

The unit normal directions for the two surfaces are opposite with each other. Let the outer surface as positive, the surface current density are

$$\mathbf{J}_s = \begin{cases} -M\boldsymbol{\phi} & (\text{Inner surface}) \\ M\boldsymbol{\phi} & (\text{Outer surface}) \end{cases} \quad (2)$$

where $\boldsymbol{\phi}$ is the tangential unit vector. The residual magnetic flux density of the permanent magnet No. 1 is \mathbf{B}_{r0} . M can be calculated as $\mathbf{M} = \mathbf{B}_{r0} / \mu_0$, where $\mu_0 = 4\pi \times 10^{-7} \text{ Tm/A}$ denotes the permeability of vacuum. The flux density at any point P generated by the permanent magnet is given as

$$\mathbf{B}(r, \phi, z) = B_r(r, \phi, z)\mathbf{r} + B_\phi(r, \phi, z)\boldsymbol{\Phi} + B_z(r, \phi, z)\mathbf{z} \quad (3)$$

where

$$B_r(r, \phi, z) = \frac{\mu_0 M}{4\pi} \sum_{j=1}^2 \sum_{k=1}^2 (-1)^{(j+k)} \int_0^{2\pi} \cos(\phi - \phi') \times d(r, \phi, z; R_c(j), \phi', z_k) R_c(j) d\phi' \quad (4)$$

$$B_z(r, \phi, z) = \frac{\mu_0 M}{4\pi} \sum_{j=1}^2 (-1)^{(j+1)} \int_{z_1}^{z_2} \int_0^{2\pi} [r \cos(\phi - \phi') - R_c(j)] \times [d(r, \phi, z; R_c(j), \phi', z')]^3 R_c(j) d\phi' dz' \quad (5)$$

$$d(r, \phi, z; r', \phi', z') = [r^2 + r'^2 - 2rr' \cos(\phi - \phi') + (z - z')^2]^{-1/2} \quad (6)$$

where r' denotes the radius of the current-carrying surface and we have $R_c(1)=R_{in}$, $R_c(2)=R_{out}$.

3.2. Modeling of repulsive force

Shown in figure 3, a repulsive magnetic force will generated between a pair of the opposite polarized magnet. Charge model is an effective way to derive the repulsive magnetic force between the two opposite polarized magnets and it is widely used for analyzing permanent magnets. The same way as the current model, a permanent magnet can be theoretical equivalent as a volume and surface charge densities ρ_m and σ_m , where $\rho_m = -\nabla \cdot \mathbf{M} = -\nabla \cdot \mathbf{Mz}$. The volume charge density ρ_m is zero, and the surface charge σ_m is $\mathbf{M} \cdot \mathbf{n}$, where \mathbf{n} is the outside normal of the magnet. The repulsive magnetic force of opposing pole face can be expressed as, suggested in [9]

$$F_{z,surf}(H) = \frac{\mu_0 M^2 N_\phi}{4\pi} \left\{ \frac{\pi (R_{out}^2 - R_{in}^2)}{N_r N_\phi} \right\}^2 \times \sum_{i=1}^{N_r} \sum_{i'=1}^{N_r} \sum_{j=1}^{N_\phi} \frac{H}{[r_i^2 + r_{i'}^2 - 2r_i r_{i'} \cos(\phi_j) + H^2]^{3/2}} \quad (7)$$

where R_{in} and R_{out} denote the inner and outer radius of the magnet. N_r and N_ϕ are the number of meshes along r and ϕ directions. Thus, the area of each element is $\Delta A = \pi(R_{out}^2 - R_{in}^2) / (N_r N_\phi)$. Let (r_i, ϕ_i) denote the midpoint of the element $\Delta A_{i,j}$, we have $r_i = (R(i+1) + R(i))/2$, $\phi_i = (j-1)\Delta\phi + 0.5\Delta\phi$, $\Delta\phi = 2\pi / N_\phi$.

Considering that each permanent magnet has two equivalent charge surfaces, the total repulsive force between the two permanent magnets should be the sum of four surfaces, and it is written as

$$F_z = F_{z,surf}(d) - 2F_{z,surf}(d+H) + F_{z,surf}(d+2H) \quad (8)$$

Take Eq. (7) into (8) and simplify, the final expression is

$$F_z = \frac{\mu_0 M^2 N_\phi}{4\pi} \left\{ \frac{\pi (R_{out}^2 - R_{in}^2)}{N_r N_\phi} \right\}^2 \times \sum_{m=0}^2 \sum_{i=1}^{N_r} \sum_{i'=1}^{N_r} \sum_{j=1}^{N_\phi} \frac{(-1)^m \alpha_m h_m}{[r_i^2 + r_{i'}^2 - 2r_i r_{i'} \cos(\phi_j) + h_m^2]^{3/2}} \quad (9)$$

where $m = [0 \ 1 \ 2]$, $h_m = d + 0.5m(H_i + H_b)$, and $\alpha_m = 1$ as $m=0$, $\alpha_m = 2$ as $m=1$, and $\alpha_m = 1$ as $m=2$.

Figure 4 shows the repulsive force versus the distance between the magnets. Obviously, the repulsive force is a nonlinear elastic force, which decreases quickly when the relative distance between the magnets increases. For Eq. (9) is hard to simulate, the repulsive force is fitted using 3-order polynomials method. Shown in figure 4, the fitted equation is

$$F_z(d) = \sum_{i=0}^3 C_i d^i \quad (10)$$

where $C_0 = 41.44N$; $C_1 = -4094.60N/m$; $C_2 = 1.4 \times 10^5 N/m^2$; $C_3 = -1.58 \times 10^6 N/m^3$.

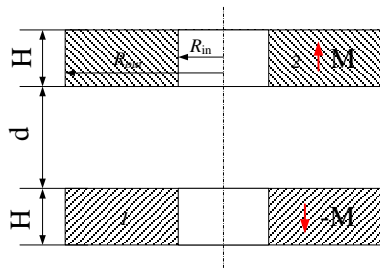


Fig. 3. Configuration of the suspended magnets.

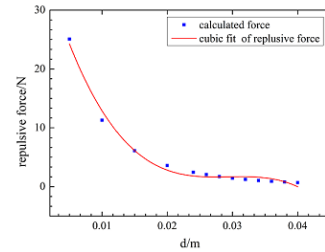


Fig. 4. Repulsive force versus the distance d between the magnets.

3.3. Modeling of electromagnetic couple

The induced EMF can be deduced according to the third equation of Maxwell (Faraday's Law), which is

$$\mathbf{E} = \xi N \int_l B_r dl \Phi = \xi C_e \Phi \quad (11)$$

where $C_e = NR_p \int_0^{2\pi} B_r d\phi$ can be called as electromagnetic coupling coefficient. N is the turns of the coils, C_e It can be found that the EMF depends on the relative velocity of the suspension magnet as well as the radial magnetic flux density. Figure 5 shows the variation of C_e with respect to the radius of the coils. It can be found that C_e decreases with the increase of the radius of the coils. What's more, the vertical position of the coils also affects C_e .

A Lorentz force will be generated when the coils are closed with any other electrical components, such as resistors, capacitors or inductors, etc. According to the Ampere's Law, it can be written as $d\mathbf{F}_d = NI d\mathbf{l} \times \mathbf{B}_p$. I is the induced current of a circuit. \mathbf{B}_p is the sum of the magnetic flux generated by two suspension magnets, which is $\mathbf{B}_p(r, \phi, z) = \mathbf{B}_{p1}(r, \phi, z) + \mathbf{B}_{p2}(r, \phi, z)$. The force is formulated as,

$$\mathbf{F}_d = -\mathbf{z} \cdot C_m I \quad (12)$$

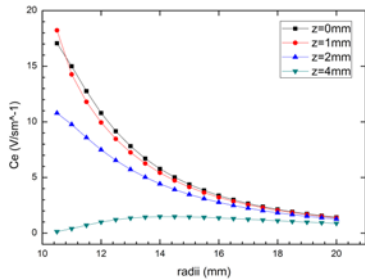


Fig. 5. C_e varies with respect to r_p .

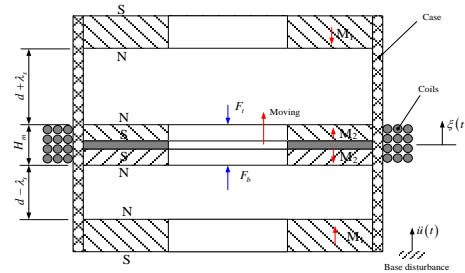


Fig. 6. Schematic diagram of the magnetic suspension system.

4. Analysis of magnetic suspension system

The schematic diagram of the proposed suspension system is shown in figure 6. When the suspension magnets have a displacement $\xi(t)$ from the static equilibrium state, that is, the suspension magnets have a relative displacement $x(t) = \lambda_s - \xi(t)$ with respect to the middle position, at which the distance between the suspension magnets and the bottom or upper magnet is d . λ_s is the static equilibrium displacement of the magnetic to relate to the middle position. The suspension magnets are supported by the upper and bottom magnets, thus, the total repulsive magnetic force can be obtained as

$$F_t(x) = F(d - x(t)) - F(d + x(t)) \quad (13)$$

Take Eq. (10) into above equation, the repulsive force is simplified as

$$F_t(x) = k_1x + k_3x^3 \quad (14)$$

where k_1 is equal to $-2C_1 - 4C_2d - 6d^2C_3$, k_3 is equal to $-2C_3$. The total force is zero at the equilibrium point, that is $F_b(d - \lambda_s) - F_t(d + \lambda_s) - mg = 0$, thus, λ_s can be obtained by solving the following equation $k_1\lambda_s + k_3\lambda_s^3 - mg = 0$. $F_b(d - \lambda_s)$ and $F_t(d + \lambda_s)$ denote the repulsive force of the bottom and upper magnet, respectively.

5. Energy harvesting

In the section, the coils will connect to a circuit with a resistor to constitute a closed loop. Then, the governing equation can be obtained according to the Kirchhoff's Law,

$$L_e \frac{di(t)}{dt} + (R_e + R_L)i(t) = C_e \dot{\xi}(t) \quad (15)$$

Assume that the base acceleration disturbance $\ddot{u}(t)$ is equal to $F_g \sin \omega t$. Take into account all the repulsive force and damping force, the suspension system can be mechanically equivalent to a liner spring with stiffness k_1 , a nonlinear spring with stiffness k_3 and a damper. Figure 7 shows the equivalent mechanical model for the magnetic suspension system. The dynamic equation can be written as

$$m\ddot{\xi}(t) + k_1\xi(t) + k_3\xi^3(t) + F_d = -mF_g \sin(\omega t) \quad (16)$$

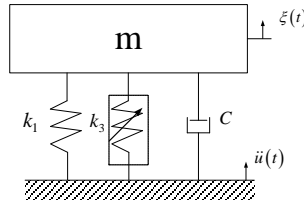


Fig. 7. Equivalent mechanical model for the magnetic suspension system.

According to the harmonic balance method, the zero step solution $\xi(t)$ of the equation is equal to $a \cos(\omega t)$, and the induced current will be

$$i(t) = -C_e \omega a \sin(\omega t - \varphi) / z_{eq} \quad (17)$$

where $z_{eq} = \sqrt{(R_e + R_L)^2 + (\omega L_e)^2}$, $\varphi = a \tan(\omega L_e / R_e + R_L)$.

Take Eq. (17) into (16), and neglect the higher harmonic component $\cos(3\omega t)$, the frequency response equation for the nonlinear system can be obtained

$$\left[(\omega_0^2 - \omega^2)a + \frac{3}{4}\varepsilon a^3 + 2C \sin \varphi \cdot \omega a \right]^2 + [2C \cos \varphi \cdot \omega a]^2 = F_g^2 \quad (18)$$

where $\varepsilon = k_3 / m$, $C = C_m C_e / 2mz_{eq}$, $\omega_0 = k_1 / m$.

Figure 8 shows the displacement frequency response as $R_L = R_e$. Figure 9 shows the variation of the displacement with respect to F_g . It can be found that: (1) the increase of the damping coefficient of the system will weaken the nonlinear effect; (2) the magnitude of disturbance affects the response of the system.

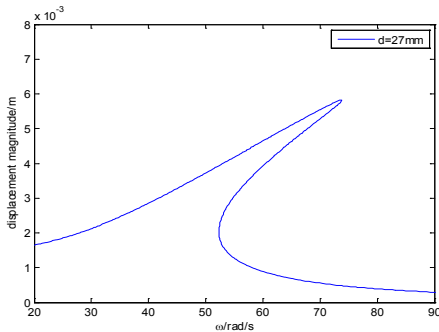


Fig. 8. Displacement frequency response for $C_m=4N/A$, $F_g=2ms^{-2}$.

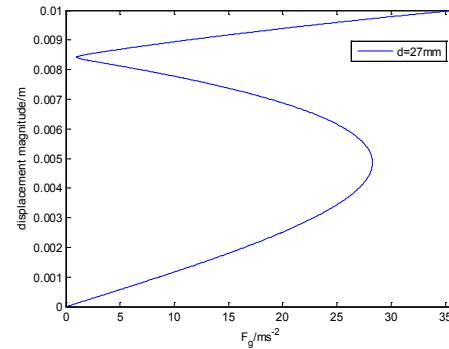


Fig. 9. Displacement vs. F_g ($\omega=100rad/s$).

6. Conclusions

In this paper, an improved nonlinear magnetic suspension device has been investigated for the energy harvesting. As the bottom magnet suffers a disturbance, the suspended magnets will move which result in the generation of EMF of the electromagnet. Hence, the vibrating energy can be harvested. The current model of the permanent magnet is given. The electromagnetic coupling coefficient of the harvester has also been obtained according to Maxwell's equation. Moreover, the theoretical analysis of the magnetic repulsive force has been conducted. The frequency response equation of the nonlinear system has been established. What's more, the numerical simulation of the suspension system has been completed and the results show the nonlinear characteristics can enhance the energy harvesting. Furthermore, the magnitude of the disturbance affects the nonlinear characteristics of the harvesting system.

Acknowledgements

This research was supported by the National Natural Science Foundation of China (Nos. 11102147 and 11177725) and "the Fundamental Research Funds for the Central Universities" (Nos. xjj2011057 and xjj20100095).

References

- [1] A. Harb, Energy harvesting: State-of-the-art, *Renewable Energy*, **36** (2011), 2641-2651.
- [2] A.F. Arrieta, P. Hagedorn, A. Erturk, and D.J. Inman, A piezoelectric bistable plate for nonlinear broadband energy harvesting, *Applied Physics Letters*, **97** (2010), 104102.
- [3] B. Yang, J. Liu, G. Tang, J. Luo, C. Yang, and Y. Li, A generator with nonlinear spring oscillator to provide vibrations of multi-frequency, *Applied Physics Letters*, **99** (2011), 223505.
- [4] B.P. Mann, N.D. Sims, Energy harvesting from the nonlinear oscillations of magnetic levitation, *Journal of Sound and Vibration*, **319** (2009), 515-530.
- [5] S.C. Stanton, C.C. McGehee and B.P. Mann, Reversible hysteresis for broadband magnetopiezoelectric energy harvesting, *Applied Physics Letters*, **95** (2009), 174103.
- [6] L. Gammaitoni, I. Neri, and H. Vocca, Nonlinear oscillators for vibration energy harvesting, *Applied Physics Letters*, **94** (2009), 164102.
- [7] L. Tang, Y. Yang and C. Soh, Improved functionality of vibration energy harvesters using magnets, *Journal of Intelligent Material Systems and Structures*, **23** (2012), 1433-1449.
- [8] A. Owens, B. Mann, Linear and nonlinear electromagnetic coupling models in vibration-based energy harvesting, *Journal of Sound and Vibration*, **331** (2012), 922-937.
- [9] E. Furlani, *Permanent magnet and electromechanical devices*, Academic Press, New York, 2001.

AC Copper Losses Analysis of the Ironless BLDCM used in a Flywheel Energy Storage System

Kai Liu, Jianhui Hu^{*}, Jibin Zou, Yanyu Wei and Guangqi Zhu

Department of Electrical Engineering, Harbin Institute of Technology, No.92, West Da-zhi Street, Harbin, China

Abstract. The purpose of this paper is to analyze the AC copper losses of the ironless brushless DC machine (BLDCM) used in the FESS. The influence factors of the AC copper losses, such as the diameter of the strands, the frequency of the phase current, and the amplitude of the phase current are analyzed. For circulating current losses calculation, an equivalent circuit model is presented and effects of the analytical model parameters are given. Two strands arrangements are compared and discussed. The results show that the ironless BLDCM using multi-strands with suitable strands arrangements can reduce the copper loss.

Keywords: flywheel energy storage system, ironless brushless DC machine, eddy current loss, circulating current,

1. Introduction

The flywheel energy storage system (FESS) is an attractive option for energy storage in high power utility applications and hybrid electric systems. The high speed permanent magnet brushless DC machine is one of the suitable motors for the FESS. Compared with the other motors, it has many advantages such as high-efficiency, high-reliability and so on.

The losses of the ironless BLDCM used in the FESS include two parts: the copper losses and the rotor eddy current losses. Techniques for modeling high frequency losses in the iron [1] and magnets [2] and minimizing these losses have been presented in the literature. In this paper, we just analysis the copper losses. The AC copper losses can be separated based on the source of the flux. Losses in a strand due to a bulk AC current in that strand are skin-effect losses and losses due to an externally imposed field on that strand are typically called proximity losses. The proximity losses can also be divided by the source: the armature field induced losses and the excitation field induced losses [3].

In order to reduce the AC copper loss, some countermeasures exist, such as using several thinner strands in parallel. However, the circulating currents which are the result of imbalances in the linked field flux may appear. For the ironless BLDCM, the impedance of the strands is small and the circulating current losses pose significant problem.

The purpose of this paper is to analyze the AC copper losses of the ironless BLDCM used in the FESS. Section 2 will give the structure of the FESS. Section 3 will discuss the influence factors of the AC copper losses, such as motor speed, diameter of the strands, frequency of the phase current and amplitude of the phase current. Section 4 will present an equivalent circuit model for circulating current losses calculation and two strands arrangements will be compared. Section 5 will give the results.

^{*} Corresponding author: Jianhui Hu, Department of Electrical Engineering, Harbin Institute of Technology, China. Tel.: +86 0451-86413613; E-mail: hujianhui@hit.edu.cn

2. Structure and Principle

The FESS presented in this paper is composed of two parts: the ironless BLDCM and its drive system. Fig.1 (a) shows the structure of the BLDCM and Fig.1 (b) shows the cross section of the BLDCM. The BLDCM includes an iron-less armature (fixed in a fiber frame), an iron core and the permanent magnets. Table 1 gives the basic specifications. The BLDCM used in the FESS is driven by a modified C-dump converter. The principle of operation, modeling and control strategy of the modified C-dump converter are shown in paper [4].

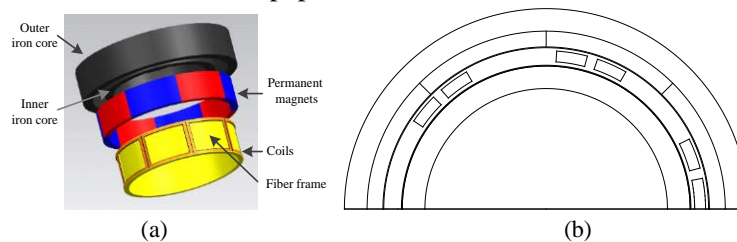


Fig. 1. The structure of the FESS

Table 1
 BLDCM Parameters

Items	Symbol	Units	Value	Items	Symbol	Units	Value
Rated Voltage	V	V	100	Poles	p		4
Rated Power	P_e	W	2000	Axial Length	L_{ef}	mm	14
Rated Frequency	f_e	HZ	2000	Air gap	L_{air}	mm	8

3. AC copper losses without considering the circulating current

The AC copper losses can be computed analytically, but it's difficult to obtain the distribution of the magnetic field with analytical modeling. Finite element (FE) modeling does not suffer from this drawback. In this paper, the AC copper losses are carried out by using two-dimensional (2D) FE model. In order to consider the skin effect and proximity effect for the winding, the models with a large number of strands inside the slots are created, as shown in fig. 2.

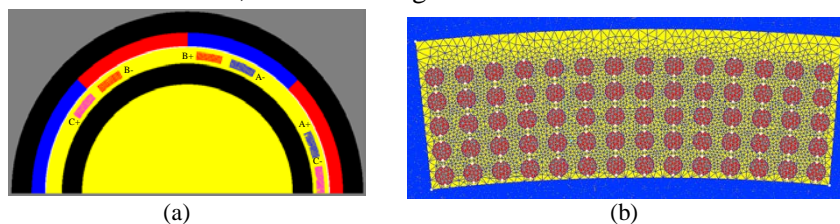


Fig. 2 (a) 2D FE model for the BLDCM, (b) 2D FE models for the winding A+ with mesh

3.1. Effect of the strand diameter

To consider the effect of the strand diameter, several winding models with different diameter strand in parallel are created. The total cross-sections of the strands are the same. The motor runs in the rated speed, and three phase sinusoidal currents $i = A * \sin(2\pi f_c * t)$ ($A=20$) are applied to the motor phase, where f_c is the frequency of the phase current and A is the amplitude of the phase current. Fig.3 shows the current density distributions of conductors with different conductor diameter. With the diameter increasing, the skin-effect and proximity effect become more significant. Fig. 4 (a) shows the AC copper losses variation with the different strand diameter in the winding A. With the strand diameter increasing, the AC copper losses increase fast.

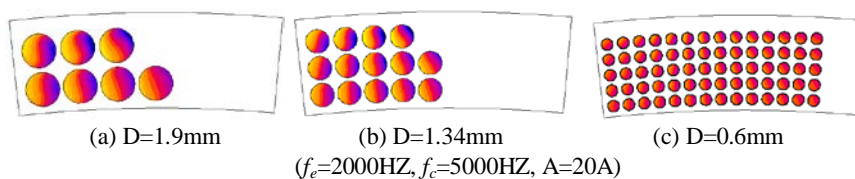


Fig.3 Current density distributions of conductors with different conductor diameter.

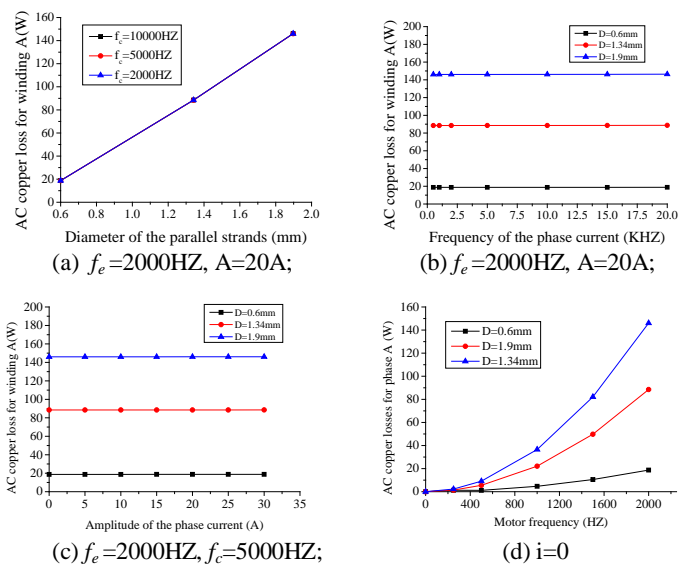


Fig.4 Influence factors of the AC copper losses

3.2. Effect of the current frequency

The motor runs in the rated speed, and three phase sinusoidal currents $i = A * \sin(2\pi f_c * t)$ ($A=20$) are applied to the motor phase. Fig. 4 (b) shows the AC copper losses variation with the current frequency in the winding A.

3.3. Effect of the current amplitude

The BLDCM runs in the rated speed, and three phase sinusoidal currents $i = A * \sin(2\pi f_c * t)$ ($f_c=5000\text{HZ}$) are applied to the motor phase. Fig. 4 (c) shows the AC copper losses variation with the phase current amplitude in the winding A.

Fig. 4 (a) (b) (c) indicate that the losses induced by the excitation field are the main part of the AC copper losses and the variation of the phase current has little effect on the AC copper losses in the ironless BLDCM. Fig. 4 (d) shows the AC copper losses variation with the motor speed when $i=0$.

The analysis indicates that in the ironless BLDCM, the efficient way to reduce the AC copper losses is to use several thinner strands in parallel.

4. Circulating currents losses

When using several thinner strands in parallel to reduce the AC copper loss, the circulating currents may appear. For circulating currents analysis, a simplified analytical model is introduced.

The windings use 10 strands ($D=0.6\text{mm}$) in parallel and 7 turns in series. The impedance of the end has been taken into account. The equivalent circuit model includes the effective part and the end part, as shown in fig.5 (a). In the effective part, each strand is modelled as a series combination of a resistance, several inductances, and an induced voltage. And in the end part, each strand is modelled as a series combination of a resistance and several inductances. The inductances include a self-inductance and 9 mutual inductances representing the magnetic coupling of each individual strand to all of the other strands. A 2D FE model without permanent magnet has been created for the end part, as shown in fig 5 (b).

Because of the limited space in the slot, the strands twist is not allowed. There are two common strand arrangements, as shown in Fig. 6. This section will discuss the effects of the analytical model parameters in fig.5 (a) and the total losses of the two strands arrangements will be shown.

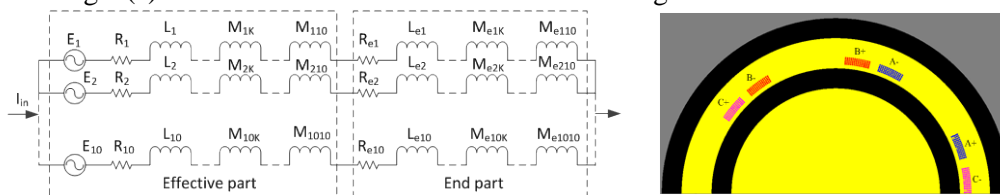


Fig.5 (a) Equivalent circuit model for 10 strands in parallel, (b) 2D FE model for the end

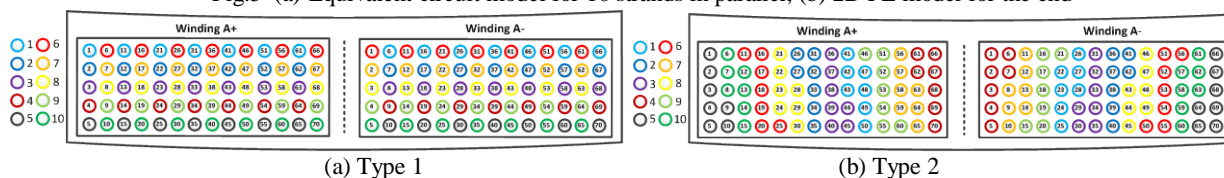


Fig. 6 Two types of strands arrangements

4.1. Induced Voltage

Each of the strands in the effective part will induce the voltage. Because of the imbalances of the linked field flux, the strands in different position will induce different voltage. Fig.7 shows the voltage matrix for the E_1, E_2, \dots, E_{10} in type 1 and type 2.

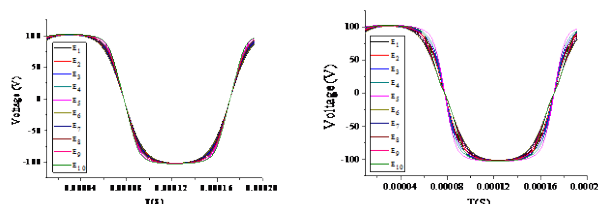


Fig. 7 Voltage matrix in (a) Type 1, (b) Type 2

4.2. Resistance

Considering the skin-effect and proximity effect, the AC resistance of the strands is greater than its DC resistance. The AC resistance can be calculated by the formula (1)

$$R_{ac} = R_{dc} \frac{\iint J_{ac}^2(t) d^2s \cdot dt}{\int J_{dc}^2 d^2s} \quad (1)$$

where R_{dc} is the DC resistance, $J_{ac}(t)$ is the AC current density, and $J_{dc}(t)$ is the DC current density. It's difficult to get the R_{ac} directly by the formula (1), so the 2D FE model has been used. The influence factors, such as the frequency of the phase current, the amplitude of the phase current and the diameter the strand are considered.

4.2.1. Resistance in the end

In the end part, the eddy current in the strand is influenced by the skin-effect and the proximity effect induced by the armature field. The motor runs in the rated speed, and three phase sinusoidal currents $i = A \sin(2\pi f_c * t)$ are applied to the motor phase. Fig. 8 (a) shows the ratio of the R_{ac} to R_{dc} variation with the different diameter of the strand when $A=20A$. With the strand diameter increasing, the AC copper losses increase fast and the ratio of the R_{ac} to R_{dc} increases also. Fig. 8 (b) shows the ratio of the R_{ac} to R_{dc} variation with the frequency of the phase current. Fig. 8 (c) shows the ratio of the R_{ac} to R_{dc} variation with the phase current amplitude when the diameter $D=0.6mm$. It shows that the ratio of the R_{ac} to R_{dc} increases with the frequency of the phase current increasing and the current amplitude nearly doesn't affect the ratio of the R_{ac} to R_{dc} .

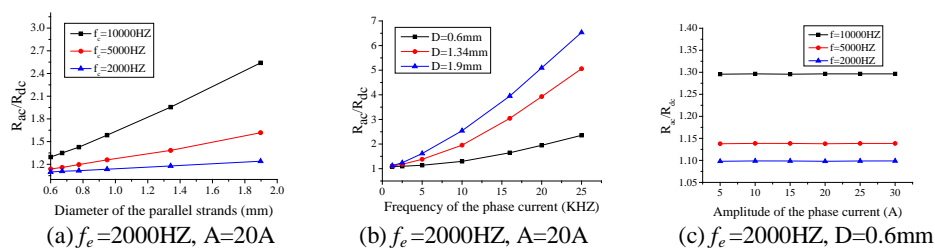


Fig.8 Influence factors of the R_{ac}/R_{dc} in the end

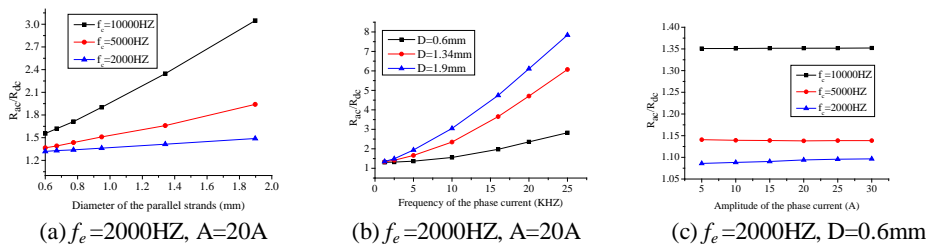


Fig.9 Influence factors of the R_{ac}/R_{dc} in the effective part

4.2.2. Resistance in the effective part

In the effective part, the eddy current in the strand is influenced by the skin-effect and the proximity effect induced by the armature and excitation field. The analytical method is the same. Fig. 9 (a) shows the ratio of the R_{ac} to R_{dc} variation with the different diameter of the strand. Fig. 9 (b) shows the ratio of the R_{ac} to R_{dc} variation with the frequency of the phase current. Fig. 9 (c) shows the ratio of the R_{ac} to R_{dc} variation with the phase current amplitude. Compared Fig. 8 and Fig. 9, it can be seen that the ratio of the R_{ac} to R_{dc} in the end is smaller than that in the effective part.

From the fig.8 and fig.9, the ratio of the R_{ac} to R_{dc} can be acquired.

4.3. Inductance

The inductance matrixes of the strands in the effective part are carried out by using 2D static FE model. For FE analysis, the rotor position is varied from 0 to 90 degrees mechanical so that it goes over one complete electrical cycle while varying the current incrementally in 7 steps from 0A to 30A. The inductance matrix in the end part is carried out by using 3D static FE model, as shown in the fig.10 (b). For FE analysis, the rotor position is varied from 0 to 90 degrees mechanical while varying the current incrementally in 2 steps from 15A to 30A.

Fig.10 (a) and Fig.10(c) shows the variation of the inductance of phase A with the rotor position and

the phase current in the effective part and in the end part. Both variations of the inductance are less than 0.002%, and the inductance matrixes of the strands can be considered as constants for calculation.

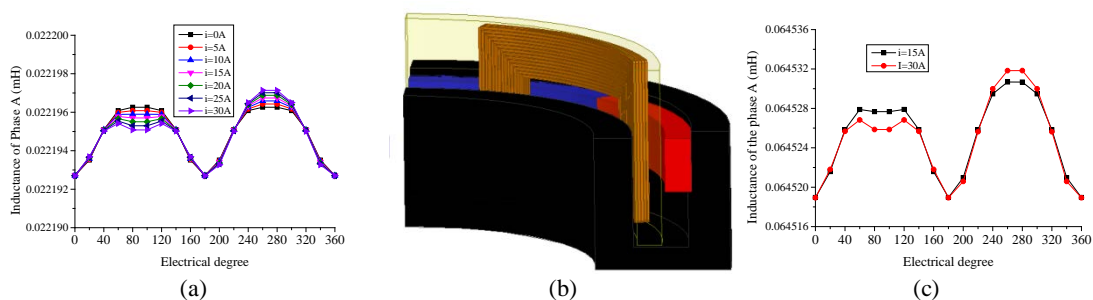


Fig.10 (a) Phase A inductance in the effective part, (b)3D FE model, (c) Phase A inductance in the end

4.4. Calculation Result

The circulating currents of the 10 strands have been shown in fig.11. For strands arrangements 1, the AC copper losses without considering circulating current are 56.94W and the circulating current losses are 5.77W. For strands arrangements 2, AC copper losses without considering circulating current are 57.11W and the circulating current losses are 7.93W. Compared with the total losses of two strands arrangements, the arrangements 1 is suitable for the FESS use.

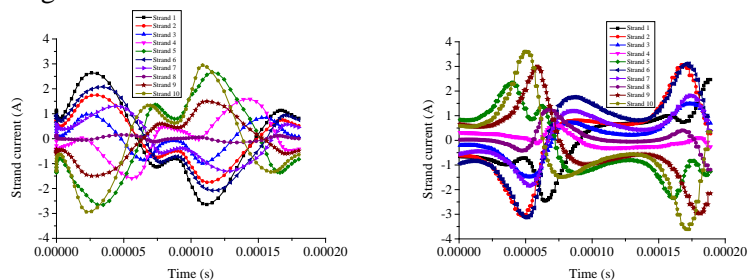


Fig.11 The circulating currents of the 10 strands, (a)Type 1, (b) Type 2.

5. Conclusion

This paper has analyzed the AC copper losses of the ironless brushless DC machine (BLDCM) used in the FESS. The influence factors of the AC copper losses, such as diameter of the strands and the variation of the phase current has been discussed. For circulating current losses calculation, an equivalent circuit model is presented and effects of the analytical model parameters are given. Two strands arrangements are compared and discussed. The results show that the ironless BLDCM using multi-strands with suitable strands arrangements can reduce the copper loss.

Acknowledgements

This work was supported in part by 973 program under grant 2013CB035605.

References

- [1] EL-Refaie, A.M., T.M. Jahns, Modified Vector Control Algorithm for Increasing Partial-Load Efficiency of Fractional-Slot Concentrated Winding Surface PM Machines, IAS2006, 2006, vol. 1, pp. 50-57.
- [2] Atallah, K., D. Howe, P.H. Mellor, and D.A. Stone, Rotor Loss in Permanent-Magnet Brushless AC Machines, IEEE Trans. Industry Applications, Nov/Dec 2000, vol. 36(6), pp. 1612-1618.
- [3] V. d. Geest, P. Henk, Stator winding proximity loss reduction techniques in high speed electrical machines, IEMDC 2013, pp. 340-346.
- [4] Jibin Zou, Kai Liu, Jianhui Hu, A Modified C-Dump Converter for BLDC Machine Used in a Flywheel Energy Storage System, IEEE Trans. Magnetics, Oct 2011, vol. 47(10), pgs. 4175-4178.

Basic Study on a High Efficient Heating of IH Earthenware Pan by the Finite Element Method

Akihiro FUJIWARA^{a*}, Junichi ARAI^a, Miki KOBAYASHI^a, Hironobu YONEMORI^b

^a Major in Electrical and Electronics Engineering, Kogakuin University Graduate School, 1-24-2, Nishi-shinjuku, Shinjuku-ku, 163-8677, Tokyo, Japan

^b Department of Mechanical and Electronic Engineering, Salesian Polytechnic, 4-6-8 Oyama-gaoka, Machida-city, 194-0215, Tokyo, Japan

Abstract. This paper discusses the achievement of a high-efficient heating of the IH (induction heating) earthenware pan. As a problem concerning with IH earthenware pan, heating efficiency of IH earthenware pan shows poor than the other pans. In order to grasp this characteristic, we started study on the magnetic flux density distribution by using computer simulation in terms of the finite element method (FEM). Then, problem of IH earthenware pan, that of heating efficiency and leakage magnetic flux density were investigated by the FEM. The following problems became clear [1]. Heating element is small and there is much leak magnetic flux [2]. Distance between heating coil and heating element is remoteness. Then, size of the heating element is enlarged and FEM analysis is conducted. As a result, it turns out, that if the heating element is enlarged, then the leakage magnetic flux become decrease.

Keywords: IH Earthenware Pan, High Efficient Heating, Finite Element Method

1. Introduction

Recently, demand of the IH cookware and IH earthenware pan are both increasing. Earthenware pan is an indispensable utensil for cooking in Japan. However, the earthenware pan itself cannot generate heat by induction heating. Therefore, heating element has been added to an IH earthenware pan. IH earthenware pan is a cookware, which generates heat by a heating element. However, IH earthenware pan has lower heating efficiency compared with other pans. Therefore, we thought that the improvement of IH earthenware pan is essential. We try to improve heating efficiency by the simulation of magnetic flux density distribution using FEM. Firstly, magnetic flux density distribution of IH pans; IH earthenware pan, three-layers stainless steel pan and enamel pan; were made clarified[1]. As a result, IH earthenware pan has much leakage magnetic flux[2]. Distance between a heating element within the earthenware pan and a heating coil will be the cause of this poor magnetic flux distribution. Furthermore, IH earthenware pan has a heating element smaller than the other pans. Aiming for the high heating-efficiency of IH earthenware pan, FEM analysis on the IH earthenware pan and other IH pans are carried out, and are presented in this paper.

2. IH earthenware pan

IH pan can be classified into three kinds, excluding aluminium or copper pan. Stainless steel pan adopts a single-layer type and a three-layer (SUS - aluminium - SUS) type. An enamel pan is a pan which added glaze of glass quality to the pan surface. IH earthenware pan is a pan which added the heating element to the earthenware pan. This IH earthenware pan structure has 3 types. Normal earthenware pan can't be heated by IH because the normal earthenware pan induces no eddy current.

*e-mail: cm13031@ns.kogakuin.ac.jp.

On account of this, IH earthenware pan installs heating element at the bottom-inside or bottom-outside of the normal earthenware pan. In this way, the IH earthenware pan can be heated. Namely, IH earthenware pan does not generate heat at the region of earthenware. Heating element within the body of earthenware pan induces eddy current, and self-generation of heat can be realized. As a result, body of earthenware pan and water in the pan becomes be heated. Fig.1 shows appearance of the IH earthenware pan. Plate type (a): Structure that placed heating element (stainless steel plate) at the bottom-inside. And this element is removable. Interior (silver paste) type (b): Structure that applied heating element like a paste; consisting mainly of silver; at the bottom-inside of the earthenware pan. Exterior (silver paste) type(c): Structure that applied heating element; like a paste consisting mainly of silver; at the bottom-outside of the earthenware pan. Heating element of the stainless steel is removable, but silver paste heating element cannot remove. As shown above, heating element usually adopts silver or stainless steel. In this paper, plate type (a) model is adopted for the study by the experiment and Finite Element Method.

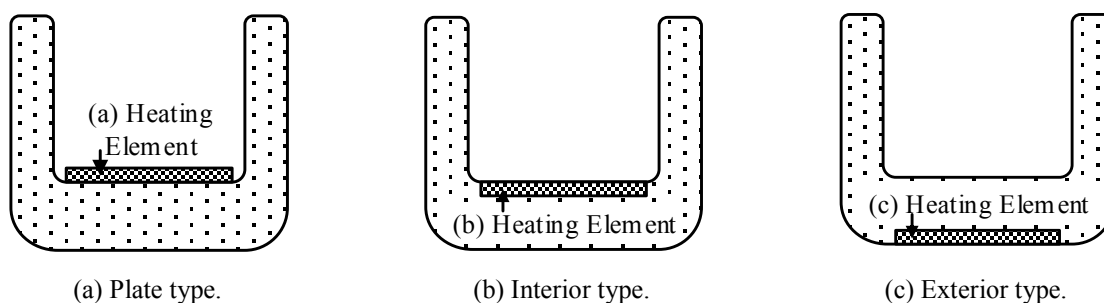


Fig. 1. Heating element of IH Earthenware pan.

3. Comparison of simulation and experiment on stainless steel pan and IH earthenware pan

The distributed heat source of IH earthenware pan is observed for a baseline assessment. And, In order to realize efficient heating of IH earthenware pan, the FEM simulation of magnetic flux density distribution is performed.

3.1. Measurement method of distributed heat source

IH cooking heater adopted in the study is a 100V input voltage and 1300W maximum output electric power. This IH cooking heater is made by ISHIZAKI ELECTRIC MFG. Co. Ltd. And, its model number is the "DIS-1300". Plate type IH earthenware pan is adopted in this study. We did observe temperature distribution from top view of IH earthenware pan using "TVS-2000Mk II" made in Japan Avionics Co., Ltd. Fig.3 shows the layout of the observation on an IH earthenware pan using thermography. However, stainless steel heating element reflects light. On account of this, observation by the thermography will fail. In order to overcome this problem, stainless steel of the heating element is painted with black. Thus, influence of the reflection of light can be eliminated. In this way, temperature of heating element, that of stainless steel is observed by the thermography. Distribution of the temperature is analyzed using a personal computer. Observation of temperature distribution is carried out 3 seconds after starting heating. Water is not put in the IH earthenware pan, because direct observation of the temperature at the heating element is intended. In other word, working of the heating element is under the empty loading.

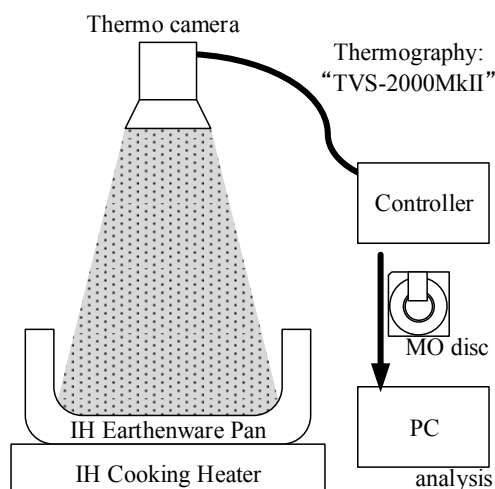


Fig. 4 Observer layout

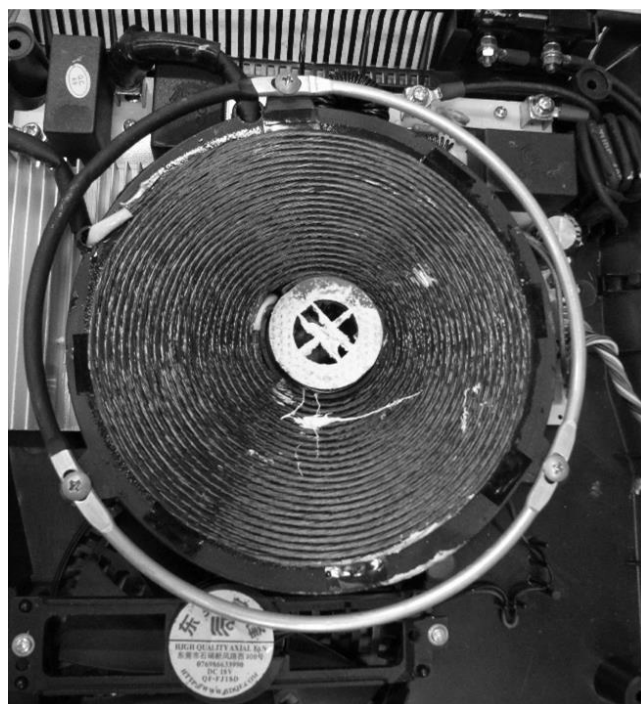


Fig. 5. Heating coil of IH Cooking Heater (top view).

3.2. Analysis of the magnetic flux density distribution by the finite element method

Finite element method analysis of IH earthenware pan was conducted using "induction heating analysis kit (Mesh 7.0, Nelson 7.0)" made from Advanced Science Laboratory, Inc. The analysis model is the same as the IH cooker and IH clay pot in Section 3.1. An analysis model is shown in Fig. 4. Fig. 5 shows top view photo of the IH Cooking Heater's heating coil. The earthenware pan part of the IH earthenware pan was unrelated to magnetic flux. So, I only show the heating element. The analysis conditions are Table 1[3] and Table 1 shows Physical constants, and table 2 shows conditions of Finite Element Method. Physical constants of Table 1 referred to the literature number 3. Size of heating coil and heating element shown in Table 2 and Fig. 4 are actual measurement, respectively.

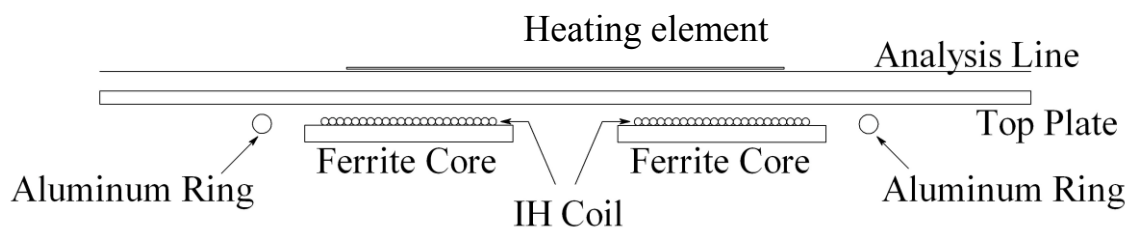


Fig. 4. Method model

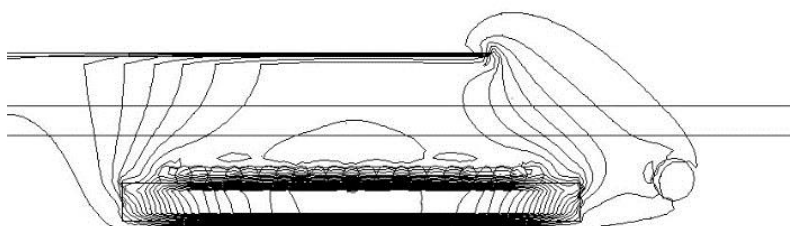


Fig. 6. Analyzed result

Table 1 [3]
 Physical constant

	Relative permeability $;\mu_r$	electrical conductivity $:\sigma$ [S/m]
Heating element (Stainless steel plate)	1.0186	7.2×10^9
Top plate (Heat resistance glass)	1	1×10^{-4}
Ferrite core	3200	0.125
Aluminum for leakage magnetic flux reduction	1	2.82×10^{-8}

Table 2
 Condition of FEM

		Specification
Heating element (stainless steel plate)	Diameter	132mm
	Thickness	0.5mm
Top plate (heat resistance glass)	Width	281mm
	Thickness	4mm
Heating coil	Diameter	147mm
	Bore	41.6mm
Diameter of Litzwire		2.3mm
	Turns	23turn
	Current	35A
	Frequency	20kHz
Ferrite core	Thickness	5mm
	length	62.7mm
Aluminum for leakage magnetic flux reduction		5.7mm
	Diameter	
	Outside diameter	188.4mm

3.3. Experimental result

Fig.6 shows result of FEM analysis. Analysis result was symmetric result from the center of the heating coil. Then, the results only show one side. Fig. 5 shows that the magnetic flux is concentrated at the heating element or at the stainless steel plate. Moreover, since the heating element is small, there is much leak magnetic flux. The temperature distribution of IH earthenware pan measured by the thermograph is shown in Fig. 7. Fig. 7 shows that temperature distribution is the same form as a heating coil. However, since a ± 3 -cm point has a hole in a heating element, temperature is low. Fig. 8 shows analysis result of the magnetic flux density distribution obtained from Fig. 6. Fig. 8 and Fig. 7 shows that magnetic flux distribution is the same form as a heating coil. As a result, temperature distribution (fig. 7) and magnetic flux distribution (fig. 8) is similar. Therefore, it is thought that an efficiency improvement becomes possible by increasing the magnetic flux density of a low-temperature portion.

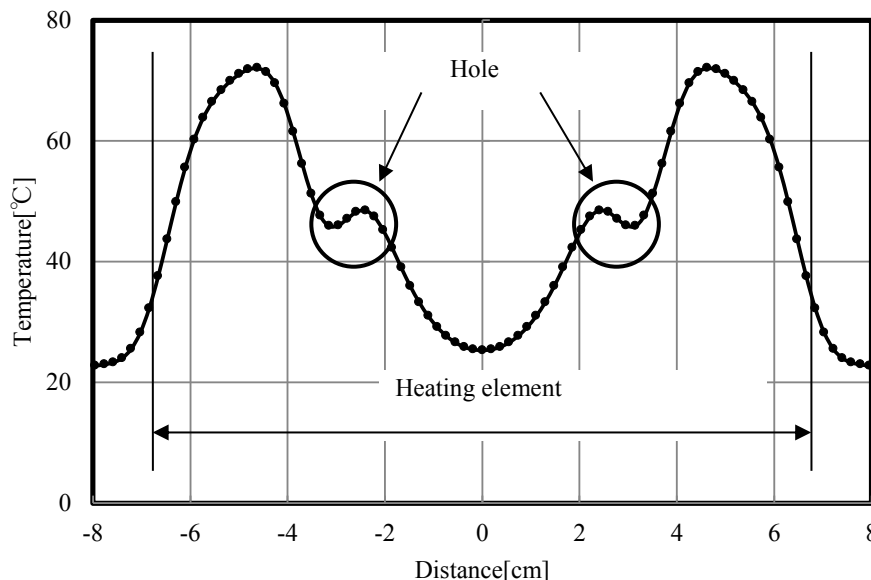


Fig. 7. Temperature distribution

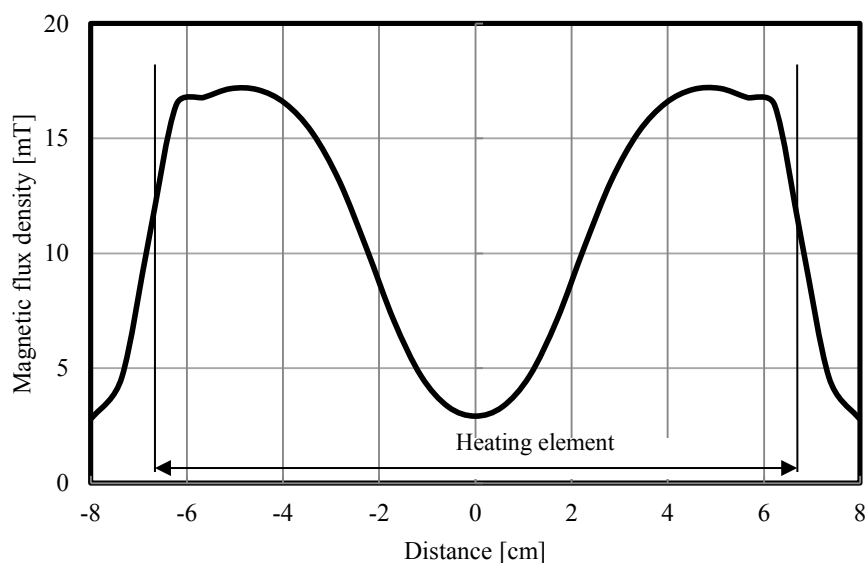


Fig. 8. Magnetic flux density distribution

4. Improvement of heating efficiency in IH earthenware pan

The simulation was performed in order to improve the heating efficiency of IH earthenware pan. The simulation is shown below. The cause of the low heating efficiency in IH earthenware pan was considered to be a size of a heating element. So, I consider change the size of the heating element. Therefore, the size of a heating element is changed and magnetic flux density distribution is considered.

4.1. FEM simulation method

Analysis was conducted using the same software as Chapter 3.2. Moreover, the analysis model of Fig. 9 was used. The heating element analyzed magnetic flux density distribution at default, 80 mm, 90 mm. Analysis conditions are Table 1 and 2.

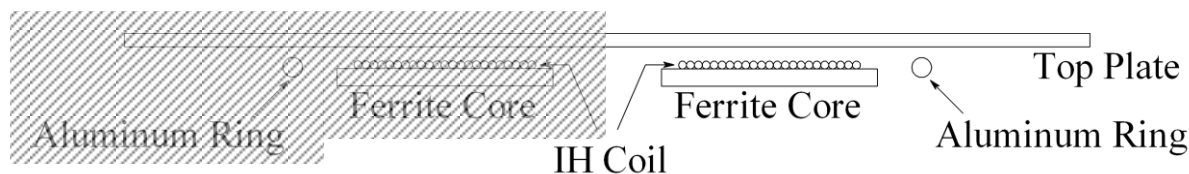


Fig. 9. Method model (No heating element and pan)

4.2. Simulation result by FEM

A simulation result is shown in Fig. 10. Fig. 10(a) has much leakage magnetic flux compared with (b)(c). And, fig. 10(b) has slightly more leakage magnetic flux than (c). In addition, fig.10(c) is very low leakage magnetic flux. Therefore, it is thought that Fig. 10(c) has much interlinkage magnetic flux to a heating element. That is, the way which enlarged the heating element of IH earthenware pan is considered that high heating efficiency.

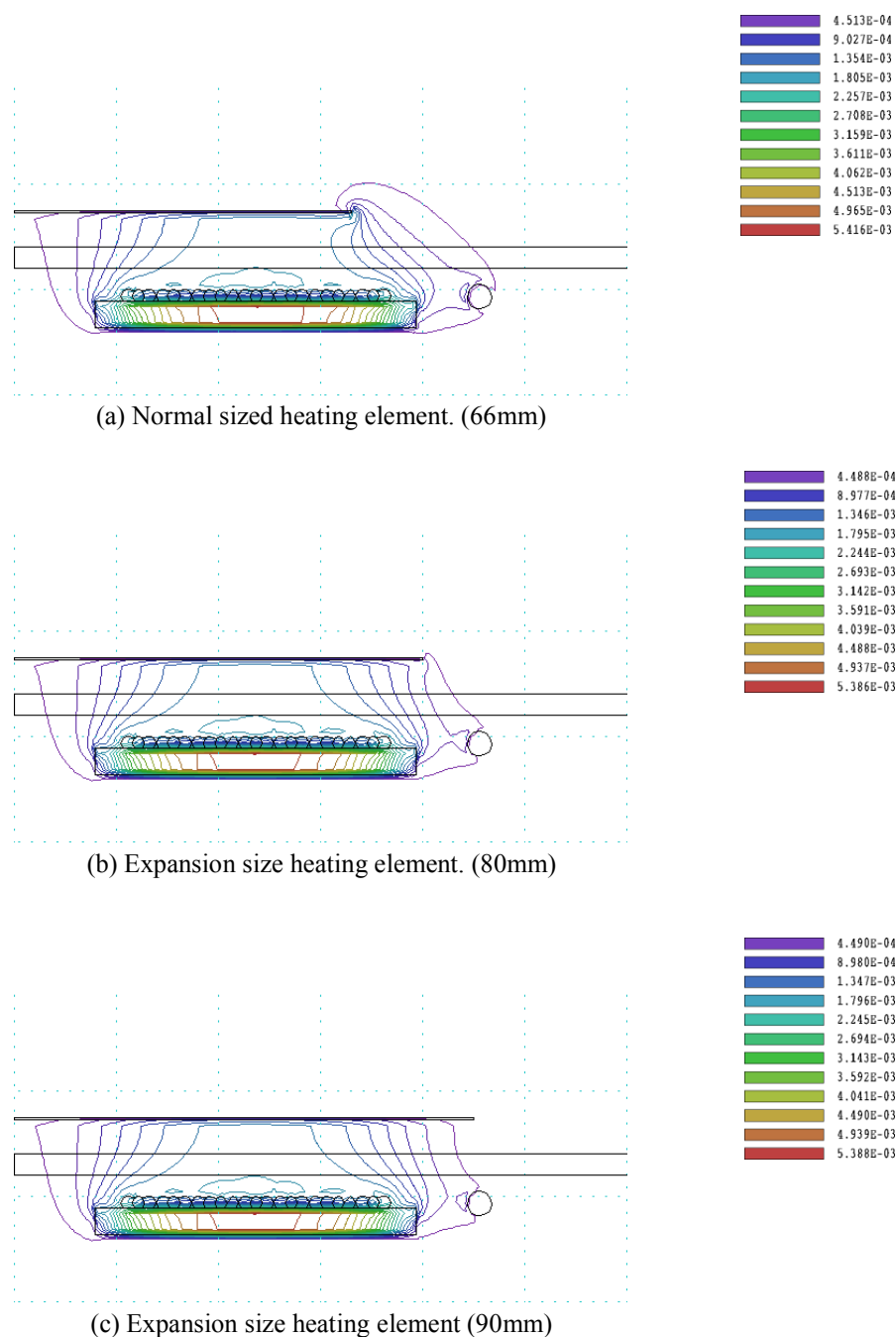


Fig. 10. Simulation results.

5. Conclusion

In this paper, in order to perform fundamental examination for making heating efficiency of IH earthenware pan high, FEM analysis was conducted. And, we clarified influence which the size of a heating element has on leakage magnetic flux. As a conclusion, we can say that high-heating-efficiency will be attained, if the heating element of the IH earthenware pan is enlarged.

References

- [1] A.Fujiwara and H.Yonemori: "A Study on the Magnetic Flux Density Distribution of IH Earthenware Pan Analyzed by Finite Element Method", IEIEJ, no. 29, 2011, pp.329-330.
- [2] A.Fujiwara and H.Yonemori: "A Study on the Magnetic Flux Density Distribution of IH Earthenware Pan Analyzed by Finite Element Method", The Consortium of Universities in Hachioji, no. 3, 2011, pp132-133.
- [3] D.Yokota, M.Kobayashi and H.Yonemori: "Study on the Improvement of Temperature Distribution and Reduction of leakage Magnetic Flux of an IH Cooking Heater", J. IEIEJ, vol. 29, No.1, 2011, pp73-78.

Design and Characteristic Analysis of Interior Permanent Magnet Synchronous Generator with Increased Magnetic Flux

Hak-Gyun Jeong^a, Ji-Young So^a, Dong-Hwa Chung^a, Chong-Hyoun Cho^b, and Dae-kyong Kim^{a,*}

^a Dept. of Electrical Control Engineering, Suncheon National University, 540-950, Suncheon, Korea

^b Sun-Tech Cop, 540-320, Suncheon, Korea

Abstract. This paper presents the design and characteristic analysis of interior permanent magnet synchronous generator (IPMSG) with increased magnet flux for a variable diesel engine generator. To analyze the characteristics of an IPMSG with the increased magnet flux accurately, a time step 2D-finite element analysis (FEA) is carried out, which is coupled with external circuit. The proposed model with increased magnet flux is increased the generated power and efficiency compared to initial model. Finally, the analysis and the design results are confirmed by the experimental results.

Keywords: Diesel generator, finite element analysis, increased magnetic flux, loading distribution method

1. Introduction

Diesel generators are widely used to supply electric power to isolated areas and emergency electricity generation. As a necessity of fixed output frequency, the engine should be rotated at synchronous speed regardless the load power demand. Especially, at light load condition, the engine is not running at the optimal speed where the fuel consumption at a given load power is minimum. In order to reduce fuel consumption and improve the system efficiency, the diesel engine speed can be varied according to the load condition [1]. Therefore, the use of effective diesel generators has remarkable economic value. In addition, interest in the design of high efficiency generators is increasing. The generator is required to maintain high efficiency against the variable load and variable speed condition. If generator is designed considering the variable load and variable speed condition, it can be required an efficient design method [1]-[4].

Normally, constant speed diesel generator system is used synchronous generator with wound rotor. Moreover, permanent magnet synchronous generator (PMSG) and doubly-fed induction generator (DFIG) have been studied for variable speed engine generator [1]-[4].

The Interior permanent magnet synchronous generator (IPMSG) has the merits of high efficiency, high generating power density and light weight. IPMSG can produce high torque due to reluctance and magnetic torque [5].

This paper presents the design and characteristic analysis of interior permanent magnet synchronous generator (IPMSG) with increased magnet flux for a variable diesel engine generator. To analyze the characteristics of an IPMSG with the increased magnet flux accurately, a time step 2D-finite element analysis (FEA) is carried out, which is coupled with external circuit. The proposed model with increased magnet flux is remained the generated power and efficiency compared to initial model. Finally, the analysis and the design results are confirmed by the experimental results.

*Corresponding author: Dae-kyong Kim, Dept. of Electrical Control Engineering, Suncheon National University, 540-950, Suncheon, Korea. Tel: +82-61-750-3546; Fax: +82-61-753-3546; E-mail: dkkim@sunchon.ac.kr

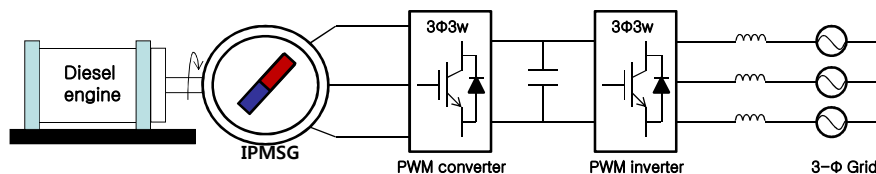
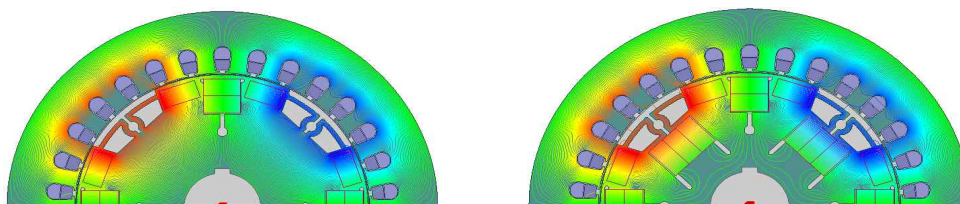


Fig. 1. System configuration of diesel generator



(a) (b)
 Fig. 2. Flux line of IPMSG (a) Initial Model (b) Proposed model

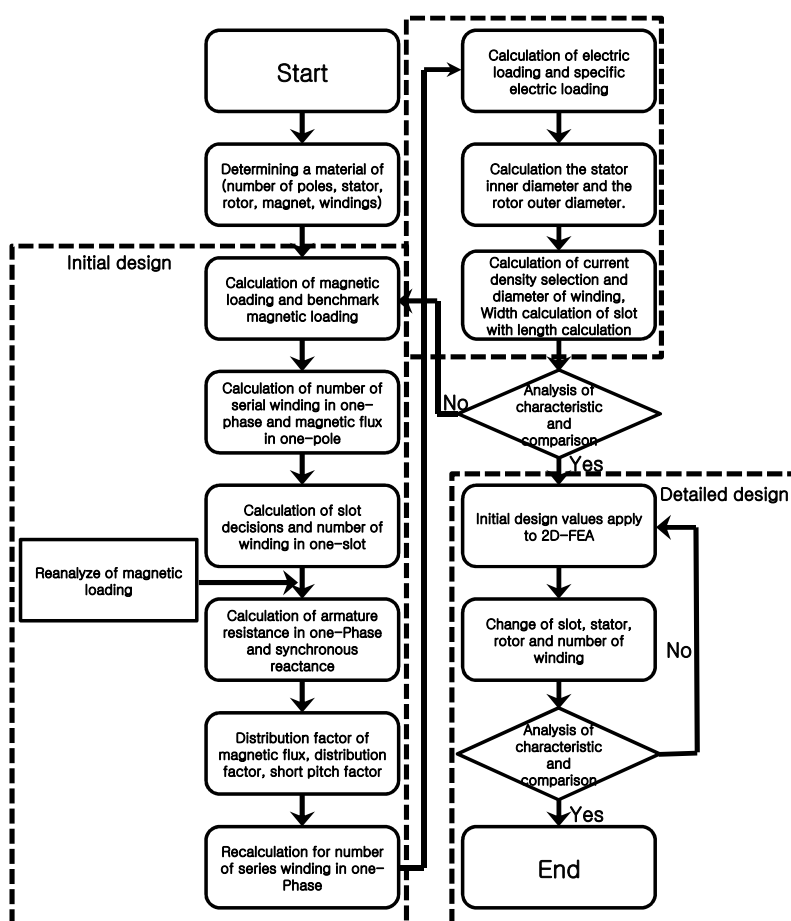


Fig. 3. Design process of IPMSG

2. Design of 4-Pole IPMSG

2.1. System configuration and structure

Fig. 1 shows the system configuration of diesel generator. Fig. 2 shows a flux line of IPMSG. Fig. 2 (a) is the initial model and Fig.2 (b) is the proposed model containing the increased magnet flux to maintain a consistent efficiency against the variable load and variable speed. The IPMSG is advantageous in terms of high efficiency and high torque. As for winding, double lap winding was used and the appropriate slot distribution was performed to improve the voltage waveform.

Table 1
 Design Results of the IPMSG using LDM

Items	Unit	Contents
Objective Specifications	Output power	[kW]
	Number of Poles	-
	Rated Voltage	[Vrms]
	Rated speed	[rpm]
Winding		Distributed winding(2Y)
Stator	Outer diameter	[mm]
	Inner diameter	[mm]
Rotor	Outer diameter	[mm]
	Inner diameter	[mm]
Magnet		NdFe35
Stack length		[mm]
Air gap		[mm]

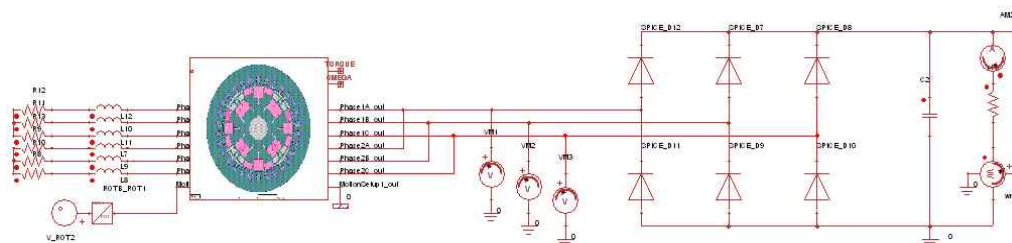


Fig. 4. 2D-FEA model coupled external circuit

2.2. Design process

Fig. 3 shows the design process for an IPMSG. The initial design and detailed values are determined using a load distribution method (LDM) which is a well-known method for designing an electric machine and a 2D-FEA which is performed for more accurate analysis of an electric machine.

Equation (1) describes the capacity per pole of an electric machine [6]. An electric machine can be designed using the electric loading and magnetic loading under a given condition such as the efficiency, output power, and power factor.

$$S[VA] = \frac{P_o}{\eta \cos \varphi p} = K_o AC \phi f \quad (1)$$

where, S is the capacity per pole, P_o is the average output power, η is the efficiency, $\cos \varphi$ is the power factor, p is the number of poles, K_o is the coefficient of the emf, AC is the electric loading, ϕ is the magnetic loading, and f is the source frequency of the electric machine.

Table 1 shows the design results of the IPMSG using LDM.

3. Characteristics analysis and experimental results

Fig. 4 shows the 2D-FEA model which is coupled external circuit. In order to simulate the generation characteristics of IPMSG model with 2Y distributed winding accurately, the winding resistance and end-turn leakage inductance derived from the equivalent circuit model have been applied to a time step 2D-FEA, and then 2D-FEA model is coupled with an external circuit.

Fig. 5 shows the generation characteristics of the initial and proposed IPMSG at DC load (22.5 [Ω]). To determine the generation efficiency, the output power W_{out} and input power W_{in} are as follows :

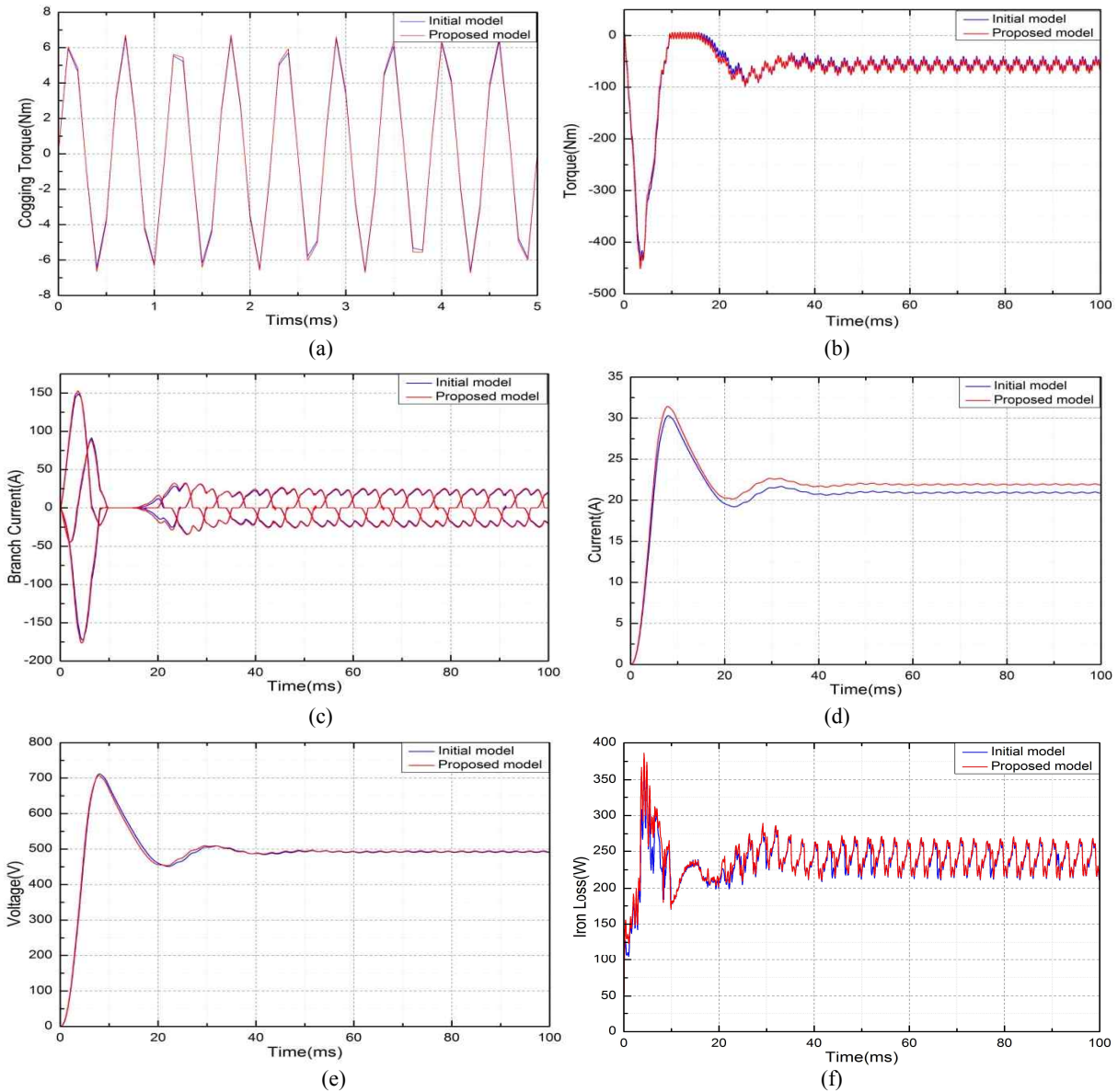


Fig. 5. Generation characteristics of the IPMSG at DC load (22.5Ω) using FEA
 (a) Cogging torque (b) Torque (c) Branch current (d) Current (e) Voltage (f) Iron loss

Table 2.
 Analysis Results of IPMSG at DC load (22.5Ω) using FEA

	Unit	Initial model	Proposed model
Input power	[W]	10,609	11,137
Output power	[W]	10,278	10,811
Torque	[Nm]	56.28	59.08
Cogging torque	[Nm]	13.13	13.31
Iron loss	[W]	239.14	242.24
Current	A	20.9	21.9
Voltage	V	491.6	493.2
Back-EMF	V	228	232
Efficiency	[%]	96.88	97.07

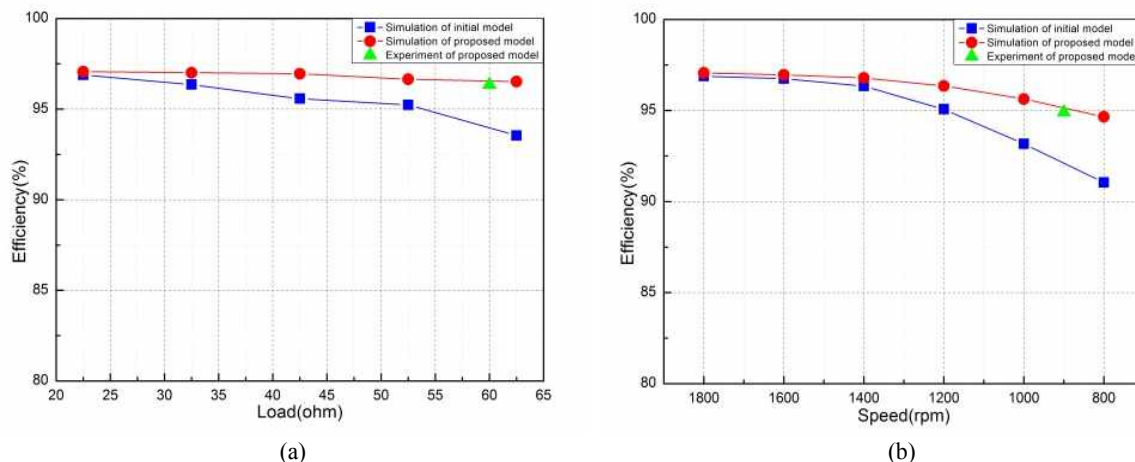


Fig. 6. Efficiency characteristics according to (a) Load variation (b) Speed variation



Fig. 7. Experimental set-up for the diesel generator

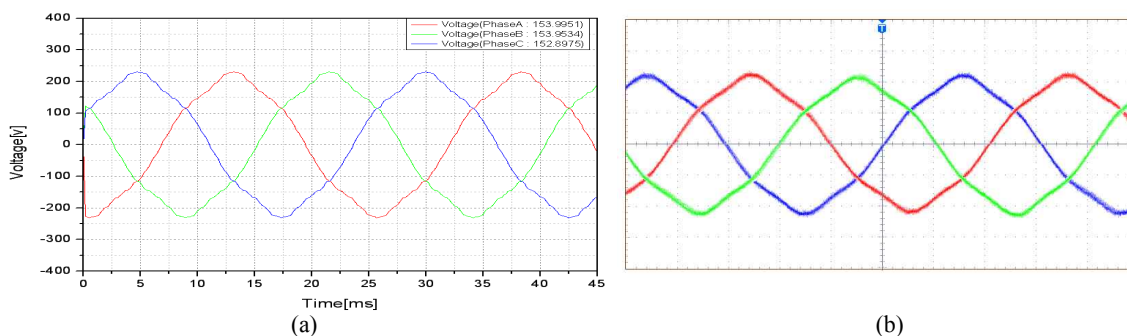


Fig. 8. Back-emf at 1,200 rpm (a) Simulation (100 [V/Div.]) (b) Experiment (100 [V/Div.])

$$W_{out} = V_{out} \times I_{out} \quad (2)$$

$$W_{in} = T_{in} \cdot \omega = T_{in} \times \left(\frac{\omega_m \times 2\pi}{60} \right) \quad (3)$$

where, T_{in} is the input torque.

In order to predict the efficiency accurately, the iron losses and the copper losses must be calculated. While a time step 2D-FEA is being analyzed, the iron losses in iron core are calculated. The iron losses consist of hysteresis and eddy-current are computed in the frequency domain. In addition, the copper loss is obtained as follows:

$$P_{cu} = I_a^2 R_f + I_b^2 R_f + I_c^2 R_f \quad (4)$$

where, R_f is the coil resistance, and I_{abc} are the branch currents.

The characteristic results of the initial model and proposed model at DC load (22.5 [Ω]) using a time-step 2D-FEA as shown in Table 2. The electrical output power of the initial model and proposed model are 10.278 [kW] and 10.811 [kW] at the rated speed, respectively, which satisfies the objective output power of the IPMSG. The efficiency of the initial model and proposed model are 96.88 [%] and 97.07 [%] at the rated speed, respectively. Therefore, the efficiency of the initial model and proposed model are almost similar at 10 [kW] electrical output power.

Normally, a variable speed diesel generator with an inverter for emergency situation can be operated at 2~3 times load conditions. In such case, if the IPMSG for diesel generator maintains a constant efficiency at the variable load and speed condition, a diesel generator can be saved the energy.

Fig. 6 shows efficiency characteristics according to load and speed variation. The efficiency of proposed model with the increased magnetic flux remains constant compared to the initial model has a sharply decreasing rate at 2~3 times load condition. The efficiency of proposed model has not a rapidly decreasing rate compared to the initial model according to the changed speed. In addition, the efficiency of proposed model have been measured experimentally at about 3 times load condition (60 [Ω]) and a low speed condition (900 [rpm]). It shows good agreement between the analytical and the experimental results as shown in Fig. 6.

Fig. 7 shows the experimental set-up for the diesel generator. The validity of the simulation model was confirmed by comparing back-emf of experiment at 1,200 [rpm] like Fig. 8.

4. Conclusion

This paper presents the design and characteristic analysis of interior permanent magnet synchronous generator (IPMSG) with increased magnet flux for a variable diesel engine generator. To analyze the characteristics of an IPMSG with the increased magnet flux accurately, a time step 2D-finite element analysis (FEA) is carried out, which is coupled with external circuit. The efficiency of proposed model with the increased magnetic flux remains constant compared to the initial model has a sharply decreasing rate at 2~3 times load condition. The efficiency of proposed model has not a rapidly decreasing rate compared to the initial model according to the variable speed. Finally, the analysis and the design results are confirmed by the experimental results.

Acknowledgments

This work was supported by the New & Renewable Energy of the Korea Institute of Energy Technology Evaluation and Planning (KETEP) Grant funded by the Korea government Ministry of Knowledge Economy. (No. 20113030060010)

References

- [1] J. H. Lee, S. H. Lee and S. K. Sul, Variable-Speed Engine Generator with Supercapacitor : Isolated Power Generation System and Fuel Efficiency, *IEEE TRANSACTIONS ON INDUSTRY APPLICATIONS*, VOL. 45, NO. 6, NOVEMBER/DECEMBER 2009
- [2] Waris, T. and C. V. nayar, Variable speed constant frequency diesel power conversion system using doubly fed induction generator (DFIG), *Power Electronics Specialists Conference*, pp.2728-2734, 2008
- [3] US patent 7876014, Permanent magnet rotor with increased magnetic flux, 2011
- [4] J. Cunshan, Research on improving permanent magnetic generator output characteristic, *ICEMS 2001*, Vol. 2. Aug 2001
- [5] J. Hemmelmann, A. Fiseni, K. Sivasubramaniam, M. Avanesov, E. Kazmin, Efficiency Measurement and Design Verification of a medium-Speed PMSG, *IEEE Power and Energy Society General Meeting*, 2010
- [6] T. Takeuchi et al., (A University Course) Design Theory of Electricity. : Ohm Corp., 1979, pp. 79–97, (book).

Transient Performance of Novel Permanent Magnet Synchronous Motors Made of Soft Magnetic Composite Core

Takeo Ishikawa, Quang Viet Ho, Kazutoshi Takahashi, and Nobuyuki Kurita
*Department of Electronic Engineering, Gunma University,
1-5-1 Tenjin-cho, Kiryu, Gunma, 376-8515, Japan*

Abstract. We have developed a novel permanent magnet synchronous motor, whose stator and rotor are made of the soft magnetic composite core. It looks like a hybrid type stepping motor utilizing three-dimensional magnetic flux flow. The hollow of the stator teeth is introduced for the reduction of copper loss and the reduction of motor volume. This paper develops their driving system as the brushless DC. The motor is driven on the d- and q-axis and the control system is realized using MATLAB on DS1104 DSP board. The speed step responses show the good performance.

Keywords: soft magnetic composite core, brushless DC motor, transient performance, DSP

1. Introduction

Recently, the demand for the downsizing and high efficiency of motors is rising more and more. One of the possible solutions for that is the adaption of a new material core. Soft magnetic composite (SMC) materials are basically iron powder particles separated with an electrically insulated layer. Then have several merits including low eddy current loss, three-dimensional (3-D) isotropic ferromagnetic behavior, flexible machine design and assembly, and relatively good recyclability. However it has a little poor magnetic property. The saturated flux density is slightly low and the unsaturated relative permeability is not high compared with laminated cores. Therefore, the exchange of the laminated core into the SMC core in conventional motors, in which the magnetic flux flows in two-dimensional direction, cannot give a better performance. Several motors utilizing the SMC material have been developed and analyzed, for example, claw pole motors [1], [2], permanent magnet motors [3]-[9], an induction motor [10] and a linear motor [11].

We have also manufactured a cylindrical type of linear actuator made of the SMC core [12], [13] and a permanent magnet synchronous motor made of the SMC core [14]. The developed permanent magnet synchronous motor looks like a hybrid type stepping motor, which utilizes 3-D isotropic ferromagnetic behavior. And we have calculated the electromotive force and the cogging torque of the developed motor by using 3-D finite element analysis, and compared with the measured ones [14]. This paper investigates the transient performance of the developed permanent magnet synchronous motors.

2. Developed motors

Fig. 1 shows a stator and a rotor of a developed brushless DC motor made of the SMC core. Fig. 2 shows a fabricated motor and magnetic flux path in the motor, in which stator windings and some cores are omitted for easy view. The shape of this motor is similar to a hybrid type stepping motor. The stator has six main teeth, whose tooth tip has two sub-teeth. The rotor is made of four cores, and each core has 10 teeth. Two disc-shaped magnets are inserted between two cores. It is noted that there are hollows of the stator main teeth, namely, the stator sub-teeth have an overhang concerning the stator main teeth. This paper introduces it for the reduction of the length of stator coil which results in the reduction of

copper loss and for the reduction of motor volume.

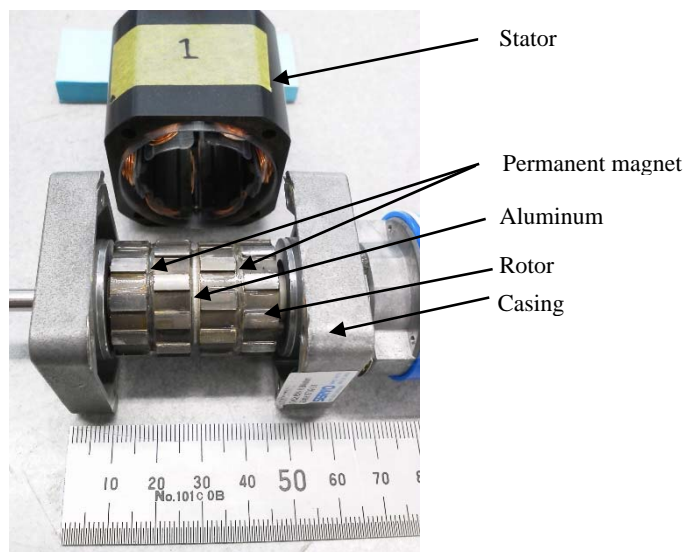


Fig. 1. A photograph of stator and rotor of the developed permanent magnet synchronous motor made of SMC core.

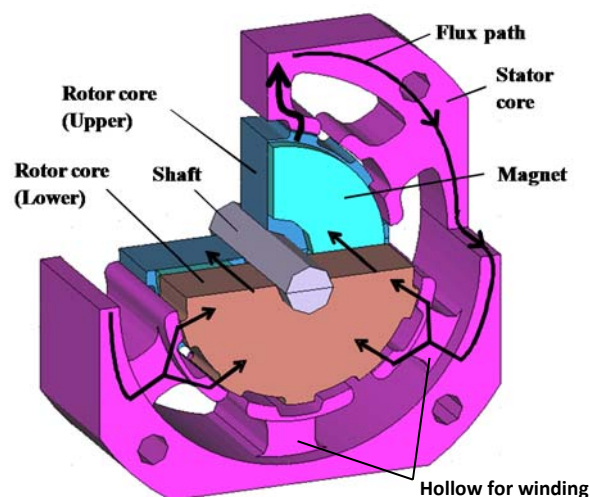
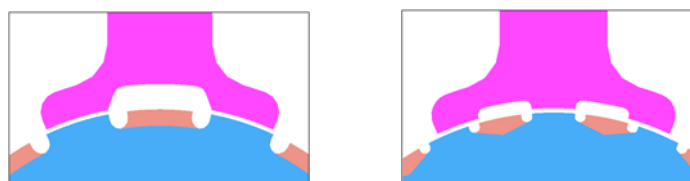


Fig. 2. The magnetic flux path in the motor.



(a) Motor model A

(b) Motor model B

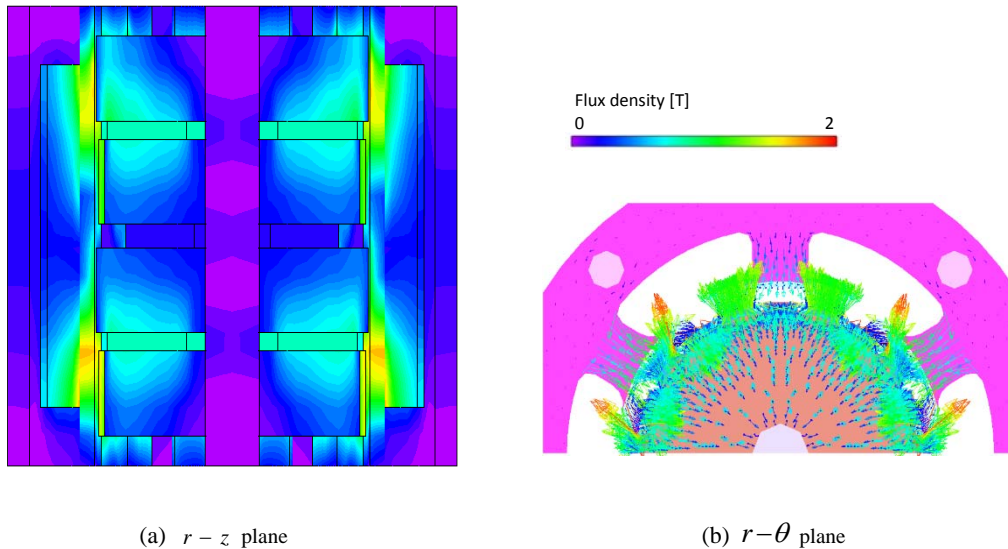
Fig. 3. Two types of developed motor.

The magnetic flux produced by permanent magnets is shown by arrows in Fig. 2. It passes through an upper rotor core, air-gap, an upper stator core, a lower stator core, air-gap, a lower rotor core, and then permanent magnet, namely, in 3-D direction. Therefore, the SMC material is suitable to this type of motor. The special features are that the permanent magnets in the rotor produce the axial magnetic flux, and that the stator teeth have the hollows to reduce the copper loss and the motor volume.

We have manufactured two kinds of motor shown in Fig. 3. Motor type A has 10 rotor teeth and 12 stator sub-teeth, and motor type B has 16 rotor teeth and 18 stator sub-teeth. The stator resistance is reduced from 0.538 to 0.456 by adapting the hollows of the stator teeth. The outer diameter of stator, the outer diameter of rotor and the air gap are 50.2 mm, 25.57 mm and 0.2 mm, respectively.

Fig. 4 shows the flux density distribution in the motor model A at no-load condition. Since the magnetic flux passes through 3-D direction in these motors, a 3-D finite element analysis is necessary.

This analysis was carried out for a half model, because of the symmetry in $r-\theta$ plane. It is shown that the magnetic flux concentrates at the stator sub-teeth and the rotor teeth, and that the maximum flux density becomes about 2 T.



(a) $r-z$ plane (b) $r-\theta$ plane
 Fig. 4. Flux density distribution of motor A at no-load condition.

3. Transient performance

3.1. Experimental setup

The experimental permanent magnet synchronous motor made of the SMC core is driven as a brushless DC motor fed by a sinusoidal stator current. The voltage equations on the d- and q-axes are given by

$$\begin{bmatrix} v_d \\ v_q \end{bmatrix} = \begin{bmatrix} R_a + PL_d & -\omega_{re}L_q \\ \omega_{re}L_d & R_a + PL_q \end{bmatrix} \begin{bmatrix} i_d \\ i_q \end{bmatrix} + \begin{bmatrix} 0 \\ \omega_{re}\Phi_f \end{bmatrix} \quad (1)$$

where v_d , v_q , i_d , i_q , R_a , L_d , L_q , ω_{re} , Φ_f , and P are d-axis voltage, q-axis voltage, d-axis stator current, q-axis stator current, stator resistance, d-axis inductance, q-axis inductance, electric angular frequency, magnetic flux produced by permanent magnets, and a differential operator, respectively.

Fig. 5 shows a control block for the brushless DC motor drive system built on a DS1104 DSP board. In this block diagram, a three-phase permanent magnet motor is fed by a three-phase PWM inverter, and two control loops are used; one is the inner loop to regulate the d- and q-axis stator currents, and the other is the outer loop to control the motor speed. In this figure, *DS1104BIT_IN_C4*, *DS1104MUX_ADC*, *DS1104ENC_POS_C1*, and *DS104SL_DSP_PWM3* are an input signal, stator current signals with AD converters, rotor position signal with an encoder connected to the rotor, and output signals to PWM inverter. The block *PI with limiter* is a proportional and integral controller with a limiter for the motor speed. The blocks *Ki_d* and *Ki_q* are the proportional controller for the d- and q-axis stator currents. The block *uvw2dq_2* translates three-phase current to the d- and q-axis currents by calculating with rotor angle. The block *dq2uvw* translates the reference signal of d- and q-axis stator voltages to three-phase voltages. The proportional block and block “+0.5” are translates the reference signal of stator voltage to the duty cycle of the PWM inverter. In order to see the signal on each scope, we have developed a layout window on a PC connected to DS1104 board shown in Fig. 6. The gains of the controller are also set in this layout window, and signals are saved in the PC.

Fig. 7 shows an experimental setup. The system is composed of the motor, a torque meter, a hysteresis brake as the load, and an inverter.

3.2 Experimental results

Fig. 8 shows the measured responses of motor A, when a speed step reference of 50 rad/s is input. Because there is a limiter in PI speed controller, i_q becomes an approximately constant value of 0.7 A. The developed torque is given by

$$T = p\Phi_f i_q + p(L_d - L_q) i_d i_q \quad (2)$$

where p is the number of pole pairs, and is 10 and 16 for motor A and motor B, respectively. The constant i_q produces a constant torque, because L_d and L_q of the motor A are the approximately same values. And thus, the slope of the speed ω_m is constant. After the motor speed reaches the reference value of 50 rad/s, it is controlled to the reference value. Fig. 9 shows the measured responses of motor B. The step responses of ω_m , i_d and i_q are almost the same as those of motor A.

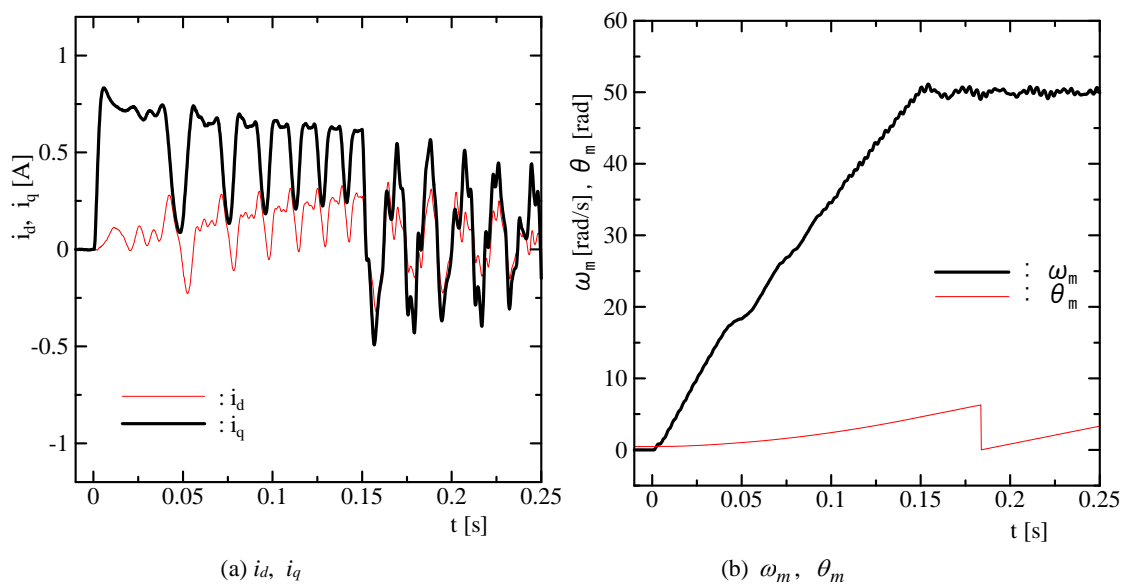


Fig. 8. Measured speed step response of motor A.

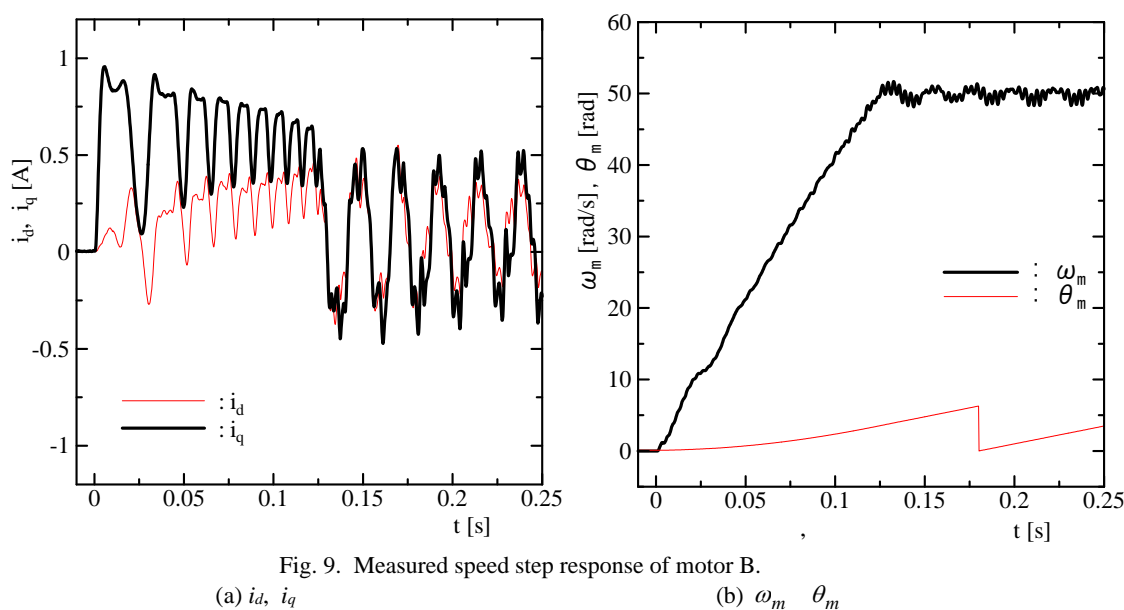


Fig. 9. Measured speed step response of motor B.

4. Conclusions

We developed the novel permanent magnet synchronous motors made of soft magnetic composite material. They have not only the 3-D magnetic flux but also the hollow of the stator teeth, which give the reduction of copper loss and the reduction of motor volume. This paper has developed their driving system as the brushless DC motor. The motor is driven on the d- and q-axis and the control system is

realized using MATLAB on DS1104 DSP board. The speed step responses have been measured and have shown the good performance. Experimental validation for the loss and the efficiency of the developed motors is the future work.

References

- [1] Y. Guo, J. Zhu, P. Watterson, and W. Wu: Comparative study of 3-D flux electrical machines with soft magnetic composite cores, *IEEE Trans. on Industry Applications*, **39**, 6 (2003), 1696-1703.
- [2] Y. Huang, J. Zhu and Y. Guo: Thermal analysis of high-speed SMC motor based on thermal network and 3-D FEA with rotational core loss included, *IEEE Trans. on Magn*, **45**, 10 (2009), 4680-4683.
- [3] A. Jack, B. Mecrow, and C. Maddison: Combined radial and axial permanent magnet motors using soft magnetic composites, *IEE Conf. Publ.*, **468** (1999), 25-29.
- [4] G. Cvetkovski, L. Petkovska, M. Cundev and S. Gair: Improved design of a novel PM disk motor by using soft magnetic composite material, *IEEE Trans. on Magn*, **38**, 5 (2002), 3165- 3167.
- [5] T. Henneron, S. Clenet, J. Cros, and P. Viaroge: Evaluation of 3-D finite element method to study and design a soft magnetic composite machine, *IEEE Trans. on Magn*, **40**, 2 (2004), 786-789.
- [6] Y. Enomoto, M. Ito, H. Koharagi, R. Masaki, S. Ohiwa, C. Ishihara and M. Mita: Evaluation of experimental permanent-magnet brushless motor utilizing new magnetic material for stator core teeth, *IEEE Trans. on Magn*, **41**, 11 (2005), 4304-4308.
- [7] M. Abu Sharkh and N. Mohammad: Axial field permanent magnet DC motor with powder iron armature, *IEEE Trans. on Energy Conversion*, **22**, 3 (2007), 608-613.
- [8] G. Cvetkovski and L.G. Petkovska: Performance improvement of PM synchronous motor by using soft magnetic composite material, *IEEE Trans. on Magn*, **44**, 11 (2008), 3812-3815.
- [9] T. Ibrahim, J. Wang and D. Howe: Analysis and experimental verification of a single-phase, quasi-halbach magnetized tubular permanent magnet motor with non-ferromagnetic support tube, *IEEE Trans. on Magn*, **44**, 11 (2008), 4361-4364.
- [10] T. Masuda, Y. Kawase, T. Yamaguchi, T. Okouchi, H. Ohno, G. Nord and K. Kanno: 3-D finite element loss analysis of squirrel-cage induction motor using SMC, *J of the Japan Society of Applied Electromagnetics and Mechanics*, **15**, 3 (2007), 230-233.
- [11] J. Wang and D. Howe: Influence of soft magnetic materials on the design and performance of tubular permanent magnet machines, *IEEE Trans. on Magn*, **41**, 10 (2005), 4057-4059.
- [12] T. Mogi, T. Ishikawa, S. Hashimoto, M. Matsunami, M. Sakamoto and A. Nakayama: Analysis of thrust and core loss of linear motor with magnetic powder core, *12th biennial IEEE CEFC*, (2006), PB8-1.
- [13] T. Ishikawa, M. Oono and M. Matsunami: Analysis of a developed linear actuator with soft magnetic composite material, *14th biennial IEEE CEFC*, (2008), PC4-3.
- [14] T. Ishikawa, K. Takahashi, Q. V. Ho, M. Matsunami and N. Kurita: Analysis of novel brushless DC motors made of soft magnetic composite core, *IEEE Transactions on Magnetics*, **48**, 2 (2011) 971-974.

Full 3D Eddy Current and Temperature Field Analysis of Large Hydro-generators in Leading Phase Operations

Ning WANG, Lei LIU, Haijuan ZHOU, Shiyou YANG*

College of Electrical Engineering, Zhejiang University, 310027, Hangzhou, China

*Corresponding Author: shiyouyang@yahoo.com

Abstract. Accurate and precise determination of the leading phase operation capacity of a large hydro-generator has always been a formidable challenge to engineers and academicians. To address this problem, the full three dimensional (3D) finite element models and methods are developed for numerical solutions of the coupled eddy current and temperature fields in the end region of a large hydro-generator. Also, the equivalent medium parameters used in the computations are comprehensively discussed. Numerical results on the coupled eddy current and temperature fields in the end regions of a 250MW hydro-generator confirm positively the feasibility of the present work.

Keywords: Hydro-generator, finite element method, eddy current field, temperature field

1. Introduction

Generally, a large hydro-generator is required to work in leading phase conditions to absorb the reactive power of the power grid under some abnormal cases. As it is well known, the high temperature rise in the end region is one critical factor to restrict the leading phase operation capacity of a generator. However, the precise determination of the temperature fields has always been formidable challenges to both engineers and academicians because of the complicated nature of the coupled eddy current-temperature fields in senses of a complicated 3D geometry and the nonlinear behavior of the ferromagnetic materials [1],[2].

To solve the electromagnetic and temperature field distributions in the end regions of a large generator including a hydro-generator, new models and methods are continuously being developed and applied [3]-[7]. In [3], the quasi-3D finite element method is applied to investigate the eddy current field in the end region of 1000 MW turbogenerator; In [4], the stator windings end part temperature field of large synchronous generators are numerically studied; In [5] and [6], the electromagnetic fields in the end region of a large turbo-generator are computed; and in [7], the influence of metal screen materials on 3-D electromagnetic field and eddy current loss in the end region of turbo-generator are studied. Nonetheless, the coupled eddy current and temperature fields in the end region of large hydro-generators in leading phase operations have not been comprehensively studied in literatures.

To comprehensively understanding the characteristics of the coupled eddy and temperature fields in the end region of large hydro-generators, the full 3D finite element models and methods are proposed and implemented on a 250 MW hydro-generator to investigate its eddy current field and temperature field distributions under no-load, leading phase, and rated operation conditions. Also, the equivalent medium parameters used in the computations are comprehensively discussed.

2. Model and method

2.1 Solid Model

As shown in Fig.1, a minimal part of the end region of a hydro-generator is studied due to its fractional slot characteristics.

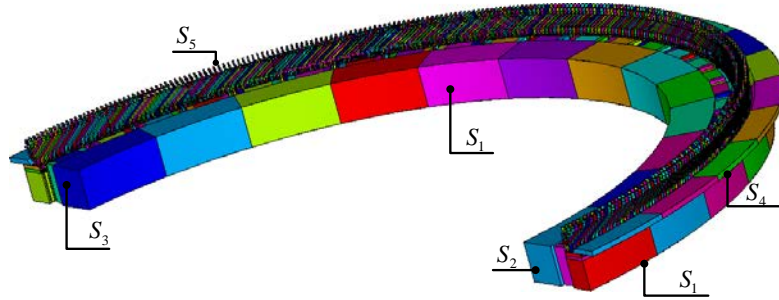


Fig. 1. The Schematic diagram of the solid model

2.2 Full 3D FEM Model of Eddy Current Fields

To precisely simulate the complicated 3D geometry of the end regions of a large hydro-generator and the saturation of ferromagnetic materials, the full 3D harmonic finite element model and method based on the vector magnetic potential A and the scalar electric potential φ are developed. Generally, the materials in the end region of a hydro-generator include conductors, ferromagnetic materials and air, and these materials correspond, respectively, to the regions V_1 , V_2 and V_3 of Fig. 2. The governing equations in these regions are:

$$\begin{cases} \nabla \times (\nu \nabla \times \mathbf{A}) - \nabla (\nu \nabla \cdot \mathbf{A}) + j\omega \sigma \mathbf{A} + \sigma \nabla \varphi = \mathbf{J}_s & \text{in } V_1 \\ \nabla \cdot (-j\omega \sigma \mathbf{A} - \sigma \nabla \varphi) = 0 \end{cases} \quad (1)$$

$$\nabla \times (\nu \nabla \times \mathbf{A}) - \nabla (\nu \nabla \cdot \mathbf{A}) = 0 \quad \text{in } V_2 \quad (2)$$

$$\nabla \times (\nu_0 \nabla \times \mathbf{A}) - \nabla (\nu_0 \nabla \cdot \mathbf{A}) = 0 \quad \text{in } V_3 \quad (3)$$

By applying the Galerkin residual method for spatial discretizations of (1)~(3), the equation sets for the 3D harmonic finite element method are developed.

The boundary conditions for the exterior surfaces include the flux parallel on surface S_1 , the symmetric condition on surfaces S_2 and S_3 , and the far field conditions on surfaces S_4 and S_5 , as depicted in Fig. 1. To consider the laminated iron core, an equivalent permeability is defined and used:

$$\hat{\mu} = \frac{\sum_i B_i^2}{\sum_i B_i H_i} \quad (4)$$

where B_i and H_i are, respectively, the flux density and the magnetic field intensity at sampling point i in the laminated iron core.

Once the eddy current fields are determined using full the 3D finite element analysis, the heat generation in the iron and the conductor are determined, respectively, from:

$$P = k p_a B^2 f^{1.3} G, \quad (5)$$

where, k is a coefficient (1.3 for the core and 1.7 for the tooth), G is the weight of the iron material, f is the frequency, and

$$P = \sigma J^2 V \quad (6)$$

where, σ is the conductivity of the conductor, V is the volume of the conductor.

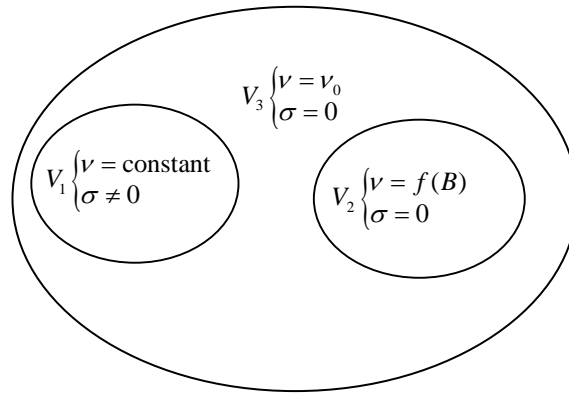


Fig. 2. The schematic diagram of electromagnetic field regions.

2.3 Full 3D FEM Model of Temperature Fields

In the thermal analysis of the finite element simulations, the air regions are excluded from the numerical model to reduce the computational burdens. Consequently, one uses an equivalent convection coefficient in the interface of the air and other medium to model the heat diffusion. Moreover, the averaged heat generation of one period in the eddy current field solutions is used in the temperature field analysis, and the governing equation for the full 3D steady-state temperature fields is:

$$\frac{\partial}{\partial x}(\mu_x \frac{\partial T}{\partial x}) + \frac{\partial}{\partial y}(\mu_y \frac{\partial T}{\partial y}) + \frac{\partial}{\partial z}(\mu_z \frac{\partial T}{\partial z}) = -q \quad (7)$$

where; T is the temperature; μ_x , μ_y , and μ_z are, respectively, the thermal conductivity in x , y , z directions; q is the heat density.

The corresponding variational form is:

$$J(T) = \int_V [\frac{\mu_x}{2} (\frac{\partial T}{\partial x})^2 + \frac{\mu_y}{2} (\frac{\partial T}{\partial y})^2 + \frac{\mu_z}{2} (\frac{\partial T}{\partial z})^2 - Tq] dV + \frac{1}{2} \alpha \int_{s_2} (T - 2T_c) T dS = \min \quad (8)$$

$$T|_{s_1} = T_1$$

2.4 Determination of the Spatial Position of Phase A of the Stator

In the leading phase capacity study, another critical issue is the determination of the relative spatial position of Phase A of the stator. According to the schematic diagram of the relationship between the stator and rotor currents, as shown in Fig.3, the angle ψ_0 is computed using

$$\psi_0 = \arctan \frac{Ix_q - U \sin \phi}{Ir_a + U \cos \phi} \quad (9)$$

Once the ψ_0 is determined, the angle between the stator field and exciting field is easily set as $\varphi = \psi_0 + \pi / 2$. Moreover, according to the principle of electrical machine, the equivalent axis of a rotating magnetic field generated by a three phase-120° different windings is exactly the same of the axis position of the phase with the maximum amplitude of the winding currents. Thus special angle between the axis of the phase A and the exciting field winding should be exactly φ if one set the amplitude and initial phase angle of the Phase A current, respectively, to the maximum value and

zero.

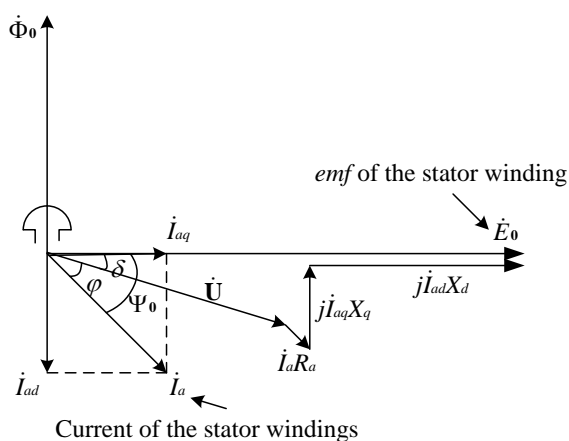


Fig. 3 The schematic diagram of the relationship between the stator and rotor current.

3. Numerical results

To validate the proposed models and methods, the coupled eddy current and temperature fields in the end regions of a 250 MW hydro-generator is computed. Fig. 4 gives the eddy current field and temperature field of the generator at the no-load operating condition while Fig. 5 presents the corresponding results for a 0.95 leading phase operation of the same generator. Clearly, these numerical results confirm positively the feasibility and advantages of the presented model and method; and moreover, they are essential for the computation of the leading phase operation capacity of a large hydro-generator.

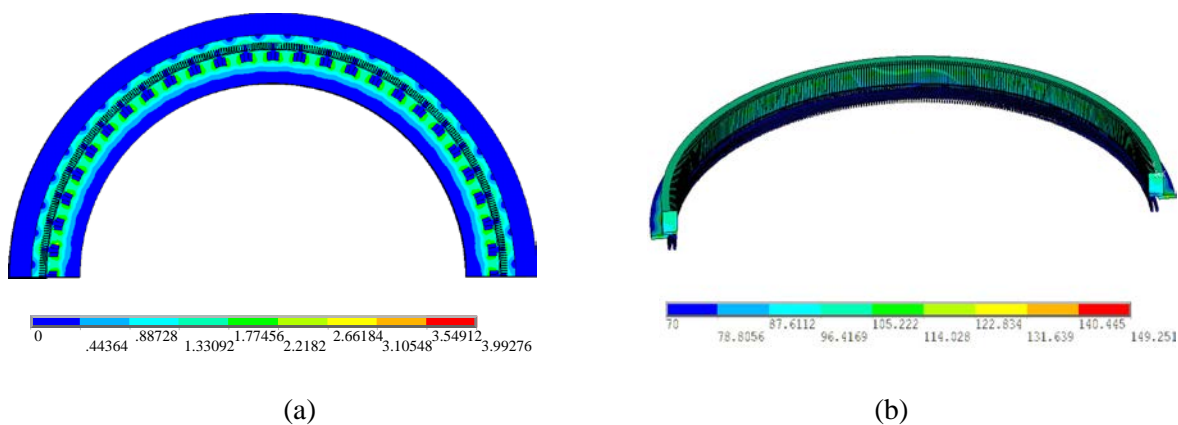


Fig. 4. The computed (a) eddy current field (flux density) and (b) temperature field at no-load operation

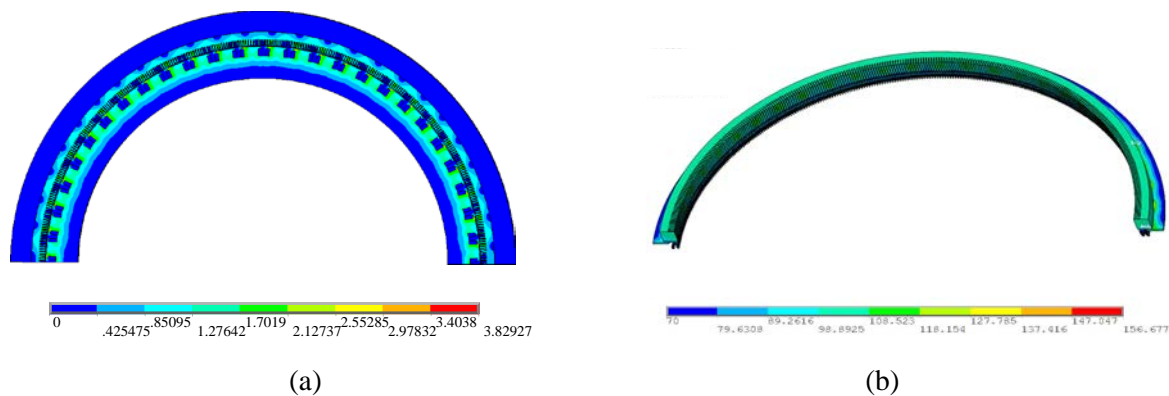


Fig. 5. The computed (a) eddy current field (flux density) and (b) the temperature field at a 0.95 leading phase operation

4. Conclusions

The three dimensional models and methods for the coupled eddy current and temperature fields in the end regions of a large hydro-generator are proposed and implanted in this paper. According to the knowledge of the authors, there are relatively fewer literatures in recent years to report the progress on this topic. The authors thus believe that this work would be helpful for engineers in computing the leading phase capacity of large hydro-generators.

References

- [1] B. Frei-Spreiter, K. Reichert, Calculation of end winding fields of turbogenerators by integral methods for modelling mechanical characteristics, *IEEE Trans. Magn.*, 34 (1998) 3636-3639.
- [2] R. Albanese, F. Calvano, G. Dal Mut, F. Ferraioli, A. Formisano, F. Marignetti, R. Martone, A. Romano, G. Rubinacci, A. Tamburrino, and S. Ventre, Coupled three dimensional numerical calculation of forces and stresses on the end windings of large turbo generators via integral formulation, *IEEE Trans. Magn.*, 48 (2012) 875-878.
- [3] Y. Yingying, X. Haixia, N. Guangzheng, et al. 3-D eddy current analysis in the end region of a turbogenerator by using reduced magnetic vector potential. *IEEE Transactions on Magnetics*, 2006, 42(4): 1323-1326.
- [4] Y. Hou, W. Li, F. Zhou, and S. Cheng, "Analysis and calculation of stator windings end part temperature field for large synchronous generator," *Proceedings of the Fifth International Conference on Electrical Machine*, 2001:1145-1148.
- [5] J. Li, Y. Sun, and G. Yang, Calculation and analysis of 3D magnetic field for end region of large turbogenerators, *ICEMS 2005. Proceedings of the Eighth International Conference on Electrical Machines and Systems*, 2005: 2079-2082.
- [6] L. Yanping, H. Hao, and H. Gang, Numerical calculation of end region electromagnetic field of large air-cooled turbogenerator, *Automation Congress*, 2008: 1-5.
- [7] W. Likun, H. Feiyang, L. Weili, Z. Yihuang, L. Qing, L. Yong, et al., Influence of Metal Screen Materials on 3-D Electromagnetic Field and Eddy Current Loss in the End Region of Turbogenerator, *IEEE Trans. Magnetics*, 2013(49) 939-945.

Three-Dimensional Simulation of a Corona Discharge in a Needle-Plane Configuration

Julio C. Momente^{a,*}, Leandro A. Neves^a, Geraldo F. D. Zafalon^a, Alex S. R. Pinto^a, Carlos R. Valêncio^a, Yang Shiyu^b and José M. Machado^a

^a São Paulo State University (UNESP), São José do Rio Preto, SP, Brazil

^b College of Electrical Engineering, Zhejiang University, China

Abstract. Corona discharges have a large applicability and are very useful for many industrial applications. Despite this fact, few works performing the three-dimensional modeling and simulation of corona discharges have been reported. This work aims to perform a finite element method (FEM), three-dimensional computer modeling of a corona discharge in a needle-plane configuration. The simulation software was based on integrated open source codes, providing good code availability for other users.

Keywords: Corona Discharges, Finite Element Method, Three-Dimensional Simulation

1. Introduction

Corona discharges are a very important phenomenon for several applications, such as ozone generation, water purification, electrohydrodynamic (EHD) flow generation, among many others. Despite the large applicability of corona discharges, including many industrial processes, few works have been addressed to the three-dimensional computer simulation of corona devices. However, these simulations could provide useful information towards the optimization of related industrial applications and processes.

Corona discharges usually occur between two or more electrodes when a high electric potential is applied and electrodes must have very different radii of curvature [1]. This electric discharge ionizes the fluid surrounding the corona electrode, the sharp one. The ionization layer occurring around the corona electrode leads the motion of the fluid between the electrodes. The fluid motion due to corona discharge is called ElectroHydroDynamic flow (EHD flow) [2, 3, 4].

The present work consists in the three-dimensional modeling of a corona discharge problem with a needle-plane setup and simulation, using the finite element method (FEM), and an iterative technique for solving the corresponding algebraic equation systems. The developed simulation program is entirely based on open source codes.

2. Related Work

Several works related to the simulation of corona discharges are found in the literature, frequently addressing the EHD flow generation and analysis, in which the corona discharge is the electrical part of the problem, for such kind of simulations, the point-plane or needle-plane configuration is commonly selected as the problem domain geometry.

For instance, Yang *et al.* [5] presented a work which describes a simulation of a needle-plane configuration, but only in two dimensions, in order to analyze the electric field. The FEM was used, in a well-refined mesh. A three-dimensional finite volume simulation of a corona discharge is discussed by

*Corresponding author: Julio Cesar Momente, momentejc@sjrp.unesp.br

Long *et al.*[6], but the problem domain is a wire and plate configuration. In this work, a corona discharge is treated by the FEM in a three-dimensional, tetrahedral mesh of a needle-plane configuration.

Adamiak and Atten [7] presented a computational simulation of a corona discharge in point-plane configuration, which used a hybrid strategy to solve the governing equations, they used Boundary Element Method (BEM) combined with FEM and the Method of Characteristics (MOC). This hybrid approach led to very consistent results and a complete analysis of the problem.

Zhao and Adamiak [3] also presented an electric and a flow analysis of a pin-plate configuration used to EHD flow generation. The relationship between the electric discharge and the flow generation is strict, but under certain circumstances the mathematical modeling and, consequently, the computational simulation is simplified.

3. Mathematical Model

Corona discharges are governed by a system of non-linear equations, which are preferably solved by numerical methods. The system consists of two equations: the first one is the Poisson equation (1), which describes the electrical potential distribution in the area of the flow, induced by the ionization layer [3].

$$\nabla^2 V = \rho_q / \epsilon_0 \quad (1)$$

The second equation (2) describes a relation between electric potential and space charge density and it is derived from electric current density (3) and continuity equation (4) [3].

$$\nabla \rho_q \cdot \nabla V = \rho_q^2 / \epsilon_0 \quad (2)$$

$$\vec{j} = \nabla \cdot (\rho_q K \vec{E} + \rho_q \vec{u} - D \nabla \rho_q) \quad (3)$$

$$\nabla \cdot \vec{j} = 0 \quad (4)$$

ρ_q is the space charge density, V is the electrical potential, ϵ_0 is the air permittivity, \vec{j} is the current density, K is the ion mobility coefficient, \vec{E} is the electric field, \vec{u} is the flow velocity and D is the diffusion coefficient.

Equations (3) and (4) are combined and some simplifications are made, leading to equation (2), which is used in the computational simulation.

4. Computational Modeling

In order to simulate the equations (1) and (2) above, they are modeled using Galerkin method, applying the suitable boundary conditions. After the conversion of the equations to matrix form, an initial set-up is necessary, comprising a geometric model, Figure 1, and a mesh, Figure 2, derived from this model.

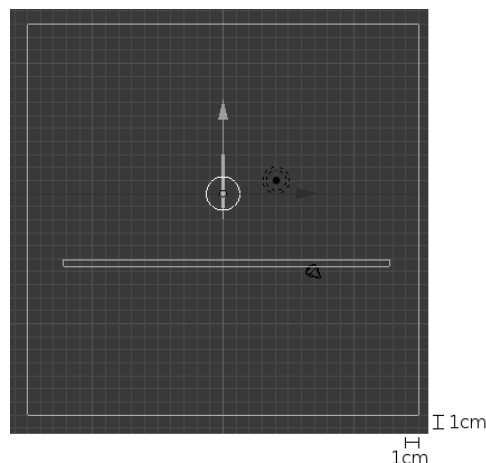


Figure 1: Geometric model of the needle-plane configuration.

The dimensions of the needle-plane configuration used in the simulation was a needle with an

hyperbolic point with $100\mu\text{m}$ of curvature radius and the separation from the plane is 3.1cm , as can be seen on Figure 1. The three-dimensional geometric model was generated by Blender version 2.49b software, free three-dimensional modeling software.

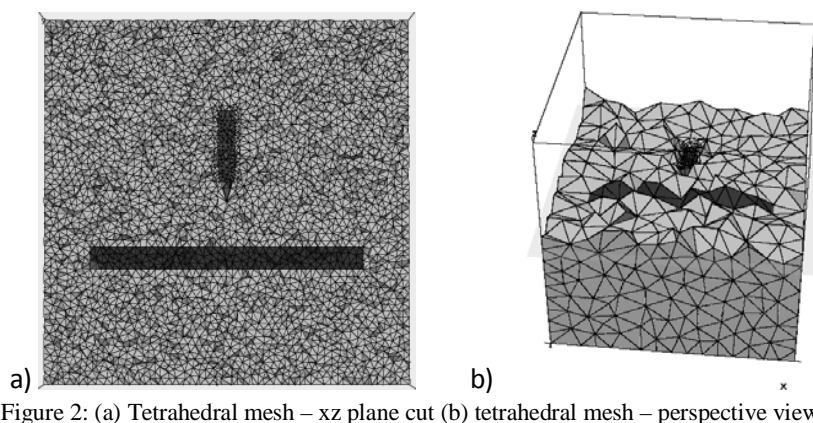


Figure 2: (a) Tetrahedral mesh – xz plane cut (b) tetrahedral mesh – perspective view.

The mesh of Figure 2 has 594274 elements and it was generated based on the geometric model, using TetGen version 1.4, a free tetrahedral mesh generator, which can provide very refined and well-structured tetrahedral mesh. TetGen can also address volume and angle constraints, in order to provide a better representation of the domain.

5. Results

Using the mesh presented in Figure 2, the system of equations was solved iteratively and both equations were solved using LU decomposition method. The Poisson equation (1) is solved using an initial guess of space charge density. Then, the results from the first equation are used to solve the second one. This process is repeated until reaching the convergence.

A transversal cut of the 3D model is used to show the Electric field, Figure 3, which results are compared with the results shown by Yang et al. [5]. The comparison, Figure 4, clearly shows the correctness of the calculated results, validating the simulation process for this model.

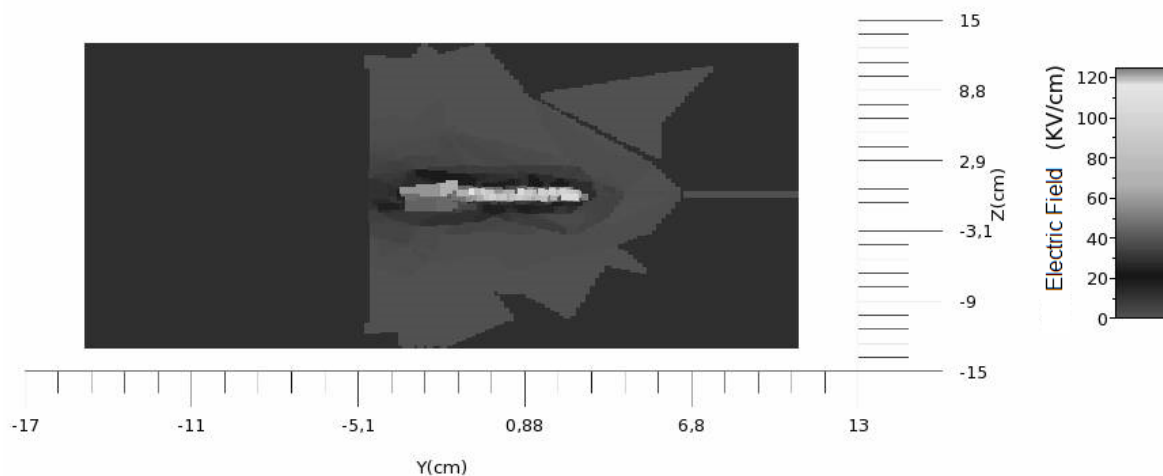


Figure 3: Electric Field of a needle-plane set-up – YZ plane.

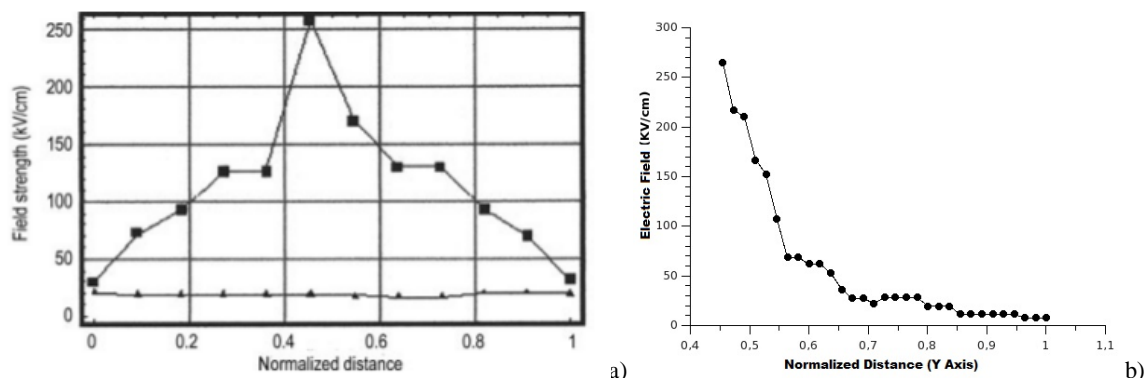


Figure 4: Comparison between results from literature (1) [5] and the results of the present work (b).

A view of the space charge density is shown in Figure 5. The values presented in this figure could not be validated due to the absence of space charge density values in the literature. The three-dimensional modeling and simulation add valuable information about the surrounding areas of the electrodes, improving the details about the model.

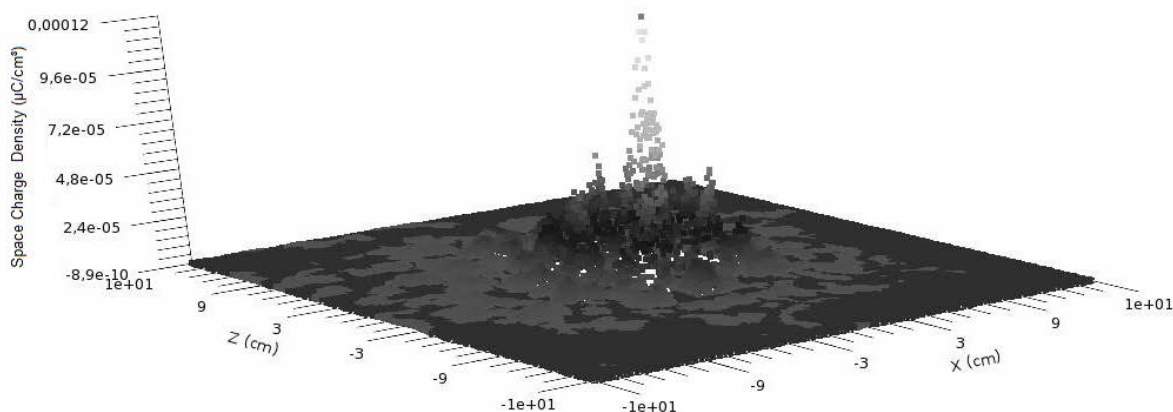


Figure 5: Space charge density along the surface of the plane.

6. Conclusion

In this work a 3D FEM simulation of corona discharges in a needle-plane configuration was performed. To the extent of our knowledge, such simulations for the needle-plane configuration were not yet extensively studied in the literature. As can be seen by the results shown, the developed solution is good and suitable to simulate corona discharges for simple geometry problems. The next steps are testing this solution to solve problems with more complex geometries and different kinds of problems.

Acknowledgements

This work was supported by FAPESP.

References

- [1] L. Zhao and K. Adamiak. Effects of EHD and external air flows on electric corona discharges in point-plane/mesh configurations. *Industry Applications, IEEE Transactions on* **45**(2009) 16-21.
- [2] A. Labergue et al. Effect of a plasma actuator on na airflow along an inclined wall: P.I.V. and wall pressure measurements. *Journal of Electrostatic, 10th International Conference on Electrostatics* **63** (2005) 961-967.
- [3] L. Zhao and K. Adamiak. EHD flow in air produced by electric corona discharge in a pin-plate configuration, *Journal of Electrostatics, Selected papers from ESA 2004 Annual Conference* **63**(2005) 337-350.
- [4] N. Brown and F. Lai. Electrohydrodynamic gas pump in a vertical tube, *Journal of Electrostatics* **67** (2009), 709-714.
- [5] S. Yang et al., Simulation of Needle-Type electrodes by Finite Element Method, *Plasma Science and Technology* **9**(2007).
- [6] Z. Long et al., Three-Dimensional Simulation of Electric Field and Space Charge in Advanced Hybrid Particulate Collector, *Journal of Electrostatics* **67** (2009) 835-843.
- [7] K. Adamiak and P. Atten. Simulation of corona discharge in point-plane configuration, *Journal of Electrostatics* **61**(2004) 85-98.

High frequency transmission line model of induction motor employing 3D electromagnetic field simulation

Hai Van JORKS*, Erion GJONAJ, Thomas WEILAND

Institut für Theorie Elektromagnetischer Felder, Technische Universität Darmstadt, Schloßgartenstraße 8, 64289 Darmstadt, Germany

Abstract. In this paper, a transmission line model for induction machines excited by high frequency common mode currents is discussed. The extended approach includes stator, rotor and end windings. Special diligence is attributed to the three dimensional modelling of eddy currents inside the core lamination as well as of the end winding fields. In conclusion, the paper compares different analytical and numerical approaches in the frequency range 10 Hz...1 MHz and tries to give benchmarks for errors which occur due to a number of commonly used model simplifications.

1 Introduction

In the literature essentially two approaches to high frequency (HF) modelling of induction machines (IMs) can be encountered. Models of the first type are based on a global equivalent circuit [e.g. 1]. This usually makes them quite compact and handy, but the RLC circuit elements have to be determined by curve fitting procedures involving measurements. Concurrently, a second type of HF machine modelling, based on transmission line (TL) theory, is used to analyse the common mode (CM) response of IMs fed by pulse width modulated inverters [2]. The main advantage of the TL modelling approach is that a physical meaning can be attributed to all model parameters, which are extracted from electromagnetic field simulations. Hence, electrical machine behaviour can be predicted directly from design parameters. However, accurate HF finite element (FE) modelling of IMs is restricted by computational resources and, therefore, various simplifications and approximation techniques have been proposed by several authors [e.g. 3]. For this paper, fully 3D simulations of the active middle part of the machine are carried out and compared to a 2D model, where eddy currents in laminations are considered by homogenized material properties. The significance of the rotor in the electrostatic and the HF magnetic field is also discussed. Additionally, motor frame and rotor axis are included to complete the magnetic simulations. The end windings of the machine are analysed separately and the full 3D simulation is compared against a 2D axisymmetric approach.

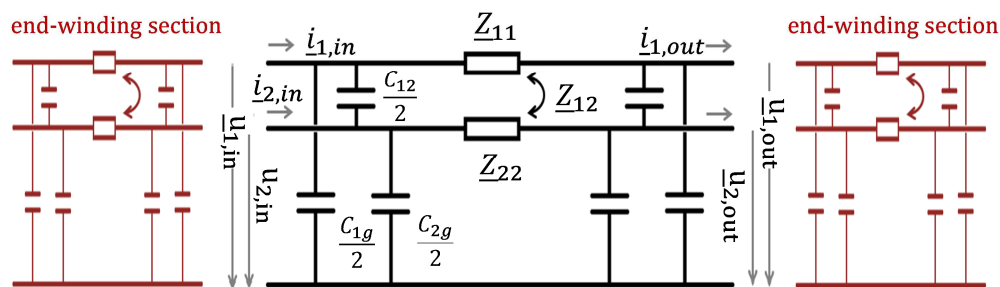


Figure 1: Schematic drawing of two-conductor lumped-Pi model with added end-winding sections

*email: jorks@temf.tu-darmstadt.de, phone: +49 6151 16-2661, fax: +49 6151 16-4611

2 High Frequency Transmission Line Model

As it is common practice the motor geometry is divided into two domains, active and end region, which are analyzed separately by FE simulation. TL theory is applied to describe the non-uniform voltage distribution along the coils [4]. Thereby, it is sufficient to divide each coil into finite number of conductors represented by lumped-Pi equivalent circuits, alternated with sections representing the end windings (Fig. 1). The network parameters for both active and end region are extracted from simulated field distributions. Fourier Transformation of the network equations results in a system of algebraic equations in the frequency domain, which can be solved by enforcing the interconnections of the conductors according to the winding scheme of the machine.

3 Results

In order to evaluate the 2D homogenization approach for motor laminations pointed out in [5] fully 3D simulations of a motor lamination employing periodic boundary conditions have been carried out (Fig. 2a). For this purpose, a specialized simulation tool, based on inhouse FE code, was created and allows to solve the magnetoquasistatic problem with 9.6 million degrees of freedom parallelized on a cluster with 60 nodes in <4 h for a sweep of 7 frequency points shown in Fig. 2b. The parameters extracted from field simulations were used to compute the CM input impedance of the machine. Again, 2D and 3D results were compared and despite the large deviations in the conductor impedances (Fig. 2b), good agreement between 2D and 3D was found in the all-over CM impedance (error <5%).

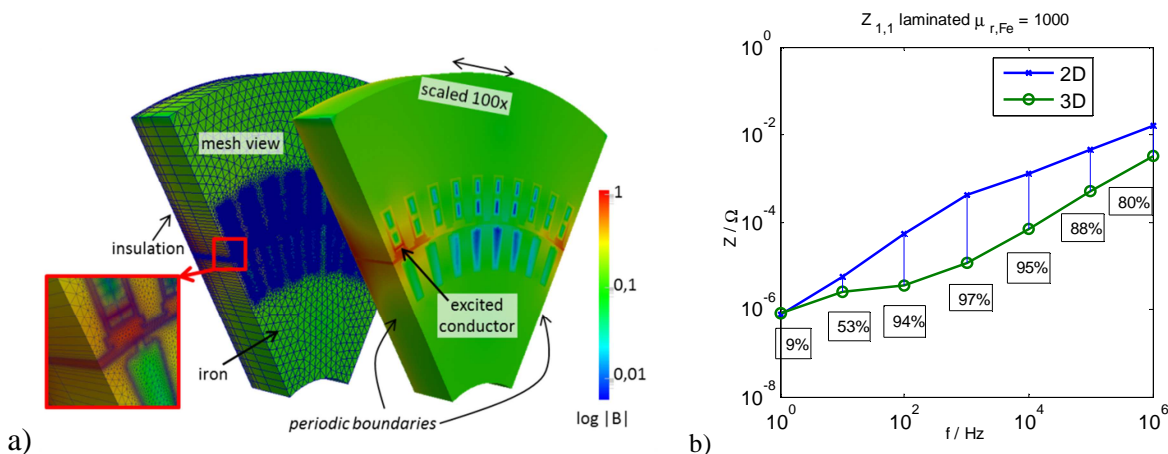


Figure 2: a) Simulation mesh and magnitude of the magnetic flux density at 1 MHz for 3D motor model, b) comparison conductor impedance (2D / 3D)

References

- [1] G. Grandi, et al., *Model of laminated iron-core inductors for high frequencies*, IEEE Trans. Magn. 40-4 (2004) 1839–1845.
- [2] S. Chen, T. A. Lipo, D. Fitzgerald, *Modeling of motor bearing currents in PWM inverter drives*, Proc. IEEE IAS 13 Annu. Meeting (1995) 388–393.
- [3] H. De Gersem, A. Muetze, *Finite-Element Supported Transmission-Line Models for Calculating High-Frequency Effects in Machine Windings*, IEEE Trans. Mag. 48-2 (2012) 787 – 790.
- [4] B. Heller, A. Veverka, *Surge phenomena in electrical machines*, Iliffe Books, London, 1968.
- [5] H. Jorke, et al., *Three-dimensional simulations of an induction motor including eddy current effects in core lamination*, IET Science, Meas. & Tech. 6-5 (2012) 344 – 349.

4-

**Electromagnetic smart
fluids, electromagnetic
processing of materials**

Vibration Control System with Digitally Adjustable Electromagnetic Damping and Stiffness

Chongpu Zhai, Minglong Xu* and Bo Feng

State Key Laboratory for Strength and Vibration of Mechanical Structures, School of Aerospace, Xi'an Jiaotong University, Xi'an 710049, China

Abstract. A vibration control system with digitally adjustable electromagnetic damping and stiffness is presented in this paper, which is used in wind tunnel test of high-rise buildings. This system consists of sensing module, data acquisition, control center, power amplifier and actuators. The vibration control system is devised to investigate the changing rule of aerodynamic damping under different wind velocity. This system was designed on the basis of the function of electrified coil in stable magnetic field. Building model is fixed on the shaking table to conduct wind tunnel test of aeroelastic model. The damping and the stiffness are able to be conditioned digitally. The system is of innovation in study of fluid-structure interaction of high-rise building under wind load.

Keywords: actuator, electromagnetic, vibration control, damping, stiffness

1. Introduction

The height of building increases with new materials and new technologies applied, leading natural frequency of building to approaching the predominant frequency of wind load and resulting in building's sensitivity to wind load. Therefore, the wind load needs to be taken into consideration as an important factor in the process of building design [1,2].

The aerodynamic damping produced by wind load is deeply rooted in fluid-structure interaction (FSI) and aerodynamic damping is negative in some cases, which is potentially hazardous to buildings. The changing rule of aerodynamic damping under different wind velocities has attracted much attention in recent years [3,4].

FSI research on high-rise buildings has registered a considerable progress since extensive use of wind tunnel test [5]. FSI is complicated in both formation mechanisms and impact analysis and it is mainly investigated by wind tunnel test of rigid model and aeroelastic model [6]. While the low natural frequency of rigid model results in poor performance in wind tunnel test and the aeroelastic model is complex and difficult to build because it needs to be in accordance with the dynamic characteristics and parameters of architecture archetype. The existing experiments could not fast and accurately achieve in adjusting damping and stiffness. Oil damper and replaceable spring are usually utilized in aeroelastic model test. On account of poor accuracy of damping regulation and frequently changing springs, the experiment process tends to be cumbersome and less reliable [7,8].

*Corresponding author: Minglong XU, State Key Laboratory for Strength and Vibration of Mechanical Structures, School of Aerospace, Xi'an Jiaotong University, Xi'an 710049, China Tel/Fax: 86-29-82669093; Email: mlxu@mail.xjtu.edu.cn

This paper describes a two degrees of freedom (DOF) vibration control system in reference with electromagnetic technologies. The damping and the stiffness are able to be regulated digitally. The system reported here could be beneficial to exploring the changing rule of aerodynamic damping under diverse wind velocities and research attempting to analyze the dynamic behavior of architecture under wind load.

2. Structure and Control Scheme

2.1. Basic structure

This system consists of four eddy current displacement sensors (MICRO-EPSILON, eddyNCDT3010), PC with data acquisition and control program, power amplifier and shaking table. The general structure of the two DOF vibration shaking table is shown in Fig.1 and Fig.2.

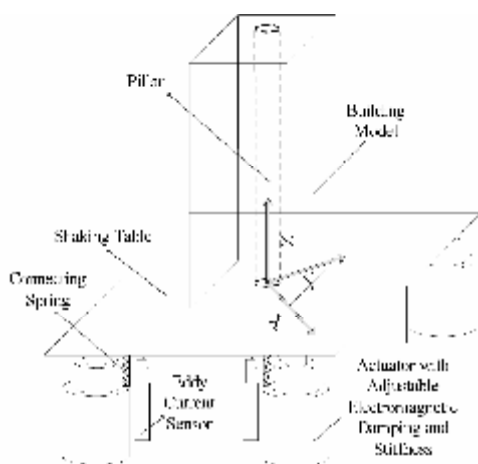


Fig. 1. General structure of the shaking table

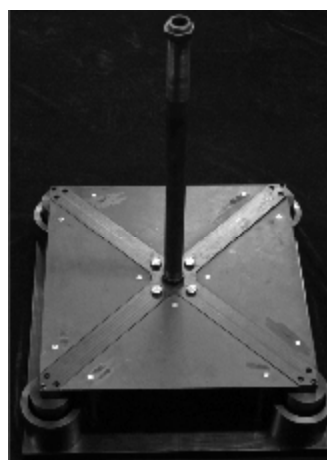


Fig. 2. Picture of the shaking table

Building model is installed on the pillar which is fixed on the table and the model can rotate around X-axis and Y-axis along with the shaking table. Four electromagnetic actuators are below the plate and connected to the table through connecting spring. Four eddy current sensors are placed under the shaking table to measure the displacement of the four corners of the shaking table. Two actuators at the opposite corners harmonize with each other to realize the function of adjusting damping and stiffness of one DOF.

This system could serve the needs of the majority of high-rise building from 300m to 600m in wind tunnel test of aeroelastic model. The range of motion of each actuator is $\pm 0.0002m$. Each actuator generates the largest damping force of 11.8N and the largest elastic force of 33.0N, when the system provides the largest damping and stiffness for building's aeroelastic model.

2.2. Operating principle

2.2.1. Damping force and stiffness provided by actuator

The motion is acknowledged as pendulum motion and it is shown in Fig.3.

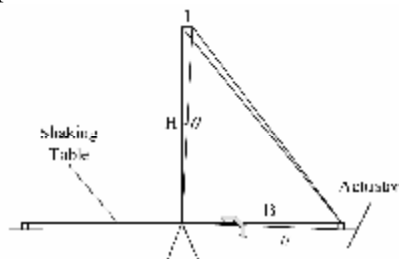


Fig. 3. Motion of one DOF

The aeroelastic model on the shaking table vibrates under wind load in wind tunnel test and the motion is regarded as reciprocating motion on account of the rather small displacement.

The motion equations of two DOFs are the same and can be defined as:

$$I\ddot{q} + c\dot{q} + kq = M(t) \quad (1)$$

Pendulum motion can be reduced to simple harmonic vibration and expressed as:

$$q = A \sin(\omega t) \Rightarrow \dot{q} = A\omega \cos(\omega t) \quad (2)$$

Damping c can be represented as:

$$c = 2I\omega z \quad (3)$$

Then, the maximum damping moment can be described as:

$$M_c = 2I\omega z \cdot A\omega = 2AI\omega^2 z \quad (4)$$

The maximum damping force provided by the actuator follows that:

$$M_c = 2I\omega z \cdot A\omega = 2AI\omega^2 z \quad (5)$$

Considering the fact that two actuators operate together to adjust damping and stiffness of one DOF, the relationship between torsional stiffness and stiffness provided by actuators is as follows:

$$K_{qp} = 2k \times q \times B^2 = 2k \times B^2 \quad (6)$$

Where K_{qp} is torsional stiffness, k is stiffness generated by each actuator, B is distance from actuator to the center of rotation.

According to the equations above, the damping force is proportional to the speed and the elastic force is proportional to the displacement. In this paper, proportional control algorithm is applied to adjust the damping and the stiffness of aeroelastic model in wind tunnel test.

2.2.2. Control scheme

The flow chart of this vibration control system is presented in Fig.4. Four eddy current displacement sensors are used to measure the vibration signals of the shaking table. The signals are sent to PC after signal processing in the signal collector. Subsequently, a control program sends out the control signals ranging from -10V to +10V. The control signals are then amplified by power amplifier to drive the actuators. The damping and stiffness of vibration are finally controlled to satisfy the experimental needs of aeroelastic model.

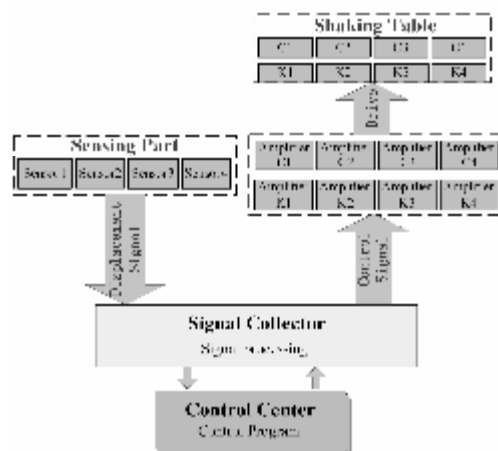


Fig. 4. Flow chart of damping and stiffness control

3. Actuator with Digitally Adjustable Electromagnetic Damping and Stiffness

3.1. Structure and principle of electromagnetic actuator

The structure of the electromagnetic actuator is presented in Fig.5.

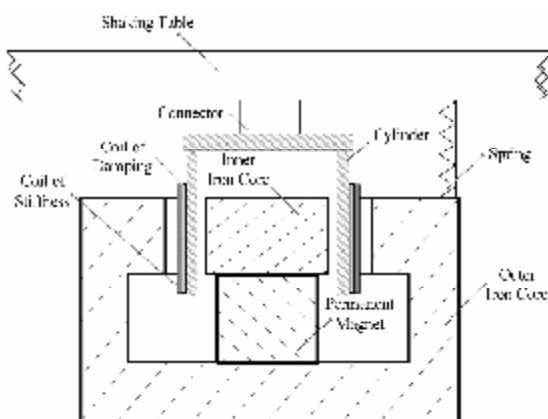


Fig. 5. Sketch of electromagnetic actuator

Two coils are wrapped around the cylinder connected to the shaking table via the connector on top. When operating, the cylinder vibrates along with the shaking table. Epoxy resin which is non-conducting material is used for cylinder to avoid disturbance from eddy current in conductors. Magnetic path is composed of one cylindrical permanent magnetic and two iron cores. The cylinder with coils stretches into the gap of magnetic path. The cylinder and the iron cores maintain contactless. The magnetic field in the gap is considered as uniform magnetic field because the gap extremely narrow. The purpose of hanging spring between the top of the outer iron core and the shaking table is to fulfil the function of providing initial stiffness for vibration system. Furthermore, to control damping and stiffness, the control signals from PC are amplified by power amplifier to drive the damping and stiffness coils. With the force outputting from the current coils in permanent magnetic field, damping and stiffness are adjusted.

3.2. Optimization of electromagnetic actuator

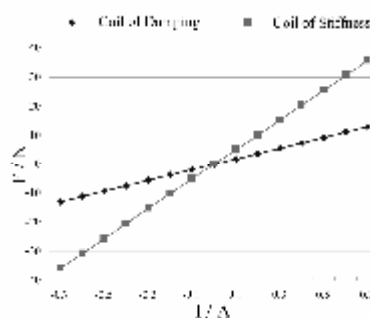
Based on the changing rule of force on electrified coil in constant magnetic field, the electromagnetic actuator was developed. Numerical simulation methods were used to estimate the size of the actuator, the turns of damping and stiffness coils. Combined with experimental results, the appropriate size and structure was determined after several times of modification.

The gap of magnetic path was designed to be quite narrow for the sake of avoiding the leakage of magnetic energy. Additionally, the part of the cylinder wrapped with coils is one and a half times as tall as the gap, so the electrified coil is in the position to take full advantage of magnetic energy.

Calibration experiment of force on the electrified coil was carried out drawing support from force sensor (Interface, SSM, 0-50N). It is shown in Fig.6 and Fig.7 shows the result which indicates favourable linearity and stability of the electromagnetic actuator. To be more exact, the damping coil of 500 circles and the stiffness coil of 1400 circles can respectively produce a maximum of ampere force of 12.7N and 37.6N with the current of 0.7A. The power amplifier (200W, 1A, 8 Channels) was devised in an attempt to drive the damping and stiffness coils. The current in damping and stiffness coils maintain proportional to the control signals. Moreover, the ampere force on the coils is immune to the small-amplitude vibration of the shaking table.



Fig. 6. Calibration of actuator



188
 Fig. 7. Relationship between force on the coils and current

4. Performance examination

In this paper, the displacement release test is conducted to examine the capacity to control damping and stiffness and Fig.8 indicates the examination experiment. An initial displacement was given by placing weights on the shaking table and the displacement signal was recorded after removing the weights. Afterwards, the displacement signal was analyzed by methods of fitting the envelope and Fourier transform with the aim of obtaining the damping factor and natural frequency. The displacement diagrams of different damping output are presented in Fig.9 and the damping control result of different output is shown in Table 1. The stiffness control result of different output is shown in Table 2.

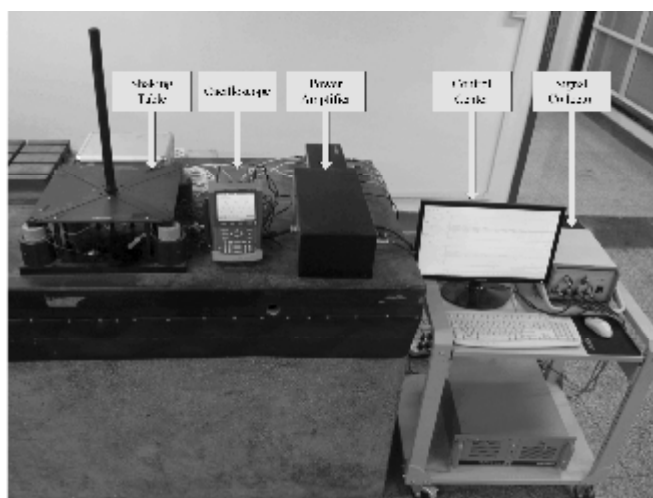


Fig. 8. Examination experiment

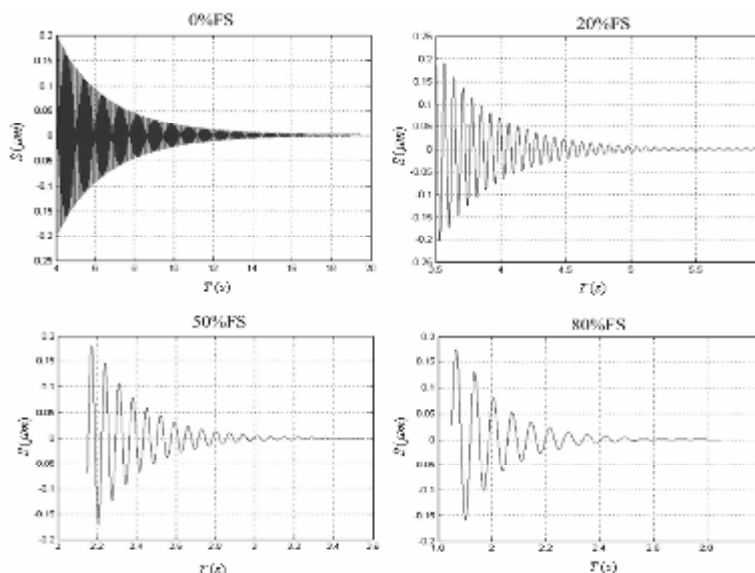


Fig. 9. Displacement diagram of different damping output

Table 1
 Damping control result of different output

Output/ FS(Full Scale)%	Damping Factor gained by experiment	Damping Factor of theoretical value
5	0.0183	0.0176
20	0.0371	0.0352
50	0.0513	0.0528
60	0.0654	0.0649
80	0.0890	0.0911
100	0.1047	0.1058

Table 2
Stiffness control result of different output

Output/ FS(Full Scale)%	Natural Frequency gained by experiment /Hz	Natural Frequency of Theoretical value /Hz
0	12.0	12.0
5	13.6	13.7
20	16.6	16.5
50	17.4	17.2
60	18.5	19.0
80	19.6	20.1
100	21.5	22.1

It can be seen that the experiment result was highly consistent with the theoretical value in terms of damping and stiffness generating. However, this system has its inherent disadvantages. The existence of coils' inductance brings about phase difference between electrified current in coil and control signal. Therefore, the control effect of this system becomes worse as the vibration frequency increases.

5. Conclusion

This paper proposed a vibration control system with digitally adjustable electromagnetic damping and stiffness in expectation of serving a useful function in aerodynamic damping research on high-rise buildings. Based on the analytical and experimental investigations presented in this paper, the following conclusions may be drawn:

1. Electromagnetic method is proposed to obtain adjustable damping and stiffness and all the regulation is capable to digitally fulfill on computer and the control result agrees well with the theoretical predictions. The largest damping force of 11.8N and the largest elastic force of 33.0N could be achieved by the electromagnetic actuator. This system could benefit the research into dynamic behavior of architecture under wind load.
2. The system proposed in this paper is competent to well control damping and stiffness when the vibration frequency is less than 50 Hz.
3. Additional experimental verification and control algorithm design will be the next work. Besides, possible future research topics can be the extension to more general vibration structures.

Acknowledgement

This work is supported by the National Natural Science Foundation of China (11172229).

References

- [1] W. Chai, M.Q. Feng, Vibration control of super tall buildings subjected to wind loads, *International journal of non-linear mechanics* **32** (1997), 657-668.
- [2] A. Kareem, Dynamic response of high-rise buildings to stochastic wind loads, *Journal of Wind Engineering and Industrial Aerodynamics* **42** (1992), 1101-1112.
- [3] M. Gu, Y. Quan, Across-wind loads of typical tall buildings, *Journal of Wind Engineering and Industrial Aerodynamics* **92** (2004), 1147-1165.
- [4] R. R. Gerges, B.J. Vickery, Wind tunnel study of the across-wind response of a slender tower with a nonlinear tuned mass damper, *Journal of Wind Engineering and Industrial Aerodynamics* **91** (2003), 1069-1092.
- [5] Y. Zhou, T. Kijewski, A. Kareem, Aerodynamic loads on tall buildings: interactive database, *Journal of structural engineering* **129** (2003), 394-404.
- [6] K. C. S. Kwok, B. Samali, Performance of tuned mass dampers under wind loads, *Engineering Structures* **17** (1995), 655-667.
- [7] L. Y. Xu, K.C.S. Kwok, Mode shape corrections for wind tunnel tests of tall buildings, *Engineering Structures* **15** (1993), 387-392.
- [8] Y. Taniike, H. Inaoka, Aeroelastic behavior of tall buildings in wakes, *Journal of Wind Engineering and Industrial Aerodynamics* **28** (1988), 317-327.

Accurate Computations of the Magnetic Field for Magnetic Fluid Seal

Zou Jibin (IEEE senior member)^{a,*}, Jiming Zou^a, Yongxiang Xu^a, Meng Zhao^a, Kai Liu^a, Yanyu Wei^a, Hao Wang^a

^a*Dept. of Electrical Engineering, Harbin Institute of Technology, Harbin 150001, China*

Abstract. The behavior of magnetic fluids is related to the applied magnetic fields because of the magnetic forces determine the surface shape of the fluid. The accurate estimations of the fields and the forces are important in the magnetic fluid applications. The coupling between the magnetic fields and magnetic forces makes the direct computation complicated. An approach using FEM and iteration algorithm to solve the coupled problem in the application of magnetic fluid seals is proposed and implemented.

Keywords: Magnetic fluid, computation, iteration, seal

1. Introduction

Magnetic fluids have been widely used in the applications such as seals and magnetic separations. Most of these applications can be roughly divided into two groups. In one group like magnetic fluid seals, the magnetic fluids are hold in special positions by the magnetic force. In the other group like magnetic separation, the property of the magnetic fluid is in certain relationship with the applied magnetic field. The magnetic field intensity and distribution will determine the behavior of the magnetic fluid.

Numerical computation is an effective way to solve complicated magnetic fields. In reference^[1] the magnetic fields in magnetic fluid seals were solved numerically. The field distributions and the isobars in the magnetic fluid were computed by finite element method. The computed results agreed with experiments. However, the nonlinear property of the magnetic fluid was not considered. Therefore, the solution was not accurate enough. In fact, there exists a coupling between the magnetic field and the magnetic forces that affect the isobars. In this paper, an iteration method is used to solve the coupling problem.

2. Theoretic Analysis

The experimental device of a single stage magnetic fluid seal is shown in Fig. 1. The device consists of permanent magnet, pole piece, magnetic yoke, and tube connected to a pump. The end sides of the seal device are closed by transparent plate. The shape of the magnetic fluid can be seen and photos can be taken by camera. When the gas is pumped into the device through the tube, the pressure inside the device will be increased and the pressure differential will be applied on the magnetic fluid. The magnetic force on the magnetic fluid will balance the applied pressure differential. The change of the position and shape of the magnetic fluid can be seen through the transparent plate.

*Corresponding author. Tel.: +0086-451-86413613; fax: +0086-451-86413613; e-mail: zoujibin@hit.edu.cn.

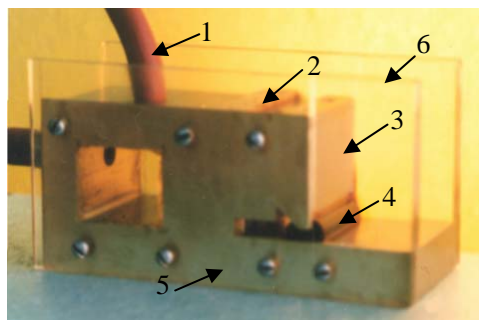


Fig. 1. Device for experiment

1-tube, 2-permanent magnet (inside), 3-pole piece, 4-magnetic fluid, 5-yorke, 6-transparent plate.

According to the electromagnetic field theory, the vector potential A of magnetic field can be used to present the field. The differential equation of A_z is

$$\frac{\partial}{\partial x}(\mu \cdot \frac{\partial A_z}{\partial x}) + \frac{\partial}{\partial y}(\mu \cdot \frac{\partial A_z}{\partial y}) = J_z \quad (1)$$

Where, A_z is the z component of A , μ is the permeability, J_z is the current density, μ represents the properties of the magnetic materials including the iron, permanent magnet and magnetic fluid. The property of the permanent magnet can be described by a kind of material with surface current density J_z and permeability μ_m . The iron is nonlinear magnetic material. Magnetic fluids are super paramagnetic nonlinear materials. Their properties are related to their saturated magnetizations as shown in Fig. 2. Therefore equation (1) is a nonlinear equation.

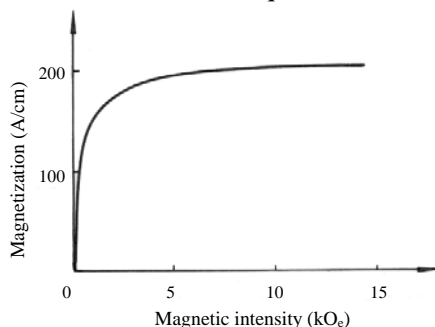


Fig. 2. Magnetization curve of magnetic fluid

Modern FEM software can be used to solve most of nonlinear magnetic field problems. However, the problem of magnetic fluid seals is a multi-physical problem, which comprises both magnetic and mechanical phenomena.

The pressure in the magnetic fluid is expressed as

$$p = \int_0^B M dB + C \quad (2)$$

Where, M is magnetization, B is flux density, and C is a constant determined by the boundary condition.

The surface boundaries of the magnetic fluid coincide with the isobars that depend on the field distributions. The shape of the magnetic fluid in the magnetic fields is determined by magnetic force. On the other hand, the shape of the magnetic fluid in turn affects the magnetic field distribution because of its different magnetic permeability from air. Therefore, the simultaneous solution of the coupling problem is complicated.

If the magnetization of saturation of the magnetic fluid is small, the permeability of the fluid is nearly equal to that of air. The magnetic field problem can be treated as linear one. When the magnetization is increased, the error of such solution will become obvious.

The coupling problem can be solved by FEM and iterative process. The procedure of the iteration used in this paper includes the following 5 steps: ① creating geometry, meshing and setting the permeability for all elements in magnetic fluid as μ_0 ; ② computing the magnetic fields by finite element method; ③ computing the isobars according to equation (2); ④ determining the surface boundaries of the magnetic fluid according to the given volume of the magnetic fluid and the applied pressure^[1]; ⑤ modifying the mesh of the field area according to the computed shape of the magnetic fluid and modifying the permeability of each element in the fluid according to the magnetization curve of the fluid. By repeating step ②~⑤, the boundary of the fluid will approach to a convergent shape. When the difference of the boundaries between the last two iterations is small enough, the iterations can be stopped. The final iteration is the accurate computation result.

3. Results of Computation

The magnetic fluid distribution, the boundary shapes of the magnetic fluid, and the seal pressure differential of the magnetic fluid seal device can be computed by the decoupled computations. The computed results can be verified by the shape of the magnetic fluid and the seal pressure differential of the device.

3.1. Boundary shape of magnetic fluid

The computed boundary shapes of the magnetic fluid with given volumes in the sealing gap are shown in Fig. 3. The photos for the cross section of the magnetic fluid are shown in Fig. 4. When there is no pressure differential applying on the two sides of the magnetic fluid, the magnetic fluid is in the natural position as shown in Fig. 3 (a) and Fig. 4 (a). When a pressure differential is applied on the magnetic fluid, its shape will change as shown in Fig. 3 (b) and Fig. 4 (b). It can be seen that the computation result agrees with the experiment result. Fig. 5 displays the difference between the boundaries computed by the decoupled solution and linear solution when the magnetic fluid volume is kept constant. There is an obvious change of the boundary shape in the area where the magnetic field intensity is high as shown by the left curves, while the dotted line is the linear solution. Whereas in the area where the magnetic field is weak, the shape computed by decoupled solution is almost the same as that computed by linear solution as shown by the right curves, while the two curves agree each other. Even though the change of the boundary shapes is not obvious, the forces on the fluid are different. The difference of the magnetic forces between the decoupled solution and linear solution is bigger in the weak field area than that in the high field area, because the permeability of the fluid tends to be μ_0 in the high field area. If the saturation magnetization of the magnetic fluid is increased, the difference between the left curves will be even clear.

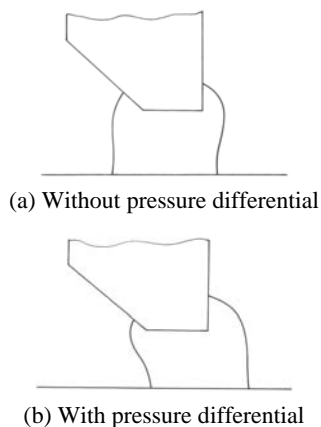


Fig. 3. Computed boundaries of the magnetic fluid

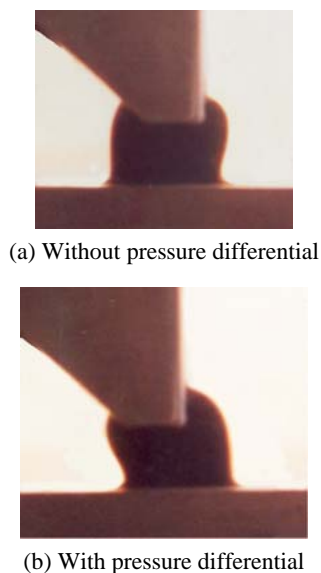


Fig. 4. Photos of cross section of magnetic fluid



Fig. 5. Comparison of the fluid boundaries between the decoupled and linear solutions

3.2. Magnetic field distribution

The magnetic field distributions on the magnetic yoke surface are shown in Fig.6. It can be seen that the flux density increases when the magnetic fluid is filled into the gap. There is a jump of flux density on the magnetic fluid surface because of the permeability jump. When the saturation magnetization of the magnetic fluid increases, the magnetic field change on the surface will increase.

3.3. Seal pressure differential

As it is earlier stated that the seal pressure differential is related to the magnetic fluid mass^[1,2]. The seal pressure differential equals the difference between the pressures on the two side boundaries. The magnetic fluid mass can be computed by multiplying the area of the fluid and the length of the fluid seal belt. The computed results of the seal pressure differential vs. the fluid mass by both decoupled solution and linear solution are shown in Fig.7. The seal pressure differential from the decoupled computation is higher than that from the linear computation and more close to the measurements. Fig. 8 shows the difference of the seal capacities between decoupled solution and the linear solution vs. magnetization of the magnetic fluid. When the saturation magnetization of the magnetic fluid increases, the change of the seal pressure differential become obvious.

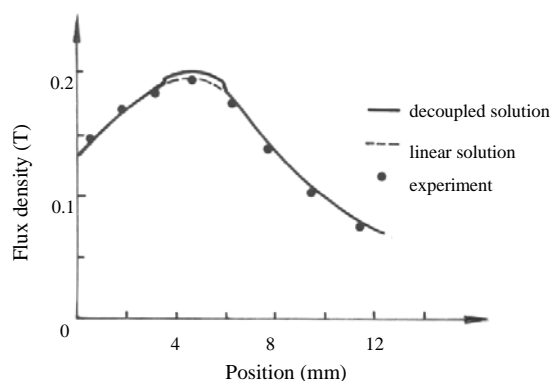


Fig. 6. Flux density distribution on surface of magnetic yoke

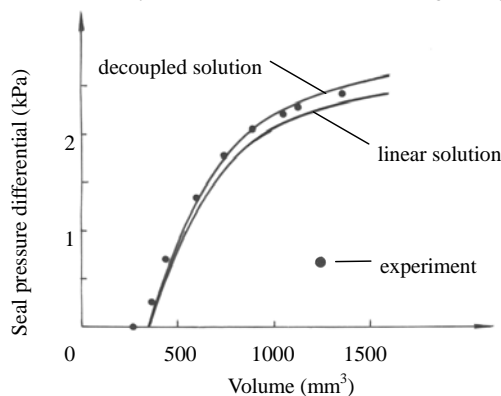


Fig. 7. Seal pressure differential vs. magnetic fluid volume

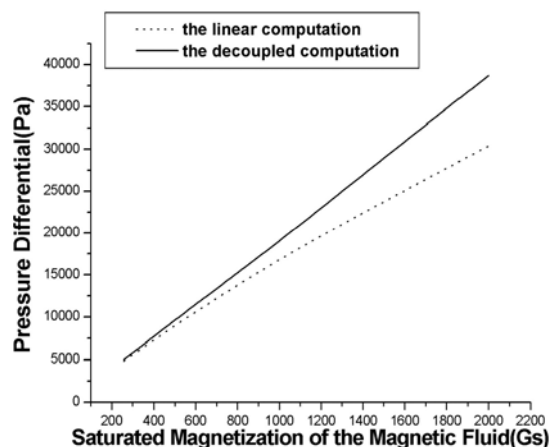


Fig. 8. The difference of the seal capacity between the decoupled solution and the linear solution vs. magnetization of the magnetic fluid

4. Conclusions

The following conclusions can be drawn from above analysis and computations. (1) Because there is a coupling between the magnetic field and magnetic force, an exact solution of the magnetic field and force cannot be obtained by using the linear computation. (2) The coupled problem of magnetic fields and forces can be solved by iterative computations. The isobars and boundary shapes of magnetic fluid in the magnetic fields can be precisely computed. (3) The seal pressure differential from the decoupled computation is higher than that from the linear computation and more close to the measurements. (4) The higher the magnetization of the fluid is, the bigger the difference between the decoupled computation and the linear computation will be.

5. Acknowledges

This work was supported by the National Key Basic Research Program of China (973 Program) under Grant 2013CB035605.

References

- [1] Zou Jibin & Lu Yongping, Numerical calculations for ferrofluid seals, IEEE Transactions on Magnetics, Vol.26, No1.6, Nov. 1992, 3367 - 3371.
- [2] Zou Jibin et al, Design and pressure control of high-pressure differential magnetic fluid seals, IEEE Trans on Magnetics, Vol.39 No.5, Sep. 2003, 2651 - 2653.
- [3] K Raj etc, Magnetic Fluid Seals for Special Applications, ASLE Trans, 1980, 23(4):422-430.
- [4] Gwan-Soo Park, Kim, Dong-Hun etc, Numerical algorithm for analyzing the magnetic fluid seals, Magnetics, IEEE Trans on Magnetics, Vol.30 No.5, 1994, 3351 - 3354.
- [5] Yoshida T., Enpuku K., etc, Magnetic fluid dynamics in a rotating magnetic field, Journal of Applied Physics, Vol.111 No.5, 2012, 053901 - 053901-10.
- [6] Popplewell, J., Rosensweig, R.E., Johnston, R.J., Magnetic field induced rotations in ferrofluids, IEEE Transactions on Magnetics, Volume: 26, Issue: 5, 1990, 1852 - 1854

A Novel MR Fluid Shock Absorber with MS Materials

Jae-Hak Lee^a, Dae-Young Kim^a, Kyung-Hwan Hwang^b, Yuk-Hyung Lee^c and Myeong-Kwan Park^{a*}

^{a*} *Department of Mechanical Engineering, Pusan National University, Busan 609-735, Korea.*

^b *Convergence Component & Material R&D Group, KITECH, Busan 618-230, Korea.*

^c *School of Mechanical Design & Manufacturing, Busan Institute of Science and Technology, Busan 616-737, Korea.*

Abstract. The paper presents a novel Magnetorheological (MR) shock absorber with Magnetostrictive (MS) materials. MR fluid is capable of controlling the absorbing system with moving part such as piston rods, etc. The behaviors of MR shock absorber is modeled as a electro current induced electromagnetic system based on the Bingham flow. In order to control the braking force along with increasing shear stress of the fluid by the electromagnetic field, it is prerequisite how to design the viscous and magnetic field component through the passage and its gap size. This paper depicts the proposal a semi-active MR shock absorber by adjusting the small gap size using Magnetostrictive (MS) material of the passage of the MR fluid. By placing the electro magnet on the outside of the valve block, a good accessibility can be achieved in order to change and maintain the magnet field more effectively.

Keywords: MR fluid, MR Shock absorber, MS Material

1. Introduction

MR fluid is a non-colloidal of suspension composed of ferromagnetic particles in a non-conductive carrier fluid which have the characteristic of rheological properties can be continuously and reversibly changed within several millisecond by applying magnetic fields. Since MR fluid was developed, advanced investigations have been improved widely. Such as MR actuator, brakes and damper, etc. Recently, A. Shafer and M. Kermani present suitability of MR clutches with feasible actuation solutions for human-robot interaction[1]. J. Huang et al. investigated method and derived design of the cylindrical MR fluid brake theoretically[2]. Some of the major parts of research area are damper and shock absorber application. F. Imaduddi et al. overviewed recent advances in rotary MR damper with comparative advantages[3]. A. Milecki, M. Hauke have been introduced the application of magnetorheological fluid in industrial shock absorbers[4], where the range of braking force remains small and constant according to the gap height, and cannot be adjusted along the applied impact. MS material shows a large resilience to a given magnetic field and high energy density. Also it provides higher efficiency in converting mechanical energy to the coupled magneto mechanical one. Moreover, magnetostrictive material such as Terfenol-D has a high force with high precision, and fail-safe operating characteristics[5,6].

In this paper, a basic scheme on semi-active MR shock absorber is suggested and analyzed by adjusting the gap of the passage of MR fluids flow which results from the shear strain rate of MR fluid and the displacement of MS material. Also, the possibility of device with static characteristics of braking force is investigated.

2. Design of a Novel MR shock absorber

The viscosity according to the MR fluid flow force generated by strength of the magnetic field and viscous force for the fluid passage has great effects on the shock absorber. In a typical MR shock absorber, gap size of MR fluid path cannot be adjust in same devices and electromagnet is located either at piston head or at the bypass valve outside of the cylinder.

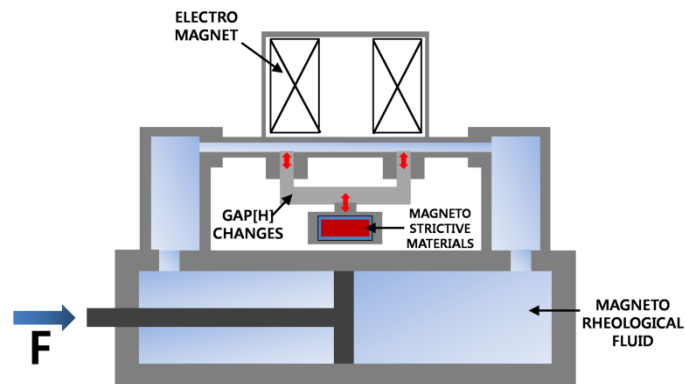


Fig. 1. Schematic diagram MR fluid shock absorber.

Both of kinds are require considerable time to reassembling to change the gap due to applying capacity of force from impact and difficult to replace the electro-magnet for malfunction or disconnecting of coils. Fig. 1 shows a schematic diagram a novel MR shock absorber, arranging a magnet to allow substituting easily and adjusting the passage gap for returning fluid can be controlled by magnetostrictive materials with displacement amplifier. The design variables are the gap height and the magnetic field which can be altered by the current through the electromagnet.

3. MS material with Displacement amplifier

Terfenol-D is one of advanced smart material of which the length under magnetic field varies. Also MS material enables to generate high extending force with reliable accuracy. Nevertheless, operating displacement range 0.036 mm is insufficient to alter height of gap in this research. Therefore, displacement amplifier makes the possibility to extend the gap size up to 7 times (about 0.252 mm) with honeycomb mechanism[7].

4. Numerical Analysis

To analyze the braking force mechanism, the absorbing characteristics must be investigated in a more quantitative way. In order to guarantee reliable mode of operation of such devices, the steady confined flow of the MR fluid in the stationary surrounding gap has to be examined. But this approaches can be quite complicated in somewhat that there is a significant coupling between each of three domains such as magnetic field, fluid dynamics, and moving part dynamics. The moving part of inside cylinder is simulated first in axial symmetry.

4.1 MR Fluid Absorber Model

$$\rho \frac{\partial \mathbf{u}}{\partial t} + \rho(\mathbf{u} \cdot \nabla) \mathbf{u} = \nabla \cdot \left[-p\mathbf{I} + \mu_{eff} \left(\nabla \mathbf{u} + (\nabla \mathbf{u})^T \right) \right] + \mathbf{F}$$

$$\rho \nabla \cdot \mathbf{u} = 0$$
(1)

The governing equation of MR fluid is expressed in Eq. (1), where ρ is density, μ_{eff} is effective viscosity. By using the effective viscosity leads easy to modeling of the MR fluid treated as a Newtonian fluid with specifying the yield stress and shear strain rate activate for each combination. Thus, μ_{eff} enables formulation of the governing equation non-linear to linear[8]. Adopting the concept of the effective viscosity, the behavior of MR fluid is given by as follows:

$$\tau = \mu_{eff} \cdot \dot{\gamma}$$
(2)

$$\mu_{eff} = \frac{\tau_y(H)}{\dot{\gamma}} + \mu$$
(3)

τ presents shear stress, τ_y is yield shear stress which is consistent with the function of magnetic field and $\dot{\gamma}$ is shear strain rate. The behavior of a MR fluid is well represented by the Bingham-Papanastasiou model [9,10] could be written as Eq.(4).

$$\mu_{eff} = \mu + \frac{\tau_y}{|\dot{\gamma}|} \left[1 - \exp(-m|\dot{\gamma}|) \right]$$
(4)

In order to use MR fluid model MRF-132DG, the yield stress based on Dr. Dave's empirical equation[11] is shown Eq. (5).

$$\tau_y = 271700C\Phi^{1.5239} \tanh(6.33 \times 10^{-6} H)$$
(5)

Eletromagnetic analysis must be taken into consideration to secure the total shear stress directly. To derive the magnetostatic equation, start with Ampere's Law for static cases $\nabla \times \mathbf{H} = \mathbf{J}$ and the current is shown as:

$$\mathbf{J} = \sigma \mathbf{v} \times \mathbf{B} + \mathbf{J}^c$$
(6)

Where \mathbf{J}^e is an externally generated current density, and \mathbf{v} is velocity of conductor. Using the definition of magnetic potential, $\mathbf{B} = \nabla \times \mathbf{A}$ and the constitutive relationship, $\mathbf{B} = \mu(\mathbf{H} + \mathbf{M})$, rewrite Ampere's law as:

$$\nabla \times (\mu_0^{-1} \nabla \times \mathbf{A} - \mathbf{M}) - \sigma \mathbf{v} \times (\nabla \times \mathbf{A}) = \mathbf{J}^e$$

In the quasi-static analysis the total braking force, F_b is composed of three types of forces as follows:

$$F_b = F_\tau + F_\mu + F_f = \Delta p_\tau A_p + \Delta p_\mu A_p + F_f \quad (7)$$

An analysis of the viscous force (F_τ) and MR fluid flow force (F_μ) is carried out using finite element method on following section whereas the friction force (F_f) can be calculated by the experimental result because it depends on the type of absorber piston rod seals and its velocity.

4.2 Simulation Method

As a first step, the hydraulic cylinder is considered as a moving mesh in an axial symmetric way shown in Fig.2. Since the shock causes driving the piston rod, the fluid inside cylinder discharges through port boundary pinhole of the cylinder. Upper half above the center line is the initial position and the other lower part shows the piston after moving. Numerical simulations are carried out with finite element method using COMSOL Multiphysics.

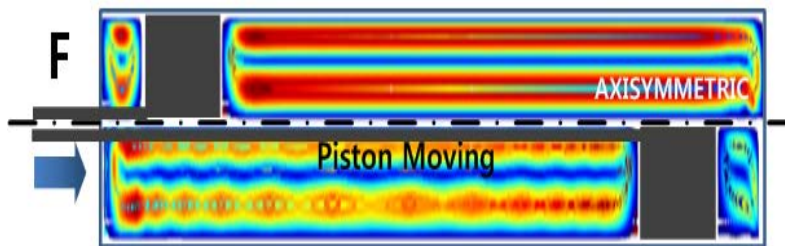


Fig. 2. Hydraulic cylinder with moving mesh in axial symmetry

Second, compose boundary pair to overlap port boundary of first step with inlet of MR shock absorber model. Assigning a boundary condition to connect the physics in the two parts. The spout velocity becomes inlet condition of the bypass device.

Fig. 3 shows the numerical simulation result of MR fluid shock absorber in 3D model. The cylindrical shapes are electromagnet and colored ring with thin narrow plate at the bottom depict MR fluid passage. The right side of passage is inlet of MR fluid and it paired with the boundary of simulation above. The arrow represents magnetic field and the results shows to be as quite appropriate for linear range of magnetic field 0 to 70 [kA/m] under saturation 250[kA/m] from technical data sheet of MR fluid-132DG. Such experimental devices are designed to make magnetic field toward the fluid effectively as shown in arrow. For increasing the current, alteration of pressure affected field is much greater than the other. After estimating pressure to force, the static force of MR fluid absorber appears about 480N for 0.5mm gap at 2.5 ampere current induced.

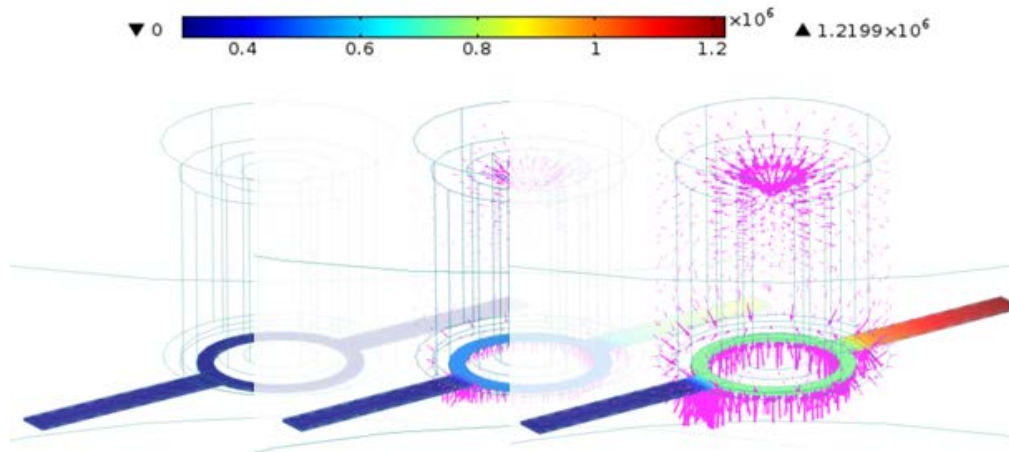


Fig. 3. Magnetic field (arrow) and Pressure [kPa] at 0, 1, 2.5 ampere

5. Experimental Results and Discussion

In order to verify the possibility of novel MR fluid absorber, principal experimental set up composed for measuring static force. Variable displacement hydraulic pump system applied to control the movement of the cylinder. Experimental apparatus is shown in Fig. 4, which is constructed to find the basic parameter such as force and displacement with respect to the piston velocity.

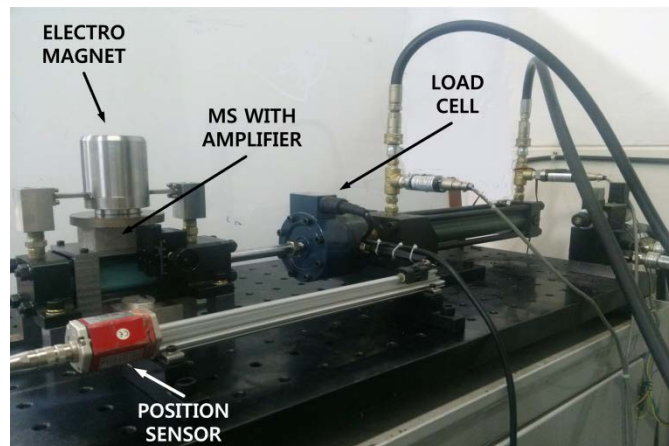


Fig. 4. Experimental apparatus

Fig. 5. present the static characteristic of a shock absorber as increasing the velocity linearly 10 to 50 mm/s in different coil current at the gap 0.75 and 0.5 mm. The maximum force 475N for the gap 0.5mm approximately is generated by absorber and it is quite correspondent to the simulation result. At the current of 0 ampere for equivalent gap, minimum force arises about 150N caused by viscous force and friction force as mentioned Eq. (7). The result shows the velocity has an small effect on the static force and this might be come from the slight increase of viscous force compare to total braking force.

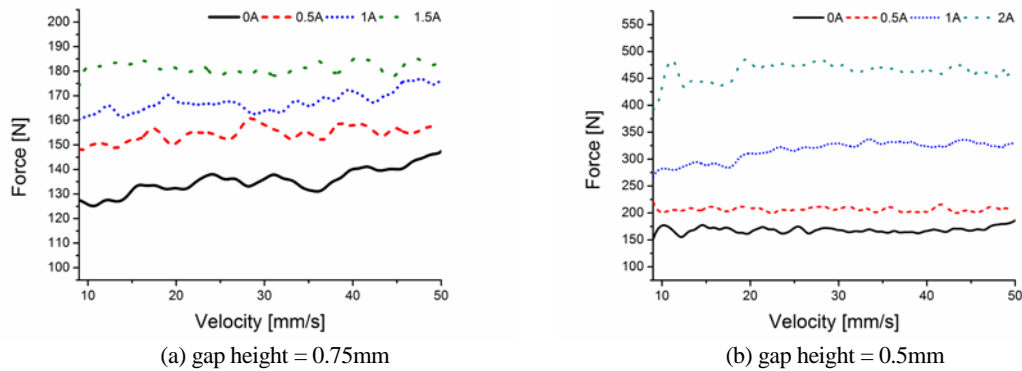


Fig. 5. Static characteristic of MR fluid shock absorber

6. Conclusion and Future Work

In this research, a novel MR fluid absorber is suggested and confirmed the possibility with principal numerical simulation and experimental setup for static characteristic of devices.

Especially, designing a novel absorber adjusting the gap height shows a great potential with various conditions which result emphasize that wide range of dependent variable such as velocity and braking force under just a single unit of MR fluid absorber. By arranging the electromagnet, the system can be selected range of magnetic field with relatively maintaining cost, and thus becomes easier to repair and reduce the set-up time. The next step of this research, finding dynamic characteristic of the absorber with innovate controller for braking force should be considered for more efficient absorbing the external impact.

Acknowledgment

This work was supported for two years by Pusan National University Research Grant.

References

- [1] A. Shafer and M. Kermani, On the Feasibility and suitability of MR Fluid clutches in human-friendly manipulators, *IEEE/ASME Transaction on Mechatronics*, **16**, 2011.
- [2] J. Huang, J. Zhang, Y. Yang, Y. Wei, Analysis and design of a cylindrical magneto-rheological fluid brake, *Journal of Materials Processing Technology*, **129**, 559-562, 2002.
- [3] F. Imaduddin, S. Mazlan H. Zamzuri, A Design and modelling review of rotary magnetorheological damper, *Materials & Design*, **51**, 575-591, 2013.
- [4] A. Milecki and M. Hauke, Application of magnetorheological fluid in industrial shock absorbers, *Mechanical Systems and Signal Processing*, **28**, 528-54, 2012.
- [5] M. J. Goodfriend and K. M. Shoop, High force, high strain, wide bandwidth linear actuator using the magnetostrictive material, Terfenol-D, Proc. of the conf. on recent advances in active control of sound and vibration, 1991.
- [6] A. Grunwald, A. Olabi, Design of a magnetostrictive (MS) actuator, *Sensors and Actuators A* **144**, 161-175, 2008.
- [7] M. Muraoka, S. Sanada, Displacement amplifier for piezoelectric actuator based on honeycomb link mechanism, *Sensors and Actuators, A: Physical A* **157**, 84-90, 2010.
- [8] E. Sadeghipour, Design and analysis of a magneto-rheological fluid damper with non-linear Surfaces to Produce Effective Variable Compliance in a Robotic Transmission, A thesis, Ohio State University, 2009.
- [9] T. Papanastasiou, T.C., Flow of materials with yield, *Journal Rheology*, **31**, 385-404, 1987.
- [10] E. Mitsoulis, Flow of viscoplastic materials: Model and Computation, *Rheology Reviews*, 135-178, 2007.
- [11] J. Carlson, MR fluids and devices in the real world. *Int. Journal Modern Physics B*, **19**, 1463-1470, 2005.

5-

**Innovative materials and
applications**

BROADBAND THERMO-ACOUSTIC ULTRASOUND TRANSDUCERS FOR NON CONTACT MATERIALS TESTING

Maxim Daschewski, Andrea Harrer, Jens Prager, Marc Kreutzbruck, Thorid Lange,
Matthias Weise and Uwe Beck
*Federal Institute for Materials Research and Tasting (BAM),
Unter den Eichen 87, 12205, Berlin, Germany*

Abstract. Airborne ultrasound transducers are increasingly used in NDT-applications where no couplant or other mechanical contact is allowed. Piezo transducers use a quarter wave acoustical adapter to compensate the impedance mismatch which unfortunately results in relatively long resonant pulses. In this contribution we present the theoretical description and the design of a simple thermo-acoustic device for the generation of post-oscillation free and broadband high pressure airborne ultrasound impulses. We report on measurements of sound pressures about 140 dB in 60 mm distance from transducer and investigate the frequency response of tested thermo-acoustic transducer in a frequency range up to 1 MHz.

The applications of non-contact ultrasound techniques for quality control and materials testing range from the detection of flaws in composite laminates, solar cells and printed circuit boards to applications in medicine and food industry.

Conventional piezoelectric-transducers move bidirectional and compress/expand the surrounding air adiabatically. However, a solid vibrating transducer is a moving mass and this leads to some drawbacks like a frequency dependent amplitude response and large post-oscillations in case of impulse excitation. Therefore are generally not well suited for impulse-echo applications on thin structures.

Thermo-acoustic transducers work without any massive moving parts. The transducer presented in this contribution consists on 30 nm thin titanium film on a 1 mm thick quartz glass substrate. Through the ohmic resistance of the titanium films it transforms supplied electric energy into an increase on kinetic energy of film atoms. The surrounding air particles, which hit at heated transducer atoms, bounce from these, get an extra portion of kinetic energy, and cool down the transducer. The increase of kinetic energy will transmit by collision on the next particles and run away from the heat source. Due to billions of particles that give simultaneously an extra kinetic impulse in the direction away from the heat source arise a sound wave. Hence a single current impulse excitation generates a single sound impulse free of any post-oscillations (see Fig. 1).

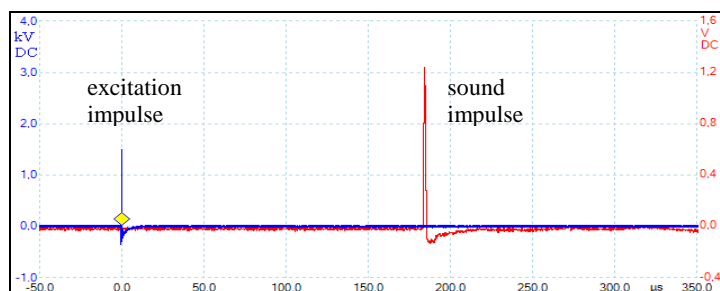


Figure 1: Measured sound impulse generated by a thermo-acoustic transducer consisting on the 30 nm thin and 1x1 cm² large titanium film on a quartz glass substrate after a 500 ns excitation with 1.5 kV. The distance from transducer is 60 mm.

The sound pressure p generated by a small thermo-acoustic transducer on a flat substrate for an arbitrary measurement point r in the surrounding air can be calculated as follows:

$$p(\bar{r}, t_i) = \frac{3 \cdot P_{\text{air}}}{16 \cdot \pi \cdot c_{\text{air}}^2 \cdot t_i \cdot |\bar{r}|} \quad (1)$$

$$P_{\text{air}} = P_i \cdot \frac{\lambda_{\text{air}}}{\lambda_{\text{sub}}} / \left(1 + \frac{\lambda_{\text{air}}}{\lambda_{\text{sub}}} \right) \quad (2)$$

P_i is the electric impulse power in Watt, λ_{sub} and λ_{air} are the heat conductivities of the substrate and the air, c_{air} is the sound velocity in the air and t_i is the impulse duration.

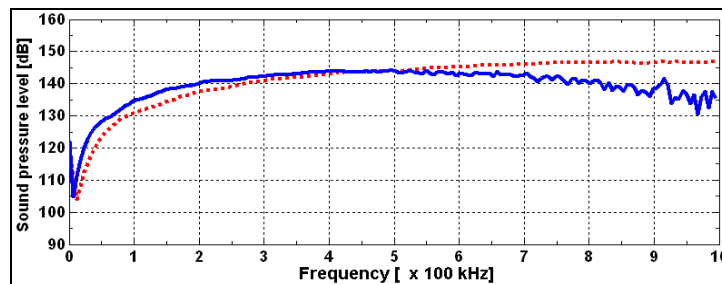


Figure 2: Frequency content and sound pressure levels of generated sound impulses after 500 ns (pointed line) and 1 μs (solid line) excitation with 1.5 kV impulses. The distance from transducer is 60 mm.

The results (Fig. 2) clearly show that the titanium thermo-acoustic transducer has a comparable acoustical efficiency like conventional piezoelectric airborne ultrasound transducers and can be applied - in contrast to the conventional transducers - as a broadband ultrasound source. Apart from that it shows no resonant behaviour. The sound pressure level is more than 140 dB at a distance of 60 mm from the transducer over a wide frequency range.

Also in comparison to literature results, our titanium transducer shows good performance. In 2002, Asamura et al. [1] reported about a thermo-acoustic device consisting of a 20 nm thin platinum film with 1 mm² surface on a 10 μm thin polyimide layer and measurements of 10 Pa (113.97 dB) sound pressure pulses at a distance of 10 mm from the transducer if electric impulses of 10 μs duration were applied. In 2005, Hwang and Kim [2] published their experimental study about pulsed nickel foils of 12, 10 and 0.75 μm thickness and reported about measured sound pressures of about 1 Pa (93 dB) at a distance of 50 mm from the foils.

References

- [1] N. Asamura, U. K. Saman Keerthi, T. Migita, N. Koshida, and H. Shinoda, "Intensifying Thermally Induced Ultrasound Emission", Proc. 19th Sensor Symposium IEEJ Tokyo, 2002, pp. 477-482.
- [2] D. In-Ju Hwang, Youn-Jea Kim, "Measurement of thermoacoustic waves induced by rapid heating of nickel sheet in open and confined spaces", International Journal of Heat and Mass Transfer 49, 2006, pp. 575-581.

CHARGE MEASUREMENT WITH FARADY CUPS AND LABVIEW

Kazem Dastoori (k.dastoori@dundee.ac.uk), David Thompson (d.s.thompson@dundee.ac.uk)

Brian Makin (b. makin@dundee.ac.uk).

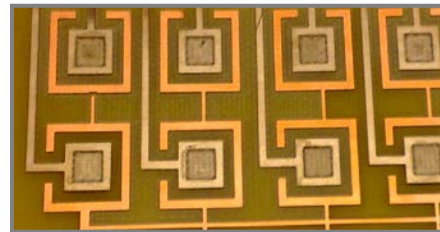
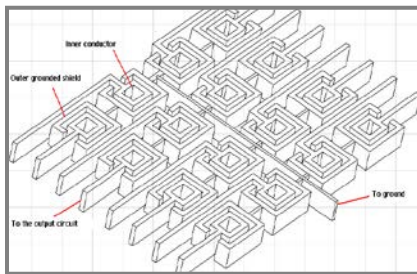
Abstract

The paper describes the design and application of an array of Faraday Cups mounted on a dielectric substrate for the PCB. The array was located in the field of a source of charged particles which were attracted to them and at the end of the charging process a measurement of the deposited charge was obtained as an identification of the level of deposition. The results were analysed statistically to confirm the validity of the technique.

Introduction

One purpose of this investigation was to establish quantitatively the amount of charge deposition from a cloud of charged particles by a method of change of capacitance to earth of each Faraday cup. The method of measurement involved the application of a capacitance sensor whose voltage to earth was measured with a Labview package.

For the purposes of this investigation a PCB of FR4 material was fitted with an array of 16 Faraday cups. Each cup was the result of a deposition of Ni on to the FR4 substrate, as shown in Figs 1 and 2.



Figs 1 and 2 shown a complete sets of arrays on FR4 substrate

Charged particles were generated in the laboratory by two methods: in one a corona charging gun was used and in the second a tribo-electrification gun was used. Results for each method are provided; corona charging produced negative pulses of voltage and negatively charged particles, whereas the tribo gun produced positively charged particles

Measurement

The amount of charge in each cup was determined from the application of the following relation for the capacitance of each cup:

$$C_{cg} = \frac{4\varepsilon_o K_{FR4} L d}{t_1} + \frac{\varepsilon_o K_{nickel} L w}{t_2} \quad (1)$$

Where: t_1 is the thickness of the FR4 substrate, t_2 the thickness of the nickel, and w the width of the bottom, L the sidewall length and d the sidewall depth of each cup respectively.

After spraying the array with charged particles the charge measurement was undertaken for each cup. Results are shown in Figs 3 and 4.

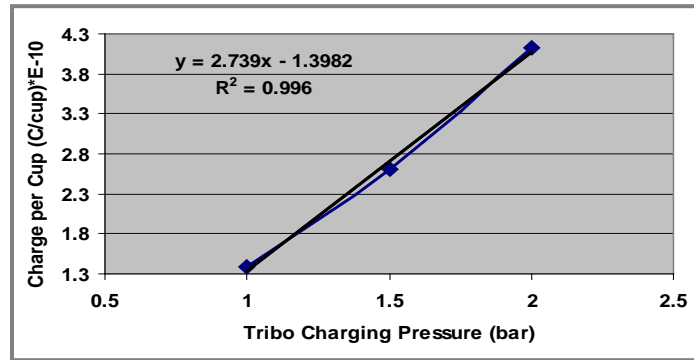


Fig 3 The Relation between the Charge per Cup for FCA1 and the Tribo Charging

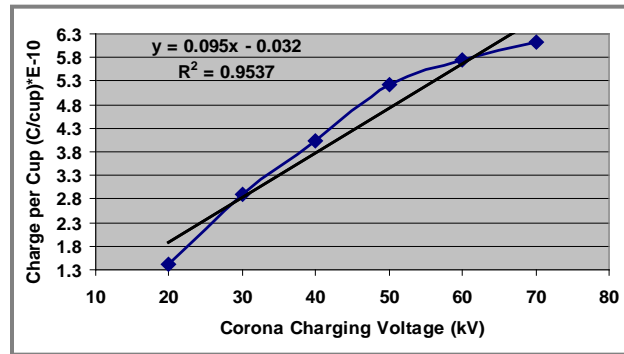


Fig 4: The Relation between the Charge per Cup for FCA1 and the Corona Charging Voltage.

Conclusion

In conclusion the results show how increasing the charge on the particles leads to, the not unexpected result of increased deposition. The results have been correlated elsewhere with observed reductions of electrical output from an array of PV converters. The results displayed in Figs 3 and 4 for each method of charging show the results of the processes and confirm the effect.

Acknowledgements

We wish to express our thanks to the University of Dundee for the facilities used in this investigation and to Mrs G. Al-Shabaan for her enthusiastic work on this project.

Design and Development of MR Actuator with Safety for Leg Power Assist Devices

Masami NAKANO

Institute of Fluid Science, Tohoku University, 2-1-1 Katahira, Aoba-ku, Sendai, 980-8577 Japan

Hiroshi NAKANO, Kouki TSUCHIYA

Graduate School of Engineering, Tohoku University, Aoba-ku, Sendai, 980-8577 Japan

Abstract. A safe and quick-response MR actuator for leg power assist devices has been designed and developed to use for walk rehabilitation. The actuator mainly consists of a developed magneto-rheological (MR) fluid clutch and a reversible DC motor with reduction gears, and will be suitable for the power assist devices of rehabilitation from a viewpoint of safety and relief, because the MR fluid clutch produces passively the magnetic field-dependent transmitting torque and makes for back-drivability. From the investigation of steady and transient performances of the developed MR fluid clutch, we found that it is suitable for leg power assist device.

1 Introduction

It is necessary for the power assist devices of walk rehabilitation to have the features of high-torque, high-controllability and high-safety. The clutch using a magneto-rheological (MR) fluid generates the magnetic field-dependent transmitting torque almost independent of the rotational speed, because the MR fluid behaves like a Bingham fluid having variable yield stress with magnetic field. Because of this inherent feature, the use of MR fluid clutch will be suitable for an actuator of the power assist devices.

In this study, the MR actuator consisting of the MR fluid clutch and a motor has been designed and developed for the use of the leg power assist device, which assists the power of knee extension and flexion during a walk rehabilitation. In this paper, the total design of the MR fluid actuator and the detailed design of the MR fluid clutch are described, and steady and transient performances of the clutch are investigated. The applicability of this actuator to the power assist device is discussed.

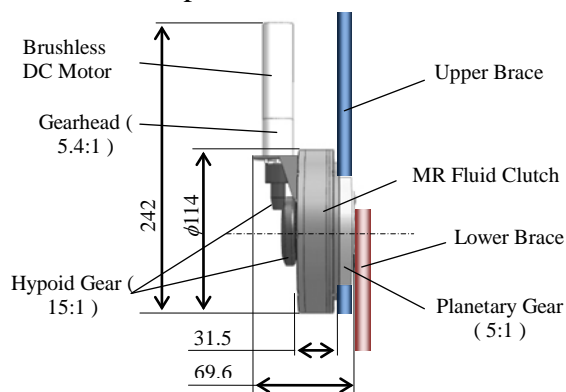


Figure 1: Developed MR actuator

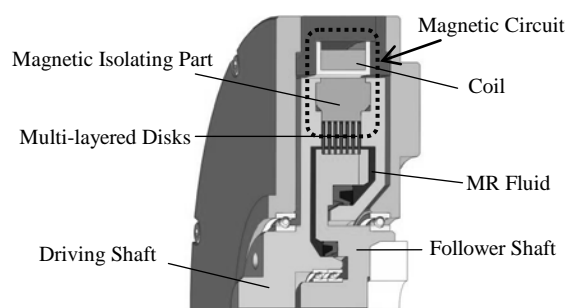


Figure 2: Cross-sectional view of MR fluid clutch

2 Design of MR Actuator

The developed MR actuator is shown in Fig.1. The actively produced motor torque is transmitted to the MR fluid clutch through two reduction gears (gear ratios of 5.4:1 and

15:1). The clutch torque controlled by the applied coil current is transmitted to the knee braces through the planetary gear (gear ratio of 5:1). The design goal of the clutch torque T is set to be 4.5 Nm based on the requirements in the normal walking of healthy person, which is the knee torque of 20 Nm [1] and the knee rotational speed of 66 rpm [2].

In wearable power assist devices, the actuator needs to be designed compactly. Therefore, the multi-layered disk type MR fluid clutch is designed as shown in Fig. 2. This clutch has 6 driving and 7 follower disks (thickness of 0.5 mm), and an MR fluid (MRF-132DG, Lord Co.) in the 14 gaps of 0.1 mm between the disks, and a magnetic coil (wire diameter; 0.3 mm, turns; 400, electric resistance; 29.9 Ω) outside of the disks. The dashed line in Fig. 2 indicates the magnetic circuit, which is formed by an electromagnetic coil.

3 Performances of Developed MR Fluid Clutch

The measurements of steady torque T as a function of coil current I from 0 to 1.0 A are conducted at constant rotational speeds N_r of 10, 30, 50 and 100 rpm. The MR fluid clutch transmits almost constant T depending on I , and the T increases with increasing I in a good agreement with the analytical one based on the magnetic field analysis, slightly depending on the rotational speed, as shown in Fig.3. It can be ensured that the MR fluid clutch transmits T of at least 7.9 Nm at $I = 1.0$ A, so that the MR actuator generates the output torque of at least 39.5 Nm at $I = 1.0$ A.

Figure 4 shows the transient responses of T and I when a step input of desired $I = 0.5$ A is applied to a coil power supply (servo amplifier). It can be ensured that this clutch is the second order lag element of torque, which has the rise time $T_r = 3$ ms, the time to peak $T_p = 12$ ms, the settling time $T_s = 23$ ms and the pure time delay $L = 3$ ms.

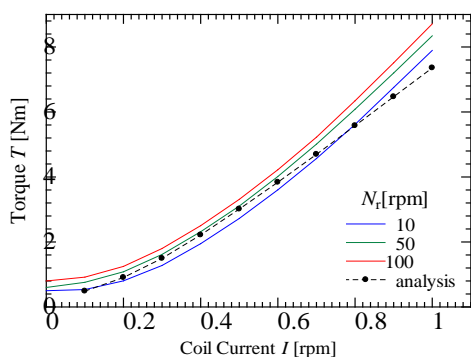


Figure 3: Analytical and experimental steady torques vs. coil current.

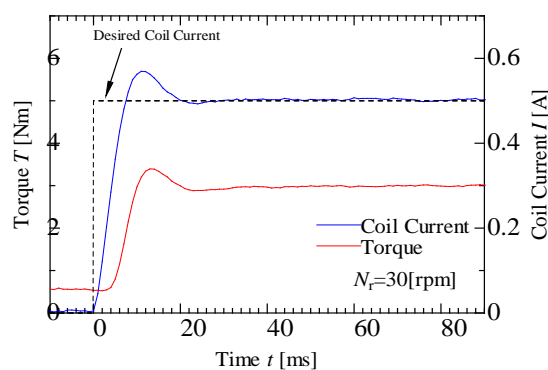


Figure 4: Step responses of torque and coil current

4 Concluding Remarks

It is found that the developed MR actuator is capable of generating the magnetic-field dependent torque up to 39.5 Nm for a coil current of 1.0 A and the MR fluid clutch has a relatively high response speed of torque. The clutch has the features of high controllability and safety because of the characteristics such as the low dependence on rotational speed, the simply controlled torque and the torque limiting function, showing that the developed MR fluid actuator is suitable for leg power assist device.

References

- [1] H. Kawamoto and Y. Sankai, *Proc. IEEE ICSMC*, Vol. 4 (2002) 447-452.
- [2] Y. Hiiragi, et al., *Rigakuryoho Kagaku*, Vol. 20(2) (2005) 93-98.

6-

**Electromagnetic functional
materials and adaptive
systems**

Two-position Magnetic Lock [□]

Mirosław Wołoszyn^{a,□□}, Piotr Jankowski^b

^a Faculty of Electrical and Control Engineering, Gdańsk University of Technology, 11/12 Narutowicza Street, Gdańsk, 80-233, Poland

^b Faculty of Marine Electrical Engineering, Gdynia Maritime University, 81-87 Morska Street, Gdynia, 81-225, Poland

Abstract. This article describes a two-position magnetic lock. This lock allows to change the position of the ferromagnetic bolt without a spring. It can be used for the protection of windows, doors and gates. The lock consists of a ferromagnetic bolt, two coils, Nd magnets, a voltage source and a switch. The operation of the two-position magnetic lock was simulated in the ANSYS EM 2D program. The results of the computer simulations have been presented in this paper. These results have been compared with experimental results.

Keywords: magnetic lock, magnetic field.

1. Introduction

There are numerous designs of magnetic locks [1,2]. The change of the position of the bolt occurs when voltage is applied to the electromagnetic coil. A two-position lock which allows for continuous protection, e.g. anti-burglary protection of doors and windows without continuous power supply to the lock coil, has been presented in this article [3]. Computer simulation of the lock operation was performed using the ANSYS EM program. The proper functioning of the system was tested using a physical model.

2. Two-position lock design

The two-position, springless electromagnetic lock consists of two coils wound around a copper tube (Fig. 1). Inside the tube there is a ferromagnetic bolt with an Nd magnet on each side. A nut made of ferromagnetic material is placed on the other side of one of the magnets. A pin made of a non-ferromagnetic material (e.g. non-magnetic steel) is screwed into the nut. The system composed of the ferromagnetic bolt, the magnets, the nut and the pin forms a joint working system in the lock. The pin is the element which blocks the protected object (e.g. a window, a door) from being broken out. The pin diameter is smaller than that of the remaining elements of the working system. The pin goes through a steel washer mounted on both sides of the copper tube. The electric current running in one of the coils causes the whole working system to move towards this coil and to stop at the steel washer. The Nd magnet draws the working system towards the washer. A change in the position of the system occurs when the electric current is applied to the other coil. The copper tube functions as an electromagnetic break for the working system. The eddy currents induced in the tube decrease the stroke of the system onto the steel washer. Applying the electric current is required only to change the position of the pin in the lock. The lock electric circuit diagram has been presented in Fig. 2, whereas its dimensions have been shown in Fig. 3.

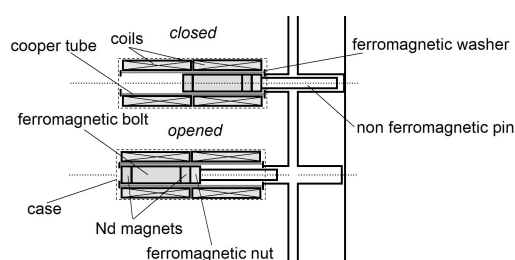


Fig. 1. Two-position lock design.

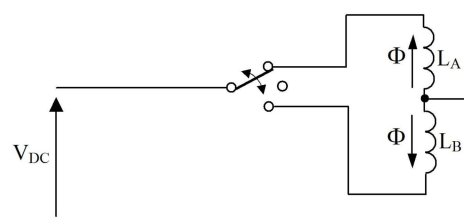


Fig. 2. Lock electrical circuit diagram (Φ - magnetic flux).

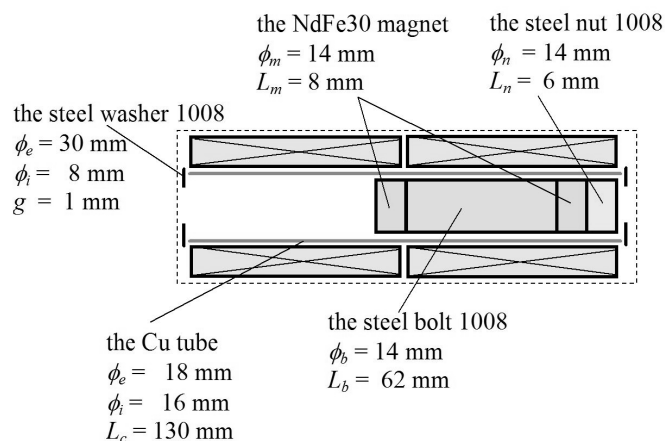


Fig. 3. Lock elements dimensions.

3. Computer simulations

Computer analysis of the operation of the two-position lock was performed using the ANSYS EM pack. The analysis was performed for both the passive and the active states of the lock. In the passive state the electric current does not run through the coil and the working system of the lock is drawn to the steel washer by the magnet. The distribution of the lines of forces of the magnetic field of the lock in the passive state has been shown in Fig. 4. Figure 5 shows the distribution of forces which act on the working system after it has been drawn to the washer. The attractive force between the working system and the washer for the assumed dimensions of the lock elements is about 1.5 N. In case the working system is set in the lock middle position, the resultant force is equal to zero (Fig. 6). After the electric current has been applied to the coil (the upper coil in Fig. 7), a magnetic force begins to act on the working system and moves it to its second position. In Fig. 7 the distribution of the lines of forces of the magnetic field of the lock in the active state has been shown. The resultant force acting on the working system depends on the force operating in the passive state (the force produced by the magnet) and the magnetic field produced by the coil (ampere-turns).

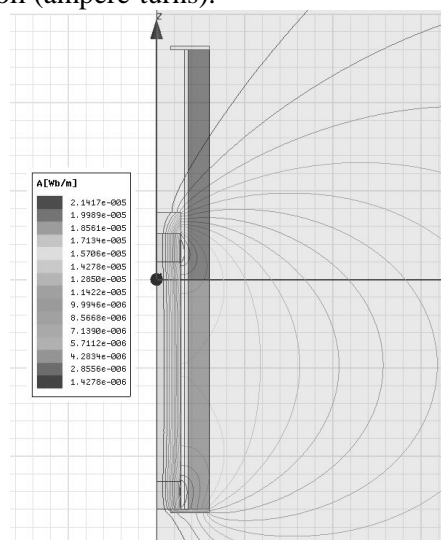


Fig.4. Distribution of the lines of forces of the lock magnetic field in the passive state.

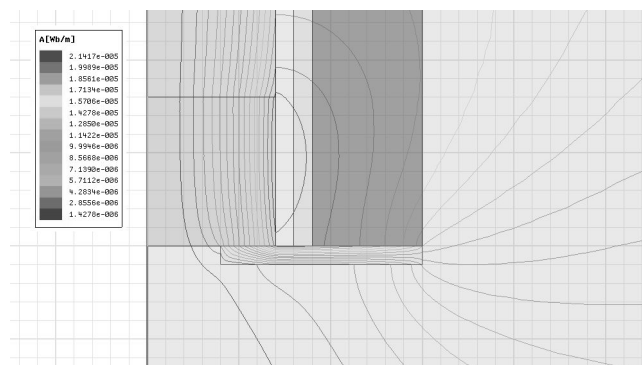


Fig.5. Distribution of forces acting on the working system near the washer.

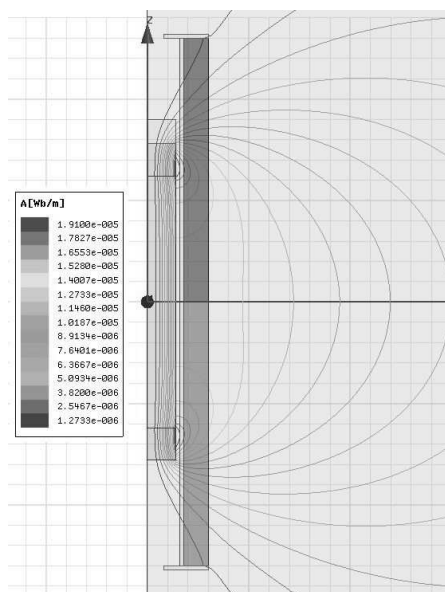


Fig.6. Distribution of the lines of forces of the lock magnetic field in the passive state in the lock middle part.

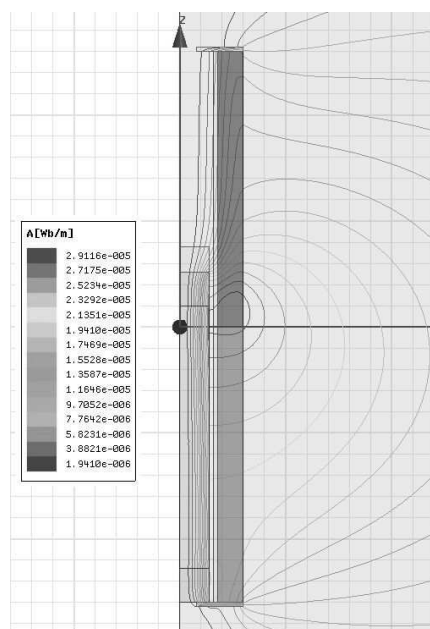


Fig.7. Distribution of the lines of forces of the lock magnetic field in the active state.

Figure 8 shows the distribution of the resultant force acting on the working system in the function of the coil ampere-turns. For the dimensions of the magnetic lock assumed for the purpose of this study, the force which results in moving the working system requires more than 400 ampere-turns.

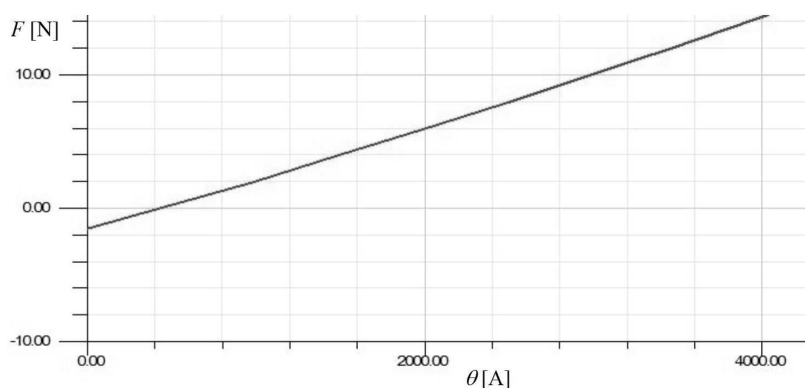


Fig. 8 Relation of the force acting on the working system in function of ampere-turns.

The value of the force in the passive state can be increased by changing the dimensions of the magnet or of those of the washer. Non-dimensional values have been used in the analysis of the relation of the

force in function of the magnet's length and the washer's thickness. Non-dimensional length of the magnet is described by the following equation:

$$L_{mn} = \frac{L_{mo}}{L_m} \quad (1)$$

where: L_m – the initial length of the magnet assumed in this study (see Fig. 3), L_{mo} – a different length of the magnet.

The non-dimensional thickness of the washer is described by the following equation:

$$g_n = \frac{g_o}{g} \quad (2)$$

where: g_m – the initial thickness of the washer assumed in this study (see Fig. 3), g_o – a different thickness of the washer.

The non-dimensional force F_n acting on the working system in the passive state is described by the following equation:

$$F_n = \frac{F_o}{F} \quad (3)$$

where: F – the force acting in the passive state for the assumed lock dimensions (see Fig. 3), F_o – the force for other dimensions of the lock.

Figure 9 presents the relation between the non-dimensional force acting on the working system of the lock and the non-dimensional length of the magnet. Figure 10 presents the distribution of the non-dimensional force in function of the non-dimensional washer. Figure 10 shows that for the tripled thickness of the washer, the force increases by nearly 300%. Further increase of the thickness of the washer does not result in a substantial increase of the force acting on the working system. In case the length of both magnets is increased, the force acting on the working system decreases due to the attracting of the other magnet to the other washer. This trend can be reversed but at the cost of elongating of the whole device. The analyzed system is asymmetric due to the lack of a nut on the side of the other magnet. If a second nut is added, the forces acting near the washers in two positions are identical. Moreover, the force acting on the working system, in which there is a steel nut between the magnet and the washer, is larger. Figure 11 presents the distribution of forces of the magnetic field of the symmetric lock in the passive state. After another nut is added, the force acting on the working system in the passive state increases 3.5 times.

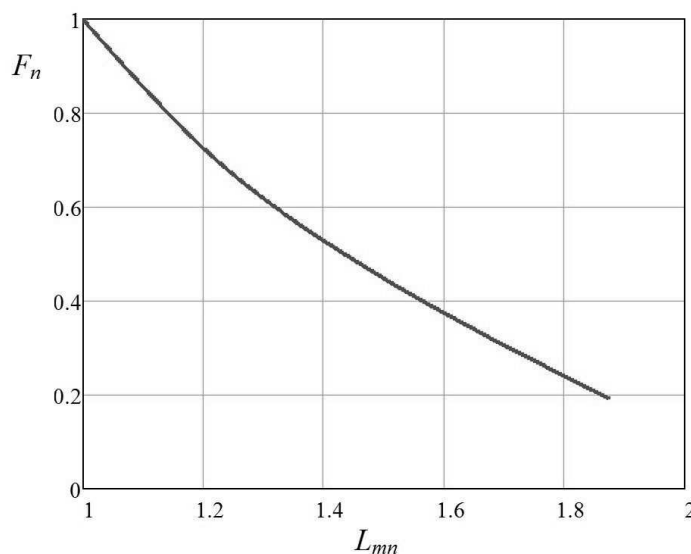


Fig. 9 Non-dimensional force acting on the working system of the lock in function of the non-dimensional length of the magnet.

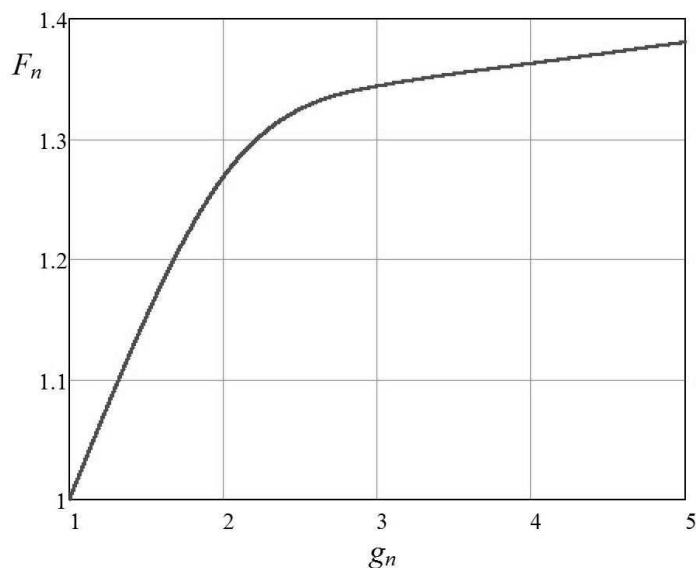


Fig. 10 Non-dimensional force of the lock in function of the non-dimensional thickness of the washer.

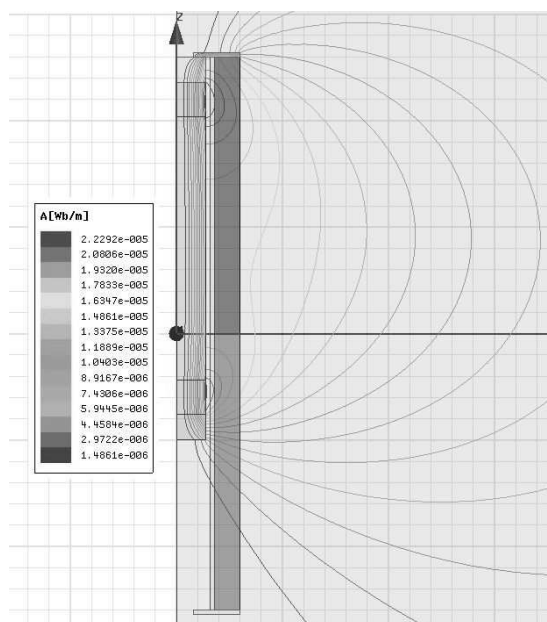


Fig. 11. Distribution of the lines of forces of the magnetic field of the symmetrical lock in the passive state.

4. Physical model of the lock

After the two-position magnetic lock has been designed and computer analysis of its functioning has been performed, its physical model has been built. Figure 12 shows a magnetic lock with a visible Nd magnet. The ferromagnetic pin is shown in Fig.13. The functioning of the magnetic lock has been tested both in the horizontal and vertical positions. In case of using the lock in a vertical position, the parameters of the device have to be set properly so that the electromagnetic force which acts on the working system is greater than the force of gravity.

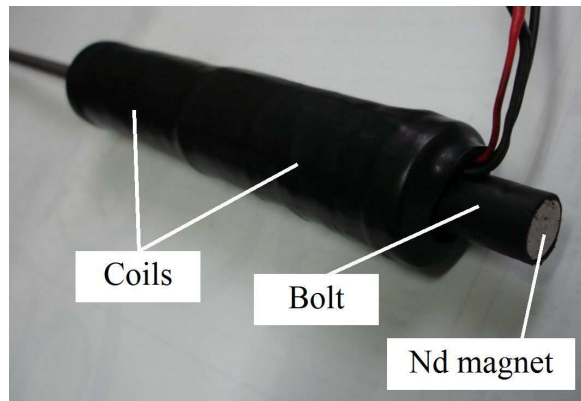


Fig.12. A physical model of the magnetic lock with a visible Nd magnet.

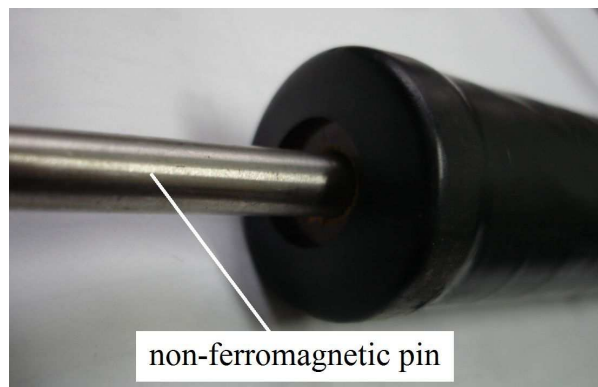


Fig.13. A physical model of the magnetic lock with the non-ferromagnetic pin visible.

5. CONCLUSIONS

This article presents a two-position magnetic lock. The value of the attractive force of the working system of the lock can be increased by adjusting the dimensions of the elements of the lock, particularly the length and the type of the magnet used. The device operates in both positions without electric current applied. Electric power supply is needed only to change the position of the working system of the lock. Practical tests carried out with the physical model of the lock have confirmed its proper functioning.

References

- [1] Separable magnetic lock for a purse or similar article US D247467 S.
- [2] Separable magnetic lock for a purse or similar article US D274883 S.
- [3] M. Olszewski, M. Wołoszyn: Patent application, 2013, Poland

Effect of the magnetic field in the air zone for receiving guided waves based on magnetomechanical effect

Jiang XU*, Dongying KONG, Xinjun WU, Ming CONG

School of Mechanical Science and Engineering, Huazhong University of Science and Technology, Wuhan, Hubei, P.R. China

Abstract. The effect of the change of the magnetic field in the air zone for receiving guided waves based on magnetomechanical effect is investigated by experiments. The area in the bias coil is divided into three zones: the air zone inside the pipe, the wall of the pipe, the air zone from the outside surface of the pipe to the bias coil. We find that the change of the flux in air is opposite to the change of the flux in the pipe wall. In addition, the change of the magnetic flux in the air zone, is almost equivalent to the change of the flux in the pipe wall but in opposite directions. These results explain why the signal amplitude becomes smaller when the receiving coil is loosen for receiving guided waves based on the magnetomechanical effect. Furthermore, these results indicate that the contribution of the change of the magnetic field in the air zone to the receiving signals cannot be ignored.

Keywords: magnetomechanical effect, receiver, air zone, guided wave, pipe

1. Introduction

The use of the guided waves propagating along the pipe wall is a very attractive solution for rapid detection of the pipeline. Since the guided waves can propagate a long distance with a little attenuation from the excited position. The guided wave technology based on the magnetostrictive effect and the inverse magnetostrictive effect (or the magnetomechanical effect) is widely applied to test the pipe, cables and so on [1-5]. By contrasting with the piezoelectric guided wave technology, the magnetostrictive technology can generate and receive guided waves with a large lift-off distance that can reach tens of milometers. The axially symmetric modes, such as $L(0,1)$, $L(0,2)$ and $T(0,1)$ modes, are the most widely used modes for pipelines. The receiving coil is encircled the pipe to receive the axially symmetric mode guided waves based on the magnetomechanical effect. In tests, the receiving coil is encircled tightly on the pipe, but occasionally the receiving coil is loosened. We find that the amplitude of the receiving signals becomes smaller when the receiving coil is loosened. Unfortunately, in the magnetomechanical model, the contribution of the change of the magnetic field in the air zone to the receiving signals is generally ignored because the air permeability is much lower than the permeability in the ferromagnetic

* Corresponding author: Jiang XU, School of Mechanical Science and Engineering, Huazhong University of Science and Technology, 1037 Luoyu Road, 430074, Wuhan, P.R. China. Tel: 0086-27-87559332; Fax: 0086-27-87559332; E-mail: jiangxu@mail.hust.edu.cn ,

material [6-8]. Based on the magnetomechanical model, the loosened receiving coil will not affect the receiving signals. The experimental phenomena are in contradiction with the model.

To explain this contradiction, this paper is investigated the contribution of the change of the magnetic field in the air zone for receiving guided waves based on magnetomechanical effect by experiments. Three group receiving coils are designed to study the contribution of the variation magnetic field in three zones to the receiving signals. The three zones are the air zone inside the pipe, the wall of the pipe and the air zone from the outside surface of the pipe to the bias coil. The experimental results show that the changes of the magnetic field in the air and in the pipe wall are basically in the same magnitude, but opposite in sign. These results indicate that the contribution of the change of the magnetic field in the air zone to the receiving signals cannot be ignored in the magnetomechanical model. Additionally, these results explain why the signal amplitude becomes smaller when the receiving coil is loosen for receiving guided waves based on the magnetomechanical effect.

The structure of the paper is as follows. The theory background is given in Section 2. Section 3 gives the experiment setup. Three group receiving coils are given to obtain the induced signals of three zones. The experimental results are given in Section 4. The contribution of the change of the magnetic field in the air zone to the receiving signals is discussed. The conclusions are provided in Section 5.

2. Theory background

The inverse magnetostrictive effect or the magnetomechanical effect is defined as: when a ferromagnetic material during magnetization is subjected to the change of a stress, the change of magnetization in the material is exhibited. The longitudinal inverse magnetostriction effect is called the Villari effect. When the longitudinal mode guided waves propagate in the pipe, the stress in the propagating position is variation. The change of the magnetic flux density is exhibited. Under a sufficiently strong axial bias field, the Villari effect of the ferromagnetic metal can be linearity and non-hysteretic when the induced magnetic field is far less than the bias field. From the principle of energy conservation, the relation of the mechanical to the magnetic properties can be expressed as:

$$B = eT + \mu^T H \quad (1)$$

where B is the magnetic flux density, e is the magnetostrictive cross-coupling coefficient, T is the stress, μ^T is the permeability at constant T , H is the magnetic field strength. The equation gives the relation between the stress and the magnetic flux density as the Villari effect. In terms of Le Chatelier's principle, the small reversible changes a thermodynamic relation between the Joule effect and the Villari effect could be given:

$$\left(\frac{\partial \lambda}{\partial H} \right)_T = \left(\frac{\partial B}{\partial T} \right)_H \quad (2)$$

where $\left(\frac{\partial \lambda}{\partial H} \right)_T$ is the rate of change of magnetostriction with the magnetic field at the constant stress and $\left(\frac{\partial B}{\partial T} \right)_H$ is the change of the magnetic induction with the stress at the constant field. Equation (2) shows that if the change rate of the magnetostriction is fixed, the change of the magnetic induction is same when the receiving coil is open and the bias magnetic field is fixed. Here the dispersion and the attenuation of the elastic waves are ignored.

The layout of the receiving position is shown in figure 1. The area in the bias coil of the receiving side is divided into three zones. To study the contribution of the change of the magnetic field in the air zone (Zone I and Zone III) to the receiving signals, we should obtain the signals of three zones separately. According to this requirement, three group coils are designed and the details are given in Section 3.

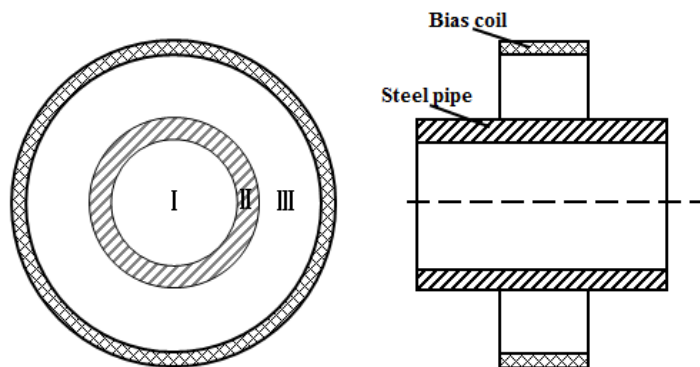


Fig.1 The layout of the receiving position

Zone I: the air zone inside the pipe;

Zone II: the wall of the pipe;

Zone III: the air zone from the outside surface of the pipe to the bias coil.

3. Experiment setup

The specimen was a steel pipe, which was about 3200 mm long with 38 mm outside diameter and 28 mm inner diameter. The bias coils on the excitation side and on the receiving side were same, which were made of No.16 gauge wire, with 500 turns, 110 mm width and 160 mm diameter. The excitation coil was made of No.26 gauge wire, with 20 turns, 11 mm width and 38.5 mm diameter, which encircled the outside surface of the pipe. There were three group receiving coils to induce the signals. The first group receiving coil (Coil A) was made of No.26 gauge wire, with 20 turns, 11 mm width and 27.5 mm diameter, which induced the change of the magnetic field of Zone I. The second group receiving coil (Coil B) was made of No.26 gauge wire, with 20 turns, 11 mm width and 38.5 mm diameter, which induced the change of the magnetic field of Zone I and Zone II. The third group receiving coil (Coil C1 and C2) consisted of the same two coils, which were made of No.26 gauge wire, with 20 turns, 11 mm width, and 55 mm height. The coils were modelled as a hollow circular section to cover Zone III. The layout of the three group receiving coils at the receiving position is shown in Fig.2.

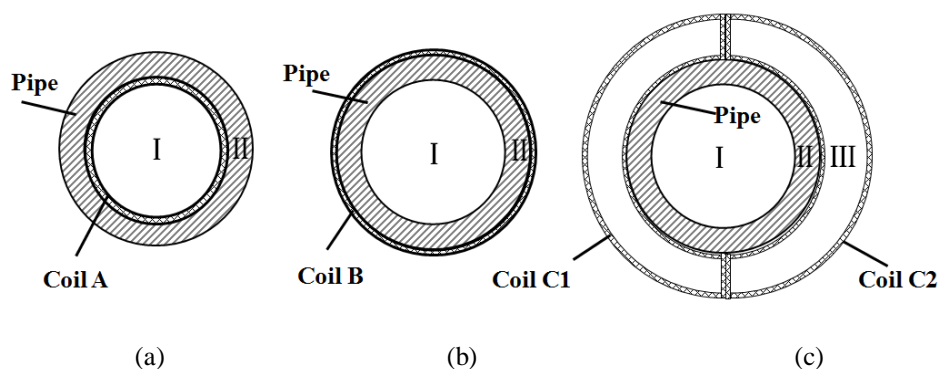


Fig.2 The layout of the three group receiving coils at the receiving position

(a) The first group receiving coil induced the signal from Zone I

(b) The second group receiving coil induced the signal from Zone I and Zone II

(c) The third group receiving coil induced the signal from Zone III

To reduce the effect of disperse, the excitation frequencies of the mode with little disperse were preferred. The axially symmetric L(0,1) mode at about 30 kHz and L(0,2) mode at about 120 kHz were selected. The bias current of the two bias coils was 3A. The exciting signal was two cycle sinusoidal tone burst with 120V peak to peak amplitude. The signals induced by the receiving coils were amplified (approximately 66 dB). The signals were subsequently digitized using an A/D card which work at 2MSa/s. To reduce white noise, the repeated time of each experiment was 300 times.

4. Results and discussions

The signal of Zone I was induced by Coil A. The signal induced by Coil B minus the signal induced by Coil A was the signal of Zone II. The signal of Zone III was induced by Coil C1 and Coil C2. The signals of three zones are shown in Fig.3 and only the first passing signals are given.

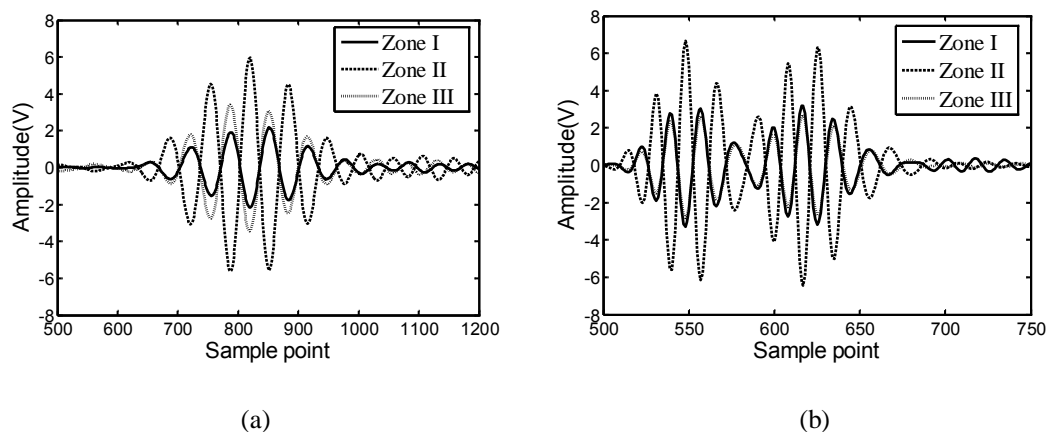


Fig.3 The first passing signals of three zones induced by the receiving coils
 (a) The excitation frequency is 30kHz;
 (b) The excitation frequency is 120kHz.

The signals of Zone I and Zone III (air zones) with the signal of the Zone II (pipe wall) were nearly out of phase at two excitation frequencies from Fig.3. The peak value of the signal of Zone II at 30kHz was 5.93V and the amplitudes the signal of Zone I and III at the same point were -2.16V and -3.56V respectively. The peak value of the signal of Zone II at 120kHz was 6.65V and the amplitudes the signal of Zone I and III at the same point were -3.29V and -2.83V respectively. The amplitude of the signal of Zone II was almost equal to the amplitudes of the signal of Zone I plus Zone III.

If the contribution of Zone II was defined as positive, the contributions of Zone I and III were negative to the induced signals. When the distance of air-gap between the receiving coil (Coil B) and the pipe surface increased, the contribution of Zone III to the induced signal would increase. Therefore, the amplitude of induced signals would decrease when the receiving coil encircled the pipe was loosened. Moreover, the change of the magnetic field in the air zone cannot be ignored in the magnetomechanical model. The change of the magnetic field, not the absolute value of the magnetic field, is induced by the receiving coil based on the Faraday's law of induction.

5. Conclusions

In this paper, the effect of the change of the magnetic field in the air zone for receiving guided waves based on magnetomechanical effect is investigated by experiments. We find that the change of the flux in the air zone is opposite to the change of the flux in the pipe wall. Furthermore, the amplitude of the induced signal in the air zone is nearly equal to that of the pipe wall. Therefore, the change of the magnetic field in the air zone cannot be ignored in the magnetomechanical model. Likewise, these results explain why the amplitude of the induced signal decreases when the air gap increases between the encircled receiving coil and the pipe surface.

Acknowledgements

This work was supported by the National Natural Science Foundation of China (Grant No. 51205148) and the National Major Scientific Instrument Development Project (Grant No. 2012YQ09017502).

References

- [1] J.L. Rose, Success and challenges for ultrasonic testing in NDT and SHM, *Materials Evaluation* **68** (2010), 494-500.
- [2] P. Cawley, M.J.S. Lowe and D.N. Alleyne, Practical long range guided wave testing: application to pipes and rail, *Materials Evaluation* **61** (2003), 66-74.
- [3] J.L. Rose, A baseline and vision of ultrasonic guided wave inspection potential, *Journal of Pressure Vessel Technology* **124** (2002), 273-282.
- [4] H. Kwun, J.F. Crane and S.Y. Kim, A torsional mode guided wave probe for long range, in bore testing of heat exchanger tubing, *Materials Evaluation* **63** (2005), 430-443.
- [5] J. Xu, X.J. Wu et al, A Magnetic Flux Leakage and Magnetostrictive Guided Wave Hybrid Transducer for Detecting Bridge Cables, *Sensors*, **12** (2012), 518-533.
- [6] D.C. Jiles, Theory of the Magnetomechanical Effect, *Journal of Physics D: Applied Physics*, **28** (1995), 1537-1546.
- [7] D.C. Jiles and L. Li, A new approach to modeling the magnetomechanical effect, *Journal of Applied Physics*, **95** (2004), 7058-7060.
- [8] Y.Y. Kim, S.H. Cho and H.C. Lee, Application of magnetomechanical sensors for modal testing, *Journal of Sound and Vibration*, **268** (2003), 799-808.

7-

Applied superconductivity

Development of noncontact Flywheel system with High Temperature Superconducting magnetic bearing

Iwanori Murakami^{a*}, Kei Nakashima, Masashi Gyoda, Takeru Shimada, and Yoshinori Ando
Department of Mechanical System Eng., Gunma University, 1-5-1 Tenjincho Kiryu, 376-8515, Japan

Abstract. In this research, we propose compact new flywheel system with high temperature superconducting magnetic bearing. This flywheel system obtains the levitation force and the restoring force by the pinning force of the high temperature superconducting magnetic bearing, and rotates by non-contact. And, because it has built-in driving part, this flywheel system is very compact. We achieved a steady high-speed revolution of the flywheel without control by this method.

Keywords: Magnetic flux concentration, Superconductor, Magnetic bearing,

1. Introduction

The Hi-Tc superconducting levitation system can achieve the stable levitation of a permanent magnet in the state of noncontact. There is no lubrication necessity in a magnetic levitating of the high temperature superconductivity because it is noncontact. In addition, the characteristic that the friction loss is a little because it is noncontact, and the high velocity revolution is possible is had. Those characteristics are made the best use of, and a lot of proposals such as magnetic bearings of the high temperature superconducting motor, the electric storing flywheel, and the centrifugal separator and contactless are done. In this research, a magnetic bearing where high-Tc superconductors were used is developed. And, the characteristic when the developed magnetic bearing is used with the electric storing flywheel is clarified.

When the flywheel is used by the purpose of the energy storage, the frictional energy loss becomes a problem. This magnetic levitating system can support it by noncontact. Therefore, the frictional energy loss is very small. In addition, a permanent magnet can be restrained by using the effect of the pin stop with the second kind superconductor at an arbitrary position

in the surfacing system that uses high-Tc superconductors. Therefore, achieving the noncontact surfacing by no control becomes possible. The electric power storing flywheel system with a little energy loss can be composed by making the best use of these advantages, and using superconducting surfacing system as a bearing.

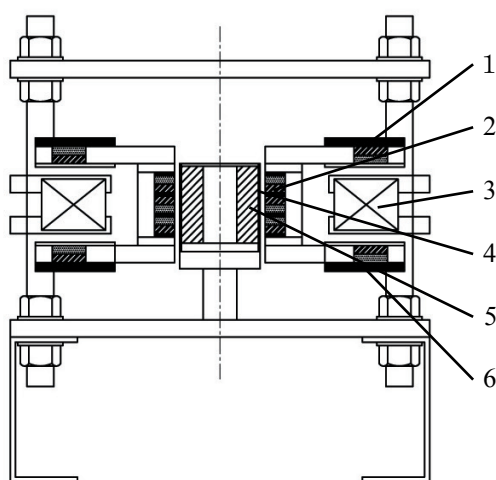
However, when the one with weight of flywheel is supported, high-Tc superconductors of the size corresponding to the size of the levitating body are needed. This is because the gaining levitating force depends on the size of the area of high-Tc superconductors and the restrained magnetic field. Then, the magnetic bunch focusing method was applied to the bearing of the flywheel in this research. It is thought that magnetic field strength and the magnetic inclination that the bearing of the flywheel makes from this can be strengthened. Therefore, big surfacing power and the restoration power can be gained from small high-Tc superconductors for the surfacing body. Moreover, cooling was enabled from the inside diameter part by using cylindrical high-Tc superconductors. Therefore, the consumption of the coolant is very little. We propose the system of a compact flywheel that uses the high temperature superconducting bearing where such a method was used by this research.

^a E-mail: murakami@gunma-u.ac.jp / TEL: +81-277-30-1564

2. Experiment device

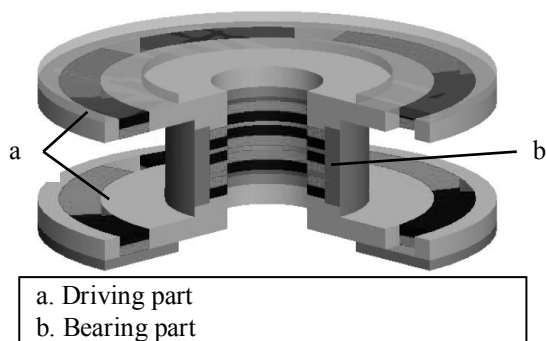
Figure 1 shows the system of the proposed high temperature superconducting magnetic levitation flywheel. The inside diameter of this superconductor is 20[mm], the outside diameter is 46[mm], and thickness is 45[mm]. The weight of the levitation rotor is 7.50[kg].

Figure 2 shows the flywheel used by this research. The flywheel is composed of the bearing part put between upper side and lower side.



1. Permanent magnet for driving
2. Permanent magnet for bearing
3. Driving coils
4. Cryostat
5. Superconductor bulk
6. Magnetic material plate

Fig. 1 Geometry of the system.



- a. Driving part
- b. Bearing part

Fig. 2 Composition of flywheel

2.1. Bearing part

The bearing part concentrate the flux of magnetic induction by set the magnetic material disc to a permanent magnet, and placing it in the direction that the magnetic pole opposes. In addition, the magnetic flux concentration part was adjusted to two places. As a result, a magnetic circuit was united, strong magnetic field strength was made in the axial direction, and a strong magnetic gradient was made in the direction of the radius along the flywheel circumference. The flywheel levitates being supported by the pinning force of the high temperature superconducting bearing in the flywheel.

2.1.1. Magnetic flux concentrated method

The magnetic induction in the space can be improved by how to arrange a permanent magnet like the Hull Bach array. It is common to arrange these arrays so that the direction where two or more magnets are magnetized may concentrate on one point. The same pole of a permanent magnet is opposed mutually in this research, and the magnetic field in the space has been strengthened with scissors of the magnetic material board among.

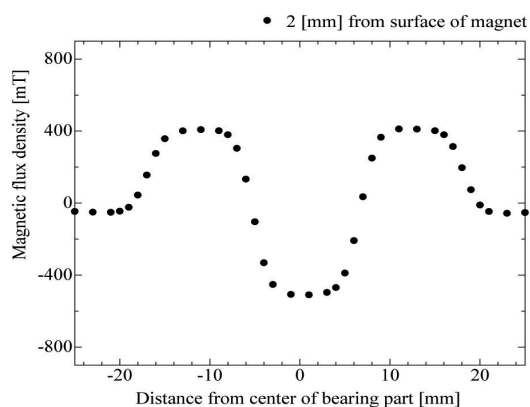
2.2. Driving part

Driving part is composed by a permanent magnet and the magnetic material disc. The composition of a magnetic circuit of the magnet adjoined mutually by making the magnetic material disc adsorb a permanent magnet has been facilitated. Therefore, driving magnetic field can be efficiently generated. In addition, a magnetic circuit is composed of the upper surface and the lower side by arranging driving part in the top and bottom of the bearing. Because this driving magnetic field is synchronized with the coil, driving power is gained.

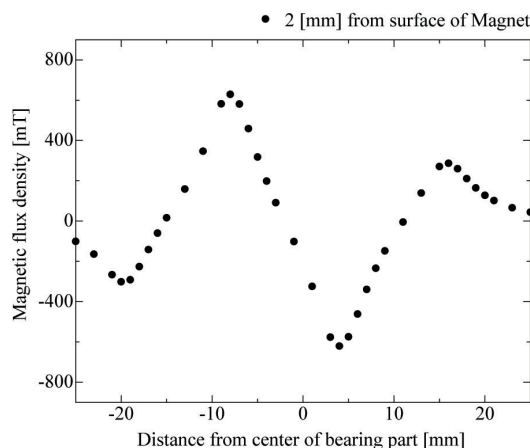
3. Experiments and results

3.1. Magnetic flux measurement

The magnetic flux in the bearing part of fly wheel is measured. Figure 3 (a) and (b) shows the result of the measurement. There are two points that focus the flux of magnetic induction as described in the column of the experiment device. It is a range from 5 to 7[mm] in the distance from the center respectively.



(a) Axial direction



(b) Radial direction

Fig. 3 Measurement of magnetic flux density

The large flux of magnetic induction was able to be created from the result in the direction of the radius of the bearing. In addition, it was confirmed to be able to create a large magnetic gradient axially.

3.2. Torque measurement

The flywheel was driven, and the torque was measured. The exchange current was thrown into driving coil with the amplifier of the fixed current type. However, the flywheel has not surfaced at this time. Figure.5 shows the result. Three coils were connected in parallel in this research, and they were assumed the set of one. Explanatory notes in figure 5 indicate the effect value of the exchange current

thrown into one coil set. The torque rises when the added voltage is raised. However, even if the rotational speed of each voltage rises, a big difference has not seen in the obtained torque. It is understood not to depend from the result to the rotational speed and to obtain a constant torque. In addition, the torque constant in this faction is obtained from the result as 0.164[Nm/A].

3.3. Restoring force measurement

We measured a axially and radial restoring force. The direction of displacement was restrained with the mechanism and constant displacement was given to the bearing part. The restoration force in that case was measured.

Figure 3(a) and (b) shows the result of the experiment. We understood to be able to gain very big restoration power of the maximum value 150[N] from a measurement result axially. It can be said that this is when enough restoration power can have been gained because the weight of the flywheel is 7.5[kg]. Moreover, the restoration power of the maximum value 50[N] can have been axially gained from a radial result. However, radial force is small in the drive method to use by this research. Therefore, it can be said enough in the restoring force that can have been gained so that it may carry out the function of the bearing.

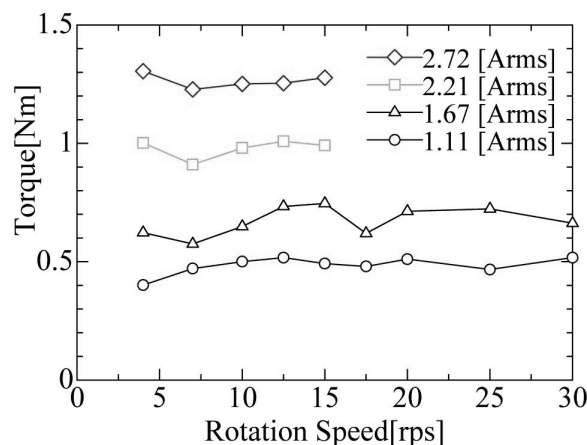
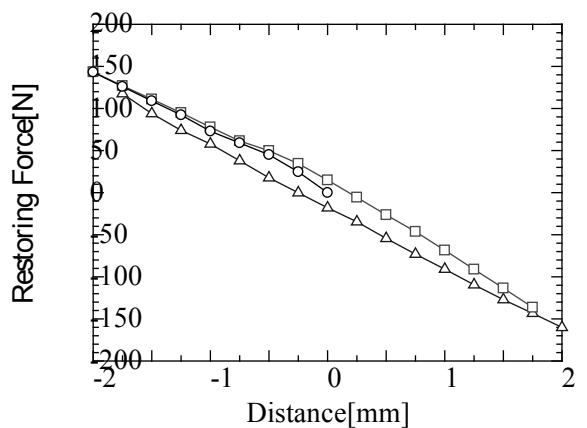
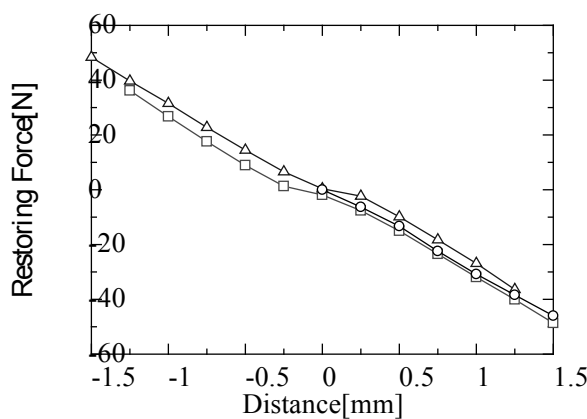


Fig. 4 Driving torque of constant current



(a) Axial direction.



(b) Radial direction.

Fig. 5 Hysteresis of the restoring force

3.4. Driving experiment

The behavior when the flywheel system that proposed it was driven was measured. The vibration displacement that happened in driving part was measured with the laser displacement sensor. The rotational speed was measured by using the tachometer at the same time. Figure 6 and 7 shows the frequency response of the result of the measurement. It is understood to increase some displacements from the result in 12[Hz]. The increase of big displacement is one of the features seen in the resonance. Therefore, we confirmed that the resonance of this system had been generated in 12[Hz]. However, the flywheel

increased the rotational speed afterwards. Moreover, the resonance point was got over without adding the control, and the flywheel was driven to 100[rps] with stability. Therefore, we thought that power generation in the high-speed rotation region was possible.

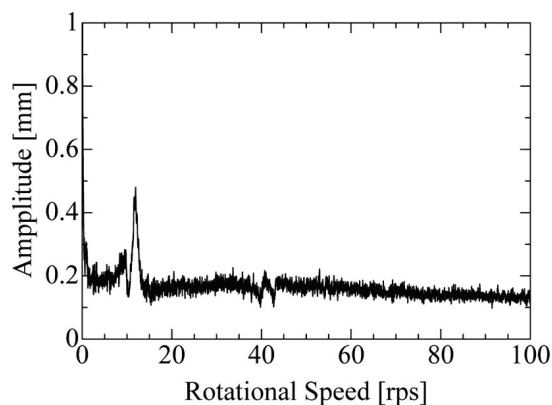


Fig. 6 Frequency response in the radial direction

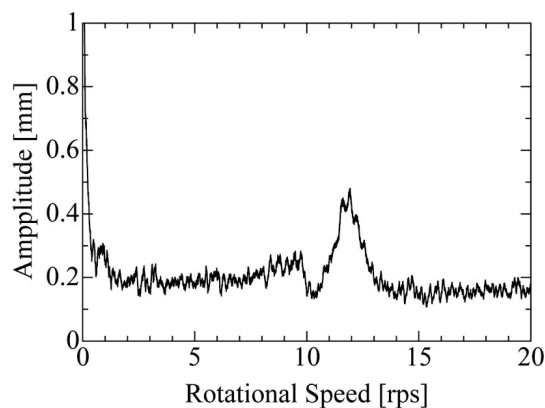


Fig. 7 Frequency response (from 0 to 20 [Hz])
 in the radial direction

3.5. Conversion efficiency measurement

We measured production of electricity in this system. The conversion efficiency of energy is calculated after the high-speed rotation region reaches and production is requested. The counter electromotive force of the exchange has generated in driving coil is used for the calculation. The procedure for calculating is as follows. The resistance of 100[Ω] was obtained for the coil, the counter electromotive force

was impressed, and the electric power was measured. Figure 8 shows the model of the circuit at this time. Power consumption P at this time was requested from the voltage given to resistance by using the following equations.

$$V = |Z + Z_L| V_L / |Z_L| \quad (1)$$

$$I = V / |Z + Z_L| \quad (2)$$

$$P = R_L I^2 \quad (3)$$

In this expression, the effect value of the counter electromotive force generated in driving coil is indicated as V . Similarly, the impedance of the coil and the load resistance that indicates the effect value of the current that flows to V_L and the circuit in the effect value of the voltage impressed to the load resistance as I is shown respectively as Z and Z_L . Moreover, it experimented until the rotational speed of the flywheel decreased to 13.3[rps] -93.3[rps]. Figure 8 shows the relation between effect value V_L of the voltage impressed to the load resistance and the rotational speed of the flywheel. Moreover, the relation between time and the power consumption requested by using equation (1-3) is shown in Figure 9. However, the value that can be calculated becomes one coil set. Three coils are treated as single-unit as written by the item of the torque measurement in the actual experiment machine, and these three sets are used. Therefore, the one that three electric powers requested here were multiplied becomes an actual electric power. Therefore, ΔE is the next expression and demonstrative in a kinetic energy amount of the change in the time base range.

$$\Delta E = J_p (\omega_1^2 - \omega_2^2) / 2 \quad (4)$$

J_p is ultra moment of inertia of the flywheel here. ω_1 is a rotation corner speed when beginning to measure it, and ω_2 is a rotation corner speed when the measurement ends. The conversion efficiency from the kinetic energy to the electric power energy calculates in except in the one that the one that integrated Figure 9 and had calculated was calculated by equation (4). Figure 10 shows the integrate Figure 9.

Figure 11 shows the time response of rotation speed. As a result of the calculation, we confirmed conversion efficiency profitable of about 79 percent.

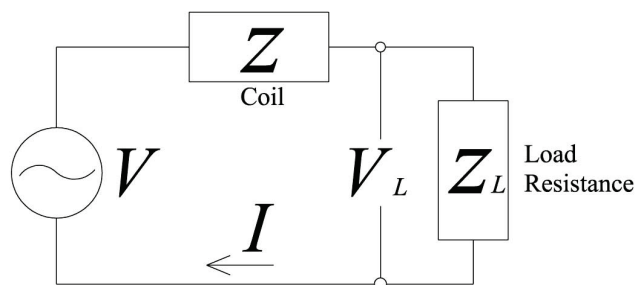


Fig. 8 Model chart of power generation circuit

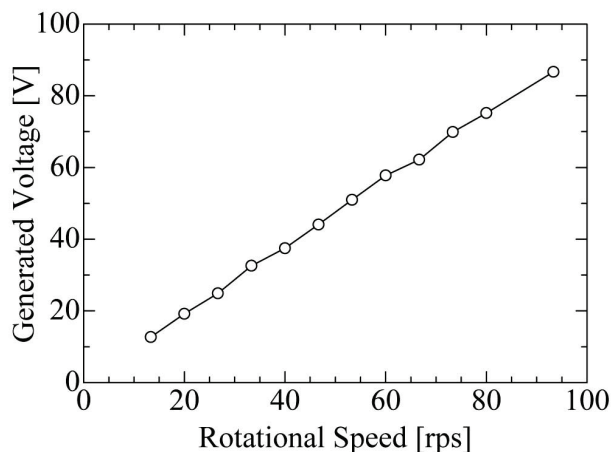


Fig. 9 Relation between generated voltage and rotation speed

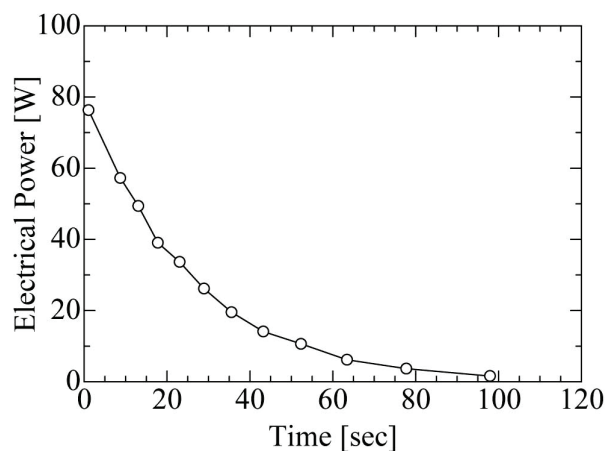


Fig. 10 Time response of electrical power

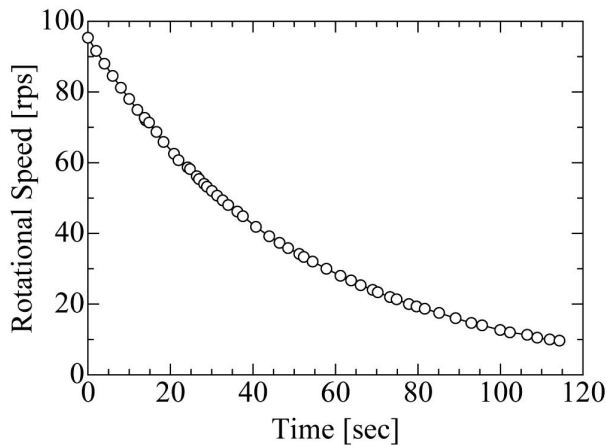


Fig.11 Time response of rotation speed

4. Conclusion

The following can be said from the experiment result of this research.

- Axially and both strong magnetic inductions and big magnetic bunch inclinations were able to be created radially by settling the flux of magnetic induction.
- The direction of the bearing and big restoration power was able to be created radially by restraining the settled flux of magnetic induction in the high temperature superconducting magnetism bearing.
- It succeeded in getting over the resonance point by no control, and doing the stability drive to the high rotation region.
- It was possible to take it out by converting about 79 [%] of the kinetic energy stored to the flywheel into the electric power energy.

Therefore, it proposed the system of a stability drive possible, new flywheel without the control.

Reference

- [1] I. Murakami, Y. Kobayashi, M. Gyoda, Y. Ando and K. Yamada, Development of magnetic levitation synchronous motor with high-Tc superconducting bearing, IJAEM 39 (2012) 97-103
- [2] I. Murakami, M. Gyoda, K. Nakashima, and Y. Ando, Characteristic Analysis of Noncontact Hi-Tc Superconducting Magnetic Bearing with Magnetic Flux Concentration Method, SEAD24 (2012)
- [3] K. Nagaya, M. Tsukagoshi, Y. Kosugi and M. Murakami, Vibration control for a High-Tc superconducting

nonlinear levitation system, Journal of Sound and Vibration 208(2) (1998), 299-311.

- [4] K. Nagaya, T. Suzuki, N. Takahashi and H. Kobayashi, "Permanent magnet pulse motor with high temperature superconducting levitation", IEEE Transactions on Applied Superconductivity, Vol.11, No.4 (2001-12), pp.4109-4115
- [5] M. Komori, T. Ide, S. Fukata and T. Matsushita, "Vibration suppression of a disk-shaped superconductor with PD control" Cryogenics, Vol.37, No.4, (1997), pp.195-199
- [6] S. Murakami, M. Ohto, H. Yahara, H. Watanabe, H. Shiotuki, H. Shimoji, and T. Todaka, Improvement of Output Power of Industrial Electric Motor Based on Magnetic Flux Concentrated Surface Permanent Magnet Array, Journal of JSAEM 17(4) (2009).

8-

**Laser and particle beams,
plasmas**

Free vibration states of a slender beam with a linear time varying mass

Chicheng Ma, Xinong Zhang*, Yajun Luo and Chunlin Zhang

State Key Laboratory for Strength and Vibration of Mechanical Structures, School of Aerospace, Xi'an Jiaotong University, No. 28, Xianning West Road. 710049, Xi'an, China

Abstract. Dynamical behaviors of a slender beam with a linear time-varying mass are studied in this article. The beam with a time varying mass is modeled by using admissible functions and the principle of separation of variables. By using appropriate functional transformations, the governing equations can be reduced to solvable equations. The solutions in the form of Bessel's functions are provided. The results reveal that the change of the time varying mass has significant effects on the dynamic characteristics of the system. A damping is generated resulting from the time varying mass. Especially, a negative damping is generated if the mass decreases, which can induce instability of the system. Smoothed pseudo-Wigner-Ville distribution (SPWVD) is utilized to investigate the time frequency features of the time varying mass system. The power spectral density of the vibration response signal is obtained by using SPWVD. SPWVD is an efficient tool to decompose non-stationary signal.

Keywords: linear time varying mass, instability, time frequency analysis, negative damping

1. Introduction

Systems involving time varying parameters are commonly encountered in engineering, such as a fuel tank with the consumption of the fuel, or a mechanical system for pouring concrete from a vessel, transportation and measuring equipment. Vibrations of systems with time varying parameters have been widely investigated for decades. A.H. Nayfeh [1] analyzed an oscillator with time varying mass. In the book of L. Cveticanin[2], results from investigations based on the general dynamics of systems with variable parameters were presented. The simplest single degree of freedom (SDoF) systems with time varying mass or stiffness were commonly investigated, and many approximate analytical and numerical methods have been developed [2, 4-13].

H.J. Holl et al. [3] simulated a Duffing oscillator with time varying mass by a BEM in time. Q.S. Li et al. [4-5] and S. Nhleko [8] reduced the dynamic equations of a oscillators with a time varying mass using functional transformations, and obtained the analytical solutions. In the papers of L. Cveticanin [9, 10], an analytical methods based on the procedure of slowly varying amplitude and phase (Krylov-Bogolubov method) were utilized. He obtained some particular solutions of the dynamic equations. Based on the dynamic equations of the variable mass systems, the stability conditions of motion have been obtained as the time varying mass can induce instability of the systems [12, 13].

Continuous structures with time varying components were widely investigated as well, such as towed cable-body systems [14, 15], a string with time-varying length[16], beams with moving mass or time varying mass [22, 23], rotors with slowly varying parameters [17, 19-22, 24], and some other systems [18]. It was found that the dynamic responses of the systems were greatly influenced by the time varying parameters. Some investigation in stability analysis of quasi-linear systems were done by L. Cveticanin [19-21], he supposed a Lyapunov function to analyze a variable rotor systems. M. Kalyoncu and F.M. Botsali [22] investigated an elastic robot carrying a time varying mass using numerical methods. They found that change of the mass changed the amplitude of vibration.

This paper presents a modest extension of previous works. The dynamic equations of a slender beam with a linear time varying mass are to be derived. Based on the functional transformation approach

*Corresponding author: Xinong Zhang, State Key Laboratory for Strength and Vibration of Mechanical Structures, School of Aerospace, Xi'an Jiaotong University, No. 28, Xianning West Road. 710049, Xi'an, China. Email: xnzhang@mail.xjtu.edu.cn

used by Q.S. Li et al. [4, 5] and S. Nhleko [8], the analytical solutions are obtained, and numerical solutions obtained by using Newmark method are also given. The accuracy of the analytical solution is validated by comparing the obtained solutions with previous ones [8, 12]. In order to study the dynamic characteristics of the time varying mass system, time frequency analysis is provided. SPWVD is utilized to map the vibration signals in the time-frequency domain, therefore the time frequency features of the time varying mass system are obtained.

2. Mathematical formulations

Figure 1 shows an Euler-Bernoulli beam of flexural rigidity EJ , and a lumped mass is attached to the beam at $x=x_1$, the length of the beam is L . dm represents a mass element flowing into or flowing out from the lumped mass $Me(t)$ from time t to time $t+\Delta t$, and $u(t)$ is absolute velocity of dm when flowing into or flowing out from the lumped mass $Me(t)$. It is assumed that the thickness of the beam is so small compared with the length and the width of the beam that the effect of shearing deformation of the beam can be neglected. Here, only the transverse resonances is considered, the transverse displacement of the beam particle instantaneously located at spatial position x is $Y(x, t)$.

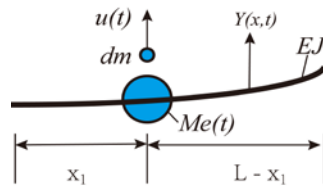


Fig. 1. A beam with a time varying mass

Considering a time varying mass, the general equation of motion of a beam with a time varying mass can be written as:

$$EJ \frac{\partial^4 Y}{\partial x^4} + \rho A \frac{\partial^2 Y}{\partial t^2} + c_b \frac{\partial Y}{\partial t} + [Me(t) \frac{\partial^2 Y}{\partial t^2} + \frac{dMe(t)}{dt} \frac{\partial Y}{\partial t} - \frac{dMe(t)}{dt} u(t)] \delta(x - x_1) = 0 \quad (1)$$

where E , J , ρ , c_b and A are elastic modulus, moment of inertia, density, damping coefficient and cross sectional area of the beam, respectively. $Me(t) = Me_0(1 + \beta t)$ represents the lumped time varying mass, where Me_0 is the initial mass of the time varying mass, β is a parameter to represent the rate of change of the mass. δ is Delta function used to assign the position of the lumped mass. Two special velocity $u(t)$ have been investigated by authors of previous literatures [4,5,8]:

$$u(t) = 0 \text{ \& } u(t) = \partial Y(x_1) / \partial x \quad (2)$$

For $u(t) = 0$, the absolute velocity of dm is so small that can be neglected, for example, when a piece of ore is taken out from a feed equipment very slowly [4], the direction of $u(t)$ is perpendicular to the direction of $Y(x_1, t)$, for example, when water flows downward from a container that vibrating in the horizontal direction. For $u(t) = \partial Y(x_1) / \partial x$, the absolute velocity of dm is equal to the velocity of beam at $x=x_1$.

For $u(t) = 0$, the additional force $\frac{dMe(t)}{dt} u(t)$ is equal to zero, and for $u(t) = \partial Y(x_1) / \partial x$, the additional force $\frac{dMe(t)}{dt} u(t)$ is eliminated by the induced damping $\frac{dMe(t)}{dt} Y(x_1, t)$. Hence, Eq.(1) can be rewritten as:

$$EJ \frac{\partial^4 Y}{\partial x^4} + \rho A \frac{\partial^2 Y}{\partial t^2} + c_b \frac{\partial Y}{\partial t} + [Me(t) \frac{\partial^2 Y}{\partial t^2} + (1 - \chi) \frac{dMe(t)}{dt} \frac{\partial Y}{\partial t}] \delta(x - x_1) = 0 \quad (3)$$

where $\chi = 1$ for $u(t) = 0$ and $\chi = 0$ for $u(t) = \partial Y(x_1) / \partial x$.

The displacement of the structure is assumed by an infinite series solution in terms of $\varphi_i(x)$ and $\eta_i(t)$, where $\varphi_i(x)$ are normal modes of the beam, and $\eta_i(t)$ are generalized coordinates. Here, $\varphi_i(x)$ is the set of uniform beam eigenfunctions that automatically satisfy the global boundary conditions of the beam.

$$Y = \sum_{i=1}^n \varphi_i(x) \eta_i(t) = \Phi^T \boldsymbol{\eta} \quad (4)$$

Substituting Eq.(4) into Eq.(3), the equation of a beam with a lumped time varying mass can be obtained by using Galerkin method:

$$(\mathbf{M}_b + \mathbf{M}_m) \ddot{\boldsymbol{\eta}} + [\mathbf{C}_b + (1 - \chi) \mathbf{C}_m] \dot{\boldsymbol{\eta}} + \mathbf{K} \boldsymbol{\eta} = 0 \quad (5)$$

where \mathbf{M}_b and \mathbf{M}_m are the mass matrix of the beam structure and the time varying mass, respectively; \mathbf{K} is the stiffness matrix, \mathbf{C}_m is the additional damping matrix induced by the time varying mass, \mathbf{C}_b is the structural damping.

Generally, lower order modes are most concerned for the system used in dynamic simulation. The first mode is mainly investigated here. In order to simplify the equation, let

$$M_0 = \int_0^L \rho A \varphi_1(x)^2 dx, k = \frac{M e_0 \beta \varphi_1(x)^2}{M_0}, m(t) = 1 + kt \quad (6)$$

$$K = \int_0^L EJ \frac{\partial^4 \varphi_1(x)}{\partial x^4} \varphi_1(x) dx \quad (7)$$

$$C = \int_0^L c_b \varphi_1(x)^2 dx \quad (8)$$

Substituting Eqs.(6-10) into Eq.(5), Eq.(5) reduces to:

$$m(t) \ddot{\eta} + [(1 - \chi) m(t) + 2\xi \omega_0] \dot{\eta} + \omega_0^2 \eta = 0 \quad (9)$$

where $\omega_0^2 = K / M_0$ and $\xi = C / (2M_0 \omega_0)$. Here, ω_0 and ξ are called initial vibration frequency and initial damping ratio, respectively.

Equation (11) can be simplified by the following functional transformations.

$$\varepsilon = \int m^{-1}(t) dt \quad (10)$$

$$m(t) = 1 + kt = Q(\varepsilon) \quad (11)$$

$$\eta(t) = \eta(\varepsilon) \quad (12)$$

Then Eq. (11) reduces to:

$$\frac{d^2 \eta(\varepsilon)}{d\varepsilon^2} + (2\xi \omega_0 - \chi \frac{1}{Q(\varepsilon)} \frac{dQ(\varepsilon)}{d\varepsilon}) \frac{d\eta(\varepsilon)}{d\varepsilon} + \omega_0^2 Q(\varepsilon) \eta(\varepsilon) = 0 \quad (13)$$

Equation (17) can be simplified further by making the following substitutions:

$$Q(\varepsilon) = e^{\lambda \varepsilon} \quad (14)$$

$$\eta(\varepsilon) = \eta(\xi) \quad (15)$$

where $\xi = e^{\lambda \varepsilon / 2}$ and λ is a constant determined by parameter $m(t)$. Finally, Eq.(17) is reduced to a Bessel type equation:

$$\frac{d^2 \eta(\xi)}{d\xi^2} + (1 + \frac{2^2 \xi \omega_0}{\lambda} - 2\chi) \xi^{-1} \frac{d\eta(\xi)}{d\xi} + \alpha^2 \omega_0^2 \eta(\xi) = 0 \quad (16)$$

where $\alpha = 2/\lambda$. The solution to Eq. (13) can be obtained by Bessel's functions as follows[25]:

$$\eta(\xi) = \xi^\nu C_1 J_\nu(\alpha \omega_0 \xi) + \xi^\nu C_2 Y_\nu(\alpha \omega_0 \xi) \quad (17)$$

where $\nu = \chi - 2\zeta\omega_0 / \lambda$. The parameters J_ν and Y_ν are Bessel's functions of the first and the second kind of order ν , respectively. C_1 and C_2 refer to the integration constants determined by initial conditions.

3. Numerical simulation

In what follows, the case of a cantilever beam with an end time varying mass will be simulated, as shown in figure 2. The host beam is made of aluminium alloy. Geometrical and physical properties of the beam from reference [22] are listed in Table 1. The cases for an increasing mass system and a decreasing mass system are investigated. In the two cases, the end mass $Me(t)$ increases from 0kg to 2kg linearly, or decreases from 2kg to 0kg linearly.

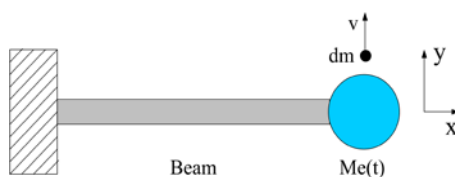


Fig. 2. A cantilever beam with a time varying mass

Table 1.
Geometrical and physical properties of the beam

Parameter	Value
Density/ ρ	2729.5 kg/m ³
Modulus of Elasticity/ E	66.26 Gpa
Length/ L	1.8 m
Cross sectional Area/ A	0.001471 m ²
Moment of Inertia/ I	1.14197*10 ⁻⁸ m ⁴

In order to verify the accuracy of the analytical solutions, comparisons of the analytical solutions and numerical solutions are shown in figure 3. Numerical solutions are obtained by using Newmark method. As demonstrated in Fig.3, the analytical solutions and the numerical solutions show very good consistence, manifesting that the analytical approach is valid. In the computation, the structural damping is not considered. From Eq.(1), a positive or negative damping is generated by the time varying mass. For $\chi=1$, the damping force is eliminated by the additional force $\dot{M}e(t)u(t)$. However, change of the mass results in change of the kinetic energy. The increase of the energy makes the amplitude grow, and the decrease of the energy induces the vibration decay, as shown in figure 3(a) and figure 3(c), respectively. For $\chi=0$, the generated damping plays an important role in the vibration. Especially when the mass decrease, a negative damping is generated to cause the system unstable, as shown in figure 3(d). When the mass increases, the generated positive damping stabilizes the system all the time, as shown in figure 3(b). Changing trend of the vibration signal coincides with the curves obtained in previous literatures ([8, 22]).

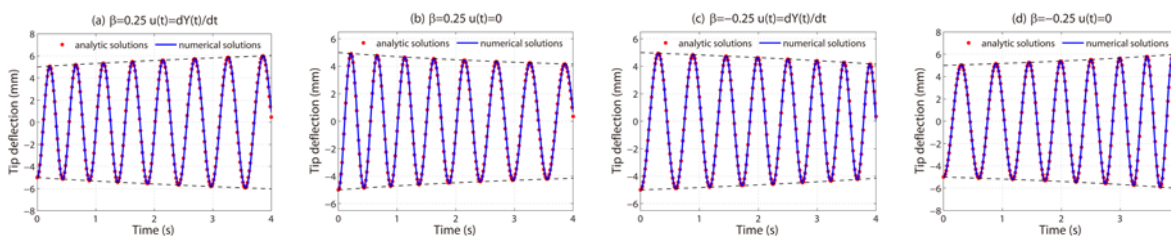


Fig. 3. Displacement response: Comparison of analytic and numerical solutions

From Eq.(1), one can find that the value of the induced damping is proportional to the rate of change of the mass. Figure 4 displays the effect of rate of change of mass on a decreasing mass system. For a decreasing mass system, the vibration period decreases with the decrease of the mass of the system. The amplitude decreases faster with a larger energy loss, as shown in figure 4(a). For $\beta=-1$, the mass decreases fastest, hence the energy decreases fastest, causing the amplitude of vibration reduced most. In figure 4(b), the effect of the negative damping is significant, therefore the amplitude of the vibration increases evidently. For $\beta=-1$, the value of the negative damping is the largest, and the amplitude of the vibration increases most notable.

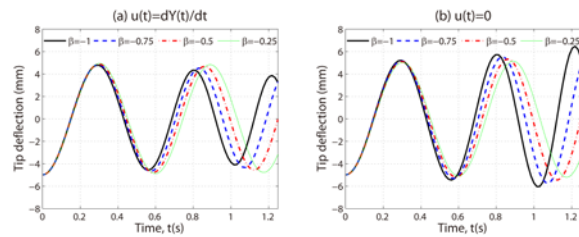


Fig. 4. The effect of rate of change of mass on a decreasing mass system

4. Time-frequency analysis

In this section, time frequency features of the time varying mass system are to be investigated. Classical Fast Fourier Transformation is a powerful tool to study stationary signals, however it only maps signals of time to signals of frequency and vice versa. The Wigner-Ville distribution (WVD) can map the vibration signals in both the time and frequency domains. Here, the WVD is given as:

$$W_f(t, \omega) = \int_{-\infty}^{+\infty} x(t - \frac{\tau}{2}) x^*(t + \frac{\tau}{2}) e^{-j\omega\tau} d\tau \quad (18)$$

where $x(t)$ is the time signal, and $x^*(t)$ is its complex conjugate. Any real signal $x(t)$ is not only contaminated by the noise, but also by the interference terms. A combination of time and frequency windowing with WVD has been developed. This approach is called the smoothed pseudo-Wigner-Ville distribution (SPWVD), and expressed as follows:

$$W_s(t, \omega) = \frac{1}{2\pi} \int_{-\infty}^{+\infty} \int_{-\infty}^{+\infty} W_f(t, \eta) W(\omega - \eta) g(t - \tau) d\eta d\tau \quad (19)$$

In this equation, two independent windows exist. The function $W(\omega)$ is a truncating window to determines the frequency resolution of the WVD, and the function $g(t)$ is a smoothing window, which determines the time resolution. The two window functions can be applied individually, or applied in combination, therefore the desired degree of interference suppression can be achieved. In the following simulation, SPWVD is applied to decompose the vibration signal in time-frequency domain.

In order to have enough data, let the mass decreases from 2kg to 0kg through 20s. Then SPWVD is utilized to obtain the time frequency responses. The power spectral density of vibration signals of the time varying system obtained by using SPWVD are shown in figure 5(a). As the mass of the system decreases, the vibration frequency increases. The vibration frequency of the system increases from 1.63Hz to 2.37Hz, which can not be found by using classical Fast Fourier Transformation. Figure 5 displays time dependent power spectral density of the vibration response signal. In figure 5(a), the power spectral density of the vibration response for $\chi=1$ is displayed, the decrease of the mass induces the decrease of the energy of the system. For $\chi=0$, the negative damping increases the energy of the system, as shown in figure 5(b). The results show that SPWVD is an efficient tool to decompose non-stationary signal.

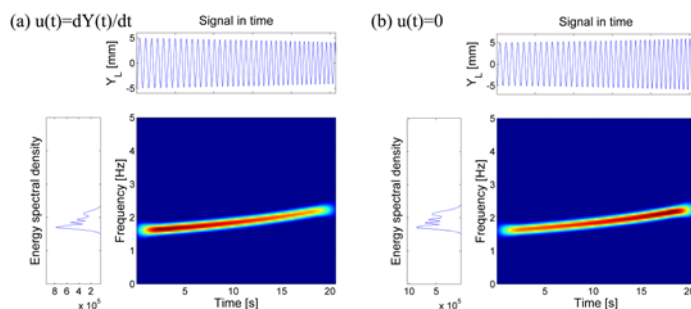


Fig. 5. Time dependent power spectral density of the vibration response signals

5. Conclusions

In this paper, free vibration states of a slender beam with a linear time varying mass were discussed. An analytical approach was used to solve vibration problems of linear time varying mass system. Using appropriate functional transformations, the governing equations were reduced to solvable equations. The solutions in the form of Bessel's functions were obtained. Numerical solutions were obtained by Newmark method. The analytical solutions compared well with the numerical solutions. It was found that the time varying mass had significant influence on the dynamic characteristics of the system.

(1) Vibration frequencies change with change of the mass. The range of the vibration frequencies can be determined by the range of the mass.

(2) Change of the mass results in change of the kinetic energy of the system and generates a damping and a reaction force. The energy influx resulting from mass influx and the additional negative damping resulting from the decreasing mass are instability parameters, which can induce the increase of the amplitude of vibration.

(3) The values of the induced damping are proportional to the rate of change of the mass.

(4) Time frequency analysis by using SPWVD was developed to study time dependent power spectral density of the vibration response signal in both the time and frequency domains. Results showed that SPWVD is an efficient tool to decompose nonstationary signal.

Acknowledgement

The authors of the paper gratefully acknowledge the financial support from NSFC (Grant Nos. 11172225 and 11102147) and RFDP of China (Grant No. 20110201110018).

References

- [1] A.H. Nayfeh, D.T. Mook: *Nonlinear Oscillations*. Wiley, New York (1979).
- [2] L. Cveticanin, *Dynamics of Machines with Variable Mass*. Gordon and Breach Science Publishers, London (1998).
- [3] H.J. Holl, A.K. Belyaev and H. Irschik: Simulation of the duffing-oscillator with time-varying mass by a BEM in time, *Comput. Struct.*, **73** (1999), 177-186.
- [4] Q.S. Li, J.Q. Fang, Liu. DK and A.P. Jeary: Exact Solutions for Free Vibration of SDOF Systems with Non-Periodically Varying Parameters, *J. Vib. Control.* (1998).
- [5] Q.S. Li and A.P. Jeary: A New Exact Approach for Analyzing Free Vibration of SDOF Systems with Nonperiodically Time Varying Parameters, *J. Vib. and Acoustics.* (2000).
- [6] J. Flores, G. Solovey and S. Gill: Variable mass oscillator. *Am. J. Phys.*, 71 (2003) 721-725.
- [7] H. Irschik and H.J. Holl: Mechanics of variable-mass systems-part 1: balance of mass and linear momentum. *Appl. Mech. Rev.*, **57**(2004), 145-161.
- [8] S. Nhleko: Free Vibration States of an Oscillator With a Linear Time-Varying Mass, *J. Vib. and Acoustics*, **131**(2009).
- [9] L. Cveticanin: Oscillator with fraction order restoring force. *J. Sound Vib*, **320**(2009), 1064-1077.
- [10] L. Cveticanin and T. Pogany: Oscillator with a sum of non-integer order non-linearities. *J. Appl. Math.*, (2012)
- [11] R.M. Digilov, M. Reiner, and Z. Weizman: Damping in a Variable Mass on a Spring Pendulum, *Am. J. Phys.*, **73**(2005), 901-905.
- [12] W.T. van Horssena, A.K. Abramianb and Hartonoa: On the free vibrations of an oscillator with a periodically time-varying mass, *J. Sound Vib*, **298** (2006) 1166-1172.
- [13] W.T. van Horssen, O.V. Pischansky and J.L.A. Dubbeldam: On the forced vibrations of an oscillator with a periodically time-varying mass, *J. Sound Vib*, **329** (2010) 721-732.
- [14] J.V. Sanders: A Three-Dimensional Dynamic Analysis of a Towed System, *Ocean Eng.*, **9** (1982) 483-499.
- [15] T.N. Delmer, T.C. Stephens and J.M. Coe: Numerical Simulation of Towed Cable Dynamics, *Ocean Eng.*, **10** (1983), 119-132.
- [16] T. Kotera: Vibrations of Strings with Time-Varying Length, *Trans. Jpn. Soc. Mech. Eng., Ser. C*, **54** (1988), 2597-2604.
- [17] L. Cveticanin: Normal Modes of Vibration for Continuous Rotors with Slow Time Variable mass, *Mech. Math. Theory*, **32** (1997), 881-891.
- [18] Kefu Liu: Extension of modal analysis to linear time-varying systems, *J. Sound Vib*, **226** (1999), 149-167.
- [19] L. Cveticanin, On the stability of rheo-linear rotor systems based on some new first integrals. *Mech. Res. Commun. Basic Appl.* **23** (1996), 519-530
- [20] L. Cveticanin: The stability of a textile machine rotor with increasing mass. *Mech. Mach. Theory*, **23** (1988), 275-278.
- [21] L. Cveticanin: Stability of a clamped-free rotor with variable mass for the case of radial rubbing. *J. Sound Vib*, **129** (1989), 489-499.
- [22] M. Kalyoncu and F.M. Botsali: Vibration analysis of an elastic robot manipulator with prismatic joint and a time-varying end mass, *Arab. J. Sci. Eng.*, **29**(2004), 27-38.
- [23] A. Nikkhoa, F.R. Rofooei and M.R. Shadnamb: Dynamic behavior and modal control of beams under moving mass, *J. Sound Vib*, **306** (2007) 712-724.
- [24] D.J. Han: Vibration analysis of periodically time-varying rotor system with transverse crack, *Mech. Syst. Signal. Pr.* **21** (2007), 2857-2879.
- [25] A.D. Polyanin and V.F. Zaitsev, *Handbook of Exact Solutions for Ordinary Differential Equations*, New York, 1995.

9-

**Micro electro-mechanical
systems (MEMS)**

System for detecting the presence of shielding wires in transmission lines by RF scattering

E. A. B. Santos^{a*}, A. J. B. de Oliveira^a, M. T. de Melo^a, J. F. A. G Wavrik^b

^a*Departamento de Eletrônica e Sistemas, Centro de Tecnologia e Geociências, Universidade Federal de Pernambuco, Av. Acadêmico Hélio Ramos, s/n, CEP 50740-530, Recife, Brasil*

^b*Divisão de Manutenção d Análise de Desempenho de Linhas de Transmissão, Companhia Hidroelétrica do São Francisco, Rua Delmiro Gouveia, 333, Recife, Brasil.*

Abstract. This paper presents the design and results of laboratory tests of a microcontrolled system to perform the detection of shielding wires on a span of a transmission line. An RF transmission system is used to radiate electromagnetic waves on the wires, which scatter the incident signal. Part of the scattered signal is then detected by an RF receiving system which indicates that the wires are present.

Keywords: microcontrolled system, detection, shielding wires, transmission lines, R.F. scattering

1. Introduction

Companies of electricity transmission suffer from theft of shielding wires that, besides causing financial losses, leaves the system unprotected. Lightning strokes to overhead an unprotected span may cause damage to the towers and power outages, generating high fines imposed by the supervisory bodies. Considering that, the authors propose in this paper an electronic system for detecting the presence of the shielding wires over a transmission line span, using basic electronic components, microcontrollers, transceivers and directive antennas. The system consists of two RF modules: a transmitter TX and a receiver RX connected to directive antennas. Both modules are installed on the same tower. The shielding wires are the obstacle to the radiated power and constitute the communication link between the transmission and reception modules. The RF signal radiated by the antenna of the transmitting module is scattered by the wires and then part of it is received by the antenna of the reception module. The advantage of using electromagnetic scattering lies in the fact that the detection system will be more protected from direct impacts of lightning strokes if it is installed on the tower instead of on the wires themselves. As far as the authors know, no similar system has been reported yet.

2. The proposed system

Scattering of electromagnetic waves [1] can be used to check if any metal object stands before a system emitting radiofrequency. This principle is here employed to a system of power transmission line in order to detect whether a pair of shielding wires is present on a given span. Fig.1 shows three different situations where an RF transmitting antenna installed on a transmission line tower radiates perpendicularly on the pair of shielding wires and, immediately below, a receiving antenna installed on the same tower detects part of the scattered power.

* Msc. Emmanuel Andrade de Barros Santos. Email:Emmanuel.andrade@gmail.com

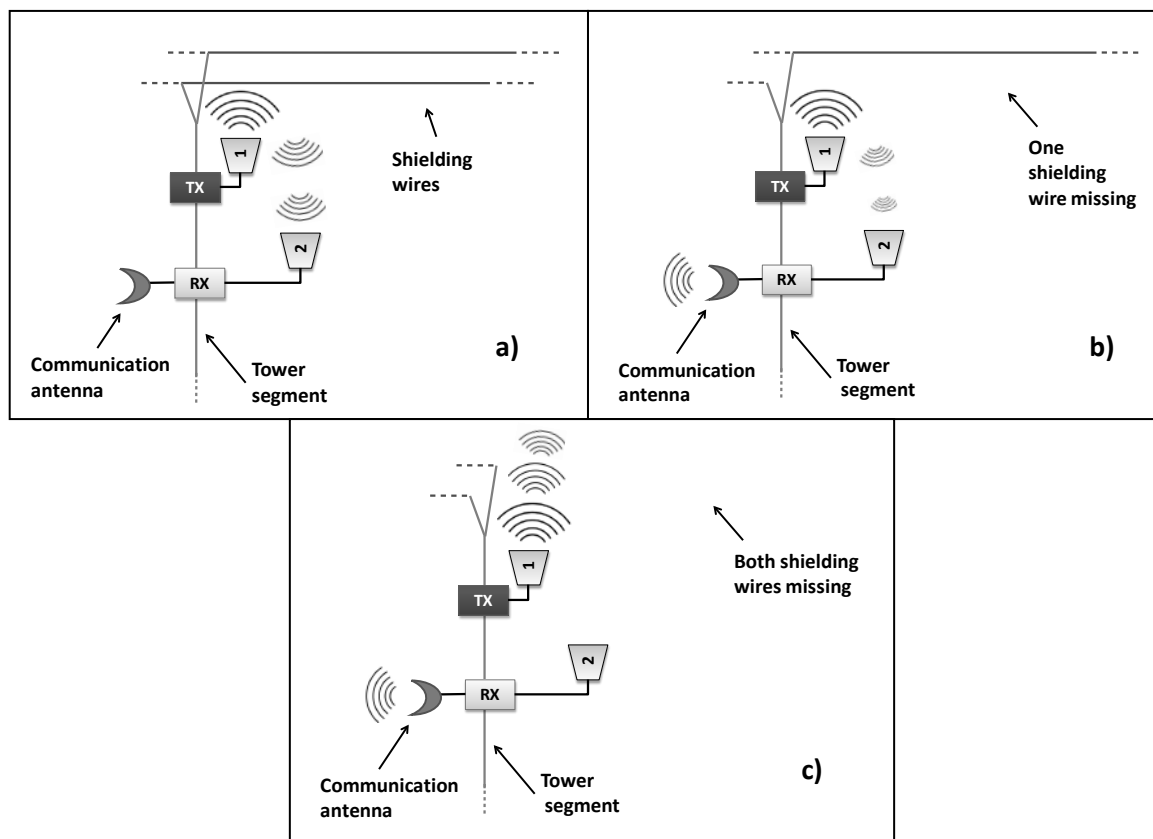


Fig.1. Three different situations that show the functionality of the system proposed

The electronic microcontroller TX, together with the first antenna, forms the transmitting system. It sends data package addressed to the receiving system formed by the microcontrolled electronic system RX and antenna 2.

If the shielding wires are present, the scattered electromagnetic waves will cause the module RX to receive the data package sent by the transmission system, establishing a communication link between modules TX and RX. This situation is shown in Figure 1a.

Figure 1b shows the situation where only one shielding wire is missing. If that happens, the system RX will detect power at reduced level which is below the level detected if both shielding wires were present (Figure 1a). Thus the system RX uses the communication antenna to send a message (which contains the address of the tower) to an operational center of the company warning about the missing of the shielding wire.

Figure 1c shows the worst case, where both shielding wires are missing. In this situation, the communication link between TX and RX will break. Thus the RX will not detect any signal. Then the RX uses the communication antenna to warn the operational center about the missing of the shielding wires.

3. Experimental results

Tests performed at Microwave Laboratory of Federal University of Pernambuco showed that the presence of the scattering wires in the communication link is associated to power levels easily detectable by a sensitive electronic reception system RX. Figure 2 shows the directive antenna used in laboratory. The project of the directive antenna was based on simulation with CST Microwave Studio 2010.

Figure 3 shows the setup to perform the experiments, which uses equipments such as Spectrum Analyzer, DC Source, etc.

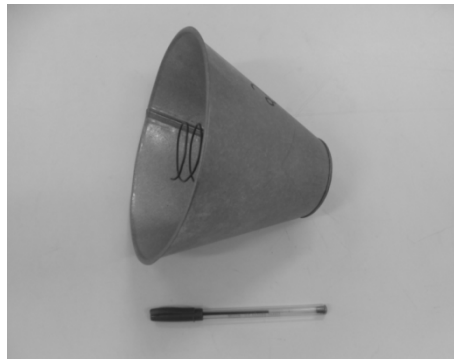


Fig. 2. Directive antenna.

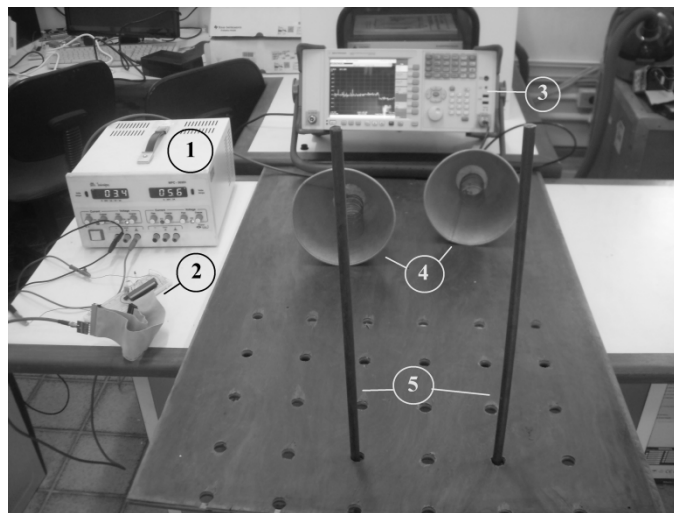


Fig.3. The setup to perform the experiments. 1 = DC Source, 2 = Transmitter TX, 3 = Spectrum Analyzer, 4 = Directive Antennas, 5 = Conducting wires.

Figure 4 shows the transceiver used in the tests. It was the nRF24L01 [2], fabricated by Nordic Semiconductor. Its power output is 0dBm at a frequency of 2.4 GHz. The transceiver was connected to a directive antenna which radiated RF power on a pair of conducting wires of approximately 1 cm in diameter, 20 cm apart. The transmitter antenna was positioned approximately 60 cm from half the distance between the wires.

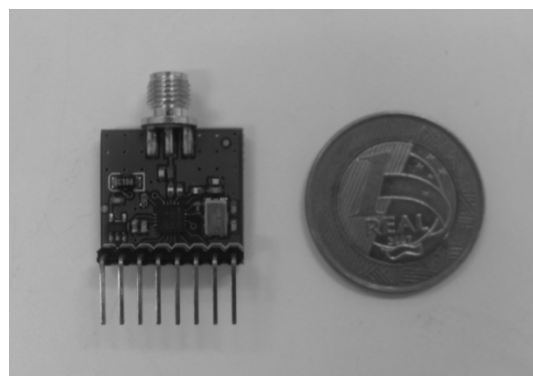


Fig.4. The transceiver used in the tests: nRF24L01.

The microcontrolled system RX was replaced by a Spectrum Analyzer, and the receiving antenna was positioned approximately 50 cm from the same midpoint between the wires, following the orientation of Fig.1. With this setup, it was possible to detect scattered power levels of the order of -40 dBm, when the wires were present. Figures 5, 6 and 7 show the screenshots of the Spectrum Analyzer for the cases of presence of both wires, presence of only one wire and absence of both wires, respectively.

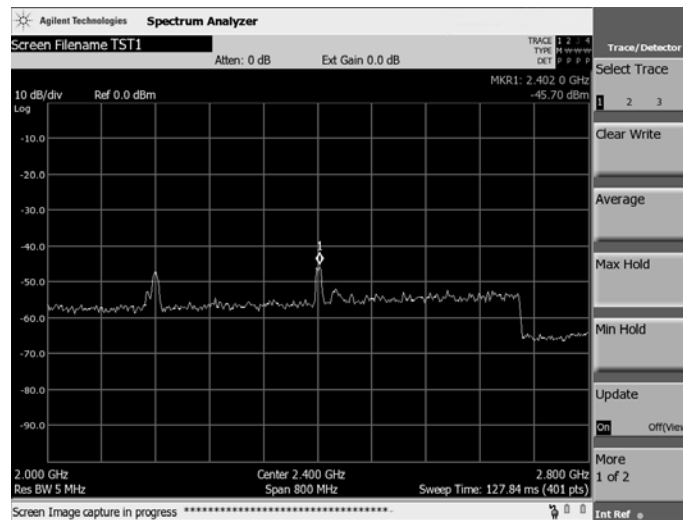


Fig.5. Power level detected when both shielding wires are present.

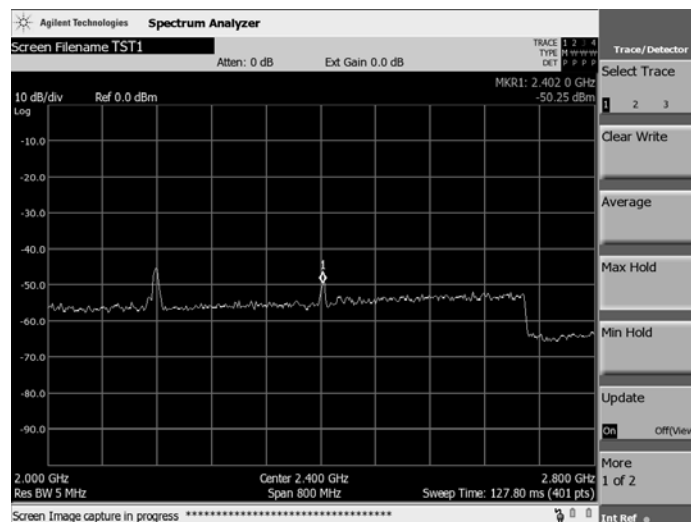


Fig.6. Power level detected when one shielding wire is missing.

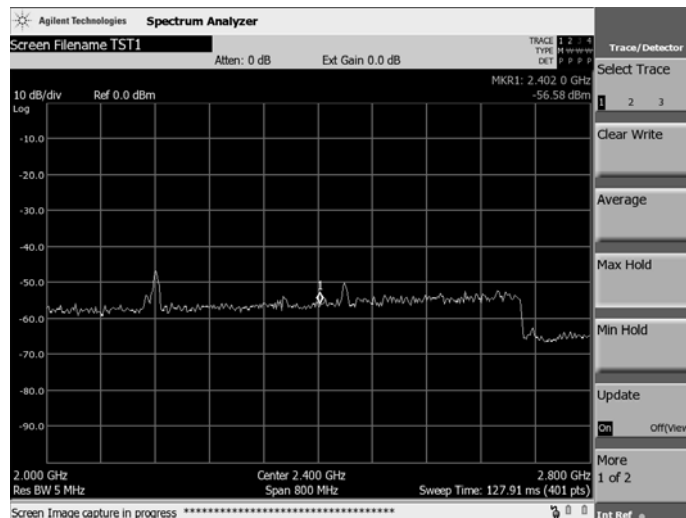


Fig.7. Power level detected when both shielding wires are missing.

Table 1 shows the power level detected for the three situations mentioned. It was based on the peaks at 2.4 GHz on the screen of the Spectrum Analyzer. The three different levels of power confirm that the power scattered by the wires can be discriminated to the point of being used as a sensor of their own presence.

Table1
 Comparison of power level for the three situations.

Situation	Power Level Detected (dBm)
Both wires	-45,70
One wire	-50,25
No wires	-56,58

4. Conclusion

Laboratory results have shown that output power from a 0dBm transmitter, radiated by a directive antenna and scattered by pair of wires, could be detected at approximately -40 dBm by another similar directive receiving antenna connected to a sensitive electronic system RX. The experimental observation results show that, by using commercial transceivers of much higher output power levels and sensitivity as high as -100 dBm, power detection at a distance near 10m, which is the real approximate distance between the receiving antenna and the wires, can be efficiently performed by the proposed system.

Acknowledgements

The authors would like to thank the company CHESF for the financial and technical support given to the development of this research.

References

- [1]Constantine A. Balanis, Advanced Engineering Electromagnetics, Clarendon Press, John Wiley & Sons, 1989
- [2]Transceiver nRF24L01 <<http://www.nordicsemi.com/eng/Products/2.4GHz-RF/nRF24L01>> Accessed in: 20/07/2013

10-
Nanotechnology
applications

The Interpolating Element-Free Galerkin Method Applied to Quantum Wells and Quantum Dots Infrared Photo-Detectors

Lucas KRIESEL SPEROTTO, Angelo PASSARO

Virtual Engineering Laboratory, ITA/IEAv, Trevo Coronel Aviador José Alberto Albano do Amarante n°1, 12.228-001, São José dos Campos – SP, Brazil

Gleber NELSON MARQUES

Department of Computing, UNEMAT, R. Santa Rita n° 148, 78.780-000, Alto Araguaia – MT, Brazil

Abstract. In this work is presented the application of the IEFGM to the study of quantum well and quantum dot semiconductor nanostructures. The effects of relevant control parameters of the IEFGM and auxiliary techniques on the precision of the solutions are explored.

1 Introduction

The characteristics of the nanostructured infrared photo-detectors based in quantum well (QW) and quantum dot (QD) can be computed from the geometrical configuration of the semiconductor layers making up the sensor [1], [2]. Computational tools allied to numerical methods are used to aid the study and development of these sensors.

In this work, the interpolating approach of the Element-Free Galerkin method (IEFGM) [3], is applied to the analysis of QW and QD problems. The IEFGM is a meshfree method alternative to the original Element-Free Galerkin method (EFGM) [3]. Both methods does not depend explicitly of a mesh and allows for solutions with arbitrary continuity, depending on the adopted weighting function [3–5]). As detailed in [4], the IEFGM enforces almost naturally essential boundary conditions and interface conditions, avoiding the use of Lagrange Multipliers. The discontinuity in the wave function derivative is evaluated in the QW material interface and the parameters inherent of IEFGM are explored.

2 The IEFGM formulation for the Schrodinger Equation

In the effective mass approximation, the wave function $\Psi(r)$ and the energy E for a particle in the domain is given by the n-dimensional Schrödinger equation:

$$-\frac{\hbar^2}{2m_{eff}(r)}\nabla^2\Psi(r)+V(r)\Psi(r)=E\Psi(r), \quad (1)$$

where m_{eff} is the effective mass of the particle and \hbar is the reduced Plank constant. Using the IEFGM interpolation, the wave function can be represented by:

$$\Psi(r)=\sum_{i=1}^n\Phi_i(r)\psi_i, \quad (2)$$

where $\Phi_i(r)$ is the interpolating shape function and n is the number of nodal points in the domain of influence, defined by the parameter D_{max} [4]. In [3] can be found the mathematical formalism to deduce the shape function for the standard formulation, the consistence formulation, and the interpolating approach.

The application of standard EFGM formulation, using Lagrange multipliers to solve the Schrödinger equation can be founded in [5]. The final eigenvalue system obtained to the IEFGM application is written as follow:

$$[A]\psi = E[B]\psi, \quad (3)$$

where $[A]$ and $[B]$ matrix is constructed as follow:

$$A_{ij} = \int_{\Omega} \frac{\beta^2}{2m_{eff}(r)} \nabla \Phi_i \nabla \Phi_j dr + \int_{\Omega} V(r) \Phi_i \Phi_j dr \text{ and } B_{ij} = \int_{\Omega} \Phi_i \Phi_j dr, \quad (4)$$

where β is the normalization constant [5].

3 Results, Discussions and Conclusions

The QW [5], [6] and QD [7] (lens, cylinder and conical shaped) models are used in this work as references to study the effect of the IIEFGM characteristic parameters.

The singularity parameter ε is used in the interpolating approach to calculate the “near” singular weight functions [3]. For two-dimensional models, $\varepsilon < 10^{-6}$ is usually adopted. For QD models $\varepsilon < 10^{-6}$ can be chosen, independent of the adopted weight function and D_{max} parameter, however, we have found that values of $\varepsilon < 10^{-10}$ have to be used for QW models.

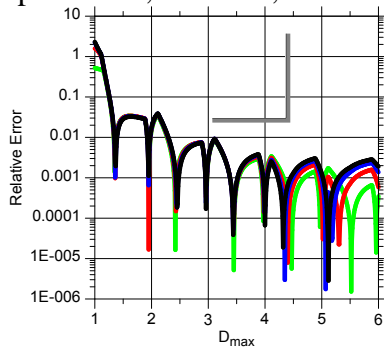


Figure 1. Relative error to the first four confined states in simply QW by exact solution present in [6].

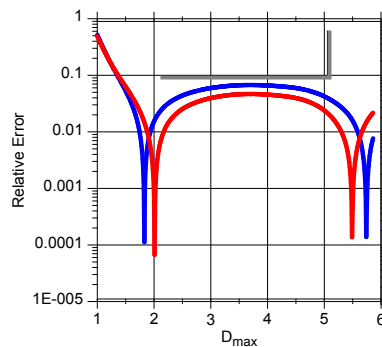


Figure 2. Relative error by solution presented in [7] and MEF solution to cylinder QD.

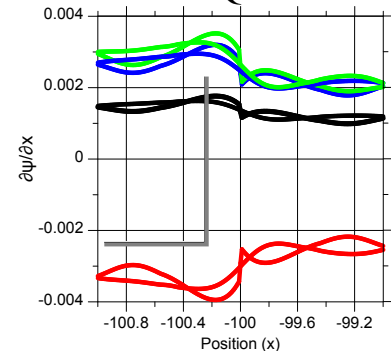


Figure 3. Discontinuity to the wave function derivative in QW material hetero-interface ($x = -100$).

The effect of the D_{max} parameter is evaluated considering the range from 1 to 6. In the QW (Figure 1) we have found that a good choice is $D_{max} > 2.30$, in order to achieve errors $< 1\%$. For QD models, two values of minimum error have been found (Figure 2), but only the first one is recommended, $1.80 < D_{max} < 2.04$, for which the error is lower than 2% . This range agrees with suggested D_{max} values in [4].

The domain truncation (DT) [4] technique is used as an auxiliary technique to reproduce the QW hetero-interface conditions [6]. Figure 3 shows results for the DT technique. The material interface discontinuity of the first derivative of the wave function is approximately respected, which does not happen if no truncation technique (NT) is used, similar as in [4].

References

- [1] B. F. Levine, Quantum-well infrared photodetectors, *J. of Appl. Phys.* **26** (1993) R1-R81.
- [2] H. Liu, Quantum dot infrared photodetector, *Opto. Rev.* **11** (2003) 1-5.
- [3] P. Breitkopf, A. Rassineux, G. Touzot, and P. Villon, Explicit form and efficient computation of MLS shape functions and their derivatives, *Int. J. for Num. M. in Eng.* **48** (2000) 451–466.
- [4] G. N. Marques, J. M. Machado, S. L. L. Verardi, S. Stephany, and A. J. Preto, Interpolating EFGM for computing continuous and discontinuous electromagnetic fields, *COMPEL*. **26** (2007) 1411-1438.
- [5] J. M. Machado, Y. Shiyu, A. Passaro, and N. M. Abe, An Application of the Element Free Galerkin Method to the Analysis of Quantum Well Structures, *ICEF 2000*, **2** (2000) 207-210.
- [6] K. Nakamura, A. Shimizu, M. Koshihara, and K. Hayata, Finite-element analysis of quantum wells of arbitrary semiconductors with arbitrary potential profiles, *IEEE J. of Quantum Elect.* **25** (1989) 889-895.
- [7] J. Lee, W.-C. Chou, C.-S. Yang, and G. J. Jan, Eigen-Energies and Eigen-Functions of Symmetroidal Quantum Dots, *Chin. J. of Phys.* **42** (2004) 102-115.

11-
Biomedical engineering

Sensitivity of Magnetic Probes for Identifying Sentinel Lymph Nodes: A Numerical Study

Masaki SEKINO, Tetsu OOKUBO, Hiroyuki OHSAKI

*Department of Electrical Engineering and Information Systems, Graduate School of Engineering,
The University of Tokyo, 7-3-1 Hongo, Bunkyo-ku, Tokyo 113-8656, Japan*

Moriaki KUSAKABE

*Research Center for Food Safety, The University of Tokyo, 1-1-1 Yayoi, Bunkyo-ku, Tokyo 113-8657,
Japan*

Abstract. Identifying the sentinel lymph nodes is important in treatment of breast cancer. Detection of magnetic fluid flowing in the lymph nodes using a magnetic probe enables us to identify the lymph nodes. In this study, we carried out numerical simulations to investigate the sensitivity of magnetic probes consisting of a permanent magnet and a small magnetic sensor. The results showed an appropriate configuration of the probe for obtaining high sensitivity to magnetic fluid.

1 Introduction

Identifying the sentinel lymph nodes is important for a diagnosis of tumor metastasis before a surgical therapy of breast cancer. Injection of magnetic fluid into lymphatics via the tumor enables us to magnetically identify the sentinel lymph nodes. The magnetic fluid can be detected using magnetic resonance imaging (MRI), magnetic particle imaging (MPI), and superconducting quantum interference devices (SQUID) [1,2]. Our group previously reported a prototype magnetic sensing system equipped with a permanent magnet, permalloy core, and Hall-effect sensors [3]. This system can be easily installed in an operating room for surgery because of its compactness and no use of refrigerant. In this study, we theoretically evaluated the sensitivity of our system with varied geometries of the permanent magnet and permalloy core..

2 Methods

The magnetic fluid, ferucarbotran, was originally developed for MRI contrast agent containing iron-oxide nanoparticles. Magnetic characteristics of the magnetic fluid was measured in external fields of up to 10^3 Oe. Our prototype system consisted of a handheld magnetic probe and a driving circuit as shown in figures 1(a) and (b). The field source for polarizing magnetic fluid consisted of a ring-shaped permanent magnet and two permalloy tubes attached to inner and outer peripheries of the magnet. The permanent magnet had a coercive force of 976 kA/m and an outer diameter of 6 mm. A Hall-effect sensor measures the magnetic field generated from the polarized fluid. For suppressing the output bias, the sensor was located at a zero-field point which existed on the symmetric axis of the field source. Magnetic field distributions around the probe head was calculated using the finite element method. The simulations were carried out for several field source designs with varied lengths of permalloy tubes, and with varied inner diameters of permanent magnets. The sensitivity of each model was evaluated based on the change in sampled magnetic flux density due to the existence of magnetic fluid in front of the sensor. We aimed at finding the probe design giving the maximum sensitivity to magnetic fluid. The volume of magnetic fluid was 1.6 mL, which corresponded to the dosage amount for adult.

3 Results and Discussion

Figure 1 (c) shows the calculated magnetic fields around the probe with magnetic fluid located at 10 mm and 30 mm from the probe head. The existence of magnetic fluid slightly influenced the magnetic field distributions. The magnetic fluid at 10 mm lead to a change in measured magnetic field of 175 μT . For the original numerical model, the calculated magnetic field change agreed well with the experimental results. The analyses for various probe designs showed that removal of both inner and outer permalloy tubes lead to an increase in magnetic flux density applied to the magnetic fluid, resulting in an improvement of sensitivity. A reduction in inner diameter also lead to an intensified magnetic field and an improved sensitivity. On the other hand, the improvement of sensitivity caused higher inhomogeneity of magnetic field at the location of Hall-effect sensor. Magnetic fluid of 1.6 mL located with a gap of 30 mm from the Hall sensor exhibited field variations of 0.8 μT in the original prototype model and 54 μT in the improved model. The results show that a practical dose of magnetic fluid gives rise to a detectable magnetic field changes at the location of Hall sensor, and that numerical simulations are effective for improving the sensitivity of the system. The results of numerical simulations will lead to an improved design of magnetic probe.

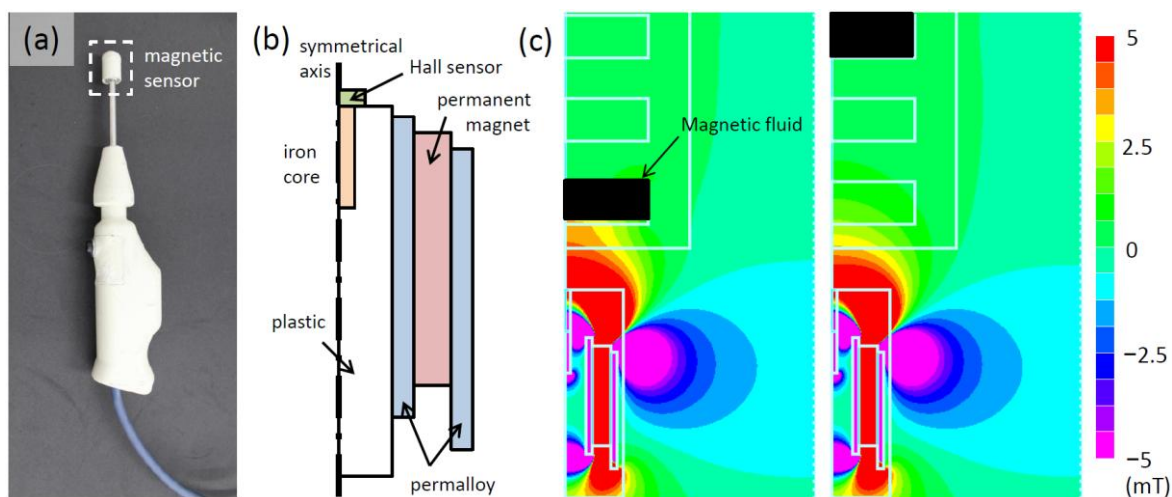


Figure 1: (a) Prototype magnetic probe for identifying sentinel lymph node. (b) Internal structure of the probe head. (c) Magnetic field distributions around the probe head with magnetic fluid located at 10 mm and 30 mm from the probe.

References

- [1] M. Shiozawa, S. Kobayashi, Y. Sato, H. Maeshima, Y. Hozumi, A. T. Lefor, K. Kurihara, N. Sata, Y. Yasuda, Magnetic resonance lymphography of sentinel lymph nodes in patients with breast cancer using superparamagnetic iron oxide: a feasibility study, *Breast Cancer* (in press).
- [2] S. Tanaka, H. Ota, Y. Kondo, Y. Tamaki, S. Kobayashi, and S. Noguchi, Detection of Magnetic Nanoparticles in Lymph Nodes of Rat by High Tc SQUID, *IEEE Trans. Appl. Supercond.* **13** (2003) 377-380.
- [3] M. Shiozawa, A. T. Lefor, Y. Hozumi, K. Kurihara, N. Sata, Y. Yasuda, and M. Kusakabe, Sentinel lymph node biopsy in patients with breast cancer using superparamagnetic iron oxide and a magnetometer. *Breast Cancer* (in press).

12- Inverse problems

Analysis of an inverse problem in QWIP device

Diogo PEDROSO

Department of physics and chemistry, UNESP- Univ. Estadual Paulista, 333 Ave. Ariberto Pereira da Cunha, ZIP code 12516-410, Guaratingueta, Brazil

Cristian DELFINO, Angelo PASSARO, Gustavo VIEIRA

Division of applied physics, IEAv Institute for advanced studies, 01 Trevo Coronel Aviador José Alberto Albano do Amarante, ZIP code 12228-001, São José dos Campos, Brazil

Abstract. In this work, we present and analyse some parameters, e.g., activation energy, Aluminium concentration and electron mobility, obtained from IxV curves of two QWIP samples processed by different methods and operators. Both samples were cut from the same wafer, grown by MBE. An analysis of sensibility of parameters as a function of temperature is also included.

1 Introduction

Two samples, cut from the same wafer with a heterostructure grown by MBE, were processed by different methods and operators. The heterostructure has 50 periods of $\text{Al}_{0,205}\text{Ga}_{0,795}\text{As}$ (barriers) and GaAs (quantum wells) layers, with thicknesses of 300Å and 56.5Å, respectively. The wells were doped with Si with concentration 10^{18} cm^{-3} . The heterostructure was designed by using the finite element method and computational optimization techniques. The activation energy (barrier energy minus Fermi energy) was designed to be 0,114 eV. A difference of one order of magnitude was observed between the dark current of the two samples for temperatures higher than 60K. Two initial hypotheses were considered to explain the differences: (1) the obvious one: different processing methods could change conductance parameters, and (2) non-uniform Aluminium deposition on MBE growing process. In this work only the second one is explored.

2 Methodology

For high temperature the thermionic effect determine the dark current on QWIPs and the electric conductance C of the structure can be computed as:

$$C = a e^{-\frac{E_a}{KT}} \quad (1)$$

where: a = constant; E_a = activation energy; K = Boltzmann constant; T = temperature. For low bias, lower than 0.2 V, a linear approximation can be adopted and the conductance computed from the angular coefficient. Considering hypothesis (2), E_a and the Aluminium concentration in barrier layers for both samples were estimated by using specific simulation software (QWS – Quantum Well Solver) [1]. Obtained E_a , the mobility was also calculated using a linear approximation for low bias:

$$J = nqF\mu e^{-\frac{E_a}{KT}} \quad (2)$$

where: j = current density; F = electric field; n = well doping concentration; q = electron charge; μ = electron mobility. Notice that the activation energy, and consequently the Al

concentration and electron mobility, can vary significantly even with a small temperature change. Dark current measures were made at different temperatures and for both samples at the same time. Numerical experiments were carried out in order to access the sensitivity of the parameters with the temperature.

3 Results

Considering hypothesis (2) only, we found a difference of 6.6% in the E_a and 5.5% in the Al concentration between both samples, far superior to the 1% usually associated to the uncertainty of the MBE deposition process. Such difference in the Al concentration could shift the absorption peak from the designed 9.3 μm to 10.04 μm and 9.6 μm .

The electron mobility as a function of T is presented on figure 1. The obtained values are lower than usually cited in Literature [2] for bulk electron mobility.

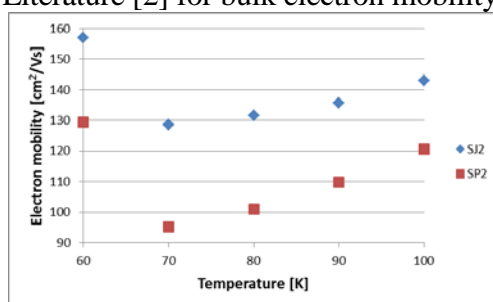


Figure 1: Electron mobility on samples at different temperatures.

The sensitivity of E_a and of the Al concentration as a function of a small perturbation in the temperature is presented on figure 2. Notice that an error of 2K in the measure of temperature results in considerable difference in these parameters.

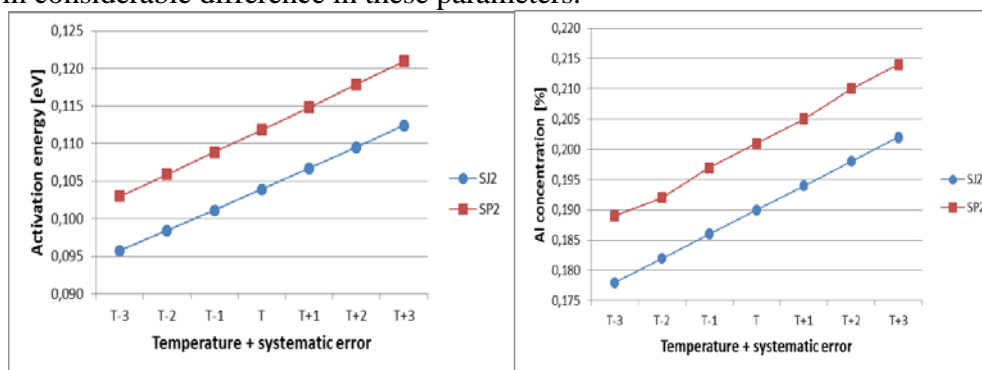


Figure 2: Sensitivity of parameters as a function of temperature.

The forecasts presented here can be confirmed by more controlled and specific experiments.

References

- [1] G. S. Vieira et al; *Resonantly enhanced photon-assisted tunnelling in a multiple quantum well superlattice*, Physical Review B, 7136-7140, 58 (1998).
- [2] N. Li et al; *Dark current of GaAs/AlGaAs quantum well infrared detectors*; Appl. Phys. A, 701, 89 (2007).

Author Index

- An Z, 91
Ando Y, 227
Arai J, 153
- Babbar V. K, 75
Beck U, 205
Bendada A, 17
Bison P, 5
Bo Y, 141
Boehnel M, 47
Bortolin A, 5
- Cadelano G, 5
Chelabi M, 63
Chen Z, 77
Chiariello A, 81
Cho C-H, 159
Cho J-H, 111
Cho Y, 117
Cho Y-H, 133
Choi D, 117
Choi J-H, 129
Chun Y-D, 129
Chung D-H, 159
Cong M, 219
- Daschewski M, 205
Dastoori K, 207
De Melo M. T, 203
De Oliveira A. J. B, 243
Delfino C, 259
Demy P, 25
Dobmann G, 79
Duan Y, 41
Dumoulin J, 11
- Feng B, 91, 185
Fernandes H, 35
Ferrarini G, 5
Fontaine J, 137
Fujiwara A, 153
Fukuoka K, 57
- Gerlach N, 25
Gjonaj E, 141
Gyoda M, 187
- Hacib T, 23
Harrer A, 165
Hassler U, 1, 7
- Hedayati Vahid P, 53
Hesabi S, 53
Ho Q-V, 165
Holub W, 47
Hong D-K, 129
Hu J, 147
Hwang K-H, 197
- Ibarra-Castanedo C, 17, 25, 29, 41
Ichihara T, 79
Ishikawa T, 165
- Jang J-H, 133
Jang J-S, 97
Jankowski P, 213
Jeong H-G, 159
Jorks H. V, 181
Jung I-S, 135
- Kang W-S, 133
Kawagoe I, 57
Kim B, 117
Kim B-T, 97
Kim D-J, 129
Kim D-K, 111, 159
Kim D-Y, 197
Kim H-Y, 131
Kim K-H, 133
Kim Y-B, 131
Kim Y-K, 135
Kobayashi M, 153
Kollorz E, 47
Kong D, 219
Koo D-H, 129
Krause T W, 75
Kreutzbruck M, 205
Kriesel Sperotto L, 251
Kurita N, 165
Kusakabe M, 255
- Lange T, 205
Le Bihan Y, 63
Lecomte-Beckers J, 25
Lee J-H, 197
Lee J-J, 135
Lee W-Y, 131
Lee Y-H, 197
Lepine B, 75
Li W, 123
Liu K, 105, 147, 191
Liu L, 171
López F, 29

Luan M-Y, 85
Luo Y, 141, 235

Ma C, 235
Machado J.M, 177
Makin B, 207
Maldague X, 11,17, 25, 29, 35, 41, 53
Mandelis A, 3
Marques G. N, 251
Mertens A, 25
Miki H, 137
Mohr S, 47
Momente J.C, 177
Montrieux H-M, 25
Murakami I, 227

Nakano H, 209
Nakano M, 209
Nakashima K, 227
Neves L. A, 177
Nicolau V, 29
Nicolazzo M, 81

Ohsaki H, 255
Ookubo T, 255
Osman A, 41

Paoletti D, 17
Park M-K, 197
Park Y-U, 111
Passaro A, 251, 259
Pedroso D, 259
Pinto S. R. A, 177
Prager J, 205

Rhyu S-H, 111, 135
Roytgarts M, 69
Rubinacci G, 81

Santos E. A. B, 243
Santulli C, 17
Sarasini F, 17
Sato S, 77
Sato T, 77
Sekino M, 255
Sfarra S, 17
Shimada T, 227
Shin P-S, 131
Smirnov A, 69
So J-Y, 71, 159

Takagi T, 77, 79, 137

Takahashi K, 165
Takahashi M, 137
Takeno T, 137
Tamburrino A, 81
Th  roux L-D, 11
Thompson D, 207
Tsuchiya K, 209

Uchimoto T, 77, 79
Underhill R, 75
Urayama R, 77

Val  ncio C. R, 177
Ventre S, 81
Vieira G, 259


Wang H, 105, 191
Wang N, 171
Wang P, 137
Wavrik J. F. A. G, 243
Wei Y, 105, 147, 191
Weiland T, 181
Weise M, 205
Woloszyn M, 213
Woo B-C, 129
Wu X, 219

Xie S, 79
Xu J, 85, 219
Xu M, 91, 185
Xu Y, 105, 123, 191

Yang S, 131, 137
Yanyu W, 123
Yonemori H, 113
Yoshida Y, 37

Zafalon G. F. D, 177
Zhai C, 185
Zhang C, 235
Zhang X, 141, 235
Zhao M, 191
Zhou H, 171
Zhu G, 147
Zhu Z-W, 85
Zou J, 105, 123, 147, 191

ISBN 978-2-9809199-4-7



É. du CAO

*à la frontière des connaissances
at the cutting edge of knowledge*